DOCTORAL THESIS

Vortex induced hydrodynamic impact upstream of sluice gates

submitted in satisfaction of the requirements for the degree of

Doctor of Science in Civil Engineering

of the Vienna University of Technology, Faculty of Civil Engineering

---

DOKTORARBEIT

Wirbelinduzierte, hydrodynamische Belastung unterströmter Schütze

ausgeführt zum Zwecke der Erlangung des akademischen Grades eines

Doktors der technischen Wissenschaft

eingereicht an der Technischen Universität Wien, Fakultät für Bauingenieurwesen

von

Dipl.-Ing. Irina KAMPEL

Matrikelnummer: 0440139

Schliemanngasse 9/21, 1210 Wien

Betreuer:

Ao.Univ.Prof. Dipl.-Ing. Dr.techn. Reinhard PRENNER

Institut für Wasserbau und Ingenieurhydrologie, Technische Universität Wien

AT-1040 Wien, Karlsplatz 13

Gutachter:

Prof. Sigurdur M. GARDARSSON Ph.D.

Faculty of Civil and Environmental Engineering, University of Iceland

IS-107 Reykjavik, Hjardarhagi 6

Prof. Dr.Eng. Dimitar KISLIAKOV

Faculty of Hydraulic Engineering, UACEG Sofia

BG-1046 Sofia, 1 Hristo Smirnenski Blvd.

Wien, September 2017 _____

Abstract

This investigation concerns three-dimensional flow effects upstream of sluice gates and the influence on the pressure conditions at the gate leaves. Depending on the gate openings of a weir structure or its location relative to the main flow, asymmetric flow conditions may be established. The piers of the weir structure are a flow obstacle causing a boundary layer to separate and the formation of a vortex, which is elongated and drawn under the gate by the flow. Its intensity and location depends mainly on the geometric parameters determined by the weir structure.

The pressure on an underflow gate depends on the local characteristics of the flow. Even in a parallel flow and with no vortex the time mean pressure deviates substantially from hydrostatic. The flow asymmetry and the vortex as well as turbulent fluctuations create additional complexity.

Using physical hydraulic models, pressure measurements were obtained at ten locations on two geometrically similar gates to obtain the pressure distribution. In order to change the flow inlet conditions, the geometry of the weir structure was altered by varying the gate openings, total hydraulic head and pier head lengths. Tests were performed at two model scales. The quasi-static and the dynamic components of the pressure were determined from the time series obtained in the model, by applying statistical analysis to the random data. Hence a stochastic description of the pressure distribution was obtained.

The measurement and modelling techniques were investigated, including the type of pressure sensors and measurement time and rate, alteration of the geometry, and impact of surface waves. Linear wave theory and spectral subtraction was successfully applied in order to filter the contribution of surface fluctuations to the pressure fluctuations.

Dimensional analysis was used in order to obtain characteristic parameters describing the geometry, flow and pressure conditions. Therefore charts could be provided to estimate both the quasi-static pressure and amplitudes of pressure fluctuations in prototypes. In addition, amplitude spectra indicate the dynamic aspect of the pressure fluctuations. The results allow estimating the location of vortex formation and the determination of the pressure conditions with and without influence of a vortex. Further a reduction of the discharge capacity due to increasing vortex intensity was identified by comparing the calculated discharge coefficients with data from the literature.

Contents

Symbols

notation	description	unit
a	gate opening	m
A	discharge area under sluice gate	m^2
b	gate width	m
B	mechanical damping coefficient	kg/s
C	spring constant	kg/s^2
C_c	contraction coefficient	-
C_d	discharge coefficient	-
C_h	piezometric head coefficient	-
C_p	pressure coefficient	-
$C_{p,d}$	pressure coefficient derived from data	-
$C_{p,f}$	fitted/predicted pressure coefficient	-
$C_{p'}$	pressure fluctuation coefficient	-
$C_{p',\mathrm{rms}}$	normalised root-mean-square of pressure fluctuations	-
C_{p+}, C_{p-}	coefficient of max. positive and negative pressure	-
$C_{p\pm}$	total maximum deviation of pressure	-
D	dynamic magnification factor	-
$|D(\tau)|$	noise spectrum	mm or -
f	frequency	Hz, 1/s
f_0	natural frequency of a system	Hz, 1/s
f_n	normalised frequency	-
F	force	N
F_d	force derived from data	N
F_f	force derived from fit/prediction	N
F	Froude number	-
g	acceleration of gravity	m/s^2
h_0	approach hydraulic head	m
$\overline{h}_0$	mean approach hydraulic head	m
h_1	downstream hydraulic head	m

$h'_{0,\text{rms}}$	root-mean-square of water surface fluctuations	m
$h'_{0,\text{rmsn}}$	normalised root-mean-square of water surface fluctuations	-
h_p	piezometric head	m
$\overline{h_p}$	mean piezometric head	m
h'_p	fluctuations of the hydraulic head	m
$h'_{p,\text{rms}}$	root-mean-square of piezometric head fluctuations	m
H_0	approach energy head	m
$|H(\tau)|$	spectrum of water surface fluctuations	mm or -
Im	imaginary	
k, l, m	fitting parameters	-
l_p	pier head length	m
L	characteristic length	m
m	mass	kg
p	hydrodynamic pressure	Pa
$\overline{p}$	mean hydrodynamic pressure	Pa
p'	pressure fluctuations	Pa
p'_{rms}	root-mean-square of pressure fluctuations	Pa
p_h	hydrostatic pressure	Pa
$P(\omega)$	hydrodynamic pressure in the frequency domain	Pa
Q	discharge	m³/s
R	Reynolds number	-
$R_p(\tau)$	auto correlation coefficient	-
$R_p(\Delta z)$	correlation coefficient	-
Re	real	
S	Strouhal number	-
$S_p(\omega)$	spectral density function of head fluctuations	m²/Hz
t	time	s
T	time period	s
TR	transmissibility ratio	-
v_0	approach flow velocity	m/s
V	characteristic flow velocity	m/s
W	Weber number	-
$x, \dot{x}, \ddot{x}$	displacement, velocity, acceleration	m, m/s, m/s²
x	streamwise coordinate	m
$|X(\tau)|$	spectrum of filtered pressure signal	mm or -
y	lateral coordinate	m
Y	relative lateral distance from left pier	-
$|Y(\tau)|$	spectrum of measured pressure signal	mm or -
z	vertical coordinate	m

Z	relative position above gate lip	-
γ	specific weight	kN/m^3
ϵ	error	-
ζ	damping factor	-
θ	phase angle	rad
$\theta(\omega)$	Fourier phase spectrum	rad
κ	amplification factor	-
λ	scale factor	-
ν	kinematic viscosity of water	m^2/s
ρ	fluid mass density	kg/m^3
σ	surface tension	N/m
τ	period	s
φ	loss factor acc. to Knapp (1960)	-
ω	radian frequency	rad/s
o-x-x	discharge under left gate	-
o-o-x	discharge under left and central gate	-
o-o-o	discharge under all gates	-

Chapter 1

Introduction

Underflow of sluice gates in free surface flow causes formation of more or less pronounced, longitudinal, vertical vortices upstream of the gate. Several parameters influence the flow conditions upstream of the gate and thereby the vortex intensity. The research topic covered within this thesis concerns the intensity and the effect of these vortices on the flow and on the pressure conditions at the upstream face of the gate leaf. Therefore a hydraulic model study was performed.

1.1   Motivation

Gates are used for various tasks of hydraulic engineering. Movable over- or underflow gates permit control over discharge and water level, which is one of the main tasks concerning the management of a reservoir for hydro power, flood control, irrigation, drinking water supply or navigable waterways. As control structures in free surface flow they influence not only the safety and reliability of the hydraulic structure itself but also that of the respective hydraulic system. A gate failure can cause flood related consequences for the up- or downstream area, such as damage, economic loss, endangering living environment or even human life. Past gate failure was caused by ice problems, gate vibrations in general or due to seal leakage, hoist or supply failures, trunnion bearing problems, damage of the gate arms, corrosion or failure of the control system.

To meet the safety requirements of control structures the design aspects of gates include hydraulic, operational, site specific but also economic considerations. A specific challenge when designing gates is that they are often intended to operate during extreme events only and hence the experience of operation is small. Additionally the design and operation of weir structures and their control installations is diverse and not at all a standard solution, due to varying requirements and site specifications.

Nowadays radial (or tainter) gates are the most frequently installed movable gates controlling free surface flow. They are advantageous as no slots and only two bearings located above water level are needed, the required hoist capacity and the height of the superstructure can be comparatively low. The mechanical equipment is simpler and the stiffness of the gate

is higher. Finally the radial shape improves the discharge characteristics. Disadvantages are the concentrated load transmission at the downstream part of the piers, which requires proper distribution and anchorage of the force by an adequate pier design.

Nevertheless sluice gates were and still are constructed. They are preferable in case installation problems related to radial gates predominate or if old structures consisting of sluice gates are rehabilitated with modern construction. The space requirement to retract is smaller for sluice gates compared to radial gates. Further they have the advantage that the water load is distributed and hence the required length of the flume wall is smaller. Disadvantages to be taken into account are the requirement of gate slots, causing turbulence at high and sedimentation at low velocities. If not a slide but roller-mounted gate, the possibility of trash jamming in the wheels and the fact that the rotating wheels have to operate under water has to be considered. The rollers are mostly spaced to take equal load of the hydrostatic force, spreading the load. The alignment of the rollers is critical, as it can lead to overload if one roller fails. The requirement of a high overhead structure increases the expenses. Further sluice gates are mostly counterbalanced, reeved 2:1, which increases the loading on the superstructure and therefore its costs. In case of height limitations the position of the gate can be changed to horizontal when lifted. A comprehensive overview of the variety of possibilities to construct control structures as well as advantages and disadvantages is given in Lewin (2001).

Design loads for vertical lift gates specifically are given in the Engineer Manual 1110-2-2701 (U.S. Army Corps of Engineers, 1997) and for radial gates in the Engineer Manual 1110-2-2702 (U.S. Army Corps of Engineers, 2000). The German standard DIN 19704-1 - Criteria for design and calculation (Deutsches Institut für Normung, 2012) deals with the design of hydraulic steel works and hence all types of gates.

In designing gates it is usually assumed that considering the hydrostatic pressure to increase linearly with depth according to Figure 1.1a is on the safe side. This is because due to the flow under the gate part of the potential energy is transferred to kinetic energy and hence the total horizontal force acting on the gate is reduced. The hydrodynamic pressure distribution is outlined in Figure 1.1b. As led by the walls of a channel, the flow approaches the gates
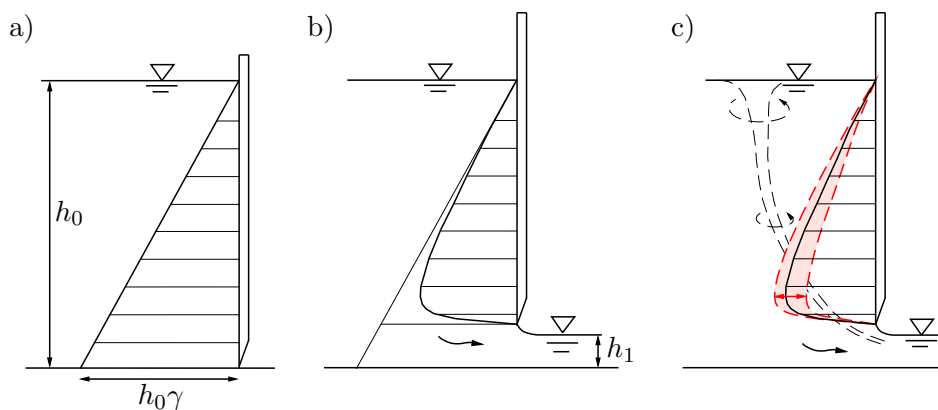
FIGURE 1.1: Pressure on gate: a) hydrostatic, b) mean dynamic, c) fluctuating (Kampel et al., 2017)

straight. Hence vortices as depicted in Figure 1.1c form symmetrically in each corner of the gate. They are rather weak and have little influence on the gate pressure.

The topics covered by scientific publications dealing with underflow gates mostly concern their discharge characteristics. For experimental investigations and numerical approaches basic flow conditions are considered by reducing the flow conditions to a two-dimensional problem and supposing irrotational flow. Within a smaller amount of publications the pressure distribution over the submerged part of gates is investigated. Analyses concerning horizontal pressure fluctuations due to upstream vortex formation have not been found during extensive literature research. Vertical and horizontal gate vibrations due to flow separation at the gate lip and its influence on the structure have been investigated intensively, especially for gates in submerged flow with a flat gate lip (*e.g* Naudascher and Rockwell, 1994).

1.2   Objectives of the study

When it is considered that weir structures are usually located at one side of a river or reservoir and consist of several gates, clearly the flow approaching the gates is asymmetric. As compared to symmetric approach flow conditions where two vortices form in each corner of the gate, only one vortex with comparatively high strength generates upstream of the gate due to asymmetric flow conditions as depicted in Figure 1.2. The flow conditions leading
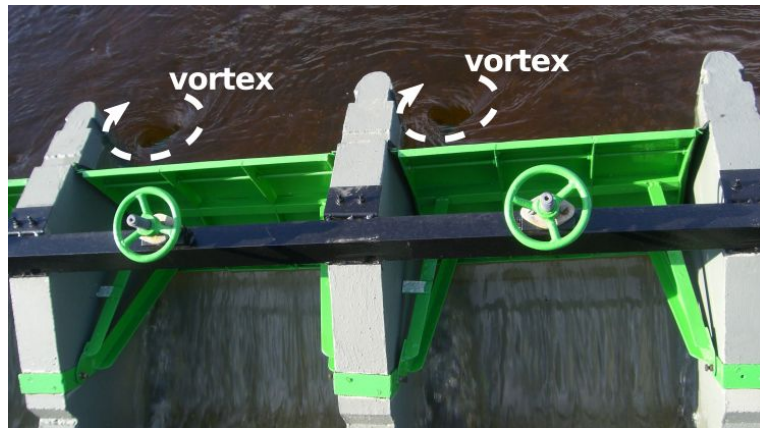
FIGURE 1.2: Flow conditions upstream of model gates

to the vortex formation influence the pressure distribution and fluctuations. The dynamic impact induced by turbulence and vortex generation is the main research topic of this thesis. To investigate this phenomenon the cross sectional view depicted in Figure 1.1 has to be analysed to a three dimensional problem.

For the investigations presented subsequently, a three dimensional physical model of a weir structure with asymmetric approach flow conditions was set up. In order to achieve well defined and simple boundary conditions planar sluice gates were used as control structures. The model set-up allows investigations of the impact on gates taking real flow effects into account.

The aims of this study include

- the interconnection of the hydraulics of underflow gates, approach flow conditions, vortex formation and hydrodynamic impact,
- the investigation of pressure distribution and fluctuations on sluice gates by means of hydraulic model tests,
- the evaluation of hydraulic model effects,
- the identification of the sources of pressure fluctuations at the gate,
- the determination of the connection of vortex formation and pressure conditions,
- further the investigation of geometric parameters influencing the vortex intensity and pressure conditions,
- the development of a general, dimensionless description of the pressure conditions,
- and the analysis of the influence of the vortex on the discharge coefficient.

The results of the investigations should enable the designer to assess the pressure distribution and fluctuations due to turbulence and vortex formation for any gate design. Thus it can be estimated if the impact is significant for the design of the structure.

Chapter 2

Fundamentals and literature review

For the analysis of the flow phenomenon in focus different fields of hydraulic engineering have to be covered. Within this chapter an overview of the most relevant aspects as well as the state of research is given. In order to reveal interrelations of gate underflow, pressure conditions, vortex formation and hydrodynamic impact the respective topics are introduced. Finally consequences for structural considerations are outlined.

2.1   Hydraulics of underflow gates

Considering the underflow of gates according to potential flow theory, *i.e.* inviscid an irrotational, the Bernoulli equation can be formed between a point of reference, indicated by the subscript 0, and an arbitrary point at the flow as

$$\overline{h} + \frac{\overline{V}^2}{2g} = \overline{h}_0 + \frac{\overline{V_0}^2}{2g} \tag{2.1}$$

Where $\overline{h}$ is the hydraulic head and $\overline{V}^2/2g$ is the velocity head. Both are averaged over time as indicated by the overline. Rearranging Equation (2.1) the dimensionless piezometric head coefficient and pressure coefficient are derived as

$$C_h = \frac{\overline{h} - \overline{h}_0}{\overline{V_0}^2/2g} = 1 - \left(\frac{\overline{V}}{\overline{V_0}}\right) \quad \text{and} \quad C_p = \frac{\overline{p} - \overline{p}_0}{\rho\overline{V_0}^2/2} = 1 - \left(\frac{\overline{V}}{\overline{V_0}}\right) \tag{2.2}$$

respectively. These dimensionless parameters can be used to characterise the pressure conditions at a point of interest for any hydraulic problem dealt with. Looking at Equations (2.2) it is obvious that the pressure coefficients can be calculated through the corresponding relative velocity $\overline{V}/V_0$ solely. Evidently the pressure conditions are directly related to the flow velocity. This interrelation can be visualized by constructing the flow net, which consists of streamlines and equipotential lines characterising the local velocity and pressure respectively. The mesh size of the net is determined in order to achieve equal flow rates between two adjacent streamlines. The equipotential lines are perpendicular to the streamlines. Once the flow net is constructed the velocity distribution can be determined from

the discharge and the mesh size. Knowing the pressure at a defined point of reference, the local mean pressure $\bar{p}$ can be derived through Equations (2.2). At this point it has to be emphasized that by applying this approach neither viscous effects nor flow separation can be considered. (Naudascher, 1991)

A cross sectional view of the basic hydraulic problem investigated herein is depicted in Figure 2.1. It defines the boundary conditions for the two dimensional flow under a planar sluice gate and the basic geometric parameters. Further the streamlines and equipotential lines according to the potential flow theory are given by the dashed lines and pressure conditions at the gate and the gate opening are illustrated.
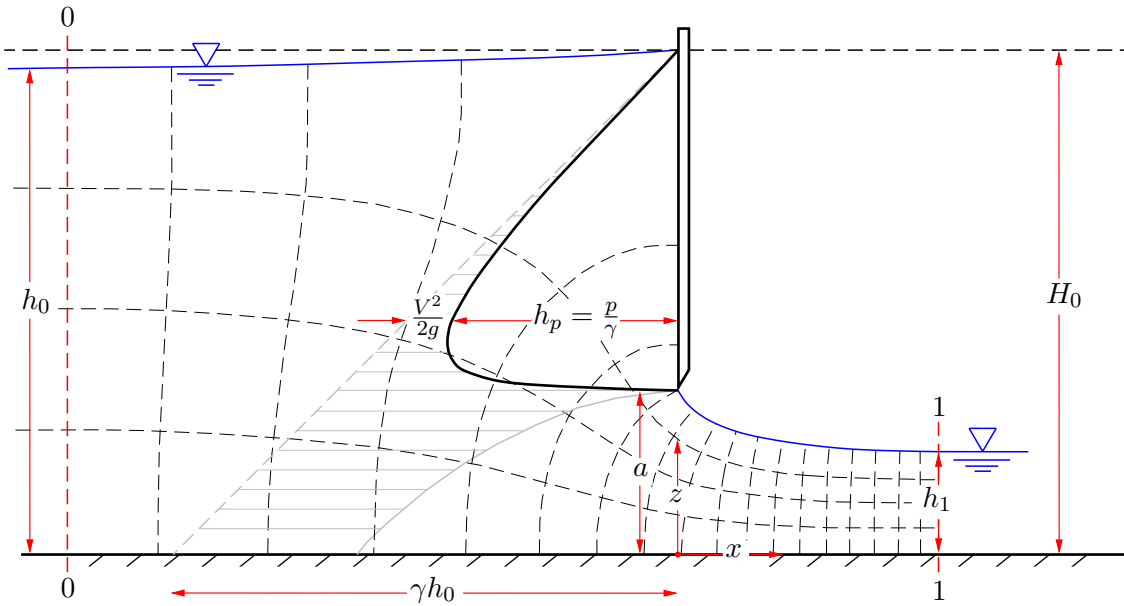
FIGURE 2.1: Hydrodynamic loading of a planar sluice gate after Knapp (1960), Naudascher (1991) or Bollrich (1996),

For the investigations within this thesis free outflow conditions are considered. That means so called modular flow conditions are assured where the downstream water level does not influence the upstream flow conditions and only losses upstream of the control section influence the upstream water level (Kolkmann, 1994). This is the case, as long as the water level downstream of the gate is smaller than the conjugate depth of the hydraulic jump. Corresponding equations to determine the downstream flow condition can be found for instance in Bollrich (1996) or Knapp (1960).

The deflected streamlines of the flow net in the figure above (2.1) allows to conclude that the velocity as well as the pressure is not equally distributed because of the gate's influence. It is known that the pressure at the gate lip and the water surface is zero and the resultant force can even be calculated through the momentum equation, but the actual velocity and pressure distribution over the submerged part of the gate as illustrated in Figure 2.1 is unknown. They depend on the shape of the flow boundaries including boundary layers and vortex formation. At the flow section directly below the gate lip the pressure increases non-linearly with depth. The highest velocities occur at the gate lip and decrease with

increasing depth and increasing pressure. Downstream of the gate the streamlines continue to converge and the water surface is inclined.

2.1.1   Discharge under gates

As long as the actual distribution of the velocity and the pressure is unknown at the area of deflected streamlines, discharge calculations at the location of the gate are precluded. Instead cross sections with parallel stream lines and hydrostatic pressure distribution have to be used. This is provided at section 0-0 and 1-1 in Figure 2.1.

The flow under a sluice gate can be described by rearranging the Bernoulli equation (2.1) formed for the energy conditions between an up- and a downstream cross section with parallel stream lines as

$$h_0 + \alpha_0 \frac{V_0{}^2}{2g} = C_c a + \alpha_1 \frac{V_1{}^2}{2g} + \Delta H_1 \tag{2.3}$$

The approach flow condition (section 0-0 in Figure 2.1) is expressed by the left side, whereas the condition at the downstream side (section 1-1 in Figure 2.1) are represented by the right side of Equation (2.3). h_0 is the upstream hydraulic head at the upstream cross section, and the corresponding velocity head is given depending on V_0. The hydraulic head at the downstream cross section is expressed as the confined jet $C_c a$, with the contraction coefficient C_c and the gate opening a, where

$$C_c = \frac{h_1}{a} \tag{2.4}$$

depending on the downstream water level h_1. The corresponding velocity head is expressed depending on the flow velocity V_1. Within Equation (2.3) viscous effects such as boundary layer and the corner eddy are represented by a total head loss ΔH_1. Further an influence of an non-constant velocity distribution can be taken into account through definition of the factors α_0 and α_1 at the respective cross section. Approaching the problem by computational methods the Navier-Stokes equations can be solved in combination with turbulence models to take turbulence effects into account. (Naudascher, 1991)

In Kolkmann (1994) a concept to consider component head losses is suggested. A factor to take entrance losses due to the change of cross section by the piers as a multiple of the velocity head into account is introduced. The coefficients α are used as before to account for non-constant velocity distribution in the flow section. At the downstream side of the gate the flow contraction has to be considered. For downstream submerged flow under a gate, further components of the total head losses are defined.

Knapp (1960) defines a coefficient of velocity φ accounting for friction and deflection of the stream lines. It is given in dependence of relative gate opening. The size of the factor is derived with experimental results by Gentilini (1947). Values for φ of 0.96-1 for relative gate openings a/H_0 from 0-0.4 where calculated for vertical sluice gates. Expressing the velocity of the confined jet by rewriting the energy equation between two cross sections with

parallel stream lines, the discharge can be calculated as

$$Q = \varphi C_c A \sqrt[2]{2g(H_0 - C_c a)} \tag{2.5}$$

where the parameters are used as noted above. In Knapp (1960) the equation is given in order to consider a lateral contraction of the discharge area and hence with two different contraction factors C_c. But as investigations concerning the lateral contraction are missing at the time of publication and the difference is of negligible size, the equation is given herein with the coefficient for vertical contraction C_c. In Knapp (1960) a universal discharge equation is derived by rearranging Equation (2.5) in order to get $q/(a\sqrt{a})$ on the left side, *i.e.* discharge curves depending on $q/(a\sqrt{a})$ and a/H_0 for different gate inclination could be derived.

To calculate the discharge under gates parallel and equidistant streamlines are assumed at the cross sections considered and viscous effects are neglected. Continuity equation is considered and a discharge coefficient is defined as

$$C_d = \frac{C_c}{\sqrt{1 + \frac{C_c a}{h_0}}} \tag{2.6}$$

expressed depending on the contraction coefficient C_c, gate opening a and approach hydraulic head h_0, which can be found in Bollrich (1996), Kolkmann (1994) or Naudascher (1991). Hence free discharge under sluice gates can be defined as a function of the discharge area A, acceleration of gravity g, approach hydraulic head h_0 and the discharge coefficient C_d as

$$Q = C_d A \sqrt{2gh_0} \tag{2.7}$$

for simplified boundary conditions. High Reynolds numbers at most prototypes support the neglect of viscous effects when calculating the discharge under gates. For a specific gate geometry the contraction coefficient C_c and therefore also the discharge coefficient C_d vary with the relation of the gate opening to the approach hydraulic head a/h_0. They are further influenced by the flow conditions specific to the gate geometry, such as the inclination of the gate or the shape of the gate edge.

2.1.2   Contraction and discharge coefficient in the literature

Due to the importance of the coefficients for determination of the discharge under gates and due to the variety of boundary conditions influencing the process, calculation and empirical determination of the contraction and discharge coefficient is a research topic widely investigated (compare Table 2.1). Historical data from empirical investigations compared and discussed in Knapp (1960), Roth and Hager (1999) or Kim (2007), lack information concerning the boundary conditions and hence are hard to evaluate by means of model and scale effects. Lewin (2001) points out the wide scatter of available data of discharge and contraction coefficients.

Belaud et al. (2009) present clear graphs comparing calculated and experimentally derived values of C_c as a function of the relative gate opening from different published studies (Figure 2.2). Kim (2007) gives an overview of theoretical and experimental investigations of
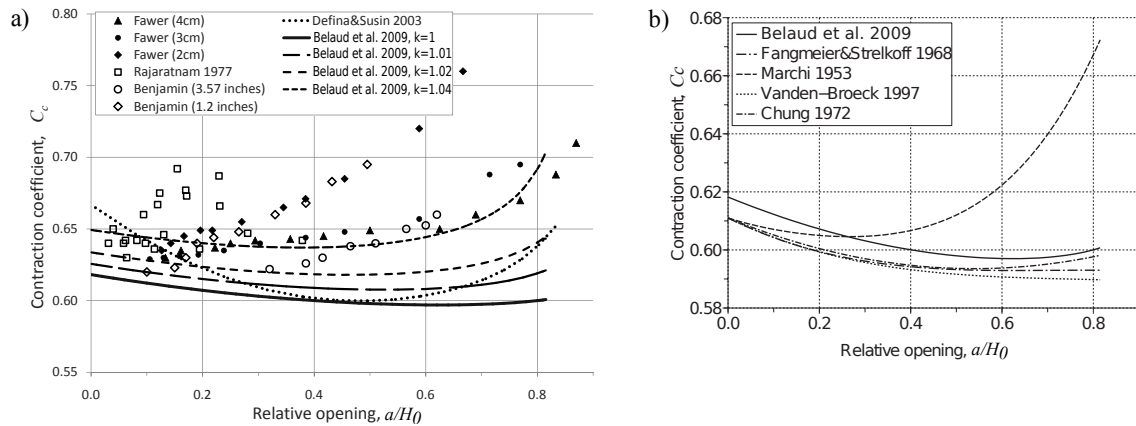
FIGURE 2.2: Contraction coefficients (Belaud et al., 2009): derived from a) experimental investigations and b) theoretical approaches

the contraction coefficient C_c. The empirical data is usually above the theoretical values, as derived from potential flow theory and hence neglecting losses, viscosity and turbulence. As a function of the relative gate opening theoretical and experimental results have opposing trends (compare Figure 2.3). Comparable discharge coefficients C_d obtained from model tests fit the theoretical data derived by potential flow theory better. The objective of experimental investigations at a later date together with numerical models, is the determination or elimination of the discrepancies of model and theoretical results as well as the investigation of real flow effects.

Discrepancies between empirical and theoretical determined contraction coefficients C_c are addressed *e.g.* in

- Knapp (1960) where experimental data of the contraction coefficient C_c by Smetana (1937) are compared to theoretical calculations by Koch and Carstanjen (1926) and are found to be 6 % above them,

- Rajaratnam (1977) where the empirically determined values of C_c were found to be 10-14 % larger compared to theoretical calculations from literature, *e.g.* Benjamin (1955), Fangmeier and Strelkoff (1986), Larock (1969), Pajer (1937) giving C_c as a function of a/H_0,

- Montes (1997) where reasons for the exceeding of experimentally derived C_c for about 10 % compared to calculations from potential flow theory are analysed,

- Belaud et al. (2009) where the calculated contraction coefficient C_c including correction factors up to 4 % (assigned to kinetic energy correction, pressure variations and head loss due to friction in boundary layers and turbulence due to large scale structures) is compared to model test results,

- Habibzadeh et al. (2011) where the discharge coefficient is calculated by neglecting energy loss and subsequent introduction of a factor based on model tests by Rajaratnam and Subramanya (1967) considering losses of 6.2 % of the velocity head, which

are mainly assigned to the horizontal recirculation zone is derived for free flow under a sluice gate,

· Webby (1999) where field data of prototype radial sluice gates is used to calculate the contraction coefficient and compared to theoretical values of C_c, where energy losses were of 1.8-4.5 % were determined for one prototype, whereas the other one could not support the hypothesis.

These discrepancies can be caused by model effects such as

· the precision of the geometry in general,

· the precision of the gate edge (Knapp, 1960; Smith, 1977; Naudascher, 1984),

· the precision of water level measurement (*e.g.* due to fluctuating water level) (Smith, 1977; Noutsopoulos and Fanariotis, 1978)

and scale effects, particularly for small scale models such as

· overestimation of frictional losses due to viscosity or boundary roughness (Naudascher, 1991),

· effects of surface tension (Naudascher, 1984)

which are indicated by

· an increasing contraction coefficient C_c with a/H_0 as it is mentioned in Knapp (1960) and Roth and Hager (1999)

· or a dependency of the discharge coefficient C_d as a function of a/H_0 on the absolute gate opening a as it occurs for gate openings below the limit value for scale effects in (Roth and Hager, 1999).

Finally real flow effects occurring in physical models as opposed to numerical ones, namely

· boundary layer formation (Rajaratnam, 1977; Montes, 1997; Naudascher, 1984),

· relative boundary roughness (Naudascher, 1984; Speerli and Hager, 1999)

· angle of departure (Montes, 1997),

· horizontal surface eddy or recirculation zone (Rajaratnam and Humphries, 1982; Montes, 1997; Roth and Hager, 1999; Nago, 1984; Habibzadeh et al., 2011; Naudascher, 1984),

· longitudinal vortex (Montes, 1997; Speerli and Hager, 1999; Roth and Hager, 1999; Naudascher, 1984),

· approach flow conditions and similarity of separation (Noutsopoulos and Fanariotis, 1978; Naudascher, 1984)

can cause discrepancies of results derived by numerical calculations or model tests compared to prototype results. Figure 2.3 shows scale and real flow effects on the contraction coefficient and thereby illustrates the opposing trend of C_c derived by theoretical and physical investigations respectively. The influence of boundary layer formation was estimated through the calculation of boundary layer thickness according to measured or calculated flow velocities
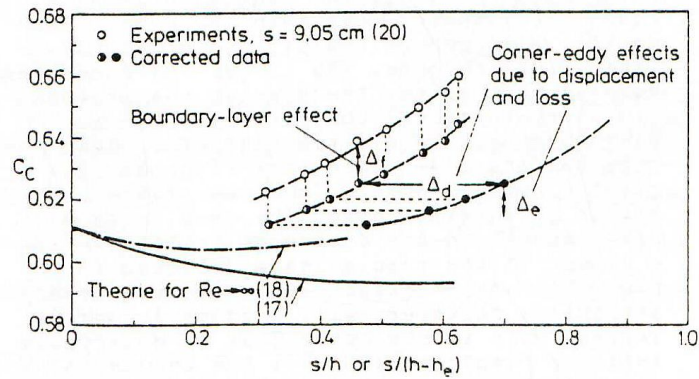
FIGURE 2.3: Scale effects concerning the contraction coefficient C_c (Naudascher, 1984)

and were found to be rather unimportant (Rajaratnam, 1977; Montes, 1997). Values for the contraction coefficient derived depending on the discharge capacity $C_c(q)$ by rearranging Equation (2.6) and (2.7) are below measured contraction coefficients C_c according to Noutsopoulos and Fanariotis (1978). Hence $C_c(q)$ are in better accordance with theoretical results from literature. Further reported discharge coefficients C_d calculated from discharge measurements agree with experimental results from literature, whereas calculated values C_d from measured contraction coefficients are closer to theoretical approaches, which generally exceed experimental results. Three-dimensional flow effects rather than boundary layer development are judged to account for the discrepancies between experimental and theoretical results. Montes (1997) relates the energy losses causing the discrepancies to the vortex system (horizontal surface vortex and vertical corner vortices) upstream of the gate, which is supported by Speerli and Hager (1999) with illustrative photographs of air entraining corner vortices in a model of a bottom outlet. Further experimental data without vortex formation presented in the closure to Montes (1997) fits theoretical results. Subsequently the vortex formation can be assumed to influence the flow characteristics decisively. Finally Montes (1999) supports the connection of energy loss and vortex formation, as the inclination of gates or radial gates, as in Webby (1999), reduce or even prevent vortex formation and the discrepancies between theoretical and measured data become very small. Knapp (1960) found that the influence of the gate inclination depends on a/H_0. Upstream leaning gates are preferable for a/H_0 below ~ 0.75, because the losses due to deflection are reduced. For larger a/H_0 frictional losses become dominant and the discharge was found to increase with increasing angle of the gate to the horizontal. In Hecker (1987) the dependency of the inlet loss coefficient on the vortex type is discussed. According to measurements by Padmanabhan (1982) swirling flow without aircores do not influence the entrance loss, whereas air entraining vortices continuing to the intake do as found in Anwar et al. (1978) and Dagget and Keulegan (1974).

Author	Methodology	Results
Von Mises (1917)	Potential flow theory (inviscid fluid, free surface upstream of the gate is a horizontal plane, neglect of gravitational effects on the contraction).	Decreasing C_c with increasing a/H_0.
Chung (1972), Perry (1957), Benjamin (1956)	Potential flow theory (inviscid fluid, free surface upstream of the gate is a horizontal plane).	Decreasing C_c with increasing a/H_0 (reported by Kim, 2007).
Fangmeier and Strelkoff (1968), Montes (1997), Vanden-Broeck (1997)	Potential flow theory.	Decreasing C_c with increasing a/H_0 (reported by Kim, 2007).
Gibson (1918), Fawer (1937), Benjamin (1956)	Phys. model tests.	Increasing C_c with increasing a/H_0 (reported by Kim, 2007).
Anwar (1964)	Derivation of C_c and C_d, streamlines and pressure distribution for different gate types assuming inviscid fluid.	Slightly increasing C_c with a/h_0, experimental results above theoretical values, measured gate pressure distribution exceeds calculated, specifically close to the opening.
Rajaratnam and Subramanya (1967)	General flow equations for free and submerged flow, validation with phys. model tests: $l = 4.87\,m$, $w = 45.72\,cm$, $h = 91.44\,cm$, $a = 2.54\text{-}15.24\,cm$, sharp edge.	C_d for free flow slightly increasing.
Rajaratnam (1977)	Phys. model tests $l = 5\,m$, $w = 31.12\,cm$, $h = 91\,cm$, $a = 2.54\text{-}10.16\,cm$, sharp edge, free flow.	C_c, downstream water surface and pressure profile, boundary layer thickness.
Rajaratnam and Humphries (1982)	Phys. model tests: $l = 5\,m$, $w = 31.12\,cm$ and $h = 91\,cm$, $a = 1\text{-}5\,cm$, sharp edge, free flow.	Velocity and pressure at the channel bottom, characterisation of horizontal surface eddy upstream of the gate (rel. thickness $= 0.28H_0$).
Nago (1984)	Phys. model tests: $w = 10, 20, 30\,cm$, $a = 1.0\text{-}12.0\,cm$, sharp edge, R and W varied.	Influence of scale effects on streamline pattern and C_c.

Continued

Author	Methodology	Results
Finnie and Jeppson (1991)	Finite element model using the $k - \epsilon$ turbulence model applied to flow under a sluice gate, validation wit phys. model tests $l = 9.1\,\mathrm{m}$, $w = 0.46\,\mathrm{m}$.	Results from the experiments were used to set the boundary conditions for the model, calculations and measurement in good agreement.
Montes (1997)	Numerical solution of inviscid flow under planar gates (conformal mapping between the physical plane and the complex potential plane).	Discrepancies to experimental results (energy loss due to vortices upstream of the gate), C_c, water surface profile, gate pressure, bottom pressure, velocity distribution at gate opening.
Roth and Hager (1999)	Phys. model tests: $l = 7\,\mathrm{m}$, $w = 24.5$, 35.0 and $50.0\,\mathrm{cm}$, $h = 60\,\mathrm{cm}$, $a = 1.0\text{-}12.0\,\mathrm{cm}$, sharp edge	Limit values for scale effects, pressure distribution on channel bottom and gate, velocity distribution, shock waves, intensity of corner vortices, C_d.
Defina and Susin (2003)	Calculations based on the Bernoulli equation, validation with phys. experiments $l = 20\,\mathrm{m}$, $h = 50\,\mathrm{cm}$, $w = 38\,\mathrm{cm}$, sharp edge tilted.	Flow regimes (submerged, free outflow, undisturbed flow) appearing at underflow gates for super- and subcritical approach flow and range of ambiguity (hysteresis as a function of F of approach flow and gate opening to critical depth).
Kim (2007)	Numerical calculation of free flow under sluice gate using Reynolds averaged Navier-Stokes equations (FLOW-3D).	Energy losses specific for $a/H_0 > 0.4$ show in the results of C_c decreasing with increasing a/H_0 until 0.4, subsequently increasing, the gate pressure distribution and the decrease of the upstream water surface profiles; rapid water surface fluctuations for $a/H_0 > 0.4$ are associated with the losses.
Belaud and Litrico (2008)	Potential flow theory (invicid fluid), assuming a distributed sink at contraction	Velocity and pressure distribution (in agreement with Montes, 1997).
Belaud et al. (2009)	Calculations based on energy conservation and momentum equation, combined with potential flow theory (Belaud and Litrico, 2008)	C_c and C_d for free and submerged flow.

<div align="center">Continued</div>

Author	Methodology	Results
Habibzadeh et al. (2011)	Calculation of C_d (Torricelli's law, Momentum equation) and introducing a loss coefficient based on model test results.	C_d for free and submerged flow.
Cassan and Belaud (2012)	Up- and dowstream flow characteristics of sluice gate are calculated (Reynolds averaged Navier-Stokes equations)	Analysis of mesh sizes and turbulence models and evaluation with experiments.
Erdbrink et al. (2014a)	Flow simulations combined with discharge model based on gate flow equations.	Determination of optimal gate operation regulation concerning discharge and water level and local flow characteristics, influencing waterway management, flow-induced vibrations, scouring, ecological topics.

TABLE 2.1: Published investigations concerning underflow of gates

The thorough research on flow under gates documents the problems to take into account when performing model tests concerning the under flow of gates. It further gives an impression of the importance of three dimensional (3D) flow effects and turbulence on the flow characteristics, their complexity and the scarce amount of investigations regarding actual flow processes at prototypes, *e.g.* asymmetric approach flow.

2.1.3 Empirical approach to calculate the discharge

In "Design of Small Dams" (USBR, 1987) it is suggested that the discharge over a gate-controlled ogee crest is similar to an orifice and is calculated after

$$Q = CDL\sqrt{2gH} \tag{2.8}$$

where H is the head to the center of the gate opening (incl. approach velocity head), D is the shortest distance from the gate lip to the crest, L is the crest width and C is discharge coefficient. The notation in Equation (2.8) is kept as in USBR (1987) as the definition of the parameters deviates from Knapp (1960), Naudascher (1991) and Bollrich (1996).

Through the coefficient C considerable parameters influencing the stream lines are the shape of the crest and type of gate. Hence the discharge coefficient is given for different angles of an opening (angle between tangent to the gate lip and tangent to the crest curve) and gate locations (at the crest or downstream of the crest). The diagram is developed on the basis of data gained form radial gate prototypes and models discharging through three or more gates (U.S. Army Corps of Engineers, 1977). According to USBR (1987) the diagram can be applied for radial and leaf gates.

U.S. Army Corps of Engineers (1977, sheet 312) gives information concerning vertical lift gates on ogee crests. In case of discharge under high head it is referred to Equation (2.8). For discharge under low head a digram relating ungated and gated discharged is derived. Its application requires the knowledge of the rating curve of ungated discharge.

2.1.4   Pressure distribution on underflow gates

Even though the pressure distribution is unknown, the resultant force can be calculated through the momentum equation if the discharge is known. The momentum equation is formed between an upstream and a downstream cross section with parallel stream lines (section 0-0 and 1-1 in Figure 2.1) as

$$F = \rho g b h_0 \left(\frac{h_0}{2} + \frac{V_0{}^2}{2g} \right) - \rho g b h_1 \left(\frac{h_1}{2} + \frac{V_1{}^2}{2g} \right) \tag{2.9}$$

Neglecting losses, the energy and continuity equation can be used to express the downstream water level h_1 and downstream velocity V_1 depending on the upstream flow conditions (h_0, V_0). If h_0 and V_0 are derived from the approach flow conditions and h_1 and V_1 are substituted in Equation (2.9) the resultant force can be calculated. According to the definitions made in Section 2.1.1, the downstream water level can also be expressed through the contraction coefficient C_c. Subsequently if substituted in Equation (2.9), the horizontal force acting on the sluice gate can be calculated according to

$$F = \frac{\rho g b}{2}(h_0 - C_c a) \left(h_0 + C_c a - \frac{4 C_c a}{1 + C_c a / h_0} \right) \tag{2.10}$$

which is given in Naudascher (1991) and in Bollrich (1996) in a rearranged form. As the actual pressure distribution is still unknown, the line of action of the resultant force can not be calculated. Therefore efforts have to be made to derive the actual pressure distribution.

As water flows under a sluice gate potential energy is transformed to kinetic energy. Compared to the hydrostatic pressure on a gate the hydrodynamic pressure is diminished by the value of the local velocity head ($V^2/2g$). As the water pressure is equal in all directions, the pressure at the gate lip as well as at the elevation of the water level equals the atmospheric pressure. Hence the overpressure equals zero. For illustration of the qualitative pressure distribution in between those two points and definition of the parameters see Figure 2.1. If the actual hydrodynamic pressure distribution is determined by flow net analysis, briefly discussed in Section 2.1, or measurements at the prototype or a model the resultant force and its point of action can be derived through integration over a vertical cross section of the gate.

In Knapp (1960) a concept to approximate the pressure distribution, without deriving the flow net or performing measurements is presented. Losses between the up- and downstream of the gate are neglected and a discharge coefficient as in Equation (2.6) is introduced. In order to determine the velocity head, which equals the reduction of the hydrostatic pressure, a correction factor for the velocity distribution at the gate opening is defined as function of

of the relative gate opening a/H_0. Finally a factor K is derived as

$$K = \frac{C_c^2}{(1 + C_c a/h_0)(1.571 - 0.571 a/h_0)^2}$$ (2.11)

Subsequently the reduction of the hydrostatic pressure over the gate can be calculated at vertical location z after

$$\Delta h = K h_0 \frac{a^2}{z^2}$$ (2.12)

The results of applying the equation are illustrated in Figure 2.4, giving the pressure distribution for two gate openings and constant head-water level. Further Knapp (1960) gives
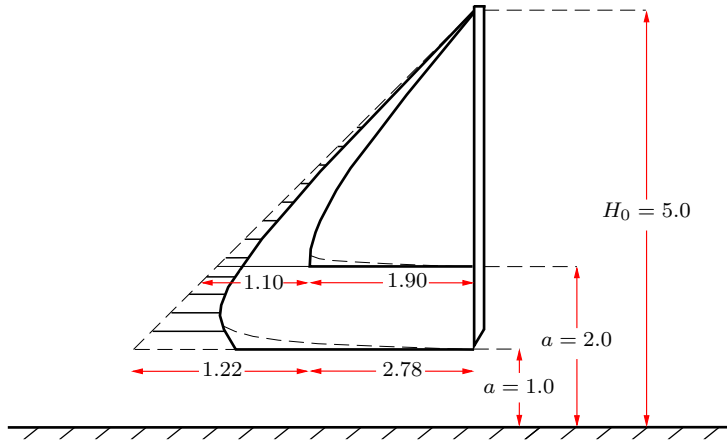
FIGURE 2.4: Pressure distribution over a sluice gate, as derived after Equation (2.12)
Knapp (1960)

a general equation, relating the total hydrodynamic pressure p to the total hydrostatic pressure p_h as

$$\frac{p}{p_h} = 1 - \frac{2K}{h_0/a - 1}$$ (2.13)

Besides the velocity distribution considered within the concept described above, the shape of the flow boundaries, boundary layer separation or reattachment and vortex formation influence the pressure distribution. (Knapp, 1960)

2.1.5   Available data concerning pressure distribution on underflow gates

Data concerning the pressure distribution on gates is mostly investigated and published together with other parameters characterising the flow under gates. The data is not as numerous and distributed as data concerning the contraction and discharge coefficient. Calculated and experimentally determined values presented in Finnie and Jeppson (1991) agree well. As do normalised pressure distributions presented in Montes (1997) in comparison with Finnie and Jeppson (1991). Normalised and to the maximum scaled results by Kim (2007) show good agreement with experimental results given in Roth and Hager (1999). A controversy was detected concerning approaches to calculate the pressure distribution of an inclined gate as the experimental data in Anwar et al. (1978) is above the calculations, but up to 4 % below the approach by Montes (1997) as presented in the closure (Montes, 1999).

From model tests Roth and Hager (1999) found the location of maximum pressure at a distance of 1/8 of the wetted part of the gate from the gate lip. From theoretical approaches Montes (1997) and Kim (2007) found the maximum in the range of about 0.1-0.3 and 0.05-0.2 of the wetted part of the gate respectively. The distance of the maximum to the gate lip increases with the relative gate opening. The pressure maximum decreases with the relative gate opening. Normalised to the velocity head at the gate lip it was found to be in the range of 0.6 to 0.9 in Montes (1997) and Kim (2007). These overall results are given in Figure 2.5 by Kim (2007).
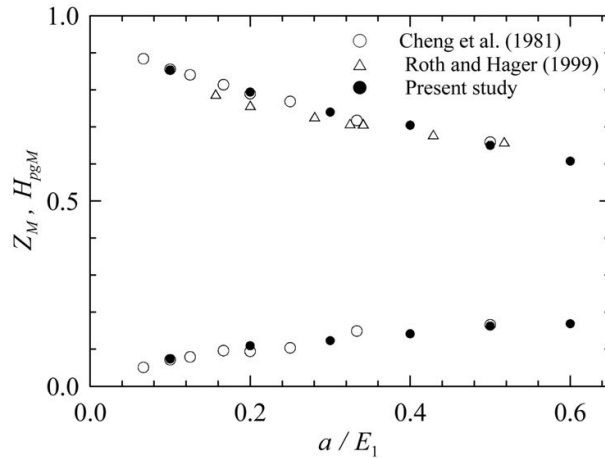
FIGURE 2.5: Normalised maxima of pressure and their location given in Kim (2007)

In Roth and Hager (1999) the pressure distribution close to the side walls was determined to decrease for 1-2 % compared to the axial measurement and the lateral upstream water surface profile at the gate indicates a decrease of the stagnation water level closer to the channel walls.

2.2 Vortices in fluid mechanics

Problems originating from vortices, *i.e.* swirl and air intake, are hydrodynamic impact, downstream effects such as hydropneumatic effects in closed conduits or shock waves in open channels, increased head loss, reduction of intake rate, vibration, cavitation and suction of debris among others. Associated air entrainment can cause the reduction of discharge capacity, generation of vibrations or noise. Hence the investigation of vortex formation is a common topic in hydraulic engineering and is frequently analysed in physical models, as it is within this thesis. The information on vortices given in this chapter provides a basis concerning the flow and pressure conditions due to vortices and for modelling vortices physically.

2.2.1 Basic properties of vortices

Swirling flow consists of a plane vortex with a superposed axial flow component (spiral vortex). To comprehend the properties of swirling flow a mathematical model of a planar

vortex named after the scientist and engineer Rankine is used. Thereby the core of the
vortex is described as solid body rotation (forced vortex) causing a flow field around it with
the characteristics of a potential (free) vortex. The tangential velocity of the particles in
the vortex core increases with the distance from the axis of rotation linearly as illustrated in
Figure 2.6a. The angular velocity in this area is constant. This is illustrated in Figure 2.6b
by the constant vorticity, which is defined to be twice the local angular velocity of the
fluid (Batchelor, 1967). The vortex core provides the kinetic energy for the free vortex
surrounding it. Hence the particles adjacent to the forced vortex have the largest tangential
velocity, which decreases with increasing distance from the axis (Figure 2.6a). As the
fluid elements do not change their direction while rotating around a common center, their
angular velocity and hence vorticity is zero (Figure 2.6b). Particles of a free vortex only
have vorticity if their axis coincides with the center of rotation of the vortex. The non-
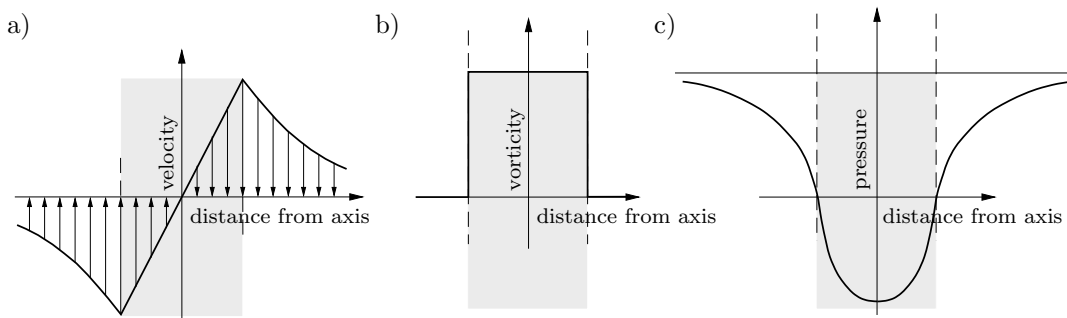
FIGURE 2.6: Flow characteristics of a vortex (after Lugt, 1983): a) velocity distribution,
b) vorticity, c) pressure distribution

linear decrease of the velocity at the outer part of the vortex part reveals shearing of the
fluid elements in the free vortex, whereas there is no shearing in solid body rotation. Due
to the shearing, kinetic energy is dissipated in the region of the free vortex. In case the
shear forces are not overcome by the kinetic energy added to the rotating system the vortex
decays due to decreasing tangential velocity with time, which obviously is accompanied by
a pressure increase. Turbulence of flow enhances the dissipation and therefore reduces the
time of decay. Further the time aspect of the decay, as well as the magnitude of the forces
acting, is influenced by the properties of the material the vortex forms in. Vortex-breakdown
comparable to a hydraulic jump occurs if the rotational component of the flow exceeds the
axial component. The break down is as a transition from a supercritical to subcritical
state, caused by the roll up of an unstable rotational flow layer, accompanied by enhanced
turbulence and fluctuation. The pressure of a Rankine vortex is distributed according to a
parabola, increasing towards the boundary of the forced vortex with increasing centrifugal
force. Increasing the distance from the axis further the range of the free vortex is reached and
the slope of the pressure distribution declines. With increasing vortex strength the pressure
at the axis of the vortex decreases. If the pressure in the center of a vortex decreases far
enough to separate water and gas, a hollow core around the axis of rotation forms.

2.2.2   Identification of vortices

As derived in Section 2.2.1 the existence of a vortex is connected to the angular velocity of flow which is described by the flow property called vorticity. Based on the concept of vorticity introduced by Cauchy and Stokes a vortex can be identified with respect to points in space in the fluid as a subject to the angular velocity. The vorticity of a flow field can be represented similar to streamlines by lines of equal vorticity. As any shear flow has vorticity, a vorticity field does not necessarily imply the existence of a vortex. But a vortex without vorticity does not exist. Even the center of rotation of a potential vortex has vorticity, referred to as vorticity line. Extending the center of rotation to a diameter exceeding zero, it consists of an isolated bundle of vorticity lines, a vortex tube. The main advantage of using the vorticity field instead of stream lines to identify a vortex is that it does not change with respect to different reference frames, as opposed to stream- or pathlines. Hence the vorticity is a convenient indicator for vortices.

Streamlines give an instantaneous picture of the velocity distribution. They are tangential lines to the velocity vectors at a point, at an instant of time. In order to identify vortices by means of streamlines regions with closed streamlines as in Figure 2.7a1 are looked for. Superposing vortex flow with parallel flow, the location of the axis of rotation is altered
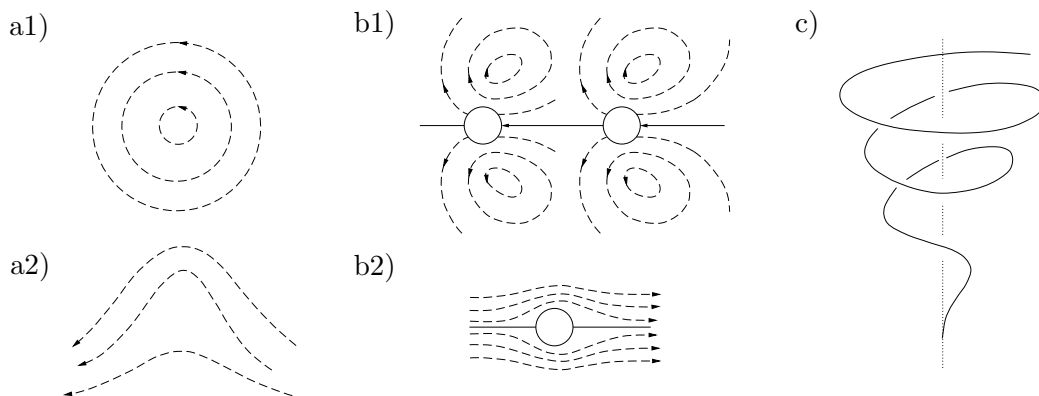
FIGURE 2.7: a1) Streamlines of a plane vortex, a2) a1 with superposed parallel flow, b1) and b2) Streamlines induced by a sphere moving from right to left in a fluid at rest different reference frames, c) path- or streakline of a spiral vortex (after Lugt, 1983)

relative to the observer. The streamlines are no longer closed but open up to wavy stream-lines (Figure 2.7a2). Nevertheless the vortex can be revealed introducing a reference frame moving with the velocity of the superposed flow. Thereby the alteration of the axis of rotation is eliminated, the flow is time independent and streamlines appear as in Figure 2.7a1. By this example after Lugt (1983) it is demonstrated that the streamlines are dependent on the reference frame. In another example it is laid out that closed streamlines can also exist if there is no vortex. Figure 2.7b1 shows the streamlines due to a sphere moving in a stagnant fluid in a reference frame stagnant relative to the fluid. Due to the conservation law of matter the streamlines have to be closed. But as a time independent common center of rotation is lacking, there actually is no vortex. Introducing a reference frame moving with the sphere time independent flow conditions are established and the streamlines are no longer closed (Figure 2.7b2). It can be summarized that closed or spiral streamlines can

be an indicator for vortices in steady flow conditions. To evaluate the time dependency of
the flow conditions in a specific reference frame, an identified region with closed streamlines
has to be compared at different instants of time. If the axis of rotation is constant a vortex
is identified.

Instead of defining the vortex with respect to the flow behaviour at a point in space by
streamlines or vorticity of flow, the properties of the fluid particles are described by path-
and streaklines. They can be made visible by adding tracers (*e.g.* ink) to the fluid (Fig-
ure 2.7c). The determination of path- and streaklines is a time-integration process. In time
independent flow the streamlines coincide with the path- and streaklines. Closed or spiral
trajectory of an individual fluid particle (pathline) indicate the existence of a vortex. If the
flow is time dependent only the streak lines are visualised by adding tracers. They connect
the locations of particles that passed the same point at any time and therefore differ from
pathlines. In case of vortex generation and stretching, streak lines of rotating fluids manifest
in spirals, directed from the outer edge toward the interior. In time dependent flow path-
and streamlines are a subject to time and reference frame.

A more recent discussion of definitions of vortices is given by Haller (2005), pointing out
the dependency on the reference frames and suggesting an objective definition on the basis
of the fluid trajectories and strain acceleration tensor.

2.2.3   Origin of vortices

For formation of vortices an initial rotation in the fluid is required. It can originate from
the slightest asymmetry in approach flow, boundary-layer flow or even non-homogeneous
temperature distribution. In the IAHR Hydraulic Structures Design Manual on Swirling
Flow Problems at Intakes (Knauss, 1987) the following aspects contribute to the initial
rotation in flow:

  · asymmetric approach flow conditions due to geometric conditions
  · eccentricity of an inlet compared to symmetric approach flow conditions
  · obstructions such as piers or separation walls
  · non-uniform velocity distribution due to boundary layer separation
  · external effects such as wind, wakes, currents

Approaching a common center of rotation the angular velocity of the fluid elements (vortic-
ity) subsequently increases with decreasing distance from the center of rotation (conservation
law of angular momentum), *i.e.* the angular momentum of a system is constant and pro-
portional to its angular velocity and the distance to the center of rotation. Accordingly in
Lugt (1983) a vortex is defined as: "... rotating motion of a multitude of material particles
around a common center."

Vorticity develops in the viscous layers adjacent to flow boundaries. If these boundary layers
detach from the surface, free shear layers are transported into the fluid. Consequently the
usually assumed frictionless flow outside of boundary layers has vorticity. Flow can separate
from its boundary either due to a body dividing the flow (kinematic separation) or due

to stagnation points at flow boundaries, induced by shearing/vorticity of the flow. The separation line is a function of the body shape and the flow and determines the vortex shape. The characteristic of the flow separation depends on the turbulence in flow and can be connected to the Reynolds number

$$\mathsf{R} = \frac{VL}{\nu} \tag{2.14}$$

depending on a characteristic velocity V and length L and the kinematic viscosity ν. Thereby the relation of inertia to viscous forces is characterised. Flow separates earlier the higher the Reynolds numbers are. Further the separation is oscillatory above and a steady state can be reached below a limit value. Lugt (1983)

2.2.4   Classification of vortices

The classification of vortices concerns the location of the origin and the time dependency. Distinctions are made between surface or subsurface vortices and steady or unsteady vortices respectively. The initial rotation along with the height of the water column (submergence) determine the strength of a vortex. Even with constant approach flow conditions vortices are more or less unsteady concerning their strength and location, whereas intense swirl appears more likely to be stable than weak vortices. The unsteadiness is caused by changes of the approach flow distribution or flow separation as well as varying turbulence intensity and energy dissipation.

The vortex strength is classified into 6 types according to Alden Research Laboratory (ARL), given in Figure 2.8 after Hecker (1987). Vortex type (VT) 5 and type 6 are defined to

Coherent surface swirl (VT1)

Surface dimple, coherent surface swirl (VT2)

Dye core to intake (VT3)

Vortex pulling floating trash, but not air (VT4)

Vortex pulling air bubbles to the intake (VT5)
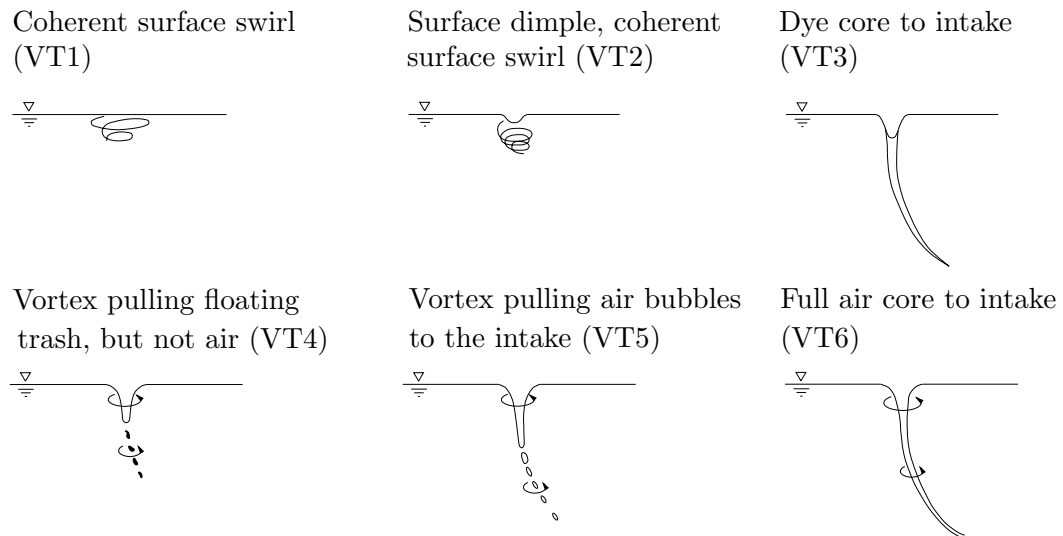
Full air core to intake (VT6)

FIGURE 2.8: ARL vortex classification (Hecker, 1987)

take air bubbles in or having an aircore to the intake respectively. Air entraining vortices, obviously can be identified visually. VT4 is defined to take in particles with higher density then air, *e.g.* trash. A vortex with further decreasing strength, but continuing over the

water column (VT3) can be identified by adding ink. The weakest swirls (VT1 and VT2) are defined as coherent surface swirls with and without a dimple respectively. By Möller et al. (2012) a condition with no activity is defined as VT0.

The vortex strength can be analysed by visual methods or by measuring physical parameters. Even small disturbances can prevent vortex formation. Hence the measurement of the tangential velocity to determine the circulation is troublesome. Optical methods have been applied to determine the circulation but frequently only parameters directly or indirectly related to vortex formation (*e.g.* entrance loss) are measured.

For objective evaluation of the intensity of swirling flow the vortex types appearing are investigated as subject to time, which could be presented in a plot giving the exceedance probability for the previously defined vortex types.

2.2.5   Vortex formation in front of sluice gates

Concerning the design of spillways of high head dams the three dimensional flow conditions upstream of the gate are discussed in Kolkmann (1984). By appropriate pier design large separation zones upstream of gates, causing vortices should be avoided. They can cause gate vibration, discharge reduction and wavy discharge in the chute.

Naudascher (1984) describes a longitudinal horseshoe vortex, forming as the horizontal vortex continues to the jet downstream of the gate in the corner of the side walls and the gate. The vorticity of the side wall boundary layers is directly connected to the circulation of that longitudinal horseshoe vortex. Due to the influence of the vortices generating in front of the gate the stream line pattern and hence the flow separation from the gate lip is affected. The importance of the similarity of flow separation upstream of the weir is pointed out illustrating the vortex zone caused by flow separation from the pier due to asymmetric approach flow.

Investigating causes for losses, Montes (1997) describes a recirculation zone with a horizontal axis developing close to the surface upstream of the gate and vortices with vertical axis due to boundary layers separation from the side walls are stretched to the downstream side of the gate due to flow acceleration.

The distance of the longitudinal vortex from the gate was found to decrease if the opening is close to the water surface, *i.e.* with increasing a/h_0 (Roth and Hager, 1999). The intensity of downstream shock waves is connected to the corner vortices, as their height could be decreased by reducing the vortices. Inviscid flow and $a/h_0 > 0.15$ provided, vortex intensities between VT4 and VT6 according to Figure 2.8 were found to be predominant.

In the closure to the discussion of Montes (1999), the correlation of the vortex formation and hence energy loss and the gate inclination is pointed out. Accordingly a gate leaning down- or upstream favours or reduces vortex formation respectively. An enhanced vortex formation due to an increased area prone to circulation (Knauss, 1987), could explain the effect of gate inclination on vortex formation.

In Levi (1972) two basic vortex types are distinguished by their origin. One induced by a constant roll up behind obstacles, induced by shear stresses and hence with an axis parallel to the separation line and are stable, the other forming independently at an intake, being unstable. In fundamental experiments it was determined that the circulation of the first type of vortices increases with the discharge of the jet and decreases with increasing static head and the characteristic jet cross section. Concerning the flow under the sluice gate spanning a rectangular channel, stable vortices near the walls, only varying in strength, as well as unstable intensely moving vortices between them were observed in the performed experiments.

2.3   Hydrodynamic forces

The properties of the phenomenon in focus and of the data, as well as the desired output are decisive for the corresponding data analysis. Basically deterministic and probabilistic approaches are distinguished. The physical properties of data describing hydrodynamic forces suggests a stochastic analysis to derive generalised descriptive parameters. Due to the amount of gathered data it can be assured that the data is statistically representative and the approach is justified. Information on random processes is given with respect to hydrodynamic impact on structures. General sources on random processes (*e.g.* Bendat and Piersol, 2010) and the IAHR Manual on Hydrodynamic Forces (Naudascher, 1991) are considered therefore. The importance of random fluctuations is indicated by outlining the response of a structure to fluctuating impact. Anticipating the explanations of Section 2.3.5 it is pointed out that even non-periodic, random fluctuations exciting a structure can cause highly periodic response. An overview of the wide variety of sources of excitation related to hydraulic gates is given as well.

2.3.1   Statistical basics: A random process

Investigating hydrodynamic pressure, every measurement results in a unique time history. Once a time series is sampled it is determined in a deterministic sense and hence not considered to be random itself. But as the exact prediction of a future pressure fluctuation through mathematical relationships is impossible the time series is considered to be part of a random process. Hence a single sample record, represents one possible realisation of a process, which basically is characterised by an ensemble of all available realisations. By averaging over this ensemble its statistic parameters are derived. Subsequently the process is known in probabilistic sense and is random by definition (as not known deterministically) and is also referred to as stochastic process. If the probability density function is estimated for a process, any realisation of the process becomes known in probabilistic sense. Its time aspect is not characterised yet.

A random process is considered to be stationary if the ensemble averages are independent of time. For a stationary process the time averaged statistical parameters, computed over short time intervals, do not deviate significantly, *i.e.* of unexpected magnitude.

A stationary Gaussian process is completely characterised by its mean value and autocorrelation function. These parameters are also used to define another property of the process, its ergodicity. A process is ergodic, if mean value and autocorrelation function are equal for all sample records of an ensemble. Therefore averaging over the ensemble gets superfluous and only a single sample function has to be considered to describe the process, which is referred to as ergodic process. Only stationary random processes can be ergodic. Accordingly all ergodic processes are stationary. Detailed information and definitions concerning random processes can be found for example in Bendat and Piersol (2010), Clough and Penzien (1993) or Vaseghi (2008).

2.3.2 Description of hydrodynamic pressure

If the velocity and hence the pressure is fluctuating due to turbulence the process is commonly assumed to be ergodic and hence stationary, *i.e.* different time series characterise the same time invariant process. Hence the mean value over time is constant and can be separated from the fluctuating part, which is clearly illustrated in Figure 2.9. Herein the total local pressure p split into two parts and is defined as

$$p = \overline{p} + p' \tag{2.15}$$

where the mean value over time $\overline{p}$ is indicated with an overbar and the fluctuating part p' is indicated with a prime. The mean value over time of the hydrodynamic pressure describes
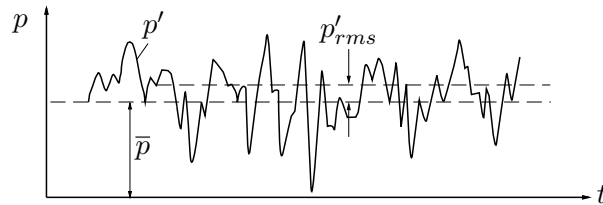
FIGURE 2.9: Mean and fluctuating part of hydrodynamic pressure

the central tendency of the data and can be calculated according to

$$\overline{p} = \lim_{T \to \infty} \frac{1}{T} \int_0^T p(t)\,\mathrm{d}t \tag{2.16}$$

The fluctuating part of hydrodynamic forces is characterised by the root-mean-square of pressure fluctuations, which is illustrated in Figure 2.9 and is defined as

$$p'_{\mathrm{rms}} = \sqrt{\overline{p'^2}} = \lim_{T \to \infty} \left[\frac{1}{T} \int_0^T p'^2(t)\,\mathrm{d}t \right]^{1/2} \tag{2.17}$$

It equals the standard deviation for fluctuations about a zero mean value. Usually the standard deviation or variance is a measure for the dispersion of the data, which is characterised by the probability density function as well. It describes the probability of occurrence of an amplitude with a specific size and hence is also referred to as amplitude-distribution function. The probability that data will fall within an interval is defined by the area between

this interval under the function. Usually data of a stationary random process is distributed according to the Gaussian normal distribution, which is commonly assumed dealing with hydrodynamic pressure fluctuations due to turbulence (*e.g.* Rogala and Winter, 1985). Investigating extreme pressure fluctuations due to hydraulic jumps Toso and Bowers (1988) show that the extreme value distribution TypeI (Gumbel) fit the experimental data better than normal distribution as derived for wind loads by Peterka (1975, 1983).

The time aspect of a process is relevant for the structural response and subsequently analysis of damage due to fatigue or vibrations of force transmitting elements. This aspect can be defined by the time history or the frequency range of a process. The time series itself as well as its Fourier transform, the complex Fourier spectrum

$$P(\omega) = \int_{-\infty}^{\infty} p(t) \ e^{-i\omega t} \ \mathrm{d}t \tag{2.18}$$

uniquely define a sample record of a process. Hence via inverse Fourier transformation the time series can be fully recovered from Equation (2.18) by

$$p(t) = \frac{1}{2\pi} \int_{-\infty}^{\infty} P(\omega) \ e^{i\omega t} \ \mathrm{d}\omega \tag{2.19}$$

In the two previous equations ω is the radian frequency, e denotes the exponential function and i is the imaginary number. For a finite signal being unequal zero in a time interval $0 < t < t_1$ the Fourier transform in Equation (2.18) can be expressed as its real and imaginary part separately as

$$P(\omega) = \int_0^{t_1} p(t) \ \cos \omega t \ \mathrm{d}t - i \int_0^{t_1} p(t) \ \sin \omega t \ \mathrm{d}t \tag{2.20}$$

The two integrals, representing the real and imaginary part contain information about the amplitude and the shift of the phase angles of the harmonics of a signal respectively. The absolute value of the complex Fourier spectrum in Equation (2.20) can be derived as

$$|P(\omega)| = \sqrt{\left[\int_0^{t_1} p(t) \ \cos \omega t \ \mathrm{d}t\right]^2 + \left[i \int_0^{t_1} p(t) \ \sin \omega t \ \mathrm{d}t\right]^2} \tag{2.21}$$

It is referred to as the Fourier amplitude spectrum and does not define the time series uniquely. As it is defined as the absolute value of the complex Fourier spectrum the information about the size of the real and the imaginary part gets lost, as illustrated in Figure 2.10. The Fourier amplitude spectrum is commonly used if only information about the dependence of amplitudes on the frequency is needed. If necessary, the information concerning the phase shift of the harmonics describing the time series can be expressed as the Fourier phase spectrum

$$\theta(\omega) = -\tan^{-1}\left[\int_0^{t_1} p(t) \frac{\cos \omega t}{\sin \omega t} \ \mathrm{d}t\right] \tag{2.22}$$

which makes it possible to recover the time series, but might not be of relevance for the description of the impact or analysis of response.
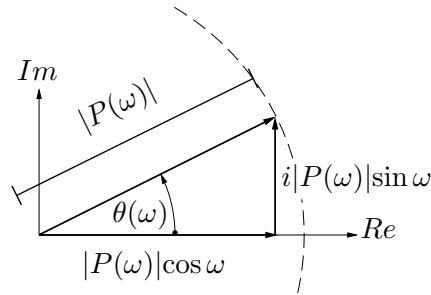
FIGURE 2.10: Components of complex numbers

In probabilistic approaches the power spectral density function of a time series is frequently used to characterise stochastic (continuous, stationary) signals. The power spectral density (PSD) can be derived by squaring the Fourier amplitude spectrum

$$S_p(\omega) = P(\omega)^2 \tag{2.23}$$

The term power spectral density might be misleading, as the signal of interest is rarely related to actual physical power (rate of work). The term simply refers to the square of the signal. The best way to comprehend the meaning of the PSD is probably to look into determining it by filtering described by

$$S_p(\omega) = \frac{\overline{p'^2_\omega}}{\Delta \omega} \tag{2.24}$$

and illustrated in Figure 2.11. A narrow band pass filter over a frequency range $\Delta \omega$ is applied to the data series. The mean square value of the corresponding amplitudes is formed and averaged over time. Subsequently the values are divided by $\Delta \omega$. The procedure is repeated over the whole frequency range of the signal. A graph with the derived values on the ordinate $S_p(\omega)$ and the respective frequencies ω on the abscissa is plotted. The area under the derived curve equals the square value $\overline{p'^2}$, i.e. the standard deviation.

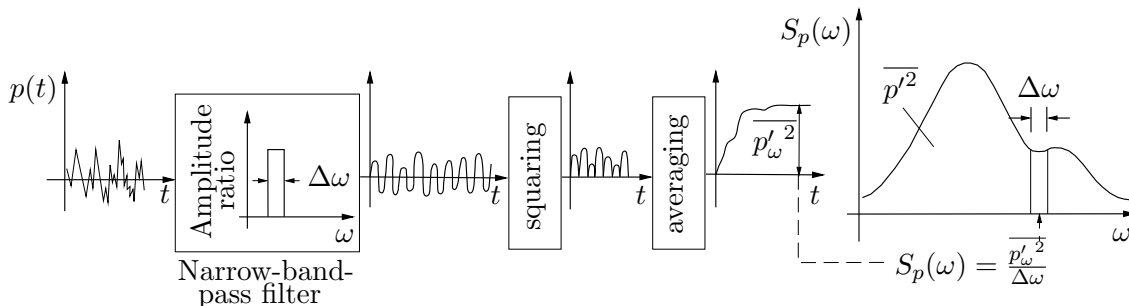FIGURE 2.11: Determination of the power spectral desity (Naudascher, 1991)

The power spectral density describes which frequency range contributes how much to the mean square value $\overline{p'^2}$. (Naudascher, 1991)

It can be summarised that the power spectral density describes how the squared amplitude of a signal is distributed over the frequency range just as well as the Fourier amplitude

spectrum gives the distribution of the amplitudes over the frequency range. The more a spectrum is spread, the more random is a process. As dealing with finite signals of pressure fluctuations their spectra vary randomly. To reduce their variance and to smooth the spectra several methods to derive them, including averaging and windowing, were derived.

The autocorrelation function

$$R_p(\tau) = \lim_{T\to\infty} \frac{1}{T} \int_0^T p'(t)p'(t+\tau)\,\mathrm{d}t \tag{2.25}$$

which represents the similarity of the sample record to its time shifted version, is the Fourier transform of the power spectral density function (Wiener-Khinchin theorem). Hence the spectral density can also be estimated by obtaining the Fourier transform of $R_p(\tau)$

$$S_p(\omega) = \int_0^\infty R_p(\tau)\,e^{-i\omega t}\,\mathrm{d}\tau \tag{2.26}$$

As the spectral density function and the autocorrelation function are a Fourier pair they contain the same information, presented in the frequency and the time domain respectively. Both functions are used to reveal the existence of repetitive patterns or randomness. A stationary process with zero mean, *i.e.* a Gaussian process is completely characterised in a stochastic sense by its autocorrelation function or spectral density function.

After describing the magnitude and the time aspect of fluctuating variables, a measure for the spatial correlation of pressure fluctuations, the correlation coefficient, is introduced as

$$R_p(\Delta z) = \frac{\overline{p'_z \times p'_{z+\Delta z}}}{\overline{p'^2_z}} = \frac{\lim_{T\to\infty} \frac{1}{T} \int_0^T p'_z \times p'_{z+\Delta z}}{\lim_{T\to\infty} \frac{1}{T} \int_0^T p'^2_z} \tag{2.27}$$

where Δz is the separation distance of the points of interest. The correlation coefficient usually decreases with increasing distance Δz. In case the flow coherence is not strengthened by the oscillation of the fluid or the structure, $R_p(\Delta z)$ drops to zero for very short distances. The correlation length, which equals the area under the correlation curve ($R_p(\Delta z)$ depending on Δz) indicates the coherence of the pressure fluctuation. It is important for the derivation of fluctuating hydrodynamic forces from pressure measurements, to derive the according impact area. It is further used to indicate the macroscale of turbulence, as it describes the mass of fluid moving consistently.

2.3.3 Sources of flow induced vibrations

The roll up frequency, the vortex strength and the path of the vortex depends on the approach flow conditions, but can be influenced by vibrations of the structure it separates from (feed-back mechanism) as well. In general the detection and determination of sources of excitation is demanding and comprehends not only the source itself but also the interaction with an fluid oscillator or oscillating structural parts. Even though different sources of excitation frequently appear together they are distinguished in

- Extraneously induced excitation (EIE)

- Instability induced excitation (IIE)
- Movement induced excitation (MIE)

to facilitate the detection of sources.

Extraneously induced excitation (EIE) can excite fluids or structures to oscillate. In case they are caused by velocity and pressure fluctuation they are referred to as turbulence buffeting. Source of excitation can be turbulent shear layers, eddies passing by or impinging a structure, or vortices shed by upstream structures. The impact can result in exciting forces with substantial magnitude. EIE results from velocity or pressure fluctuations of the flow, independent from interaction with the structure. Hence the structural properties are only relevant to evaluate the response of a structure placed in the flow. Therefore EIE can be described independently from structural vibrations, but causes forced vibration onto a system, as considered in the next section (2.3.5). Both, predicting the fluctuating load and analysing the response of the structure has to be considered to evaluate the actual consequences of a dynamic impact. In case of flow separation unstable, free shear layers are formed and break up into vortices. They cause a decrease of the mean pressure $\overline{p}$ and intense pressure fluctuations p'. The lowest mean pressure $\overline{p}$ and biggest pressure fluctuations are located close to the separation streamline. Longitudinal vortices, forming due to flow separation upstream of underflow gates or a pier enhance pressure fluctuations and cavitation (Naudascher, 1991). Other sources of EIE than turbulence are cavitation, two-phase flow, oscillating flows (waves), machinery or earthquakes and are discussed in Naudascher (1991).

Impacts due to flow instabilities induced by the structure of concern are referred to as instability induced excitation (IIE). In case of IIE the impact is highly correlated with the vibration it excites. Included in IIE are excitation due to vortex shedding behind a body, impinging shear layers, instability of a gas-liquid interface and bistable or swirling flow instability due to flow conditions in between two stable states or vortex break down respectively.

Finally movement induced excitation (MIE) is caused by a vibrating fluid or body oscillator itself. An accelerated body in a fluid, influences the forces due to the unsteady flow it induces itself. It is distinguished if MIE is independent or due to different possibilities of coupling, given in Naudascher and Rockwell (1994).

2.3.4   Examples of pressure fluctuations

The following examples are used in Naudascher (1991) to illustrate the remarks on fluctuating hydrodynamic forces. Table 2.2 gives an overview of the magnitude of pressure fluctuation coefficients $C_{p'}$ in different cases. By means of normalisation, the root-mean-square of pressure fluctuations p'_{rms} are related to the dynamic pressure $\rho V^2/2$, according to Equation (2.44). Depending on the boundary condition of different cases, velocities V at different cross sections are chosen as basis for the normalisation. They are given in the third column of Table 2.2. Herein $\overline{V}$ is the mean velocity of approach flow, $\overline{V}_1$ is the mean

velocity of supercritical flow before the hydraulic jump and V_c is the average velocity at the ideal vena contracta.

Author	Source of excitation	Boundary conditions	Basis	$C_{p'}$ [-]
Emmerling (1973)	boundary layer flow $R \approx 2.1 \times 10^4$ smooth boundary	parallel, laminar, uniform flow, $V_0 = 8.5$ m/s	$\overline{V}$	0.01
Emmerling (1973)	boundary layer flow $R \approx 2.1 \times 10^4$ rough boundary	parallel, laminar, uniform flow, $V_0 = 8.5$ m/s	$\overline{V}$	0.05
Suzuki et al. (1973)	boundary layer flow	turbulent, supercritical flow $V_0 = 33$ m/s	$\overline{V}$	0.011
Khader and Elango (1974)	beneath free hydraulic jump	$F = 6.6$ $F = 4$	$\overline{V}_1$	0.08 0.05
Khader and Elango (1974)	beneath submerged hydraulic jump	$F = 6$ $F = 2$	$\overline{V}_1$	0.03 0.07
Narayanan and Reynolds (1972)	free shear layer, beneath standing eddy	$h/h_0 = 0.33$, $R \approx 10^5$	$\overline{V}_c$	0.09
Narayanan and Reynolds (1972)	free shear layer, side wall	$h/h_0 = 0.33$, $R \approx 10^5$	$\overline{V}_c$	0.13
Keir et al. (1969)	sluice gate in submerged hydraulic jump	$F = 10$ $F = 6$	$\overline{V}_c$	0.015 0.02

TABLE 2.2: Pressure fluctuation coefficients $C_{p'}$ in different cases

The first two examples in 2.2 refer to wall pressure fluctuations due to the turbulent boundary layer in non-turbulent, uniform flow, parallel to the wall according to Emmerling (1973). The mean velocity was 8.5m/s. The parameters characterising the magnitude of the pressure fluctuations are given in the table. The derived power spectrum, describing the time aspect of the fluctuation has a flat gradient from about 15 to 700 Hz and subsequently decreases with a steep incline. This development is characteristic for process with random characteristics.

Further the investigations of supercritical flow over a slab as part of a spillway by Suzuki et al. (1973) are given. Measurement on a slab with overflow of a velocity up to 33 m/s were performed. Even though the power spectrum of the pressure fluctuations implied their randomness, the vibrations of the slab peak at its natural frequencies.

Parameters characterising the fluctuations beneath a hydraulic jump are presented according to Khader and Elango (1974). Magnitudes $C_{p'}$ at the bottom beneath the hydraulic jump were found to increase with the Froude number F in case of a free hydraulic jump. Contrary was observed for the bottom pressure fluctuations beneath a submerged hydraulic jump due to the larger rate of growth of the dynamic pressure $\rho V_1{}^2/2$ in the denominator of the

pressure fluctuation coefficient $C_{p'}$ compared to p'_{rms}. Spectra at the point of maximum pressure fluctuations were found to be similar for free and submerged jump.

Toso and Bowers (1988) investigated the pressure fluctuations at the bottom of a hydraulic-jump stilling basin and looked into the effect of the runtime on the magnitude of C_p^+ and C_p^-. According to the authors C_p^+ and C_p^- reach the ten- to twenty fold magnitude of $C_{p'}$. The values depend on the incident Froude number, boundary-layer development, inflow angle and runtime. Long term measurement of 24 hours in model scale have been performed for some parameter combinations. Extreme values were reached after 12-24 hours. Anyway the presented results concerning intensive parameter study were gathered through measurements of 10 minutes duration. Based on an extrapolation of the short term measurements $C_{p\pm}$ are suggested between 0.6 and 1.2. Corresponding measurements of ten minutes gave dimensions of about the half. Using a 1% probability to determine the maximum is criticized to be on the non-conservative side.

Narayanan and Reynolds (1972) investigated the fluctuating pressure beneath and aside a turbulent eddy forming downstream of a sharp crested leaf gate in a square air duct. The worst case was found at a relation of the height of the leaf gate to the total height of the duct of 0.33.

The pressure fluctuation coefficient $C_{p'}$ is given for a sluice gate exposed to a submerged hydraulic jump downstream of the gate after Keir et al. (1969). $C_{p'}$ is of the dimension 0.015-0.02 for parts of the gates, permanently exposed to the surface roller. Due to the stronger increase of the dynamic pressure $\rho v_1^2/2$ with increasing Froude number compared to p'_{rms}, the pressure fluctuation coefficient $C_{p'}$ decreases. Frequencies contributing the most to the energy of pressure fluctuations were found to be below dimensionless frequencies $(y_1/V_1)f$ of 0.008.

In Lesleighter (1971) pressure fluctuations in different types of stilling basins (hydraulic jump, dividing walls, roller bucket) were observed, depending on probability of occurrence and percentage of velocity head, concluding that a significant part of the velocity head should be considered as dynamic pressure. The derived spectra were characteristic for random fluctuations, with dominat frequencies between 0.2 and 0.5Hz.

Rogala and Winter (1985) derive equations for the mean pressure and the characteristics of fluctuation acting upon an overflow gate, based on dimensional analysis, experimental tests and numerical calculations. Fluctuations were found to be caused by fluctuation of flow velocity due to turbulence, the frequency range was found to be the same along the gate, intensity is depending on the location.

2.3.5   Oscillation of a system

As a matter of course the vulnerability of a system to oscillate is highly dependent on the properties of the system itself and not only on the impact. Describing the dynamic equilibrium of a system with a single degree of freedom the equation of motion in Equation (2.28) includes the forces due to the system properties on the left and the forces due to the impact

on the right side. It thereby defines a system with damped, forced oscillation.

$$m\ddot{x} + B\dot{x} + Cx = F(t) \tag{2.28}$$

In Equation (2.28) the variable m denotes the mass of the body, B the coefficient of mechanical damping, C the spring constant and x the displacement or its derivatives with respect to time denoted by the dots. Hence the equilibrium of the inertial force $m\ddot{x}$, the damping force $B\dot{x}$, the elastic (spring) force Cx and the exciting force $F(t)$ is described. This formulation represents the equation of motion for a system with a single degree of freedom (SDOF). As illustrated in Figure 2.12 Equation (2.28) represents a single lumped mass which can move in one direction solely. When idealising real systems as SDOF systems, the
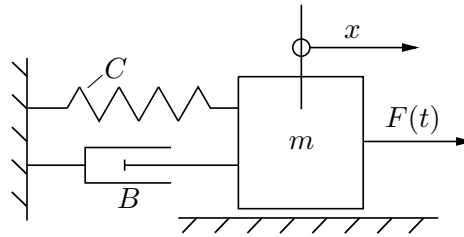

FIGURE 2.12: Basic components of a SDOF system

deformation has to be restricted to one direction or one specific shape with corresponding structural properties, whether the system is represented by a rigid body with deformations at local spring elements or with distributed flexibility. Further explanations can be found in Clough and Penzien (1993).

Damping

If the term for damping $B\dot{x}$ in Equation (2.28) is positive the system is dynamically stable and flow turbulence is the only source of excitation. Contrary if the term is negative, a force in the direction of the vibration velocity is induced and the system is vulnerable to self-excitation. Self-excitation of a system is a destabilising feed back of a fluid or structure oscillator, increasing the amplitude of oscillation. Considering Equation (2.28) as a homogeneous equation with F(t)=0, free vibration of a system is defined. Hence only parameters of the system are taken into account. With these constraints it can be derived easily that a system can be prevented from vibrating and oscillating by a sufficient damping force. With increasing $B/2m$ the amplitude of an oscillating system decreases faster, indicating that not only damping but also the mass of the system, is of relevance for the development of oscillation. Its reciprocal is referred to as relaxation time, which characterises the time a system needs to return to a static equilibrium. If the natural frequency of a system

$$\omega_n = 2\pi f_0 = \sqrt{\frac{C}{m}} \tag{2.29}$$

equals $B/2m$ the oscillation fades away within one period due to sufficient damping and the system can not be excited to oscillate. Hence a critical value for B can be derived from the

requirement that the natural frequency equals $B/2m$ as

$$B_{\mathrm{crit}} = 2\sqrt{mC} \tag{2.30}$$

Subsequently the damping factor used to characterise a systems damping properties is defined as

$$\zeta = \frac{B}{B_{\mathrm{crit}}} \tag{2.31}$$

Systems with $\zeta < 1$ are undercritically damped, *i.e.* the oscillation occurs with decreasing amplitude, whereas if $\zeta \geq 1$ the system is overcritically damped and does not oscillate, but returns to equilibrium in an exponential fashion.

Determining the damping factor is more demanding than calculating the mass or stiffness of a system, as the mechanisms of energy loss are diverse and mostly unknown. In case of impulse loading the maximum response amplitude is reached within a very short period of time, before much energy is absorbed by damping forces. Hence damping effects have only a small influence on the maximum response and might be neglected to simplify the system. But they are essential for the response to arbitrary oscillatory loadings. Consequently the type of loading has to be considered when the relevance of damping is evaluated. To determine an equivalent viscous damping property mostly experimental methods are used. Viscous damping is dependent on the exciting or response frequency. In order to get an frequency independent damping factor, the damping force is sometimes expressed in dependency of the elastic stiffness force. Subsequently the elastic and the damping resistance are expressed in one term (complex stiffness), reducing the equation of motion for the term representing the damping force. Considering the dependence of material properties on the frequency, analysis in the frequency domain, as described in Section 2.3.5, instead of the time domain is preferable.

Amplification, transmission, isolation

Finding the solution of the differential Equation (2.28) for forced oscillation by a sinusoid load without the term $B\dot{x}$ (*i.e.* an undamped system), a rather simple term, depending on the frequency ratio ω/ω_n, representing the dynamic aspect of the interaction can be identified. The term is referred to as magnification factor and determines the amplification of the displacement due to the dynamic characteristic of the impact. Consequently it can be concluded that the amplification increases as the difference of the natural frequency of the system to the excitation frequency decreases. If damping is included, the dynamic magnification factor is not only dependent on the frequency ratio ω/ω_n but also on the damping factor ζ and is defined as

$$\mathrm{D} = \frac{1}{\sqrt{[1 - (\omega/\omega_n)^2]^2 + [2\zeta(\omega/\omega_n)]^2}} \tag{2.32}$$

Further the transmissibility ratio TR is introduced which is the ratio of the maximum amplitude of system response (force, motion or acceleration) to the amplitude of impact (exciting force, motion or acceleration), as well as it can be expressed depending on of the

magnification factor, damping factor and frequency ratio as

$$\text{TR} = D\sqrt{[1 + [2\zeta(\omega/\omega_n)]^2}$$ (2.33)

In Figure 2.13 the transmissibility ratio TR is plotted against the frequency ratio for different values of damping factors. If the transmissibility ratio is below unity, as it is the case for
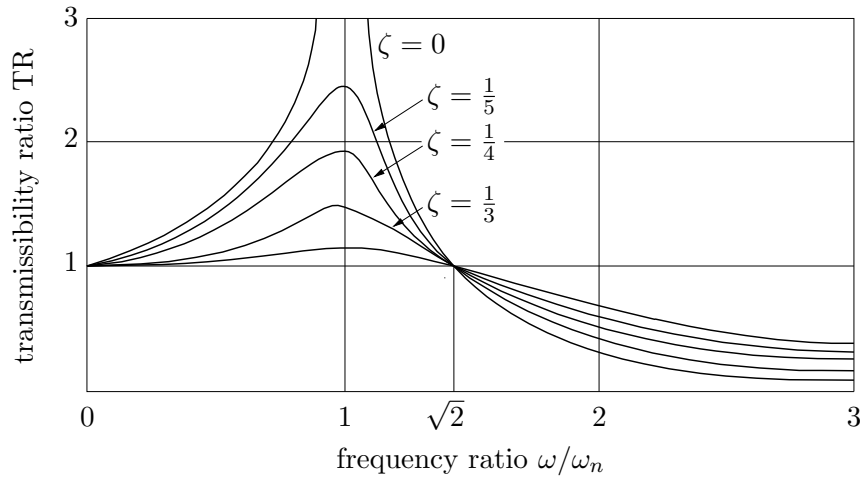

FIGURE 2.13: Transmissability ratio TR as function of the frequency ratio ω/ω_n and the damping factor ζ

frequency ratios above $\sqrt{2}$, the amplitude applied to a system will decrease. Evidently it is advantageous to operate at higher frequency ratios if possible. The effect of damping inverts at the frequency ratio of $\sqrt{2}$. Increasing damping ratios decrease the transmissibility at frequency ratios below $\sqrt{2}$, but increases transmissibility at frequency ratios above $\sqrt{2}$.

Comparable to the magnification factor for the undamped forced oscillation the transmissibility ratio for small damping can be approximated as a function of the frequency ratio solely by

$$\text{TR} = \frac{1}{(\omega/\omega_n)^2 - 1}$$ (2.34)

If the transmissibility of a force, motion or acceleration is restricted due to load limitations of a construction, the isolation effectiveness defined as $\text{IE} = 1 - \text{TR}$ rather than TR is used to define sufficient isolation of a system. If the maximum amplitude of response of a system is limited and the amplitude of a harmonic impact is given, the maximum acceptable TR and hence the minimum required IE can be calculated from their amplitude ratio. Subsequently the goal is the determination of the required support stiffness of the isolation system (*e.g.* a spring) from the deflection of the spring. The deflection is dependent on IE and the exciting frequency which for example can be taken from a diagram as given in Clough and Penzien (1993).

Analysis in the time domain

Periodic excitation of a system can be expressed as its individual harmonic components as a Fourier Series. Subsequently the response of a linear system can be derived in the time

domain by superposing the response to the individual harmonic loadings.

Dealing with an arbitrary loading $p_z(t)$ the impact is looked at as a sequence of impulse loadings. The response of the system is determined for each impulse separately $d\chi(t)$. These unit impulse functions have to be superposed to receive the total structural response. The parts of the response are summarised by integration, forming the Duhamel integral equation, which has to be solved numerically for an arbitrary loading. The approach is sketched in the top row of Figure 2.14.
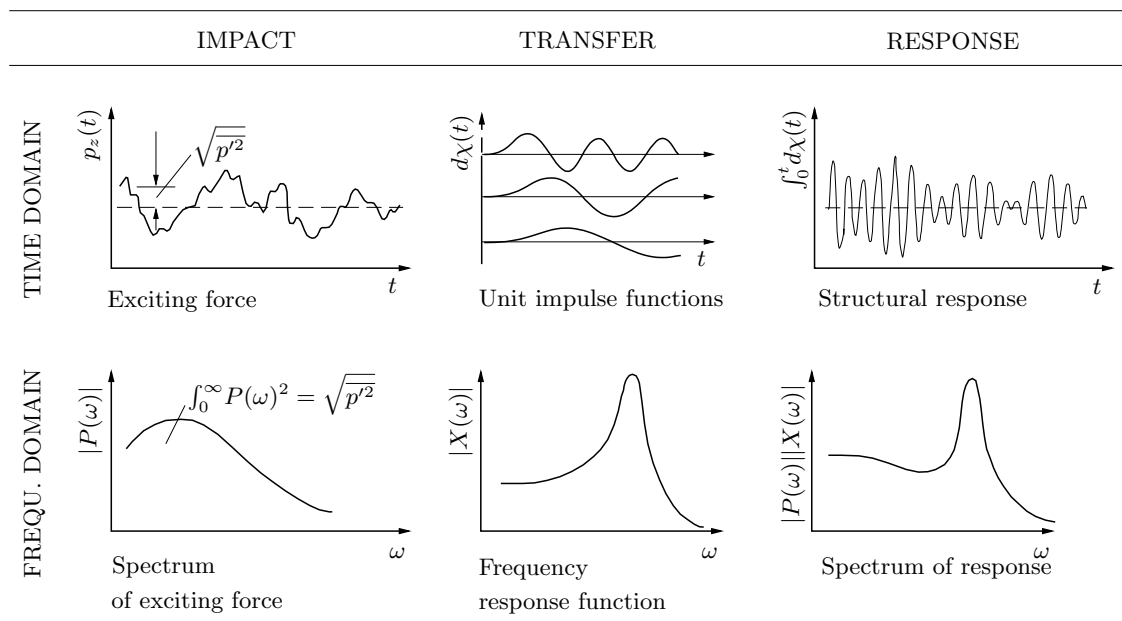
FIGURE 2.14: Determination of system response to arbitrary loading

As the unit impulse functions are superposed only linear system behaviour can be considered but it can be extended for an exponential decay behaviour to take damping into account. An option to derive the response of a system in the time domain, avoiding superposition, are step by step methods. Instead the loading and the response history are split into time sequences to analyse the response for each step from the initial conditions at the beginning of the step while the structural properties are assumed to be constant during one step. Thus the step by step method consists of a sequence of linear analysis. As they don't involve superposition they can also be applied for non-linear behaviour of a structure and it can be extended for multi degree systems. Depending on the size of the time steps they can be highly accurate and effective and hence they are more often used than the Duhamel integral method.

Analysis in the frequency domain

The first step when analysing oscillation of a system in the frequency domain is the transformation of the loading to the frequency domain. As mentioned before periodic loading

can be expressed as a series of harmonic terms, i.e. a Fourier Series, which actually resembles the transformation of the impact from the time to the frequency domain. An arbitrary loading has an infinite period (*i.e.* is non-periodic) and can be described through its harmonic components by a Fourier series given by the direct Fourier transform defined in Equation (2.18). The direct Fourier transform of an arbitrary, time depending loading results in the complex Fourier spectrum, giving complex amplitude intensity as function of specific frequency sequences. The second step involves the derivation of the response of the system to unit amplitudes at each specific frequency sequence, resulting in the complex frequency response coefficient. Multiplying the complex frequency response coefficient by the complex amplitude intensity the complex response amplitude coefficient is derived for all frequency sequences. This function includes the entire information of the structural response to the loading. Hence the time dependent structural response, can be derived by inverse Fourier transformation.

For practical problems approximate numeric solutions such as the Discrete Fourier Transform (DFT), which actually is periodic and the Fast Fourier Transform (FFT), based on an highly efficient and accurate algorithm derived by Cooley and Tukey (1965) to solve DFT are commonly used. The analysis in the frequency domain has advantages, especially if parameters (*e.g.* damping, stiffness) depending on the frequency have to be considered.

Equivalent to the analysis of the complex Fourier spectra described above, the absolute value of the spectra can be used. The procedure is illustrated in comparison to the analysis in the time domain in Figure 2.14. Of course using the absolute value comes with the disadvantage of losing the information about the relative phase shift of the components, which would be necessary for the transformation of the response to the time domain (compare Section 2.3.2). The Fourier amplitude spectrum $|P(\omega)|$ defined in Equation (2.21) is used as input, the unit response is defined by the amplification function $|X(\omega)|$ and the convolution of the spectra $|P(\omega)||X(\omega)|$ results in the spectrum of structural response. The illustration of the derivation of structural response in the frequency domain (Figure 2.14) shows clearly the relevance of the frequency ratio ω/ω_n to the magnitude of response, as concluded from Equation (2.34). Dealing with white noise, which is characterised by a constant spectrum, the response spectrum of an undercritically damped system peaks at its natural frequency. The lower the damping factor the higher is the area under the response spectral density function concentrated at the natural frequency of the system.

Stochastic response

Besides using the statistical values defined in Section 2.3.2 it is a common approach in stochastic analysis to describe the time aspect of vibration by the squared Fourier amplitude spectrum, *i.e.* the power spectral density as defined in Equation (2.23). The procedure is similar to the analysis in the frequency domain illustrated in Figure 2.14. The input is the squared Fourier amplitude spectrum and hence the amplification curve has to be squared as well. Similar to the previously described procedure the response is derived by multiplying the power spectral density by the in this case squared amplification curve. Frequently the normalised power spectral density is used, where it applies that the area under the function

equals one defined as

$$\int_0^\infty S_p \, d\omega = 1 \tag{2.35}$$

As the power spectral density is the Fourier transform of the autocorrelation function (Equation (2.26)) the equivalent analysis in the time domain would use the autocorrelation function as input. In this case the derived response would also be characterised by the autocorrelation function.

2.4 Hydrodynamic impact on sluice gates

As frequently designed for emergency situations the reliability of control structures plays a major role for the risk assessment of dams. Malfunction of control structures can be the reason for dam failure due to overtopping during flood events and can also be critical if a reservoir has to be emptied in case of emergency. Reliable gate operation during standard and hazardous events, like floods or earthquakes ensure the safety of the dam and the catchment area. Reasons for gate operation failure can be structural problems (trunnion friction, ice formation, debris accumulation, gate vibration, damaged hoists, jammed gates causing rope or chain failure), mechanical problems (motor or brake failure), electrical problems (power supply, power failure) or failing control mechanism (limit switch).

In Lewin (2001) the following failures of hydraulic gates are reported:

- Asymmetric lifting due to increased trunnion friction, low lateral stiffness of the arms and unequal chain length due to corroded links supposedly caused the collapse of a spillway gate of Folsom Dam, California (Todd, 1999). Later investigations by Anami and Ishii (2003) showed the possibility of non-eccentric instability of the Folsom-gate by model tests (1:31) and theoretical approach. A coupling mechanism of rigid body vibration with a streamwise bending mode of the gate and flow rate variation was identified.

- Similar dynamic instability caused failure of gate with eccentric bearings at Wachi Dam, Japan.

- The gate of Tarbela Dam, Pakistan collapsed as it got stuck while lowering it, because the distance of the gate from the side-sealing plates diminished over time.

- Accumulation of debris caused gate collapse at a dam in Sweden, which also broke loose as it passed the upper limit switch while opening at another incident.

Problematic gate vibrations were observed

- at Dundreggan dam, Scotland, were gate lip vibrations were induced at small gate openings due to flow reattachment causing concentration of stress and fatigue cracks and

- at a hydraulic model with multigate sluice installation, were self-exciting wave oscillation at specific gate operation combination are investigated in Kolkmann (1984).

Reported gate damages due to other reasons than vibration:

- Seton Dams gate lifting ropes broke during a lifting operation and the gate fell on the sill, causing damage.

- Damage was caused at the same structure as a power supply damage occurred due to frost.

- A screw-stem hoist driven sluice gate damaged the sill as it was forced downwards at a closing operation (Terzaghi Dam, Canada).

- The rather long screw-stem hoist systems are vulnerable to congealed lubricant and dirt, causing the gate to be stuck (Terzaghi Dam, Canada and Bray Weir, Thames river).

2.4.1   Flow induced excitation of sluice gates

Unforeseen gate vibrations can limit gate operation or even cause damage. Partly opened gates induce energy dissipation associated with turbulence, possibly exciting the fluid or structural parts to oscillate.

The three basic sources of excitation as introduced in Section 2.3.3 are

- random flow or pressure fluctuations (extraneously induced excitation)

- fluctuating flow conditions, independent of a fluid or body oscillators (instability induced excitation) and

- fluctuating forces due to movement of a fluid or body oscillators (movement induced excitation).

Variable gate positions together with different combinations of up- and downstream water levels cause a great variety of impact and response frequencies. The excitation mechanisms and sources of gate vibration are diverse, they can occur simultaneously and interact. A substantial discussion can be found in Kolkmann (1976), Naudascher and Rockwell (1994) or Ishii et al. (2017). Further problems concerning the awareness of gate vibrations is the scarcity of the occurrence of events and that the phenomenon leading to the gate vibrations is often hard to reproduce.

Gate vibrations and dynamic response can be caused if the arms of radial gates or girders of the skin plate of vertical lift gates are affected by turbulent discharge conditions downstream of a gate or an unsteady roller. Flow turbulence in the vicinity of the gate such as a downstream hydraulic jump (Keir et al., 1969) or turbulent discharge of an adjoining gate (Lewin, 2001) are potential sources for extraneously induced excitation (EIE). Systems with free water surfaces are likely to be affected by fluid oscillation, caused by different mechanisms, including asymmetric operation conditions causing oscillating head water (Kolkmann, 1984) or downstream submerged gates exposed to oscillating tailwater levels (Thang and Naudascher, 1986b). Low placed structural members can induce structural vibrations to the gate if a free water surface or a free shear layer attaches to them (Lewin, 2001).

Discharge fluctuations due to high tailwater levels (Lewin, 2001) controlling the flow rate or due to a shear layer separating from the gate lip, reducing the effective discharge area (Ishii

and Knisley, 1990), can cause gate excitation. Leakage through seals can cause oscillation of the seals (self-excitation), the fluctuating discharge leaking through side or sill seals can cause instability induced excitations (IIE) (Naudascher and Rockwell, 1994).

Excitation mechanisms involving free shear layer containing turbulence and rolling up into vortices eventually, are highly dependent on the geometry of the flow boundaries determining the separation point and zones of reattachment or impingement. Corresponding examples for EIE are separation from the edge of the gate slot impinging on the withdrawn gate located close to the ceiling, or separation from an upstream gate in case of tandem gates (Naudascher and Rockwell, 1994; Shuy and Chua, 1999). Details concerning the excitation related to the shear layer separating from the gate lip are given in the subsequent chapter.

2.4.2   Excitation due to free shear layers

The excitation of bluff bodies due to two interacting shear layers is a fundamental research topic. Naudascher (1991) refers to investigations by Parkinson et al. (1968), Novak (1971), Sarpkaya (1979), Bearman (1984), Naudascher (1987), etc. to illustrate the basic mechanisms of flow induced oscillations. The basic mechanism concerning the dynamics of alternating shear layers as investigated for bluff bodies applies for gates with simultaneous over- and underflow or lowering of gate leaves or stop logs (Naudascher, 1962; Husain, 1999). The excitation mechanisms investigated for underflow of gates are caused by a single free shear layer, separating from an upstream boundary such as the leading edge of a gate lip. Figure 2.15 gives a comparison of the shear layers forming at a rectangular prism and a flat bottomed underflow gate. In Figure 2.15a the pressure distribution and respective flow conditions at a rectangular prism are illustrated. Figure 2.15b&c show the pressure conditions at a flat bottom of a underflow gate depending on different flow characteristics, inducing vertical and horizontal forces respectively. Non-dimensional parameters are intro-
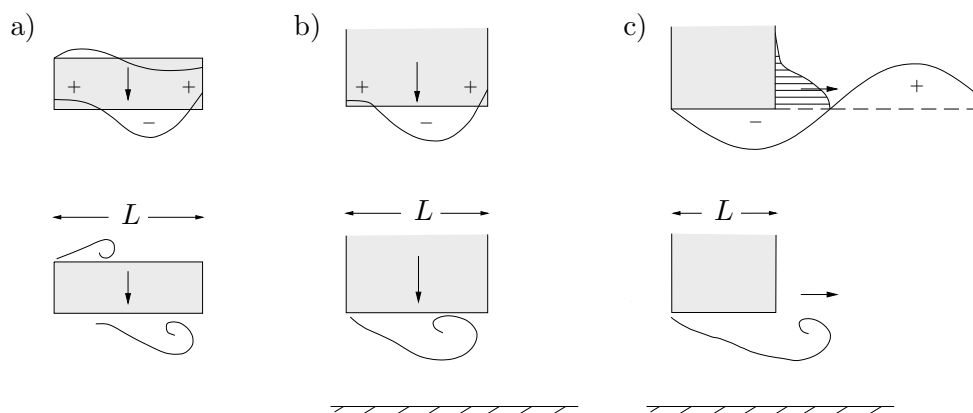
FIGURE 2.15: Excitation mechanisms after Thang (1990): a) excitation of a rectangular prism, b) vertical excitation of a gate, c) horizontal excitation of a gate

duced to characterise the dynamics of the mechanism. The dynamic property of a shear layer rolling up into vortices is characterised by the Strouhal number $\mathsf{S} = fL/V$, with the vortex frequency f, the distance between leading and impinging edge L and the characteristic flow velocity V. It depends on the Reynolds number defined in Equation (2.14), surface

roughness and the initial turbulence, if the flow separation point is unstable or combined with reattachment. The dependence on the Reynolds number disappears with fixation of the separation point. The flow induced excitation process is characterised by the so called reduced velocity, which is the relation of the typical flow frequency (V/L) to the body natural frequency (f_0). The intensive research concerning the excitation mechanisms due to a shear layer separating from the leading edge of a gate lip contribute to the awareness of possibly hazardous flow phenomena and is therefore briefly discussed below.

Cross-flow vibrations (vertical direction)

Vertical excitation due to the boundary layer separating from the leading edge of a downstream submerged sluice gate with flat bottom was investigated by Hardwick (1974) and Thang and Naudascher (1986b). Hardwick (1974) found that excitation was enhanced by the movement of the gate and that small gate openings were unfavourable. Separation from a fixed point leads into smaller, random eddies and no reattachment. In Thang and Naudascher (1986b) power spectra measured at a rigid gate were found to be broad banded and the frequency was found to increase with the velocity, whereas for an elastic gate locked-in oscillations were found in a critical range, but if no resonance occurred oscillations with a broad spectrum were measured. Suppressing oscillation of the downstream water level (avoiding a fluid oscillator) led into a considerable reduction of the amplitude of oscillation. Further mass and damping were shown to have a strong influence on the amplitude.

The movement induced excitation for an inclined, sharp edged gate was investigated in Thang and Naudascher (1986a). By testing variable geometry it was found that the distance of the free shear layer to the boundary reduces excitation. Adapting structural mass and damping galloping could be avoided. An approach to use the mean lift coefficient to evaluate the sensitivity to self-excited vibrations is introduced.

Thang (1990) analysed the critical range for vertical and horizontal vibrations and points out the similarity of the critical relative gate opening and alternating critical reduced velocity. The excitement of an underflow gate is explained by unstable flow separation and reattachment of leading edge vortices. Increasing amplitudes and frequency ranges were found to be caused by an extended downstream gate lip. A free downstream water surface enhances vibration. The stability criterion also used in Thang and Naudascher (1986a), based on the slope of the function of lift coefficient depending on gate opening to conduit height is suggested to identify critical conditions for vibrations, which is the transition from separation combined with steady reattachment and steady separation without reattachment. The range of critical gate opening depends on the gate geometry.

The effect of turbulence of approach flow on discharge characteristics, cavitation and hydrodynamic forces of high head gates was investigated by Thang and Naudascher (1983) in hydraulic model tests. In case of complete separation of the shear layer turbulence of the approach flow increases the downpull force (pressure reduction) and increases the discharge capacity. In case of separation with reattachment turbulence in the approach flow has the opposite effect.

According to experiments and 2D numerical analysis presented in Erdbrink et al. (2014b) vertical gate vibrations can be reduced by ventilation of the flat gate lip, removing flow instabilities from the gate lip and reducing pressure gradients.

Kostecky (2011) applies the boundary element method and the random vortex method (describing spreading of vorticity by advection and diffusion) to the problem of an submerged bottom outlet gate with rectangular gate lip in order to analyse flow instabilities and fluctuations due to vortex detachment and to express them as velocity, vorticity and pressure field. The mechanism of impinging leading edge vortices as well as dowstream vortex structures could be identified. The pressure on upstream face is almost constant, whereas the large vortex structures downstream of the gate induce pressure fluctuations. The method applied was verified by comparing downpull forces from experiments documented in Naudascher (1991).

In-flow vibrations (horizontal direction)

Horizontal excitation of underflow, downstream-submerged, flat-bottomed model gates are analysed in Jongeling (1988) and Ishii and Knisley (1990).

A feedback mechanism between a separating shear layer inducing in-flow movement and the exposed gate is analysed in Jongeling (1988). The movement of the gate induces the shear layer to be wavy, effecting a periodic downstream velocity and pressure distribution. Thereby in-flow vibrations of the gate plate can be induced, determined by the gate's bending mode. A feedback mechanism could be confirmed as the gate's natural frequency and the vibration frequency were the same. The effective flow opening is affected by the wavy shear layer. Increasing the distance of the area affected by the free shear layer from the gate by larger gate openings, causing the shear layer to bend away or a bevelled gate lip causing separation from the trailing edge is found to be advantageous.

Similarly the alternately expanding and contracting wake region between the shear layers separating from the gate lip is referred to as wake breathing in Naudascher and Rockwell (1994) and is argued to excite the gate horizontally.

The shear layer dynamics at the gate lip of a sluice gate are analysed depending on forced horizontal vibrations in Ishii and Knisley (1990). Upstream pressure fluctuations causing horizontal vibrations are induced by the fluctuating discharge related to the shear layer dynamics. By analysing the energy transfer due to pressure fluctuations the self exciting mechanism could be confirmed.

Multi degree of freedom

Billeter and Staubli (2000) analyse the gate excitation in horizontal and vertical directions and their interaction. The mechanisms were analysed by force, pressure and velocity measurements at a fixed gate and the response was measured at a gate with two degrees of freedom whereas the possibility to fix one direction was used to suppress one component and thereby identify possible interactions. Different excitation mechanisms are given for the

relation of natural frequencies of the gate in horizontal and vertical direction and the reduced velocity. For rather small gate openings impinging leading edge vortices were found to induce vertical or horizontal vibrations depending on the natural frequencies. With increasing reduced velocities a mechanism inducing horizontal oscillation due to self-excitation by leading edge vortex shedding is identified. Movement induced excitation gains importance for large gate openings. Dependency of horizontal gate oscillations on head- and tail-water waves and added mass were found.

Erdbrink (2012) performed model tests concerning the design of underflow gates with flat gate lips in order to reduce vertical vibrations at small gate openings. Horizontal dynamic response was found to be smaller in amplitude and consisting of more than one harmonic or even irregular if vertical amplitudes were low. Harmonic horizontal oscillations had the same frequency range as the vertical response with a phase shift of 90 degrees.

2.4.3   Gate design

Structural analysis of a gate can either be performed 2D or 3D, in which case analysis complex structural arrangements can be considered. Dynamic analysis is recommended in Lewin (2001) for structures with natural frequencies below than 33 Hz, which applies commonly. Limit states considered are the serviceability and ultimate limit state. The gate has to be designed to fulfill its intended purpose, which is guaranteed by use of appropriate safety factors, which vary with the design element considered and the impact. Lewin (2001)

Subsequently the loads on sluice gates according to design standards DIN 19704-1 (Deutsches Institut für Normung, 2012) and EM 1110-2-2701 (U.S. Army Corps of Engineers, 1997) as well as some conclusions from former sections concerning hydrodynamic impact are given.

Design Loads according to standards

There are two design standards concerning gates. The German standard DIN 19704, Part 1 on Criteria on Design and Calculation of Hydraulic Steel Structures based on limit states and the US standard EM 1110-2-2701 based on load and resistance factors design.

According to DIN 19704-1 the self-weight of the structure has to be considered. Ten percent of the net weight has to be added, considering adhesive water or ice, plant cover or dirt. Live loads are the hydrostatic load according to the specific weight of water, as well as hydrodynamic loads, which are partly taken into account by adjusting the hydrostatic load (surge and drawdown, pressure surge, pressure due to waves). Further flow around (under or over) the control structure and the impact of a jet by stern screws of ships have to be considered. The impacts can be determined by model tests. Further remarks on flow induced loads or vibrations are lacking. Loads due to the movement of the gate, ice formation, traffic load, loads due to acceleration of the mass, changes of the support conditions, temperature influences, ships, wind, stages of transportation and construction and pressure exerted by freshly poured concrete. Further accidental loads to be considered are given and friction coefficients are given for the determination of frictional forces and moments.

In the Engineering Manual EM 1110-2-2701 the load types are given depending on the gate type. Specifically for vertical lift gates the hydrostatic loading is given for the site-specific upstream water level. For underflow of single-section spillway crest gates an uplifting hydrostatic load is considered. For multiple section gates overflow has to be considered as well. Gravity loads include dead weight, ice and mud. Impact of ice and debris at the upstream water level is considered as well was wind loads. Earthquake loads are considered according to Westergaard's simplified equation (Westergaard, 1933), assuming that water and structure move together. Hydraulic studies should be performed to determine downpull forces based on flow conditions and the shape of the gate.

Remarks on flow induced loads

A common simplification is assuming that the hydrostatic pressure acting on the gate is the worst case concerning water pressure, because the hydrodynamic pressure is decreased by the velocity head (illustrated in Figure 2.1). The stiffening members of the load bearing structure are arranged in order to divide the load equally in order to avoid non-uniform deflection. The hydrostatic pressure distribution can be distributed equally by a graphical method, determine the horizontal location of the stiffening members, as described *e.g.* in Naudascher (1991) or Bollrich (1996).

Vertical hydrodynamic forces on gates in free surface flow are caused by the pressure drop due to the flow acceleration. Knowing the hydraulic parameters governing the flow under a gate, where approach flow effects can have an influence, as well as knowing the location of the skin plate (up- or downstream) and the geometry of the gate lip and the bottom seal the vertically acting force can be calculated. These down pull or lift forces have little effect on the structural considerations and the hoist forces of gates in free surface flow (Lewin, 2001).

Hydraulic conditions relevant for gate vibrations are

- the stability of flow pattern, the stability of separation and reattachment and
- dynamic phenomena like steep waves and hydraulic jumps, or water hammer and cavitation for high head gates.

Considerations relevant for gate vibrations are

- geometries vulnerable to self-control, self-excitation due to suction forces, which is often dependent on the location of the leading edge and the gate seals,
- unloaded roller wheels, causing allowance for clearance,
- play in bearings and joints and
- the location of the girders of the support structure (possibility of drowned discharge).

Desirable mechanical properties for TR > 1 are

- natural frequencies distinctly above excitation frequencies as defined by the isolation range in Figure 2.13,

- increasing rigidity, which increases natural frequencies and

- high damping (*e.g.* sliding gates)

The natural frequency of a gate is dependent on the rigidity per unit mass of the vibrating system, which depends on the gate structure and the water moving with it, as it oscillates. Hence it is obvious that the natural frequency is not constant, but varies with the gate opening and the upstream water level. The transmissibility ratio TR, according to Equation (2.33) or (2.34) is used to quantify the sensitivity of a system to excitation. The range of transmissibility ratio between 0 and 1 is called isolation range. The goal is a design with low transmissibility and hence a high percentage of isolation.

For determination of the impressed force for a vibrating gate structure, its own mass and the hydrodynamic mass (mass of water vibrating with the gate) as well as damping and rigidity of the gate and the added mass has to be known. Concerning the damping forces structural damping and even though not necessarily valid, constant friction damping (slide or roller friction and seal friction) are usually considered. An undercritically damped system, oscillating with diminishing amplitude, is also referred to be positively or stable damped. This is given if damping is greater than zero and smaller than the critical damping coefficient determined by Equation (2.30).

Determination of the total suspended mass, rigidity of the system, added mass, damping forces, critical damping coefficient and damping ratio as well as resonance frequency are dependent of the gate construction and hence not topic of this investigation, whereas the excitation frequency due to asymmetric inflow conditions and a vertical vortex forming upstream of a gate is investigated extensively.

2.5   Dimensional analysis

Through dimensional analysis, performed according to the Buckingham π-theorem, the basic governing variables of a physical process are arranged in order to find the characterising non-dimensional hydraulic parameters π. Thus the number and complexity of variables influencing a physical phenomenon is reduced. With n different variables and k (mostly three) corresponding basic dimensions [m], [s] and [kg] of the basic physical variables length L, time T and mass M respectively, $n-k$ dimensionless parameters consisting of $k+1$ basic variables can be derived. For determination of the non-dimensional parameters k (three) basic variables with different dimensions, including all basic dimensions, have to be chosen. (Knapp, 1960)

The dimensional variables considered for analysis herein are given with the corresponding units and dimensions in Table 2.3.

The associated function describing the relation of the variables can be written generally as

$$f_1(\underline{a}, H_0, b, l_p, v_0, \underline{v_a}, p, p', f, g, \underline{\rho}, \nu, \delta) = 0 \qquad (2.36)$$

The three basic variables used to set up the π-theorems in combination with one of the other variables are emphasised in Equation (2.36).

Type	Notation	Unit	Dimension	Description
geometry	a	[m]	L	gate opening
	H_0	[m]	L	approach energy head
	b	[m]	L	gate width
	l_p	[m]	L	pier head length
external effects	v_0	[m/s]	L T^{-1}	approach flow velocity
	v_a	[m/s]	L T^{-1}	velocity at the gate lip
	p	[kg/(m s^2)]	M L^{-1} T^{-2}	hydrodynamic pressure
	p'	[kg/(m s^2)]	M L^{-1} T^{-2}	pressure fluctuations
	f	[1/s]	T^{-1}	frequency
	g	[m/s^2]	L T^{-2}	acceleration of gravity
fluid properties	ρ	[kg/m^3]	M L^{-3}	density
	ν	[m^2/s]	L^2 T^{-1}	kinematic vicosity
	σ	[kg/s^2]	M T^{-2}	surface tension

TABLE 2.3: Governing parameters of flow under a sluice gate

A simplified case is given if a variable has the same dimension as one of the three chosen basic variables. The relation of two variables with the same dimensions results in a non-dimensional parameter immediately (Knapp, 1960). This is for example the case for geometric parameters of dimension [m]. The non-dimensional parameters are simply formed by the ratio of the variable and the gate opening a, which was chosen to be one of the basic variables. Accordingly the relative gate opening is defined as

$$\pi_1 = \frac{a}{H_0} \tag{2.37}$$

and the dimensionless pier head length is

$$\pi_2 = \frac{l_p/a}{b/a} = \frac{l_p}{b} \tag{2.38}$$

Further a non-dimensional parameter characterising the asymmetry of the approach flow conditions is derived as

$$\pi_3 = \frac{v_0}{v_a} \tag{2.39}$$

To derive a non-dimensional parameter from variables with a dimension deviating from the basic variables the π-number is expressed by the three basic variables, their unknown exponents (x, y, z) and the variable of interest, e.g. concerning any pressure p or pressure difference

$$\pi_4 = a^{x_3} v_a^{y_3} \rho^{z_3} p \tag{2.40}$$

is written and expressed by their basic physical variables the theorem becomes

$$\pi_4 = [L]^{x_3} \left[\frac{L}{T}\right]^{y_3} \left[\frac{M}{L^3}\right]^{z_3} \left[\frac{M}{LT^2}\right] \tag{2.41}$$

or

$$\pi_4 = L^{(x_3+y_3-3z_3-1)}T^{(-y_3-2)}M^{(z_3+1)} \tag{2.42}$$

As the principle of dimensional homogeneity applies, the exponents can be derived to be $x_4 = 0$, $y_4 = -2$ and $z_4 = -1$. Substituted in Equation (2.40) it results in

$$\pi_4 = \frac{p}{\rho v_a^2} \tag{2.43}$$

As the derived non-dimensional parameters can be extended by any exponent or factor according to Knapp (1960) the pressure coefficient C_p and hence the piezometric head coefficient C_h as in Equation (2.2) could be derived to be a characterising non-dimensional parameter for the problem investigated herein. Accordingly all parameters describing the hydrodynamic pressure conditions of dimension $[\mathrm{kg}/(\mathrm{m\,s^2})]$ are normalised similarly, *e.g.* the pressure fluctuation coefficient is

$$C_{p',rms} = \frac{p'_{\mathrm{rms}}}{\frac{1}{2}\rho v_a^2} \tag{2.44}$$

and the coefficient of maximum positive C_{p+} and negative deviation of pressure C_{p-} are

$$C_{p+} = \frac{\Delta p^+}{\frac{1}{2}\rho v_a^2} \quad \text{and} \quad C_{p-} = \frac{\Delta p^-}{\frac{1}{2}\rho v_a^2} \tag{2.45}$$

Further parameters characterising the rapidity of pressure variation are derived by following the procedure outlined from equations 2.40 to 2.43. The normalised frequency f_n is defined to be

$$\pi_5 = \frac{a}{v_a}f = f_n \tag{2.46}$$

according to the Strouhal number as defined in Section 2.4.2 describing oscillating flow mechanisms. Correspondingly the normalised period τ_n is defined as

$$\tau_n = \frac{1}{f_n} = \frac{v_a}{a}\tau \tag{2.47}$$

Finally we obtain the well known non-dimensional hydraulic parameters Froude F, Reynolds R and Weber number W, which express the relation of inertia to gravity forces, viscous forces and surface tension respectively from g, ν and σ as

$$\pi_6 = \frac{v_a}{\sqrt{ga}} = \mathsf{F} \tag{2.48}$$

$$\pi_7 = \frac{v_a a}{\nu} = \mathsf{R} \tag{2.49}$$

$$\pi_8 = v_a\sqrt{\frac{\rho a}{\sigma}} = \mathsf{W} \tag{2.50}$$

characterising the flow conditions at the intake.

2.6   Model similitude and scale effects

The parameters determining the stream line pattern of a flow process and therefore pressure and velocity conditions are the geometry and roughness of the flow boundaries, the entrance flow conditions, and the forces affecting the flow. For incompressible flow with a free surface, inertia, gravitational and frictional forces as well as surface tension have to be considered. Their relation for a specific flow process is expressed by the dimensionless parameters Froude, Reynolds and Weber number F, R and W respectively. Further the aeration conditions and the flow unsteadiness is of relevance. The influence of corner vortices and eddies upstream of a gate cause the transformation of energy to turbulence, which should be considered. (Naudascher, 1984)

If all parameters affecting the flow are taken into account, no scale effects occur. This means to satisfy the similarity of the flow process entirely all π-values derived in Section 2.5 have to be equal in the model and the prototype. Downscaled hydraulic models have the restriction that the ratio of all considered forces can not be equal. In case Froude and Reynolds number are aimed to be the same either the acceleration of gravity g or the kinematic viscosity of the fluid ν would have to be manipulated. By choosing the most dominant forces for the investigated process a compromise is made in this regard.

Considering the flow under gates, gravity and inertia are the dominant forces. Hence Froude similarity is applied. Other relations of forces, characterising a dynamic process like inertia to viscosity or inertia to surface tension, represented by Reynolds number R and Weber number W respectively, can not be scaled in the model correctly as long as the same fluid as in the prototype is used. Therefore effects due to viscosity and surface tension, are likely to be overestimated in models scaled according to Froude similarity. The Reynolds number in a downscaled model is too low in comparison with the flow in the prototype. Consequently frictional losses in the boundary layers are generally overestimated. Concluding from the fact that not all forces can be scaled simultaneously scale effects have to be considered when planning and performing model tests and concluding from the results. Hence it is a common practice to test a scale family, namely models in different scales to increase the awareness of scale effects.

2.6.1   Scale factors

The specific laws of similarity are derived corresponding to the most significant forces. Subsequently the flow parameters can be scaled according to the scale factors summarised in Table 2.4. The geometric similarity is fulfilled if the shape of the prototype is preserved in the model, *i.e.* the ratio of length in the prototype L and the model L_m giving the model scale

$$\lambda = \frac{L}{L_m} \tag{2.51}$$

is the same for all dimensions. A particle passing the length L or L_m needs the time t or t_m in the prototype or the model respectively. The scale of time therefore is defined by

$$t_r = \frac{t}{t_m} \tag{2.52}$$

The factor for the velocities in prototype V and V_m is

$$v_r = \frac{V}{V_m} \quad \text{or} \quad v_r = \frac{\lambda}{t_r} \tag{2.53}$$

when substituting $V = Lt$ and $V_m = L_m t_m$. Similarly the factor for accelerations in prototype $a = V/t$ and the model $a_m = V_m/t_m$ is

$$a_r = \frac{a}{a_m} \quad \text{or} \quad a_r = \frac{\lambda}{t_r^2} \tag{2.54}$$

when considering Equations (2.52) and (2.53). The kinematic similarity of motion is given if the ratio of velocities and acceleration at corresponding locations in the model and prototype are the same. Thus the streamline pattern is ensured to be equal. The magnitude and direction of all acting forces determine the velocity and acceleration. Their relation is defined by

$$f_r = \frac{F}{F_m} = \frac{m}{m_m}\frac{a}{a_m} \quad \text{or} \quad f_r = m_r \frac{\lambda}{t_r^2} \tag{2.55}$$

considering Newton's second law of motion to be valid in model and prototype and further substituting according to Equation (2.54) and introducing the relation of masses

$$m_r = \frac{m}{m_m} \tag{2.56}$$

Using the same fluid and if acceleration of gravity is the same in model and prototype the relation of masses m_r equals λ^3 and Equation (2.55) becomes

$$f_r = \frac{\lambda^4}{t_r^2} \tag{2.57}$$

By rearranging and substituting the so far derived formulas the basic similarity conditions can be given as subject to the model scale λ and the scale factor for forces f_r. Subsequently the specific scale factors are determined by defining the scale factor of forces f_r as a subject to the most significant forces of a specific problem.

As gravitational forces are defined to be significant the driving force is the weight of the fluid and $f_r = m_r = \lambda^3$. Subsequently the scale factors for Froude similarity can be derived. The resulting scale factors are given in Table 2.4. The derivation of the scale factors is discussed in more detail for example in Knapp (1960).

Hydraulic models are distinguished according to the significant force and the corresponding dimensionless parameter that is the same in the model and the prototype. Therefore models concerning investigations of underflow gates are referred to as Froude scaled model. Further hydraulic models differ concerning the dimensions of the flow process of interest. 2D and 3D models consist of a cross sectional or spatial part of the flow problem respectively. Another category of models involves the investigation of the vibrations of the structure itself. Hence besides the challenge to model the flow properly, also the structural properties influencing the response have to be concerned about, which is time and cost intensive.

Parameter	Symbol	Basic relations	Scale factor
acceleration	a_r	$\lambda^{-3} f_r$	λ^0
length	λ	λ^1	λ^1
pressure		$\lambda^{-2} f_r$	λ^1
time	t_r	$\lambda^2 f_r$	$\lambda^{-1/2}$
velocity	v_r	$\lambda^{-1} f_r^{1/2}$	$\lambda^{1/2}$
force, mass	m_r	m_r	λ^3
discharge		$\lambda f_r^{1/2}$	$\lambda^{5/2}$

TABLE 2.4: Scale factors according to Froude similarity

2.6.2   Limits for scale effects

As the influence of vortex formation on the discharge under a gate is investigated herein the possibility of scale effects concerning both flow processes is discussed.

Just as the underflow of a gate, the critical submergence concerning the formation of air entraining vortices is a gravity influenced parameter and hence the Froude scale law is applied (Ranga Raju and Garde, 1987). Consequently the Reynolds number can not be the same in model and prototype, if the same fluid is used. As a result attention has to be drawn to the effects of the viscosity of a fluid, when performing model tests in reduced scale and interpreting the data. It influences the velocity profiles as well as the intensity, distribution and structure of turbulence and hence the dimension of losses of a process. Further the formation of corner and side eddies in front of a gate depend on the viscosity. Both boundary layer effects and effects due to vortices influence the head loss in physical models. With large Reynolds numbers, as is the case for prototypes, one can assume that the influence of boundary layer effects on the flow is marginal. Therefore calculations neglecting boundary layer effects and losses might suit the prototype data better than data gained from model tests. Anyway the displacement of the streamlines due to vortex formation, as most probably also generate in prototypes if observed in models, is of relevance to the flow characteristics. Basically the Reynolds number of a boundary layer increases with increasing Reynolds number of the flow upstream of the separation. But as a critical value of R is exceeded and the flow changes from laminar to turbulent the characteristic of separation remain the same, as mentioned in Section 2.2.3 concerning the vortex formation. Dealing with scale effects in hydraulic models due to viscosity, the critical Reynolds number ($\mathsf{R}_{crit} \approx 2320$) has to be exceeded. Alternatively turbulent separation could be introduced artificially (Naudascher, 1984).

Scale effects concerning the surface tension are caused by the fact that the Weber number can not be scaled correctly in case of a model scaled according to Froude similarity. If the Weber number is smaller than a critical number a standing layer, causing losses similar to a fixed boundary, could form upstream of the horizontal surface eddy (see Rajaratnam and Humphries, 1982). Downstream of the gate the relatively decreased Weber number influences the curvature of the streamlines which increases the contraction coefficient Naudascher (1984).

When investigating formation of vortices in a Froude scale model the approach geometry and boundary roughness have to be modelled sufficiently and limit Reynolds and Weber number have to exceeded in order to minimise scale effects and get flow patterns representing the circulation of flow properly. Anwar (1965) mentions the importance of a large scale for physical models concerning the modelling of free vortices and suggests a scale of 1 to 20. Further attention is drawn to the appropriate modelling of total circulation supplying the energy to the free vortex and smooth boundaries to avoid losses. In order to eliminate the influence of viscosity and surface tension numerous investigations for different inflow geometries have been published concerning the critical values for the Reynolds and Weber number. The results are reviewed in Hecker (1987) and Chang and Prosser (1987). From the reported limit values it can be concluded that the scaling laws are not universally valid but a subject to geometry and vortex type. Other, less documented methods to deal with scale effects are the introduction of correction factors to the results or the increase of the approach flow velocity in relation to the Froude scale laws to account for viscous effects. The increase of the water temperature in the scale model could be used to increase the Reynolds number (Ranga Raju and Garde, 1987).

Possible scale effects concerning vortex formation are a decrease of the circulation strength and hence a smaller drawdown or air core due to an increased viscosity. Consequently the critical submergence concerning the formation of air entraining vortices would be decreased. Noteworthy effects of surface tension on the discharge coefficients (Dagget and Keulegan, 1974) or the critical submergence (Jain et al., 1978) have not been found within the range of the Weber numbers tested.

For flow conditions of free vortex generation empirically derived limit values concerning the scale effects due to viscous effects and surface tension are investigated for the influence on vortex formation and critical submergence for example in

- Anwar et al. (1978) for free vortices generating due to a horizontal intake
- Dagget and Keulegan (1974) for free surface vortex flow in a cylindrical tank
- Jain et al. (1978) for free vortices generating at a vertical pipe intake

Limit values determined therein for the respective boundary conditions in order to achieve negligible effects due to viscosity and surface tension are given in Table 2.5.

Author	Limit Reynolds number	Limit Weber number
Anwar et al. (1978)	$\mathsf{R}_h = Q/h\nu = 3 \times 10^4$	$\mathsf{W}_h = \rho Q^2 h/A^2 \sigma = 10^4$
Dagget and Keulegan (1974)	$\mathsf{R}_D = Q/D\nu = 5 \times 10^4$	no influence of surface tension was found
Jain et al. (1978)	R_{min} increases with F	$1.2 \times 10^2 < \mathsf{W}_D = \rho D v^2/\sigma < 3.4 \times 10^4$

TABLE 2.5: Limit values for modelling vortices

Anwar et al. (1978) derives the limit values on basis of the submergence depth, and Dagget and Keulegan (1974) and Jain et al. (1978) on the size of the intake. Scale effects concerning

the underflow of gates, following Froude law of similarity arise from the fluid viscosity if the losses exceed a limit value. For very small gate openings surface tension gets decisive. Limit values for the geometry of sluice gates given in literature are obtained from

- published model test results (e.g. Smetana, 1937 by Montes (1997));

- overflow of a sharp crested weir by (Speerli and Hager, 1999);

- empirical investigations, where the dependency of the limit gate opening on the channel width was found and subsequent derivation of a general relation of channel width and limit gate opening as a subject to viscosity effects described in dependency of the downstream flow depth, contraction length ($2a$), friction slope and contracted velocity (Roth and Hager, 1999).

The values derived through these investigations are summarised in Table 2.6.

Author	Limit gate opening [mm]	Channel width [mm]
Nago (1984)	60 for $a/h_0 < 0.5$	considered to be negligible
Montes (1997)	60	-
Speerli and Hager (1999)	50-70	300
Roth and Hager (1999)	45	>1000
	50	500
	70	350
	90	245

TABLE 2.6: Limit values for model tests concerning underflow of gates

2.7   Concluding remarks

The hydrodynamic source of excitation investigated herein results from the turbulence upstream of a sluice gate due to energy dissipation and a shear layer separating from the pier, rolling up into a vortex, which is stretched and ends at the surface of the tail-water downstream of the gate. The pier induces flow instabilities upstream of the gate, which consequently experiences extraneously induced excitation. Due to the properties of the shear layer and the vortex a pressure drop and enhanced pressure fluctuations, which are expected to be stronger than turbulent fluctuations due to flow under the gate. The vortices shedding from the pier cause a horizontal impact on the gate leaf. Further the separation from the gate lip is influenced by the upstream vortex formation. Depending on the characteristics of vortex formation the impact might be periodic, but even if the impact is non-periodic a feedback mechanism with the structure can cause periodic fluctuation. An influence of the vortex formation on the discharge capacity of underflow gates should be investigated.

Chapter 3

Methodology

The analysis of vortex formation and its influence on the upstream face of a sluice gate is investigated by means of physical modelling. For a first impression pre-tests were performed, using simplified measurement equipment installed at an existing model. The experiences gained could be used to plan the model rigs in two scales for systematic tests. Finally the processing of the acquired data is introduced within this chapter.

3.1 Pre-tests

First tests were performed on a spillway intake structure at a model scale of 1:35 consisting of four radial gates. For the pre-tests the two left gates were closed and the two gates furthest to the right were operated. A planar sluice gate with twelve boreholes, used as pressure taps, was placed into the slots for the stop-log of the third gate. Therefore the pier head length was 107.8 mm. The radial gate behind the planar gate was fully opened during the tests and did not influence the discharge capacity or downstream flow. A plan view of the inlet structure, a cross section of the sluice gate and the spillway crest as well as a view illustrating the measurement equipment is given in Figure 3.1.

3.1.1 Observations

To observe the mean pressure distribution at the gate, flexible hoses were connected to the pressure taps and attached to a vertical scale for observation of the water elevation in the hoses. The discharge was documented according to the water supply system. The gate operation for the tests was set in order to generate an intense vortex upstream of the gate. Hence its effects on the pressure could be investigated. Due to the optimised shape of the right separation pier vortices were not generated at the first gate. Instead eccentric flow from the left, where the gates were closed, caused vortex formation at the left side of the third gate (see Figure 3.2). During all tests the fourth gate was fixed at an opening of 143 mm, enhancing the total discharge, velocity and hence the vortex formation at the third gate. The pressure was observed for three different gate openings at the third gate. The
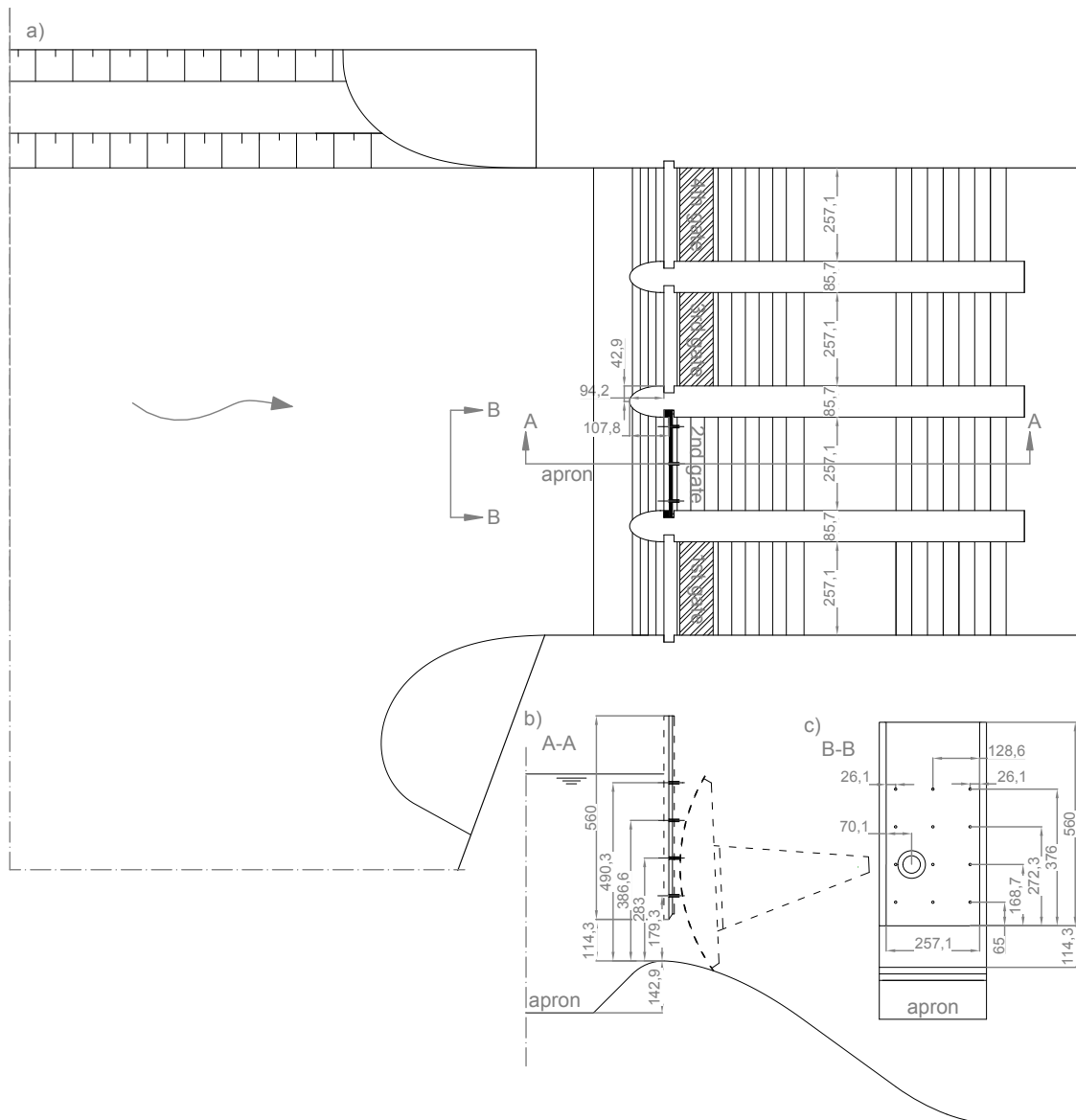
FIGURE 3.1: Gate structure of the spillway model (measurements in mm): a) plan view, b) cross section of the gate spillway crest c) view of the gate equipped with pressure taps connected to hoses and one flush mounted sensor

FIGURE 3.2: Vortex in front of the planar sluice gate during pre tests

total head in the reservoir was aimed to be kept constant for the three gate openings by adjusting the discharge accordingly. A discharge Q of 170, 210, and 258 l/s resulted in total heads H_0 of 514, 529 and 526 mm for gate openings a of 114, 200 and 257 mm, respectively.

Figure 3.3 shows the observed hydrostatic pressure in dimensionless form as the pressure coefficient C_p defined in Equation (2.2) depending on the dimensionless vertical location at the gate $Z = (z - a)/(H_0 - a)$. The graphs in Figure 3.3 are arranged according to
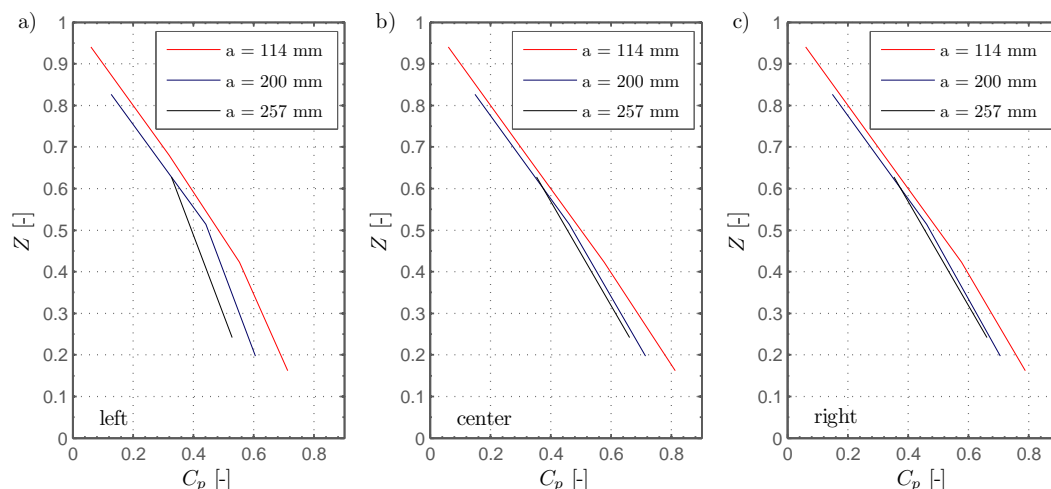
FIGURE 3.3: Pressure coefficients C_p derived from observed hydrostatic pressure at a) the left, b) center and c) right side of the second gate

the location of the pressure taps. The results for the different gate openings are identified by different colours. As the gate opening increases, the absolute submerged hight of the gate decreases and not all pressure taps are below the water level anymore. Therefore the corresponding graphs representing the pressure along the gate get shorter with increasing gate opening.

The data obtained shows that not only the absolute hydrodynamic pressure but also the normalised pressure expressed by the pressure coefficient C_p decreases with increasing gate opening at all locations at the gate. This effect is particularly distinct at the left side of the gate, where the main vortex formed. Concerning the pressure coefficient C_p at the center and on the right side of the gate it decreases only marginally with increasing gate opening a from 200 to 257 mm. Looking into the lateral pressure distribution the difference was found to be rather small between the center and the right side of the gate. If there was a noticeable difference, the pressure was smaller at the right side. Compared to that, the pressure drops clearly with increasing gate opening at the left side of the gate.

3.1.2 Measurements

To record the pressure and its fluctuations over time two piezoresistive pressure sensors were installed. These sensors of Keller Series 21 have chamber-mounted membranes, a measurement range of 0-1 bar, with a total error band of 0.5 % (0-50 °C) of the full scale. Hence simultaneous measurements could be performed at two locations at the gate. Successively the sensors were connected to all pressure taps located at the lowest and second lowest row.

Therefore time series were measured at six locations in total. The gate opening a was set to 114 mm for the investigation. In a next step a capacitive pressure sensor with a diaphragm, Keller Series 46 X, 0-0.3 bar, maximum error band of 0.3 % (0-50 °C) of the full scale, was mounted next to the left tap in the second row from the gate lip. Thereby the results obtained from sensors with different principles for pressure measurement could be compared, with the goal to identify a suitable measurement technique for further experiments. For the location of the pressure taps and the directly mounted sensors see Figure 3.1c. The vortex formation was captured by a video camera simultaneously. Thus the correlation of the visual vortex strength and the recorded time series could be evaluated.

3.1.3   Results

Throughout all measurements at the left side, a distinct pressure drop at the left side of the gate was identified and could be related to the vortex forming upstream of the gate. A sudden breakdown of the vortex resulted in an abrupt pressure maximum. As an example for the pressure development time series measured simultaneously at the lowest row on the left side and at the center are plotted for comparison in Figure 3.4. The information from
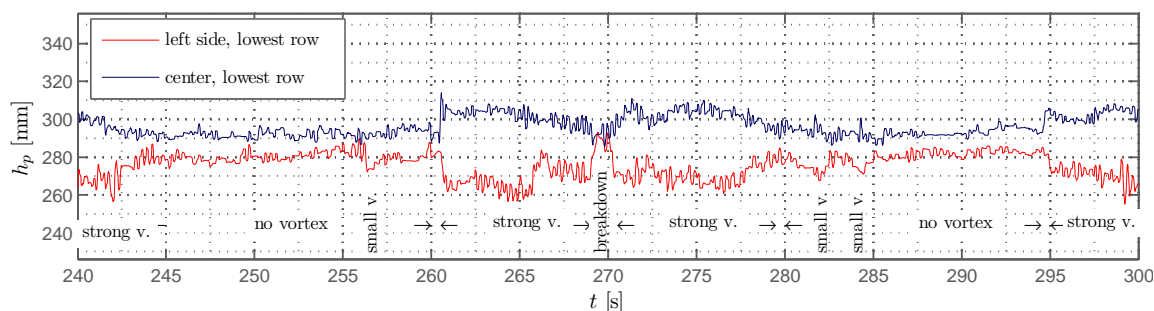
FIGURE 3.4: Comparison of the data series of pressure measurement at the lowest row on the left side and the center

the video was used to identify the state of the vortex. During phases without vortices or with very weak short term ones (marked as 'no vortex') the pressure at the left and the center are approaching each other. As a vortex starts to form the pressure diverges (marked as 'strong v.'), as it increases at the center of the gate and decreases on the left side. A sudden breakdown causes the pressure to level out for a short time span. The visually observed vortex extension was limited to the left part of the gate, stretching to the center. Accordingly measurements in the bottom row on the right side of the gate did not show any vortex related effects. Evaluating measurements at the second lowest row it was found that the effects described above decrease with distance from the gate lip.

Differences in the performance of the two different sensor types are illustrated in Figure 3.5 showing the first minute of a measurement. The measurement series depicted, were acquired at the second lowest row, on the left side. The sensor with the flush-mounted diaphragm delivers a smoother time series as compared to the sensor with the chamber-mounted membrane connected via a hose. It was assumed that the smaller area of the latter has an increased sensitivity to the pressure fluctuations or that a presumably fluctuating water column in the elastic plastic hose influenced the measured signal.
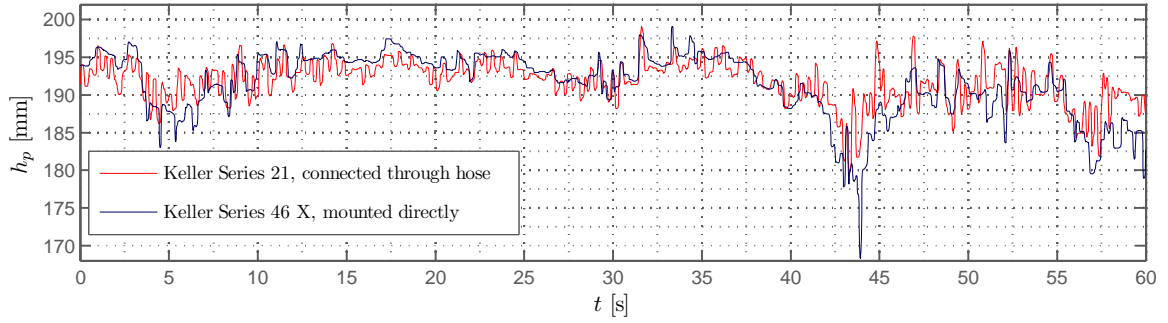
FIGURE 3.5: Comparison of data series measured with Keller Series 21 connected through a hose and Keller Series 46 X mounted directly, measurement at the left side of the gate in the second lowest row

To compare the results, obtained with the different sensors the mean pressure, root mean square and extreme fluctuations were calculated and given in Table 3.1. The maximum

		Left side	Center	Right side
	z	$\overline{h}_p$ [mm]	$\overline{h}_p$ [mm]	$\overline{h}_p$ [mm]
	283	192	199	204
	179	270	299	291
measuring method	z	$h_{p,\mathrm{max}}$-$h_{p,\mathrm{min}}$ [mm]	$h_{p,\mathrm{max}}$-$h_{p,\mathrm{min}}$ [mm]	$h_{p,\mathrm{max}}$-$h_{p,\mathrm{min}}$ [mm]
diaphragm	283	34		
hose	283	21	24	18
hose	179	73	45	26
measuring method	z	$h'_{p,\mathrm{rms}}$ [mm]	$h'_{p,\mathrm{rms}}$ [mm]	$h'_{p,\mathrm{rms}}$ [mm]
diaphragm	283	3.7		
hose	283	2.6	2.5	2.5
hose	179	5.6	5.5	5.5

TABLE 3.1: Mean pressure $\overline{h}_p$ and maximum pressure deviation $h_{p,\mathrm{max}}$-$h_{p,\mathrm{min}}$ recorded by pressure sensors connected through hoses or direct (diaphragm)

pressure deviations obtained from the time series measured with the flush-mounted and the chamber-mounted diaphragm was 34 mm and 21 mm respectively. Calculating the root mean square value of pressure fluctuations $h'_{p,\mathrm{rms}}$ measured with the two different sensor types the differences are much smaller as compared to the extreme values. $h'_{p,\mathrm{rms}}$ deviates only by 1.1 mm. A damping effect due to the hoses or the chamber-mounted diaphragm is supported by the increased peaks measured with the flush-mounted sensor. Concerning the pressure distribution over the gate the values given in the last row of Table 3.1 make clear that the pressure reaches its minimum on the left side, increases to a maximum at the center of the gate and again decreases to the right side with a smaller extent. In the second lowest row, the mean values $\overline{h}_p$ increase from the left to the right. The maximum of the pressure fluctuations, indicated by the differences in the measured $h_{p,\mathrm{max}} - h_{p,\mathrm{min}}$ was found at the left side of the lowest row. They decrease from the left to the right. Comparably the maximum deviation in the second lowest row are reduced. Concerning the root mean square

value $h'_{p,rms}$ there is no significant horizontal trend, but the increase, when approaching the gate lip is explicit.

Figure 3.6 illustrates the results given in Table 3.1 expressed as normalised parameters. The pressure coefficient C_p, normalised root-mean-square of pressure fluctuations $C_{p',rms}$ and normalised extrema C_{p+} and C_{p-}, according to Equation (2.2), (2.44) and (2.45) are given for the measurements through the hose. The extreme values of pressure fluctuations appear
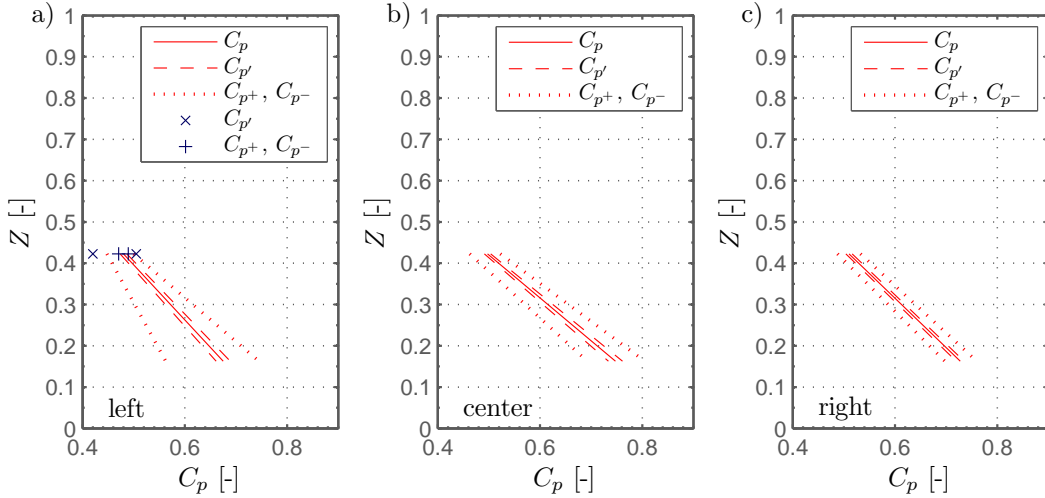
FIGURE 3.6: Pressure coefficient C_p, root-mean-square of the pressure fluctuations $C_{p',rms}$ and extrema C_{p+}, C_{p-} observed at a) the left, b) center and c) right side of the gate

on the left side and they decrease with increasing distance from the vortex from the left to right side and with increasing relative location Z at the gate. As a comparison the same parameters characterising the pressure fluctuations ($C_{p',rms}$, C_{p+} and C_{p-}), were evaluated for the sensor with the diaphragm. The results are given in Figure 3.6 as blue crosses. The discrepancy between the measurements with the different sensors, is emphasised by the derived minimum occurring at the left side of the gate in the second lowest row indicated by C_{p-}.

3.1.4   Summary

An asymmetric load distribution at the gate is caused by the eccentric approach flow and the induced vortex, which could be obtained by time independent and time dependent measurement methods. An influence on the maximum pressure fluctuations C_{p+} and C_{p-} could be identified from the time series. The instability of the vortices cause remarkable amplitudes of fluctuations and could cause non-stationary characteristics of the time series, which is supported by that shown in Figure 3.4. Concerning the equipment for pressure measurement, it was found that sensors with flush-mounted diaphragms are the most straight forward opportunity for acquisition of pressure and especially the extent of pressure fluctuations. This agrees with the discussion in Toso and Bowers (1988), where sensor diameter and the location of the diaphragm are addressed.

3.2   Experimental setup

The model setup for the systematic study of parameters influencing vortex generation and pressure conditions at the upstream gate leaf could be planned on the basis of the knowledge gained from the pre-tests. The investigations were performed on two hydraulic models of different scales. The models were set up in the Hydraulics Laboratory of the Institute of Hydraulic Engineering and Water Resources Management of the Vienna University of Technology. Details concerning the model setup and boundary conditions are given in the following sections.

3.2.1   Experimental facilities

The required discharge for the model tests could be provided by the pumps and supply system of the lab. It consisted of a reservoir below the laboratory with a total capacity of $1000 \, \text{m}^3$, pumps and the corresponding pipelines with gate valves to regulate the discharge. The magnetic flow meters were used to set the discharge and to record it for further analysis.

Model rig of the small scale model

The first small scale model of an idealised weir structure was constructed in a flume with a length of 15.5 m, a width of 1.7 m and a height of 0.5 m. The estimated maximum required discharge for the tests was 140 l/s. The water was pumped from the tank to the upstream end of the flume, where the flume has a depth of 1.15 m, forming a water pillow below the outlet of the pipe to dampen turbulence due to the inflow (see Figure 3.7 and 3.8a). Along the length of the flume flow irregularities such as unequally distributed flow velocity or waves were expected to level out. Several measures were tested to reduce water surface fluctuations. Figure 3.7 gives a plan view and a sectional view. In order to dampen fluctuations of the water surface caused by the inflow from the pipe a vertical floating baffle was installed just downstream of the plunge pool below the intake. Two rows of perforated bricks caused a uniform spread of the water to the flume. Propagating waves downstream of the bricks were suppressed by a horizontal board, which was fixed slightly below the mean water level. These measures are pictured in Figure 3.8a. A free flow section of 8.73 m followed. During the tests it has been found out that randomly placed stones forming a scattered riprap were the most effective way to avoid wave propagation all the way to the gates. The riprap was located in front of another row of perforated bricks, spreading the water uniformly. Honeycombs on top of the bricks were used to homogenise the top layer of the flow at water levels exceeding 0.4 m. The total space needed for these two measures was 1.07 m. For a picture of the arrangement see Figure 3.8b. Another free flow section (3.45 m) followed to guarantee undisturbed flow approaching the gates (see Figure 3.8c).

The actual gate structure used for the investigations consisted of three planar gates located in the left half of the flume looking downstream, supposedly causing an asymmetric flow to the gates. A plan view of the model is given in Figure 3.9a. The boundary condition on the left side of the structure was formed by a half of a pier fixed at the wall of the flume. On
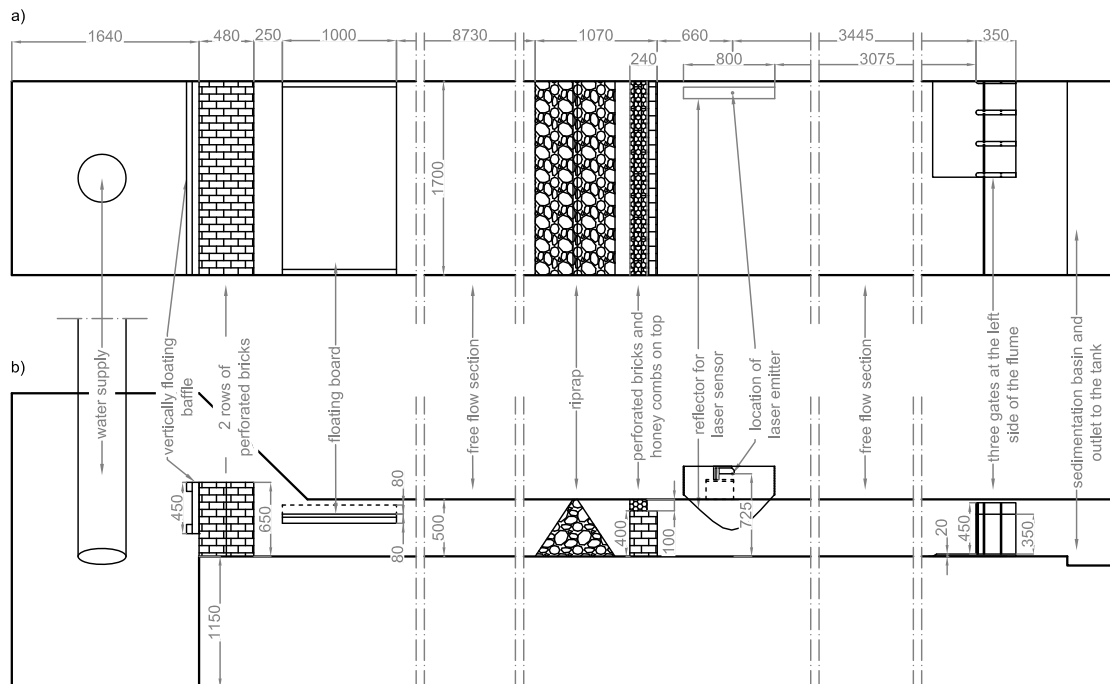
FIGURE 3.7: Model rig of the small scale model, setup of the flume: (measurements in mm): a) plan view, b) cross section
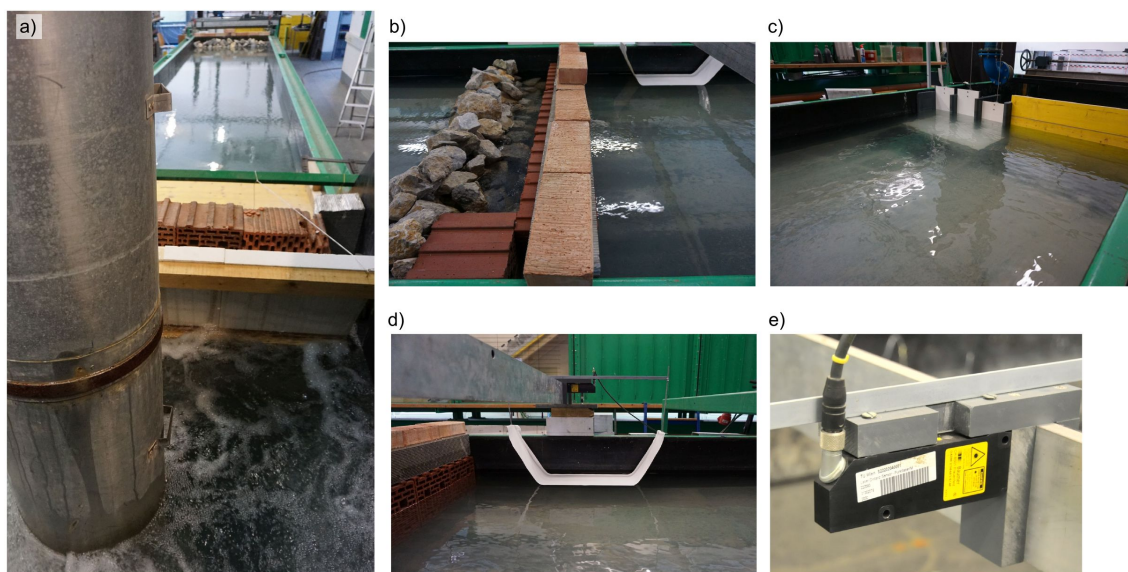
FIGURE 3.8: Details of the model flume: a) inlet, b) riprap and perforated bricks, c) gate structure, d) water level measurement, e) laser sensor
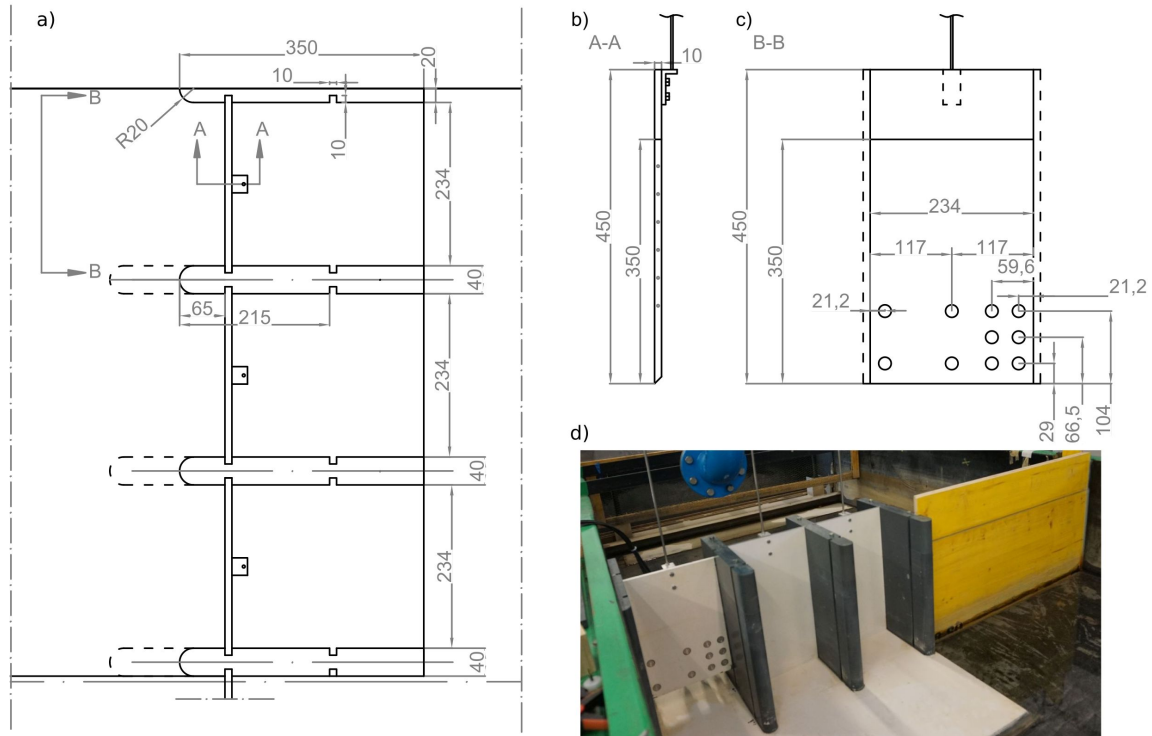
FIGURE 3.9: Final construction of the gate structure (small scale model): a) plan view, b) cross section of the gate, c) upstream view of the gate and locations of the sensors, d) overview

the right side a vertical board was used to block the free half of the flume. Thus the water level in front of the gates was defined by the discharge and the gate opening. One gate had a total width of 234 mm. The width of the piers was 40 mm and they had a total length of 350 mm. The shape of the piers on the upstream side was formed by half circles with a radius of 20 mm. At two different locations (65 mm and 215 mm downstream of the pier head) notches were cut in the piers. Hence the pier head length could be changed by setting the gates to the constructed front or the back slot. For further investigations concerning the influence of the pier head length movable extensions made of sheet metal were used. Including the apron of 20 mm, the total height of the structure was 370 mm for the first investigations, but was extended to 470 mm for further experiments. The gate openings could be set by pins, which could be fixed every 40 mm. With the extension of the model height the system to lift the gates was changed as well. Through a construction above the gates the gate opening could be set by fixing a tie bar with a screw. Figure 3.9b shows the cross section of the planar gates and the construction to lift the gates via a tie bar. The gate equipped with the pressure cells is depicted in Figure 3.9c. The basic measurement grid consisted of two rows located 29 and 104 mm from the lower edge of the gate and three columns at the left and right side and the symmetry axis of the gate. Due to the eccentric arrangement of the weir structure, the strongest vortex was expected to develop at the right side of the gates. Four extra pressure sensors were used to increase the density of the measurements in this region. An extra column of sensors was located just left of the outer right row. Two more sensors were placed in between the top and the bottom row. Thus six sensors could be used to survey the effect of the vortex on the gate. A picture of the final

model construction can be found in Figure 3.9d.

Model rig of the large scale model

In order to look into scale effects a single gate of the weir structure described before was then constructed at twice the size. A minimum wall height of the reservoir of 1.0 m was required. The basic concept was kept according to the small scale model. Hence the outlet of the pipe supplying the water was located under the reservoir water level. Further measures to suppress waves in the reservoir and affect homogeneous approach flow conditions were a vertical floating board upstream of a wall of perforated bricks and a horizontal floating board. About 5.8 m of the reservoir was a free flow zone. The laser sensor used to measure the water level was located 2.3 m upstream of the underflow gate. The plan view and cross sectional view are given in Figure 3.10.
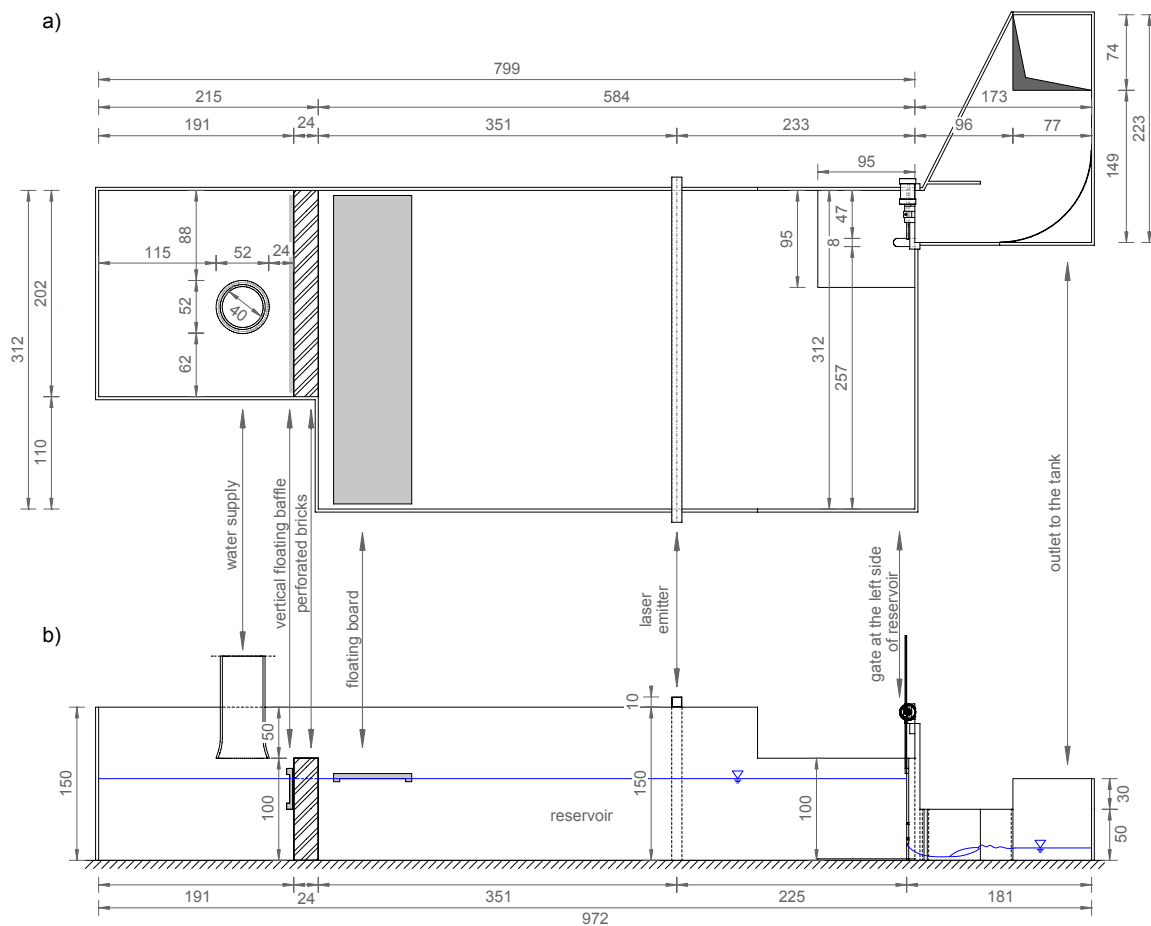
FIGURE 3.10: Model rig (Köpf, 2017), measurements in cm: a) plan view, b) cross section

The gate dimensions as well as the locations of the pressure sensors were exactly twice the size of the small scale model. The main elements of the hydraulic model are given in Figure 3.11 along with a photograph of the model structure. One pier with the length of 130 mm was constructed on the right side of the gate, which determined the inflow conditions just upstream of the gate. The gate opening could be set through a motor
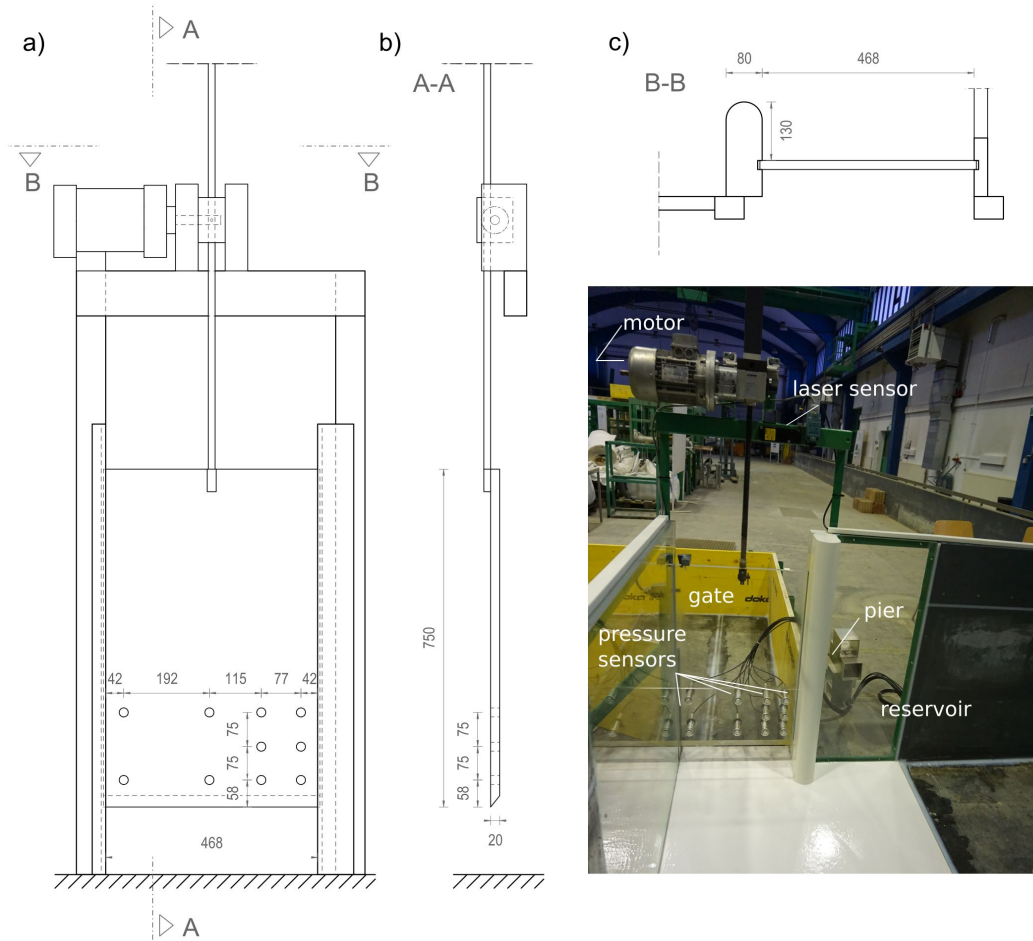
FIGURE 3.11: Model rig, large scale model: a) upstream view, b) cross section, c) plan view of the gate (Köpf, 2017) and d) picture taken from the reservoir in downstream direction

driven mechanism. To set specific gate openings a laser sensor surveying the gate location was calibrated accordingly. This improvement allowed a fast adaptation of gate opening and water level according to the experimental program compared to the small scale model, where the gate opening was set with spacer blocks.

3.2.2 Measurement instrumentation

As measurement equipment, ten pressure sensors, a laser sensor and a magnetic flow meter were used. The pressure impact on the gate, the water level upstream of the structure and the discharge could be documented. In the larger scale model another laser sensor was installed in order to set the gate opening depending on the measurement of distance. Two "Spider 8" by HBM (Hottinger Baldwin Messtechnik GmbH) were used as measurement amplifier and connection to the laptop. The data was stored to ASCII-files for further analysis.

For the velocity measurement in front of the gate and the determination of the approach flow condition an Acoustic Doppler velocimeter ("Nortek-Vectrino") was used.

Pressure measurement

The pressure measurements at the gate were performed with sensors by Keller AG, whereas two sensor types were tested in the smaller scale model. Those were of series 46 X and series 35 X by Keller AG, which are depicted in Figure 3.12a&b respectively.
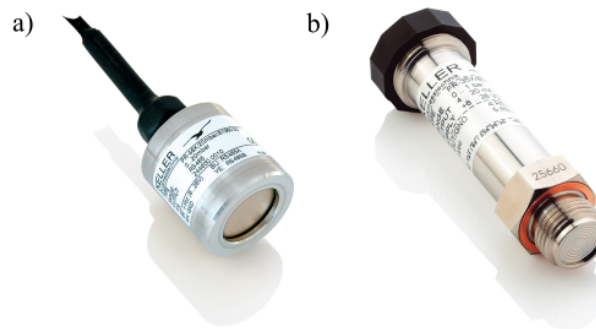
FIGURE 3.12: Pressure sensors: a) series 46 X by Keller AG, b) series 35 X by Keller AG

Sensors of the series 46 X are capacitive transmitters. In this case sensors with a measurement range of 0-0.3 bar, a typical error band of 0.2 % and maximum error band of 0.3 % with reference to the full scale at a temperature of 0-50 °C were used. The signal output was 0-10 V. They had an outer diameter of 38 mm. The housing of the sensor had a thickness of 7 mm, which lead to an actual diameter of the ceramic diaphragm of 24 mm. The diaphragm was not chamber-mounted, but set back compared to the front edge of the sensor.

The final sensors installed, of the series 35 X, which were also used in the larger model, worked on the basis of piezoresistive transducers. They had a pressure range from 0-3 bar, scaled to 0-10 mwc. The maximum error band was given with 0.1 % with reference to full scale between 10 an 40 °C. With each sensor the calibration data and therefore the actual accuracy was submitted. The error for all ten sensors used was between 0.04 and 0.112 % concerning the measurement range according to the calibration records. The signal output from 0-10 V was used. Their output rate is 400 Hz. The outer diameter of the sensors is 18 mm. This sensor type had a flush-mounted diaphragm.

Water level measurement

Laser distance sensors by Baumer electronics (OADM21I6481/S14F) with a measurement range of 200-1000 mm and a linearity error of 0.8-2.0 mm were used to record the water level. One was located upstream of the gate, on the left side of the flume. For the location of the sensor in the two models see Figure 3.7 and Figure 3.10 respectively. An appropriate floating reflector was installed underneath the sensor. Figure 3.8d shows the laser sensor during operation and in Figure 3.8e a detail picture is given. For the adjustment of the gate opening of the larger model a laser sensor was fixed to the overhead structure of the gate measuring the distance to the top edge of the gate. By appropriate calibration the gate opening could be set during the model tests.

Measurement of discharge

For the measurement of the discharge the magnetic flow meter "Promag 33" installed at the conduits of the supply system for discharge regulation could be used. Its measurement range and errors are given depending on the flow velocity which is 0-12.5 m/s with 0.01 % full scale accuracy and 0.5 % accuracy of the measured value.

Visual survey

For the visual documentation of the vortex a video camera was located above the gate structure. Therefore the locations of the vortices and their strengths could be monitored. In the small scale model in the flume, the shape of the vortex could only be surveyed through the water surface. As an improvement, transparent walls were used in the larger scale model. The documentation of the vortex characteristics could be done from the top and the left side by video and photographs. Therefore a reference grid was drawn on the side of the pier facing the vortex.

Measurement of velocity

3D water velocity profiles were recorded with a side-looking "Vectrino" Acoustic Doppler velocimeter by Nortek AS. The measurement range was 0.01-4 m/s and its accuracy was 0.5 %. The output rate was 25 Hz. The data communication was established through the corresponding "Vectrino" software, which was used to configure the instrument and collect and store data. The location of the probe *i.e.* of the measurement was set through the measurement bridge system of the flume.

3.2.3 Experimental program

The goal of the final experimental program was the determination of the pressure distribution and the pressure fluctuations on the upstream face of the gate leaf depending on the gate opening a, the approach energy head H_0, the pier head length l_p and the gate operation effects. The list of the final experiments is given in Table 3.2. Measurement series in the top part of the table were performed in the small scale model. Series A1-1 and A2-1 were repeated in the large scale model and are given in the bottom part of the table as A1-2 and A2-2. The gate operation conditions are indicated by "o" for open and "x" for closed. The symbols are arranged according to the location of the gates looking at the weir structure from the upstream direction, *i.e.* "o-x-x" indicates that the first (left) gate is open, whereas the second (central) and the third (right) are closed. In series A, only the first gate was operated and the other parameters of interest were varied. The range of variation is given in Table 3.2. For determination of the smallest gate opening the limit values according to Table 2.6 were taken into account. Thereby the limit gate opening for the model tests was determined to be 60 mm. Series B and C were performed with discharge under three gates in order to increase the relative approach flow velocity.

Series	Gate operation	a [mm]	h_0 [mm]	l_p [mm]
A1-1	o-x-x	60-140	300	65
A2-1		80	170-400	65
A3		80	300	65-265
B1	o-o-o	60-120	300	65
B2		80	200-400	65
B3		80	300	65-265
C1		80	200	65-265
A1-2	o-x-x	120-280	600	130
A2-2		160	340-800	130

TABLE 3.2: Experimental program (small model: A1-1 to C1, large model: A1-2 and A2-2)

The influence of the pier head length on the pressure characteristics was investigated in series A3 and B3 at a constant gate opening of 80 mm. As the pier head length l_p affects the discharge coefficient the discharge Q had to be adapted slightly to keep the mean value of the approach hydraulic head $\overline{h}_0$ almost constant for each test. The pier head lengths tested were 65, 95, 135, 165, 215 and 265 mm. The gate was set in the front slot and the pier head length was extended to a length of 165 mm. Further measurements were performed with the gate located in the back slot. The front slot was covered during these tests to avoid an effect on the pressure fluctuations. In measurement series C1 the influence of the pier head length with reduced hydraulic head was investigated.

For the case of a/H_0 with the largest pressure fluctuations, the influence of the pier head length was checked in series C1.

3.3 Data analysis

Within this section the data analysis performed on the collected sample records is introduced. The derivation of the mean pressure distribution along the gate and the amplitudes of fluctuations is introduced. Preliminarily it is discussed how the data was standardised to establish comparability apart from mean pressure.

3.3.1 Water surface fluctuations

The mean piezometric head $\overline{h}_p$ derived from the time series was independent of pressure fluctuations distributed about the mean. In contrary the amplitudes of the fluctuating component of the hydrodynamic pressure $\overline{h'}_p$ are a result of all pressure fluctuations induced by any source. The superposed water surface fluctuations were one of the most obvious effects. The time series acquired with the laser sensor represented the water surface fluctuations in the flume. The approaches described in this section, were used to achieve equivalent preconditions for the analysis of dynamic pressure characteristics introduced later.

In order to identify longitudinal and transverse oscillations in the flume a model of two-dimensional standing waves was used. Thereby the frequency for particular wave modes in longitudinal and transverse directions can be determined using

$$\omega_{mn} = \sqrt{g\kappa_{mn} \tanh \kappa_{mn}d} \tag{3.1}$$

where the radian frequency of the waves ω_{mn} is calculated depending on the water depth and the wavenumber κ_{mn} by

$$\kappa_{mn}^2 = \left(\frac{m\pi}{L}\right)^2 + \left(\frac{n\pi}{W}\right)^2 \tag{3.2}$$

The wave modes in longitudinal and transverse directions is defined by m and n respectively, and L is the channel length and W its width.

The goal is to standardise the data by eliminating the effect of these water surface fluctuations, so that it might be possible to analyse the influence of the flow turbulence and vortex formation on the amplitudes of pressure fluctuations solely.

Influence of water surface waves on pressure

Linear wave theory is considered, to give a relationship between the surface elevation and the pressure at any point below the water surface. Basics can be found *e.g.* in Dean and Dalrymple (1991), the application as used herein is derived in Fenton (2015) where a filter is introduced to connect free surface water levels and subsurface pressures due to waves. For waves that are long, longer than several times the water depth, there should be little diminution with depth. However there is a diminution as the wavelengths become small. Hence high frequency components should have almost no effect on the pressure.

The pressure p in the fluid is given by

$$\frac{p}{\rho g} = -z + \frac{H}{2} \frac{\cosh k \left(z + d\right)}{\cosh kd} \cos kx \sin \omega t \tag{3.3}$$

with z the elevation of a point relative to the undisturbed surface level, H being the crest to trough wave height, k the wave number, d the water depth and ω the radian frequency. From now on the end of the flume at $x = 0$ will be considered. Two general Fourier series with zero mean describe the fluctuations of the surface elevations and the pressure

$$h'(t) = \sum_{j=1} H_j \sin \frac{2\pi jt}{T}$$

$$\frac{p'(t)}{\rho g} = \sum_{j=1} P_j \sin \frac{2\pi jt}{T}$$

where T is total length of record. According to linear wave theory their relation is given as

$$\frac{P_j}{H_j} = \frac{\cosh k_j \left(z + d\right)}{\cosh k_j d} \tag{3.4}$$

and where k_j satisfies

$$\omega_j = \frac{2\pi j}{T} = \sqrt{g k_j \tanh k_j d} \tag{3.5}$$

Ordinarily for each j it would have to be solved numerically for the k_j, however a formula by Guo (2002) is an accurate approximation to the linear dispersion relation

$$k_j = \frac{\sigma_j^2}{g} \left(1 - e^{-\left(\sigma_j \sqrt{d/g}\right)^{5/2}} \right)^{-2/5} \tag{3.6}$$

In the form of equation (3.4) the quantity P_j/H_j is difficult to evaluate for all j as the k_j become large for increasing j, and the hyperbolic functions enormous. Here we obtain an alternative formula to (3.4) for computing P_j/H_j. From the definition of cosh we write

$$\cosh\theta = \frac{e^\theta + e^{-\theta}}{2} = \frac{e^\theta \left(1 + e^{-2\theta}\right)}{2}$$

giving

$$\begin{aligned} \frac{P_j}{H_j} &= \frac{\exp\left(k_j \left(z + d\right)\right) \left(1 + \exp\left(-2k_j \left(z + d\right)\right)\right)}{\exp\left(k_j d\right) \left(1 + \exp\left(-2k_j d\right)\right)} \\ &= \exp\left(k_j z\right) \frac{1 + \exp\left(-2k_j \left(z + d\right)\right)}{1 + \exp\left(-2k_j d\right)} \end{aligned} \tag{3.7}$$

As z is negative for all subsurface measurements, $-d \leqslant z < 0$; d is positive; $z + d$ is the elevation above the bottom, always positive; and k_j is positive, so the arguments of all three exponential functions are always negative. Any software could handle the exponential of a large negative quantity, there should be no problems evaluating P_j/H_j in the form of equation (3.7).

All the high frequency components of P_j as calculated here will be vanishingly small and the physical system itself removes all effects of surface waves for the high-frequency components. Whatever the surface waves are, possibly two-dimensional standing waves (cross-channel also), the effects of all surface waves decay very quickly down into the water, no more than half their wavelength.

Spectral subtraction

The pressure component induced by water surface fluctuations is supposed to be additive noise to the pressure fluctuations induced by turbulence and vortex formation. The estimate for the noise can be derived from the sample records of water surface fluctuations filtered according to the explanations in the previous section. It is suggested that the influence of the water surface fluctuations is eliminated by subtraction of the superposed noise from the pressure records in the time domain. Thereby similar preconditions for the analysis of all measurements are established.

Fluctuations of the water surface are caused by external effects and/or the flow under the gate itself. It was measured upstream of the gate. Hence an unknown time lag is between the

measurement series of water surface and pressure. Therefore trying to achieve independence of the pressure measurements from water surface fluctuations through subtraction of the sample records of pressure and water surface fluctuations in the time domain did not show any remarkable effect.

Expressing the sample records in the frequency domain, the pressure component due to water surface fluctuations can be subtracted independent of the time. Generally spectral subtraction is a method to separate a clean signal from a signal with additive noise as often required for speech signals. The additive noise model is defined in the time domain as

$$y(m) = x(m) + d(m) \quad m = 0, ..., N-1 \tag{3.8}$$

with the signal $y(m)$, the undisturbed signal $x(m)$ and the superimposed noise $d(m)$. Accordingly it is expressed in the frequency domain as

$$Y(k) = X(k) + D(k) \quad k = 0, ..., N-1 \tag{3.9}$$

with the Fourier transform of the signal $Y(k)$, the undisturbed signal $X(k)$ and the superimposed noise $D(k)$, with m and k being the time index and frequency variable respectively.

In terms of magnitude ($Y_k = |Y(k)|$, $X_k = |X(k)|$, $D_k = |D(k)|$) and phase (θ_{Y_k}, θ_{X_k}, θ_{D_k}) of the frequency spectra, as introduced in Section 2.3.2, Equation (3.9) can be expressed according to

$$Y_k e^{i\theta_{Y_k}} = X_k e^{i\theta_{X_k}} + D_k e^{i\theta_{D_k}} \tag{3.10}$$

where θ_{Y_k} is the phase of the Fourier transform $Y(k)$. Applying spectral subtraction either the magnitude or power spectrum of the noise is subtracted from the corresponding spectrum of the original signal. In general the estimated spectrum of the undisturbed signal $\hat{X}_k = |\hat{X}(k)|$ is obtained through spectral subtraction after

$$\hat{X}_k^b = Y_k^b - \alpha(k)\overline{D_k^b} \tag{3.11}$$

where the exponent b equals 1 or 2 in case of magnitude or power spectral subtraction respectively. Concerning speech enhancement, α is a factor used to control the amount of removed noise and the average noise spectrum $\overline{D}_k = \overline{|D(k)|}$ has to be estimated from periods of absence of the actual signal. For this purpose the magnitudes of the noise spectra of several recorded frames are averaged.

The undisturbed signal is restored in the time domain according to

$$\hat{x}(m) = \sum_{k=0}^{N-1} \left(\hat{X}_k e^{i\theta_{Y_k}} \right) e^{i2\pi km/N} \tag{3.12}$$

which is the inverse discrete Fourier transform of the estimated magnitude spectrum $|\hat{X}(k)|$ combined with the phase θ_{Y_k} of the original signal frequency. (Vaseghi, 2008)

Applied in the context of this thesis Equation (3.11) gets

$$\hat{X}_k = Y_k - D_k \tag{3.13}$$

as the exponent $b = 1$, because magnitude spectral subtraction is applied, $\alpha = 1$. The estimate of the noise is the filtered spectrum of the water surface fluctuations $D_k = |D(k)|$. Averaging the noise spectrum to achieve an estimate as in Equation (3.11) is not needed for this application, because the estimate of the noise was measured independently of the signal of interest throughout the whole measurement period. Still the derived noise spectrum is an estimation, as the location of measurement differs from the pressure measurement. But as the location of measurement was the same for all experiments the estimate it is considered to be suitable for data standardisation.

Evaluation of stationarity

Stationarity of time series is a precondition for the determination of time averaged parameters as introduced in Section 2.3. It can be evaluated by performance of a so called run test, where mean values of fragments of the data series are calculated and compared. The null hypothesis of the test states that the values of a data set are in random order, *i.e.* the data has no trend or periodicy. In order to test the hypothesis the number of runs is determined by counting how often the values change from below to above the mean value. The expected value of runs are dependent on the number of samples divided by the standard deviation of the number of runs. Subsequently the test statistic of a sample is calculated from the actual number of runs minus the expected value of runs. The null hypothesis is rejected in case the test statistic exceeds a limit, set as a quantile of the normal distribution by the level of significance. For a level of significance of $5\,\%$ the test statistic has a value of 1.96.

Herein the statistical parameters concerning the run test were calculated before and after application of spectral subtraction as defined above. Therefore mean values were calculated over 10 seconds. Subsequently it was tested if the null hypothesis is accepted at a level of significance of 5%.

3.3.2 Mean pressure

Within this section the determination of the mean pressure distribution along sluice gates is described. The basis for the data evaluation are the time series obtained at a discrete number of measurement points. The relevant parameters are found on the basis of generalised flow conditions. The vertical pressure distribution can be described by a function following its shape. Finally the fitting parameters of this function are depending on the horizontal location and the flow conditions. To provide appropriate charts the discrete amount of data is linearly interpolated.

Establishing general flow conditions

The mean piezometric head $\overline{h}_p$ and hence the mean hydrodynamic pressure $\overline{p}$ can be acquired from the sample records according to Equation (2.16) for each measurement point at the gate. According to the illustration in Figure 3.13 the Bernoulli equation between the gate

lip, indicated by the index a used as point of reference and an arbitrary point at the gate can be formed with reference to the channel bottom ($z = 0$) as

$$z_a + h_a + \frac{v_a{}^2}{2g} = z + h + \frac{v^2}{2g} \tag{3.14}$$

Introduced in Section 2.1.4 and illustrated in Figure 3.13, it applies that $h_a = 0$ and hence
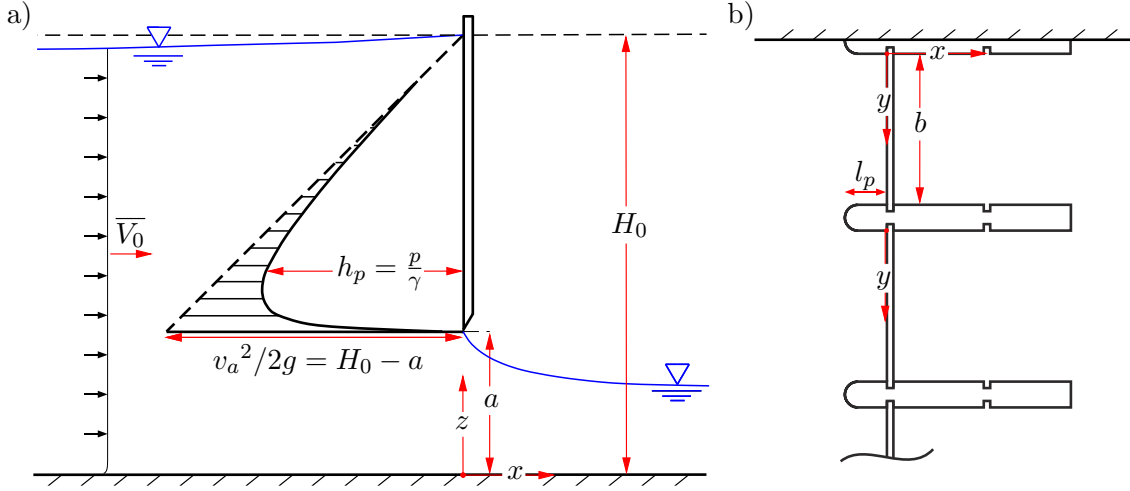
FIGURE 3.13: The hydraulics problem

$v_a{}^2/2g = H_0 - a$. Further $\Delta z = z_a - z$ is defined and Equation (3.14) becomes

$$h = \Delta z + H_0 - a - \frac{v^2}{2g} \tag{3.15}$$

where Δz, a and H_0 are known from the geometrical and hydraulic boundary conditions in each experiment. It follows that the flow velocity at the point of interest is the only unknown parameter for determination of the pressure conditions at this point. The dependency of the pressure on the velocity is emphasised by the definition of the pressure or piezometric head coefficient in Equation (2.2). Consistent with the dimensional analysis specified in Section 2.5, the velocity at a point on the gate is stated to be functional dependent according to

$$v = f(a, H_0, b, l_p, v_0, v_a, g, \rho, \nu, \sigma, z, y) \tag{3.16}$$

including the coordinates (y, z) of the point illustrated in Figure 3.13 were added to the function, leading to twelve parameters influencing the velocity along the gate.

By introducing the non-dimensional parameters derived through dimensional analysis the amount of determining parameters can be reduced remarkably as it is revealed by

$$v = f\left(\frac{a}{H_0}, \frac{l_p}{b}, \frac{v_0}{v_a}, \mathsf{F}, \mathsf{R}, \mathsf{W}, Y, Z\right) \tag{3.17}$$

Herein the non-dimensional parameters identifying the location of the point at the gate are the relative distances Y and Z. The former one determines the relative distance from the

left pier

$$Y = \frac{y/a}{b/a} = \frac{y}{b} \tag{3.18}$$

where the lateral coordinate and the gate width are normalised and set in relation resulting in dividing the lateral location of a point against the maximum distance from the left pier (gate width b). The latter is the relative position above the gate lip

$$Z = 1 - \frac{H_0 - z}{H_0 - a} = \frac{z - a}{H_0 - a} \tag{3.19}$$

which simply is the ratio of the vertical distance above the gate lip to the height of the submerged part of the gate.

Dealing with a model according to Froude similarity the influence of viscous forces and surface tension is assumed to be negligible as the Reynolds number and Weber number exceed limit values, which is discussed in Section 3.2.3. Hence they can be eliminated from Equation (3.17). For the case of free flow under a sluice gate the Froude number $\mathsf{F} = v_a/\sqrt{ga}$ is dependent on a/H_0 and therefore not an independent variable (Naudascher, 1984 or Miller, 1994), which justifies its elimination from Equation (3.17). It follows that the velocity at a point at the gate can be described as a function according to

$$v = f\left(\frac{a}{H_0}, \frac{l_p}{b}, \frac{v_0}{v_a}, Z, Y\right) \tag{3.20}$$

The normalised values of the mean hydrodynamic pressure $\bar{p}$ or mean piezometric head $\bar{h}_p$ are the pressure coefficient C_p or piezometric head coefficient C_h respectively. Equation (2.2) defines

$$C_h = \frac{\bar{h} - \bar{h}_0}{\overline{V_0}^2/2g}$$

From Figure 3.13 it is obvious that the velocity head at the gate lip $v_a{}^2/2g$ equals the height of the submerged part of the gate $H_0 - a$. Defining the gate lip as point of reference in Equation (2.2), the velocity head in the denominator can be substituted by $H_0 - a$. Furthermore, as the hydraulic head decreases to zero at the gate lip, $\bar{h}_0$ can be eliminated from Equation (2.2). Substituting the hydraulic head at the point of interest $\bar{h}$ by the time averaged piezometric head $\bar{h}_p$ derived from the sample records, the piezometric head coefficient gets

$$C_h = \frac{\bar{h}_p}{H_0 - a} = C_p \tag{3.21}$$

Of course the piezometric head coefficient C_h equals the value of the pressure coefficient C_p. Subsequently, although derived from the mean piezometric head $\bar{h}_p$, the results concerning the mean hydrodynamic pressure are be labelled as C_p as it is common in literature when discussing hydrodynamic forces. Finally it can be defined that the pressure coefficient C_p is functional dependent on the parameters found by deriving Equation (3.20) as

$$C_p = \Phi\left(\frac{a}{H_0}, \frac{l_p}{b}, \frac{v_0}{v_a}, Z, Y\right) \tag{3.22}$$

where the function Φ can be found by considering the values derived from the measurements in the model tests.

Hydrodynamic pressure distribution for general flow conditions

The normalised pressure along a vertical cross section of the upstream face of the submerged gate can be described as a function of the relative position above the gate lip by

$$C_p(Z) = k(m - Z)Z^l \tag{3.23}$$

as used in Roth and Hager (1999), whereas the fitting parameter k stretches the function, l influences the location of the maximum on the ordinate and m, as it deviates from unity introduces an offset of the top end of the function at the ordinate. This equation can be fitted to the mean values calculated from the sample records at the locations of the pressure sensors. The lateral differences of the pressure distribution are obtained from Equation (3.23) at the four sections of the gate equipped with pressure sensors. The four graphs in Figure 3.14 are placed in order to represent the lateral location of pressure distribution. The dimensionless and absolute vertical locations are given by the ordinate on
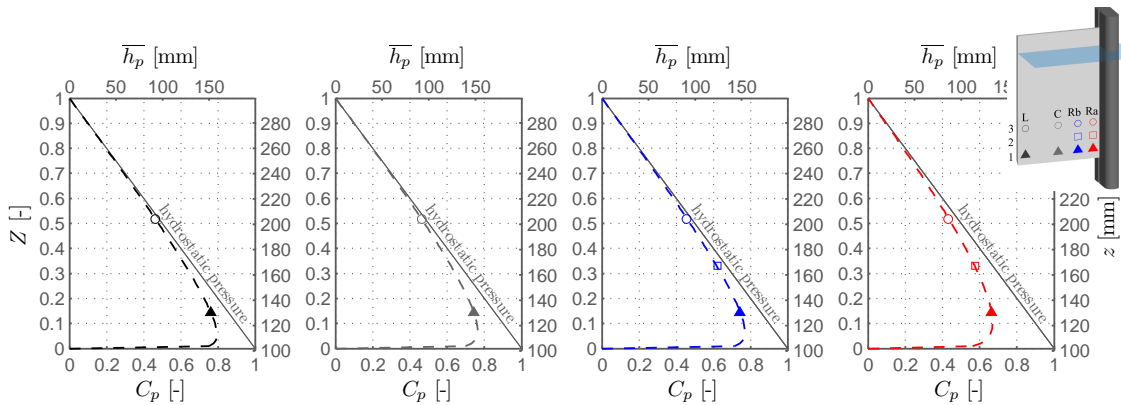
FIGURE 3.14: Dependency of mean piezometric head $\overline{h}_p$ on the vertical location z and pressure coefficient C_p on the relative position above gate lip Z

the left (Z) and the right side (z) of the graphs respectively. The dimensionless pressure coefficient C_p is given on the abscissa plotted against the relative position above the gate lip Z. The corresponding vertical location z is indicated by the secondary axis.

By considering Equation (3.23), describing the pressure distribution along vertical gate sections, the relative position above the gate lip Z can be eliminated from Equation (3.22). Therefore it can be written in terms of a function Φ:

$$C_p(Z) = k(m - Z)Z^l = \Phi\left(\frac{a}{H_0}, \frac{v_0}{v_a}, \frac{l_p}{b}, Y\right) \tag{3.24}$$

where a/H_0, v_0/v_a and l_p/b represent the relative gate opening, the dimensionless form of the approach flow velocity v_0 which is a function of the gate operation and the dimensionless form of the pier head length l_p respectively. These parameters are covered by the measurement series summarised in Table 3.2. On the basis of the experimentally gained data the

fitting parameters k, l and m can be derived. The overall goal is to define these fitting parameters as subject to the relative lateral location Y and the relative gate opening a/H_0, the relation of velocities v_0/v_a and the relative pier head length l_p/b respectively.

Parameter model for hydrodynamic pressure distribution

The parameters k, l and m of Equation (3.23) were fitted to the data points. From the results a three dimensional dataset giving the three fitting parameters as function of a/H_0 and Y was derived. Linear interpolation was used to increase the density of the data obtained in the model tests. The resulting data grid is illustrated in Figure 3.15a-c. A smoothed surface as in Figure 3.15d to f can be fitted to the grid, preserving the actual trend of the data. A sensitivity analysis was performed in order to evaluate the effect of the mesh size used
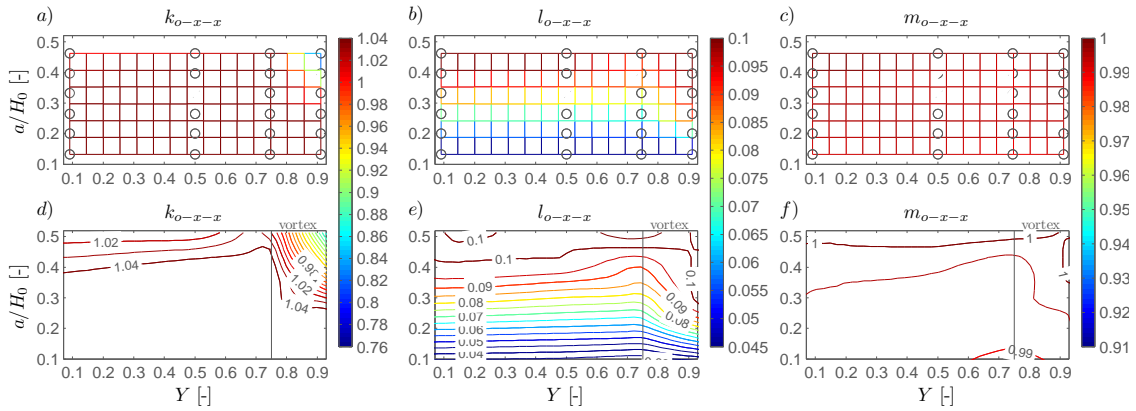
FIGURE 3.15: Fitting parameters k, l, m: a-c) linear interpolation, d-f) contour lines

for linear interpolation an smoothing. The analysis included the combination of mesh sizes between 0.01 and 0.06 for the linear interpolation and smoothing. Two goals were followed to find the optimal combination of mesh sizes. At the one hand errors of the redetermined pressure coefficients C_p compared to the measurments should be low and at the other hand overfitting needs to be avoided. Deviations of the pressure coefficient were sensitive to the grid size for linear interpolation. A grid size of 0.05 led to the smallest errors. Increasing the grid size for smoothing from 0.01 to 0.02 and 0.03 increased the errors slightly, but the contour lines became smoother as overfitting was avoided. From the results of the sensitivity analysis it was decided to use a mesh of 0.05 for interpolation and of 0.02 for smoothing. Results appear as depicted in Figure 3.15.

Accuracy of the parameter model

In order to evaluate the accuracy of the parameter model two criteria are introduced. The deviation of the pressure coefficient derived from the data sets $C_{p,d}$ to the prediction $C_{p,f}$ is defined as

$$|\epsilon C_p| = |C_{p,d} - C_{p,f}| \tag{3.25}$$

and for further assessment of the approach the resultant horizontal force is calculated by integrating the pressure distribution over the gate height. The resultant force is calculated

depending on the fitting parameters directly fit to the measurement points (F_d), as well as depending on the fitting parameters according to the parameter model (F_f). The error of the resultant forces ϵF is defined as

$$\epsilon F = F_d - F_f \tag{3.26}$$

Thereby the deviation at each measurement point is defined, as well as the general accuracy due to the parameter model is indicated.

3.3.3 Pressure fluctuations

The fluctuating part of the hydrodynamic pressure is defined to be the recorded time series with a zero mean, achieved by subtracting the sample mean value as defined in Equation (2.15). The properties of the fluctuations can be described by their probability of occurrence (standard deviation and extreme values), spatial distribution and dynamic characteristics.

Probability of amplitudes

To investigate the required shape of the distribution describing the probability of the pressure amplitudes, histograms of the time series are obtained. Fitting a theoretical probability density distribution, the goodness of fit can be evaluated graphically on the basis of the histograms. Due to the large sample size the cumulated errors of theoretical distribution to sample data, frequently used as test statistics in goodness of fit tests such as the χ^2-test, are large and the hypothesis of being a sample from a specific distribution is rejected. Hence visual inspection must be relied upon. The visual goodness of fit of distribution functions becomes more distinct if the ordinate, giving the cumulative probability, is scaled in order to depict the normal distribution as a straight line. A comparison of the histograms and probability plots is given in Figure 3.16. The sample data in Figure 3.16a&c represents data
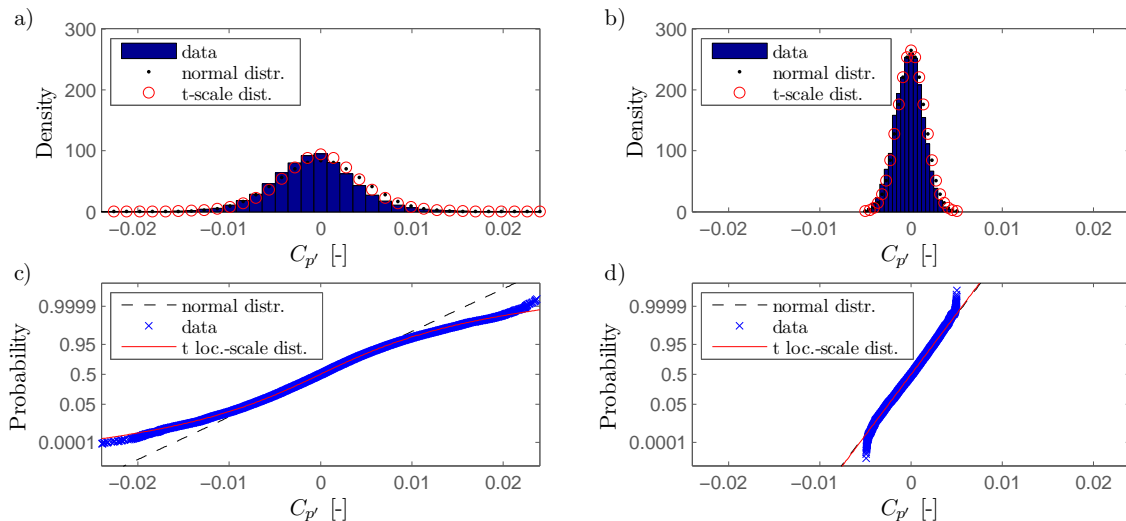
FIGURE 3.16: Probability density function and probability plot

exposed to intense fluctuations, which is indicated by a wide spread histogram, as opposed to the data in Figure 3.16b&d, which is a centred histogram typical for data with rather small pressure fluctuation. The probability density functions (Figure 3.16a&b) show that using a normal distribution is reasonable, which is supported by the central limit theorem, stating that large sample size of random variables will be normally distributed. Deriving the probability plots (Figure 3.16c&d), the weakness of the normal distribution, to model the tails of the data distribution is revealed, which is also discussed in Toso and Bowers (1988). The probability plot in Figure 3.16c shows the deviation of the data from the normal distribution. Extending the normal distribution by a shape parameter, leading to the t location-scale distribution, the accuracy at the tails of the distribution are altered. Figure 3.16c gives the t location-scale distribution as well, which fits the distribution of the data much better. The two distributions almost coincide for data with less pronounced fluctuations, *i.e.* shorter tails, as illustrated in Figure 3.16d. The t location-scale distribution approaches the normal distribution, with increasing scale parameter. To describe data by the t location-scale distribution the shape parameter has to be given additionally to the mean value and standard deviation, whereas the two latter are sufficient to define the normal distribution.

By comparison of Figure 3.16a&b it becomes clear that probability density functions of time series affected by intense fluctuations have longer tails. Using the t location-scale distribution the fit of the function at the tails is improved. Thereby it can be expected that the quantiles for the estimation of extreme values are modelled appropriately and more likely to be overestimated, which is considered to be on the safe side. For data distributions with less pronounced tails the normal distribution is considered to be sufficient. The disadvantage of the t location-scale distribution is the additional parameter required to define the distribution.

Characteristic parameters for the magnitude of pressure fluctuations

The root-mean-square of pressure fluctuations p'_{rms}, as a characteristic parameter for the mean deviation of the pressure from the average, is calculated from Equation (2.17) and equals the standard deviation of the sample record. The normalisation of the root-mean-square of pressure fluctuations p'_{rms} is defined in accordance with the normalisation of the pressure coefficient given in Equation (3.21).

$$C_{p',rms} = \frac{h'_{p,\text{rms}}}{H_0 - a} \tag{3.27}$$

Subsequently the normalised root-mean-square of pressure fluctuations can be used to describe the mean deviation from the normalised mean pressure defined by Equation (3.21).

Taking the probability of the pressure amplitudes as a basis, the extreme pulses can be defined as quantiles exceeding a level of occurrence, *i.e.* 0.01 and 0.99. The maximum pressure fluctuations at the upstream gate leaf can be characterised by quantiles of the sample data as well as of the fitted probability density distributions. The values are compared to the absolute maximum obtained during the measurement interval of 10 minutes. Just as the

normalised root-mean-square of pressure fluctuations, the normalised maxima and minima of the data are derived corresponding to Equation (3.21) by

$$C_p{}^+ = \frac{h_{p,\max} - \overline{h_p}}{H_0 - a} \quad \text{and} \quad C_p{}^- = \frac{h_{p,\min} - \overline{h_p}}{H_0 - a} \tag{3.28}$$

describing the deviation from the normalised mean pressure defined by Equation (3.21).

An envelope function containing the maximum pressure amplitudes is introduced subsequently. It is assumed that the pressure fluctuations can be described by Equation (3.23), if the fitting parameters are derived on the basis of the pressure extrema instead of the mean values. This envelope function for the minimum and maximum of the fluctuations can be determined in dependency of the fitting parameters derived for the mean values, whereas the stretching parameter k is adapted in order to describe the extent of the fluctuations. An amplification factor κ is introduced to derive k_{min} and k_{max} as

$$k_{min} = k(1 - \kappa) \quad \text{and} \quad k_{max} = k(1 + \kappa) \tag{3.29}$$

Thereby the reduction and the enlargement of the mean pressure is represented, and an envelope function containing the pressure amplitudes along the cross section is established.

Spatial correlation

The correlation coefficient R_p, as defined in Equation (2.27) can be derived using the time series obtained simultaneously. By the size of R_p the spatial correlation and hence the spatial extension of a flow phenomenon supposedly inducing pressure fluctuations is characterised.

Amplitude spectra

The amplitude spectra are derived on the basis of normalised parameters according to Section 2.5 and Equation (3.21). Hence the normalised time series of pressure fluctuations are

$$C_{p'}(t) = \frac{h'_p(t)}{H_0 - a} \tag{3.30}$$

and the normalised frequency or period are defined in Equation (2.46). For convenience of interpretation the spectra are given in dependence of the period of fluctuations $\tau = 1/f$.

In accordance with the definitions in Section 3.3.1 the undisturbed signal is denoted as $x(t) = C_{p'}(t)$ and $X(\tau)$ in the frequency domain. An envelope function over the spectra derived for each measurement series is derived to show the dominant periods of fluctuations depending on the parameters covered by the performed model tests.

Chapter 4

Results

Results are presented concerning the examination of the hydraulic model setup. The mean pressure distribution and magnitude of pressure fluctuations at the upstream face of a gate leaf are evaluated in context with vortex formation and its dynamics. The dependence of vortices and their appearance on parameters of the problem are illustrated.

4.1 Model verification

Before the final experimental program was determined several tests were performed to optimise the hydraulic model. The investigations concerned the performance of the pressure sensors, the measurement rate, the approach flow conditions and the boundary conditions due to the model construction.

4.1.1 Pressure sensors

Sensors of the series 46 X, as used for the pre-tests introduced in Section 3.1 were implemented to test the functionality of the setup, before installing the flush mounted sensors used for the final model as described in Section 3.2.1. Due to the different diameter and construction of the sensors, illustrated in Figure 3.12, the locations of the two sensor types were different. Sensors of the series 35 X finally installed, which have a smaller diameter could be mounted closer to the gate edge and the piers as well as with decreased vertical distance to each other. The locations of the sensors are illustrated in Figure 4.1 and the notation indicating the locations of sensors of series 46 X is introduced, whereas L, C and R refer to the right, central and left column and 1 and 2 refer to the bottom and top row respectively. The locations of sensors of series 35 X are given as comparison.

Data was collected with six sensors of series 46 X with variable pier lengths l_p between 65 and 215 mm and gate openings a of 41, 80 and 120 mm. The measurement rate was 50 Hz. Resultant pressure coefficients C_p are published in Kampel (2014). Trend lines following the data points describing the dependency of C_p on l_p/b are given in Figure 4.2. In the lower measurement row 1 the pressure coefficient is in the range of 0.75 and about 0.52
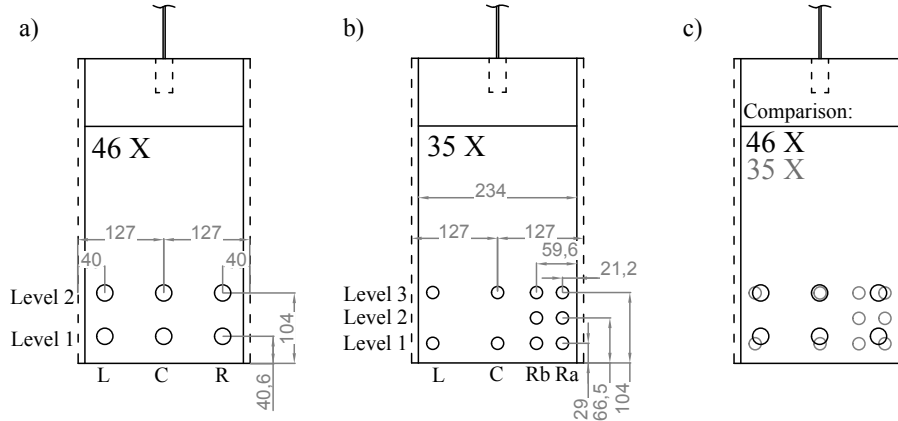
FIGURE 4.1: Locations of sensors of series 46 X in comparison to series 35 X at the measurement gate (measurements in mm)
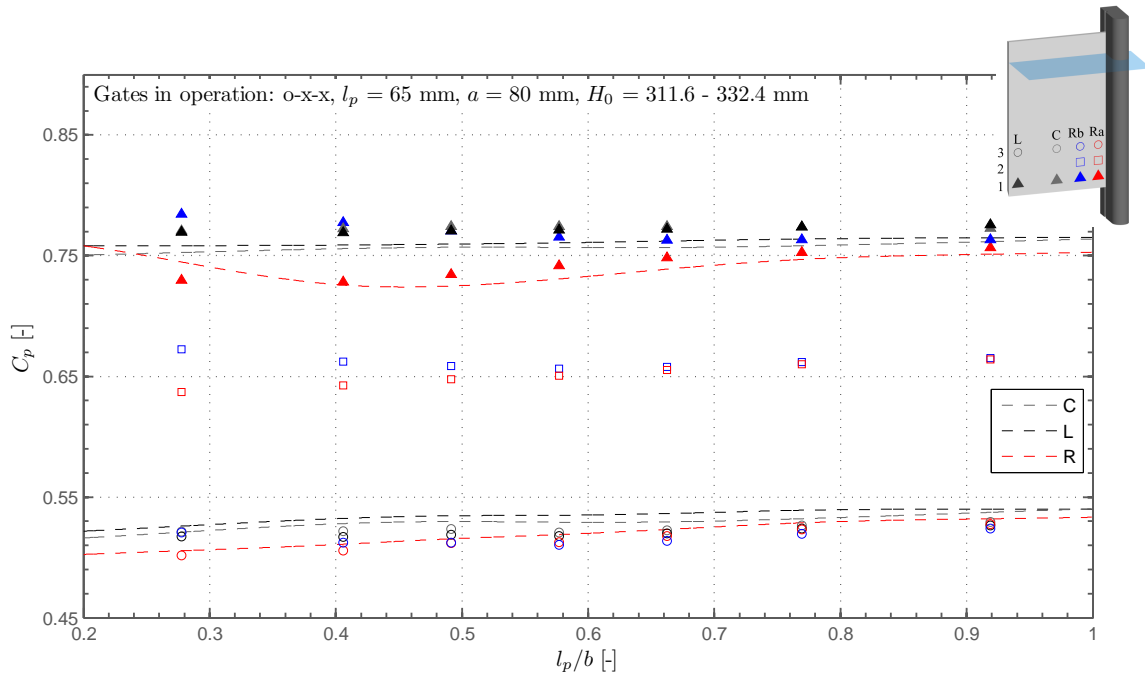
FIGURE 4.2: Pressure coefficient C_p as a function of relative pier head length l_p/b, comparison data points from series 35 X and trendlines from series 46 X

in the upper row 2. Pressure coefficients at the right side, where the vortex formed were consistently the lowest. The trend line of measurement row 1, located close to the gate lip shows a pressure minimum at about $l_p/b = 0.4$. The trend line increases after reaching a minimum at about $l_p/b = 0.4$.

For comparison data points obtained with sensors 35 X, with 50 Hz measurement rate are illustrated as well. Basically row 1 and 2 of sensors 46 X have a similar location as row 1 and 3 of sensors 35 X. Figure 4.1 as well as the graphical legend in the top right corner of Figure 4.2 indicate the arrangement of the sensors. Additional sensors 35 X at column Rb or at row 2 between the top and bottom row are not available from measurements with sensors of series 46 X. The measurements with sensors 35 X result in the same basic trend concerning the dependency of the mean hydrodynamic pressure C_p on the pier head length.

As the sensor location and approach energy head H_0 are not identical, it was not expected that the values of C_p derived in different experiments coincide precisely, but the results were found to be consistent.

The concentration of the sensors (series 35 X) near the location of the vortex provides additional information about the vortex induced pressure distribution at the gate. The data measured with the series 46 X was found to be unsuitable for dynamic analysis. This might be due to the comparable large area of the diaphragm, but also due to intense water surface fluctuations interfering with the presumable vortex induced fluctuations.

4.1.2   Measurement rate and sample time

The sensitivity of the parameters derived from the time series collected at the ten sensors was looked into concerning the measurement rate, sample size and duration of measurement. The data was evaluated by means of two parameters. These are the normalised root-mean-square of pressure fluctuations $C_{p',rms}$ and the normalised difference of the 95 %-quantile and 5 %-quantile of the hydrodynamic pressure denoted as $C_{p\pm}$ subsequently. The final measurement series were recorded with the maximum possible measurement rate of the pressure sensors of 400 Hz for a sample time of 600 s.

Various measurement rates, equal sample time

To analyse the influence of the measurement rate, data was collected with 50, 100 and 400 Hz. The flow conditions were aimed to be kept constant. The boundary conditions for each measurement are summarised in Table 4.1. The discharge Q and the resulting

f [Hz]	t [s]	Q [l/s]	a/H_0	$h'_{0,\mathrm{rmsn}}$
50	600	76.1	0.2653	0.0026
100	600	76.1	0.2650	0.0028
400	600	75.9	0.2649	0.0034

TABLE 4.1: Boundary conditions for the measurements testing the measurement rate

relative gate opening a/H_0 vary only marginally with sampling frequency. The derived normalised root-mean-square of water surface fluctuations $h'_{0,\mathrm{rmsn}}$ was found to increase with the measurement rate.

Tables 4.2, 4.3 and 4.4 give the calculated parameters for the sensors located at columns Ra, Rb, C and L respectively. The parameters indicating pressure fluctuations increase with increasing measurement rate. Next, it is examined whether or not the increase of the pressure fluctuations is connected to the sample size.

f [Hz]	$C_{p'_{\text{Ra1}}}$	$C_{p\pm_{\text{Ra1}}}$	$C_{p'_{\text{Ra2}}}$	$C_{p\pm_{\text{Ra2}}}$	$C_{p'\,_{\text{Ra3}}}$	$C_{p\pm_{\text{Ra3}}}$
50	0.0073	0.0238	0.0046	0.0148	0.004	0.013
100	0.0073	0.0238	0.0047	0.0151	0.004	0.013
400	0.0081	0.0274	0.0052	0.0169	0.0046	0.0148

TABLE 4.2: Evaluated parameters $C_{p',rms}$ and $C_{p\pm}$ at column Ra depending on the measurement rate

f [Hz]	$C_{p'\,_{\text{Rb1}}}$	$C_{p\pm_{\text{Rb1}}}$	$C_{p'\,_{\text{Rb2}}}$	$C_{p\pm_{\text{Rb2}}}$	$C_{p'\,_{\text{Rb3}}}$	$C_{p\pm_{\text{Rb3}}}$
50	0.0051	0.0166	0.004	0.0126	0.0036	0.0119
100	0.0053	0.0177	0.004	0.0133	0.0037	0.0123
400	0.0058	0.0191	0.0043	0.0144	0.0039	0.013

TABLE 4.3: Evaluated parameters $C_{p',rms}$ and $C_{p\pm}$ at column Rb depending on the measurement rate

f [Hz]	$C_{p'\,_{\text{C1}}}$	$C_{p\pm_{\text{C1}}}$	$C_{p'\,_{\text{C3}}}$	$C_{p\pm_{\text{C3}}}$	$C_{p'\,_{\text{L1}}}$	$C_{p\pm_{\text{L1}}}$	$C_{p'\,_{\text{L3}}}$	$C_{p\pm_{\text{L3}}}$
50	0.0038	0.0123	0.0032	0.0108	0.0039	0.013	0.0031	0.0101
100	0.0039	0.0126	0.0032	0.0108	0.0039	0.013	0.0031	0.0101
400	0.0044	0.0141	0.0037	0.0119	0.0042	0.0133	0.0036	0.0119

TABLE 4.4: Evaluated parameters $C_{p',rms}$ and $C_{p\pm}$ at column C and L depending on the measurement rate

Various measurement rates, equal sample size

For this analysis the measurement series used before were adapted in order to get records with the same sample size, *i.e.* samples with a constant number of values $n = 30\,000$. The measurement rate was set to 50, 100 and 400 Hz. Obviously the sample time of the records varies depending on the measurement rate as summarised in Table 4.5. Even though the

f [Hz]	t [s]	Q [l/s]	a/H_0	$h'_{0,\text{rmsn}}$
50	600	76.1	0.2653	0.0026
100	300	76.1	0.2651	0.0027
400	75	75.7	0.265	0.003

TABLE 4.5: Boundary conditions for the measurements testing the sample size

sample time decreases with increasing measurement rate, $h'_{0,\text{rmsn}}$ slightly increase with increasing measurement rate. Compared to the values of $h'_{0,\text{rmsn}}$ given in Table 4.1 are smaller, due to the reduced sample size.

Again, the calculated parameters are presented in Table 4.6, 4.7 and 4.8 depending on their location. Despite the very short measurement time, when measuring with 400 Hz, almost all values exceed the parameters of samples with lower measurement rate or are at least equal. The exceptions are the parameters $C_{p',rms}$ and $C_{p\pm}$ at location Rb3.

f [Hz]	$C_{p'\mathrm{Ra1}}$	$C_{p\pm\mathrm{Ra1}}$	$C_{p'\mathrm{Ra2}}$	$C_{p\pm\mathrm{Ra2}}$	$C_{p'\,\mathrm{Ra3}}$	$C_{p\pm\mathrm{Ra3}}$
50	0.0073	0.0238	0.0046	0.0148	0.004	0.013
100	0.0072	0.0238	0.0046	0.0151	0.004	0.013
400	0.0078	0.0256	0.0051	0.0162	0.0044	0.0137

TABLE 4.6: Evaluated parameters $C_{p',rms}$ and $C_{p\pm}$ at column Ra depending on the measurement rate

f [Hz]	$C_{p'\,\mathrm{Rb1}}$	$C_{p\pm\mathrm{Rb1}}$	$C_{p'\,\mathrm{Rb2}}$	$C_{p\pm\mathrm{Rb2}}$	$C_{p'\,\mathrm{Rb3}}$	$C_{p\pm\mathrm{Rb3}}$
50	0.0051	0.0166	0.004	0.0126	0.0036	0.0119
100	0.0051	0.0166	0.004	0.0133	0.0036	0.0119
400	0.0058	0.0184	0.004	0.0133	0.0035	0.0115

TABLE 4.7: Evaluated parameters $C_{p',rms}$ and $C_{p\pm}$ at column Rb depending on the measurement rate

f [Hz]	$C_{p'\,\mathrm{C1}}$	$C_{p\pm\mathrm{C1}}$	$C_{p'\,\mathrm{C3}}$	$C_{p\pm\mathrm{C3}}$	$C_{p'\,\mathrm{L1}}$	$C_{p\pm\mathrm{L1}}$	$C_{p'\,\mathrm{L3}}$	$C_{p\pm\mathrm{L3}}$
50	0.0038	0.0123	0.0032	0.0108	0.0039	0.013	0.0031	0.0101
100	0.0038	0.0126	0.0032	0.0108	0.0039	0.013	0.0031	0.0105
400	0.0045	0.0148	0.0037	0.0123	0.0039	0.0126	0.0035	0.0115

TABLE 4.8: Evaluated parameters $C_{p',rms}$ and $C_{p\pm}$ at column C and L depending on the measurement rate

Compared to the results derived for 400 Hz and sample time of 600 s as given in Table 4.2, 4.3 and 4.4 most of the parameters for the sample time of 75 s are smaller or the same. At locations apart from the vortex, where smaller fluctuations were expected the parameters are almost not influenced by the reduction of the sample size and time. Hence it can be concluded that increasing sample time increases the probability of recording pressure fluctuations of higher magnitude caused by the vortex dynamics. Increased values for $C_{p\pm}$ were derived at locations C1 and Rb3 as well.

Equal measurement rate, various sample time

To analyse the sufficiency of the measurement time of 600 s the data measured with 400 Hz was evaluated concerning different sampling time, which of course results in different sample size. Table 4.9 gives the boundary conditions. For the time series measured with 400 Hz the parameters used before where evaluated for sample time between 100 and 600 s and are given in Table 4.10, 4.11 and 4.12.

According to Toso and Bowers (1988) the absolute maxima of pressure fluctuations are approached asymptotically with increasing measurement time. As the values are rather constant as the measurement time exceeds 100 s, it can be assumed that the measurement time of 600 s is sufficient to characterise the pressure distributions. Hence a further increase of the measurement time was found not to be essential for the parameter study.

t [s]	Q [l/s]	a/H_0	$h'_{0,\mathrm{rmsn}}$
100	75.8	0.2651	0.003
200	75.8	0.2652	0.0033
300	75.8	0.2653	0.003
400	75.8	0.265	0.0036
500	75.9	0.265	0.0036
600	75.9	0.2649	0.0034

TABLE 4.9: Boundary conditions for the measurements with 400 Hz, evaluated for different sample lengths

t [s]	$C_{p'\mathrm{Ra1}}$	$C_{p\pm\mathrm{Ra1}}$	$C_{p'\mathrm{Ra2}}$	$C_{p\pm\mathrm{Ra2}}$	$C_{p'\,\mathrm{Ra3}}$	$C_{p\pm\mathrm{Ra3}}$
100	0.008	0.026	0.005	0.0162	0.0043	0.0137
200	0.008	0.0264	0.005	0.0162	0.0043	0.0144
300	0.0078	0.0256	0.0049	0.0159	0.0042	0.0137
400	0.0082	0.0274	0.0054	0.0177	0.0047	0.0151
500	0.0081	0.027	0.0052	0.0173	0.0046	0.0151
600	0.0081	0.0274	0.0052	0.0169	0.0046	0.0148

TABLE 4.10: Evaluation of data at column Ra for measurements with 400 Hz, evaluated for different sample lengths

t [s]	$C_{p'\,\mathrm{Rb1}}$	$C_{p\pm\mathrm{Rb1}}$	$C_{p'\,\mathrm{Rb2}}$	$C_{p\pm\mathrm{Rb2}}$	$C_{p'\,\mathrm{Rb3}}$	$C_{p\pm\mathrm{Rb3}}$
100	0.0055	0.0177	0.0039	0.0133	0.0035	0.0115
200	0.0062	0.0199	0.0045	0.0152	0.0041	0.0137
300	0.0059	0.0188	0.0043	0.0141	0.0038	0.0126
400	0.0057	0.0188	0.0044	0.0148	0.0041	0.0133
500	0.0057	0.0184	0.0043	0.0141	0.004	0.0133
600	0.0058	0.0191	0.0043	0.0144	0.0039	0.013

TABLE 4.11: Evaluation of data at column Rb for measurements with 400 Hz, evaluated for different sample lengths

t [s]	$C_{p'\,\mathrm{C1}}$	$C_{p\pm\mathrm{C1}}$	$C_{p'\,\mathrm{C3}}$	$C_{p\pm\mathrm{C3}}$	$C_{p'\,\mathrm{L1}}$	$C_{p\pm\mathrm{L1}}$	$C_{p'\,\mathrm{L3}}$	$C_{p\pm\mathrm{L3}}$
100	0.0041	0.0137	0.0034	0.0112	0.004	0.0126	0.0035	0.0115
200	0.0044	0.0144	0.0038	0.0123	0.004	0.013	0.0036	0.0119
300	0.0041	0.0137	0.0034	0.0039	0.013	0.0034	0.0116	
400	0.0044	0.0144	0.0038	0.013	0.004	0.013	0.0037	0.0123
500	0.0044	0.0141	0.0038	0.0126	0.0042	0.0137	0.0037	0.0123
600	0.0044	0.0141	0.0037	0.0119	0.0042	0.0133	0.0036	0.0119

TABLE 4.12: Evaluation of data at column C for measurements with 400 Hz, evaluated for different sample lengths

4.1.3   Approach flow

The 3D velocity distribution was observed between the wave barrier (riprap) and gate structure. For illustration of the measurement area see Figure 3.7. The approach flow conditions in the flume could be visualised through the data recorded with an acoustic doppler velocimeter. Cross sections for the measurement were 1800, 900, 570 and 245 mm upstream of the gate. The goal was to confirm symmetric flow conditions upstream of the flow field influenced by the weir structure and to visualise the asymmetric approach flow in front of the gate. The flow velocity fields presented in Figure 4.3 to 4.6 were measured upstream of the weir, where the left gate was opened for 120 mm and the discharge set to $\sim 37.0\,\text{l/s}$. The contour plots shows the flow velocity in direction of the x-axis. Further the velocity components along y- and z-axis are given as vectors.

At a section 1800 mm upstream of the gate the two dimensional vectors characterising the lateral and vertical flow velocity are almost zero, as depicted in Figure 4.3. There is no
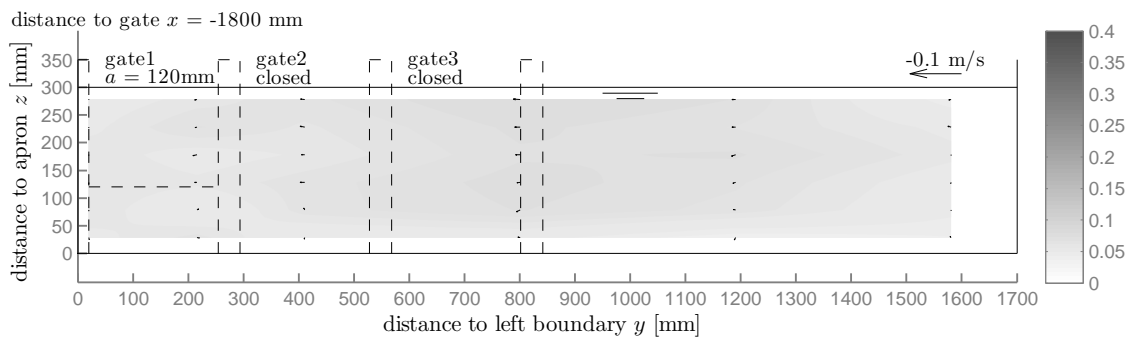
FIGURE 4.3: 3D velocity distribution 1800 mm upstream of the gate

significant current in the lateral or vertical direction recognisable and therefore the velocity distribution is considered to be homogeneous in the main flow direction. The velocity in the main flow direction at the center of the flume was measured to be 0.082 m/s. Approaching the walls or floor of the flume the velocity slightly decreases.

The following figures show the change in the flow field, as the gate is approached. The cross section pictured in Figure 4.4 shows that the velocity in the main flow direction declines from the left to the right. A lateral velocity component with a maximum in the middle of the flow field of approximately 0.03 m/s was observed. They are illustrated by the vectors at a distance of 800 mm from the left boundary. The vertical velocity components are almost zero.

A further increase of the velocity in the main flow direction causes a steeper decline of the velocity distribution as depicted in 4.5. An increase of the lateral velocity component at the left side of the flume was measured as well. Its maximum was determined to bee 0.05 m/s and occurred at a distance of 400 mm to the left boundary

Finally the profile closest to the gate (Figure 4.6) shows a distinct concentration of the longitudinal velocity to the gate opening. At almost the half-way point of the flume the longitudinal velocity component is zero. From the vectors depicting the lateral and vertical
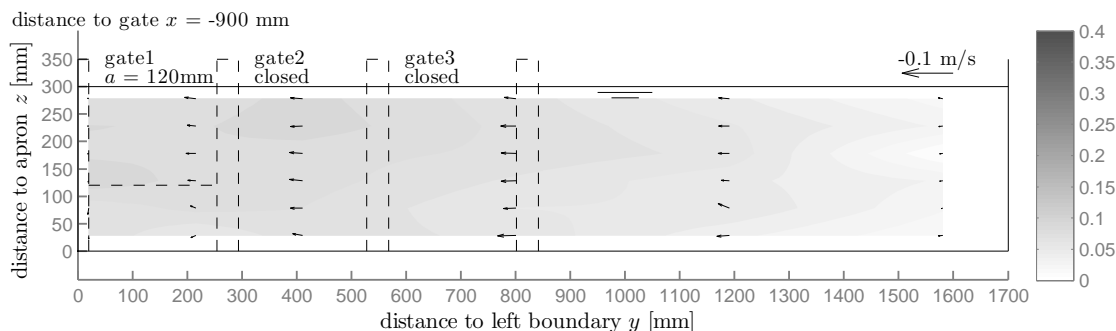
FIGURE 4.4: 3D velocity distribution 900 mm upstream of the gate
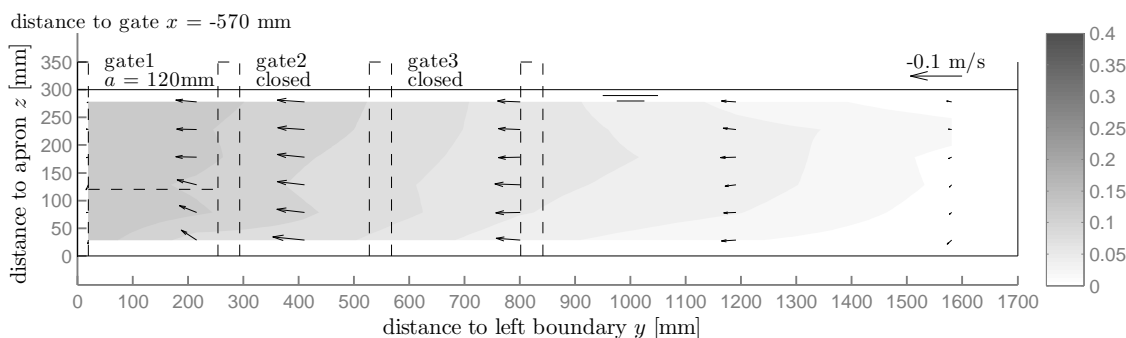
FIGURE 4.5: 3D velocity distribution 570 mm upstream of the gate

velocity, the strong current to the gate opening is noticeable. The lateral component exceeds 0.1 m/s.
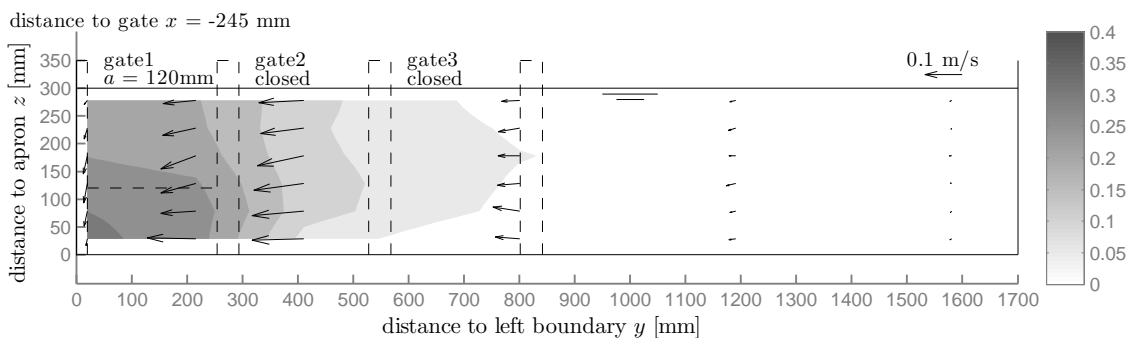
FIGURE 4.6: 3D velocity distribution 245 mm upstream of the gate

Further downstream the flow field adjusts according to the conditions determined by the geometric and hydraulic boundary conditions.

4.1.4   Discharge coefficient

As discussed in Section 2.1.2, data regarding the analysis of discharge coefficients for flow under gates is a frequently discussed topic. In the case of these investigations the analysis of the discharge coefficient was not a main goal. The discharge is rather a boundary condition

to set the water level for the respective measurement series. Anyway the opportunity to record the signal of the magnetic flow meter installed in the water supply system was taken to reproduce the model tests properly. Hence performing the analysis of the discharge coefficient is obligatory. The discharge coefficient C_d can be derived from Equation (2.7) in rearranged form. They are given in Figure 4.7 as a function of the relative gate opening a/H_0 for the experiments summarised in Table 3.2. In Figure 4.7a&b the slopes of measurement
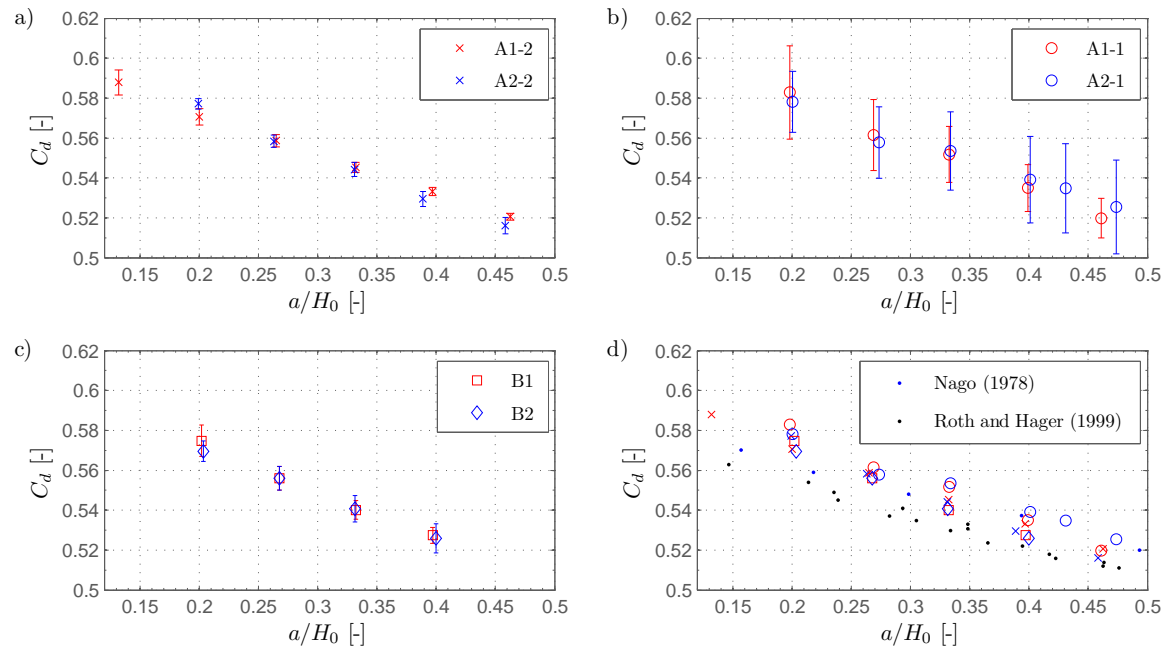
FIGURE 4.7: Discharge coefficient C_d depending on the relative gate opening a/H_0 including deviations due to presumed errors in discharge measurement (a-c) and comparison of all measurement series (d)

series with variable gate opening an variable energy head diverge slightly. In Figure 4.7a measurement series A2-2 with variable energy head is steeper, whereas measurement series A1-1 with variable gate opening is steeper in Figure 4.7b. Supposing that the discrepancy is caused by an inaccuracy of the discharge measurement or signal an error range caused by a systematic error of $0.8\,\mathrm{l/s}$ is plotted. The error defined as a fixed value of discharge rather than a proportion leads in a variable range concerning the error of the discharge coefficient. Considering the upper limit of the error bars in Figure 4.7a the divergence of the values is almost eliminated, just as the divergence can be eliminated by using the lower limits of the error bars in Figure 4.7b. These two graphs give the results from the larger and the smaller scale model respectively, *i.e.* two different supply systems were used, whereas the discharge is underestimated by the first and overestimated by the latter. The large error range in Figure 4.7b results from the comparatively low discharge in the small scale model. Figure 4.7c gives the discharge coefficient and error bars for measurements of the smaller scale model, with discharge under three gates, leading in increased discharge, decreased divergence of the two measurement series and smaller relative errors. Assuming the overestimation of the discharge, as concluded from Figure 4.7b to be constant, the lower limits of the error bars would be valid. The comparison of the figures clearly depict the sensitivity of the discharge coefficient to errors in discharge measurement, if the discharge is low. Figure 4.7d finally gives the discharge coefficients for all measurement series compared

to data derived from model tests with symmetric approach flow given in Nago (1978) and Roth and Hager (1999). The calculated values of C_d from the tests performed within this thesis were found to be larger. The discrepancy increased as relative gate opening decreased. Further analysis and discussion concerning the discharge coefficients derived in the larger scale model are topics in Köpf (2017).

To complete the discussion for all measurement series the discharge coefficients depending on the relative pier head length are plotted in Figure 4.8. They are given for discharge
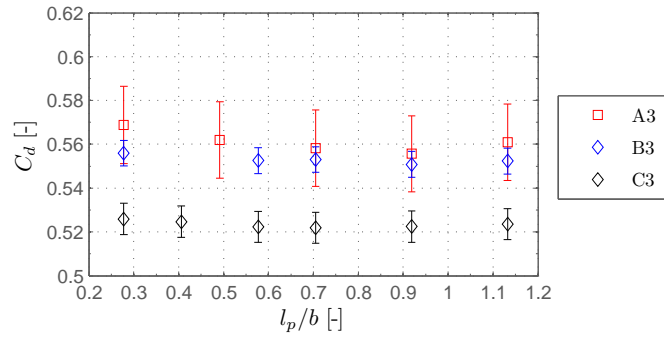
FIGURE 4.8: Discharge coefficient C_d depending on the pier head length lp including deviations due to errors in discharge measurement

under one (A3) and three gates (B3) respectively, whereas the latter are constantly lower. Additionally the discharge coefficient for decreased hydraulic head are given, as derived from measurement series C3. Lowest discharge coefficients were found at a relative pier head length in the range of 0.7 to 0.9. Further increase of the pier head length improves the approach flow conditions, by means of losses.

4.1.5 Model effects, constraints of the model setup

The separation point of the free shear layer forming the vortex upstream of the sluice gate is assumed to be dependent on the pier head length. For the investigation of this task the piers were equipped with vertical slots at two locations. If the gates were located at the further upstream slots the pier head length was 65 mm and was extended to 215 mm if they were located at the further downstream slots. The vertical board, blocking the right half of the flume was fixed in its location. Intermediate pier head lengths were simulated with extensions made of bent metal sheets, which could be plugged on to the existing piers. The left half pier was originally assumed not to have an influence on the pressure fluctuations induced by the vortex separating from the right pier.

During performance of the tests investigating the influence of the pier head length inconsistencies concerning the pressure fluctuations were observed. Hence the indistinct boundary conditions concerning the modification of the pier head length were investigated. These were assumed to be

- the half of the pier fixed to the left wall, which could not be extended by movable extensions made of sheet metal,

- the front slot, in case the gates are located at the back slot,

- the movable extensions plugged on to the piers,

- the longitudinal location of the fixed vertical board blocking the right half of the flume.

The model configurations tested, to analyse the influence of these model characteristics are sketched in Table 4.13.
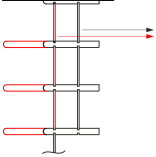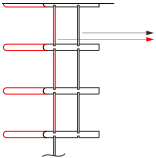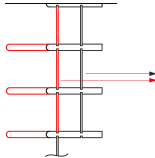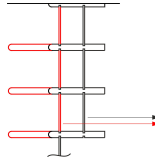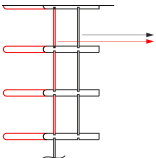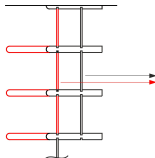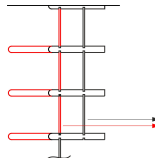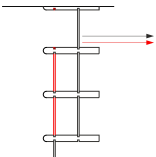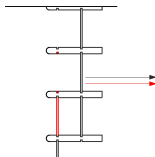
Measurement at	first gate (o-x-x)	second gate (o-o-x)	third gate (o-o-o)
Goal	Model configurations		
Influence of the left pier			
Influence of the front gate slot			
Influence of the pier extensions			
Influence of the right boundary conditions (gate location)			

TABLE 4.13: Limit values for modelling vortices

The mean pressure coefficient C_p was found to be independent of those boundary conditions. To the contrary the pressure fluctuation coefficient $C_{p',rms}$ is sensitive to some of them. The relevant boundary conditions and according deviations are discussed subsequently.

Influence of the left half pier

During the first tests performed at the left gate only the right pier head was extended, until it reached 210 mm. For further lengthening the gate was set to the back slot. Hence the left pier head was changed to 215 mm abruptly. Evaluating the parameters characterizing the pressure fluctuations an inconsistency was observed at the left side of the gate. An instantaneous increase of the fluctuations was identified, as the gates were moved to the back slot, presumably caused by the change of the left pier head length from 65 mm to 215 mm. To verify this effect the following test was performed. Time series were obtained, with the gate located at the back slot, *i.e.* the pier head lengths were 215 mm at the right

and the left side. The front slot was covered in order to avoid an influence. Moving the gate to the front slot, only the right pier was extended to 215 mm, whereas the left pier head had a length of 65 mm. Figure 4.9 gives a comparison of the pressure fluctuation coefficient $C_{p',rms}$ plotted against the relative relative location above gate lip Z, at the ten locations of pressure measurement. At the center of the gate (location C1 and C3) the $C_{p',rms}$ is similar,
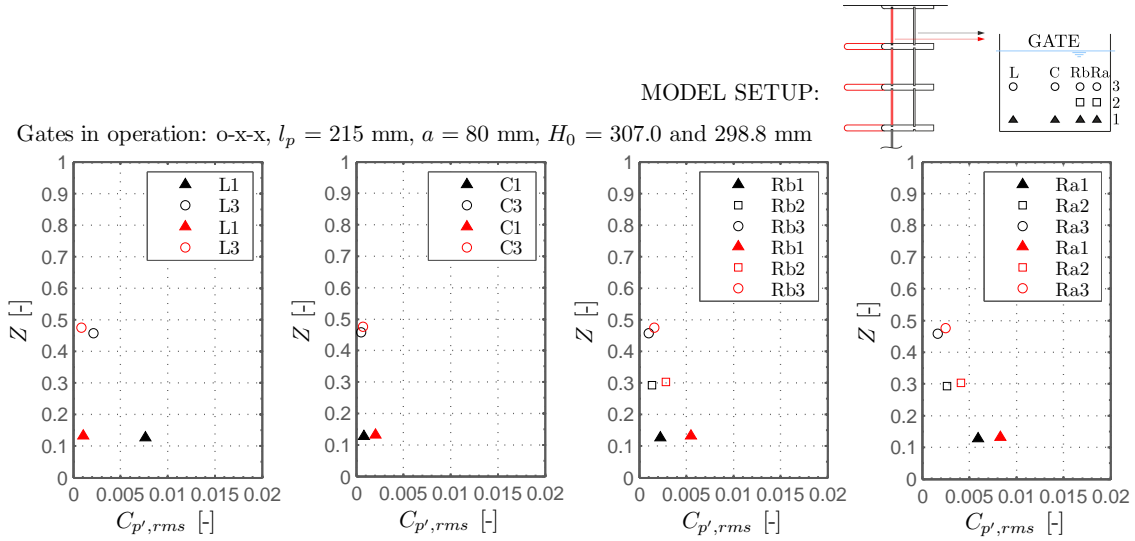
FIGURE 4.9: Pressure fluctuation coefficient $C_{p',rms}$ at 1st gate, located at the front slot with pier extention (l_p=215 mm) on the right side and located at the back slot (l_p=215 mm)

as the influence of the corner vortices is reduced. Indistinct deviations were determined at the top row. Values for $C_{p',rms}$ derived from measurements at a model setup with both pier heads having a length of 215 mm (black), show an almost symmetrical distribution of the pressure fluctuation. If only the right pier has a length of 215 mm a clear drop of the pressure fluctuations from the right to the left can be observed. The biggest differences, comparing the two setups, occur at the left side of the gate, due to the influence of the left pier head.

The comparison illustrates that the left half pier influences the pressure fluctuations. Hence for further analysis of pressure fluctuations at the first gate the left and right pier have to be extended equally in order to get consistent results. As expected measurements taken at the second or third gate were not influenced by the left half pier.

Influence of the front gate slot

Further the influence of the front slot on the pressure fluctuations induced by the vortex separating from the pier was investigated. This has been tested for the discharge under the first, the first and second, and all gates, as summarised in the second row of Table 4.13. For the first and second case the biggest deviation of $C_{p',rms}$ with slot compared to a smooth wall was determined at the right side of the gate. The influence of the slot reduced $C_{p',rms}$ at columns Ra and Rb. The biggest difference at the first gate (o-x-x) and at the second gate (o-o-x) appeared at location Ra1. The deviation decreases with increasing relative distance from the gate lip Z. No differences were observed at columns L1 and C1. In contrast to

the effect described before, the main difference at the third gate (o-o-o) appears on the left side. Due to the unexpected effect at the third gate it was assumed that another boundary condition could be the cause.

Influence of the pier extensions

The validity of applying pier extensions to change the pier head lengths was tested. Data was obtained with the gates located at the back slots with covered front slot and with the gates located at the front slot using the movable pier extensions. The same pier head length of 215 mm was maintained. The model configurations tested are given in the third row of Table 4.13. For the test performed on the first gate also the left half pier was extended. Therefore all indistinct boundary conditions identified before are presumably avoided. The maximum deviation of the pressure fluctuation coefficients $C_{p',rms}$ at the first gate were determined at location Ra1, whereas the use of the applicable extensions reduced the fluctuations slightly. At all other locations almost equal pressure fluctuation coefficients were determined. The pressure fluctuation coefficients $C_{p',rms}$ for operation of two and three gates showed almost equal values at all locations, hence it is assumed that the gate location, is not a boundary condition affecting the results. It is conceivable that the offset of the metal sheet of the pier extension or inaccuracies of the comparatively long extensions can affect the pressure fluctuations to a marginal amount. The general trend concerning the effect of the pier head length on $C_{p',rms}$ is assumed not to be falsified by the approach.

Influence of the right boundary conditions (gate location)

Although unlikely, as the measured velocities in the vicinity of the vertical board at the right side of the flume were close to zero, an influence of its location on the approach flow was tested. The right boundary condition of the third gate has been simulated at the first and second gate. This was realised by moving the operating gates to the back slot, whereas the others were located at the front slot, coinciding with the longitudinal coordinate of the vertical board blocking the right part of the flume. See Table 4.13 for the configurations tested. It could be demonstrated that there are no or insignificant deviations of the pressure fluctuation coefficient. Hence it was assumed, for the systematic investigations that the approach flow to the gates is independent of the position of the closed gates and thus independent of the location of vertical board to the right as well.

4.1.6 Scale effects

The minimum gate Reynolds number defined as $a\sqrt{2ga}/\nu = 5 \times 10^4$ is used to derive the limit gate openings in Roth and Hager (1999). As the limit gate openings derived therein were considered in the experimental program in Table 3.2, the requirements concerning the gate Reynolds number are met. The smallest gate Reynolds number in the experiments was 6.5×10^4.

Even though not dealing with free vortex formation in the case of underflow gates the limit values defined by Anwar et al. (1978) or Dagget and Keulegan (1974) summarised in Table 2.5 are considered in order to evaluate the possibility of scale effects concerning the vortex formation. The limit Reynolds numbers were found to be exceeded in all experiments, whereas Weber numbers W_h as defined by Anwar et al. (1978) fall below the limit value in measurement series A2-1 and B2. Therefore the values of $W_h = \rho Q^2 h_0/(A^2\sigma)$ are given in Table 4.14 for each experiment of measurement series A2-1. For comparison values of series A1-1 with the same relative gate openings are included in the table as well. The

A1-1	a/h_0	0.20	0.27	0.33	0.40	0.46
	W_h	8360	7490	7380	6940	6690
A2-1	a/h_0	0.20	0.27	0.33	0.40	0.43
	W_h	14270	7710	4730	3110	2650

TABLE 4.14: Weber numbers W_h for measurement series A1-1 and A2-1

Weber numbers for series A1-1 decrease only slightly with increasing a/H_0, whereas the values drop to a fifth of the maximum value in series A2-1. Thereby W_h drops below a half of the limit value $W_h = 10^4$ at relative gate openings exceeding 0.27 in measurement series A2-1. These values are remarkably below the values of measurement series A1-1. The exceedance of these limit values were overcome by the experiments performed in the larger scale model (A1-2 and A2-2). For these experiments Weber numbers with respect to the gate opening were found to exceed the upper limit value of 3.4×10^4 for about 40 %. As the general conclusions from the small and the large scale model investigated in this study are the same, even though the limit values of W_h are not maintained, the surface tension is supposed not to be causing scale effects. Further it is concluded from the consistent results obtained from the small and large scale model that the critical values of Weber numbers for a vortex caused by separation due to asymmetric flow conditions are lower as compared to free vortices investigated in Anwar et al. (1978) and Dagget and Keulegan (1974).

4.1.7   Wave damping and absorption

Concerning the approach flow condition the main concern was the elimination of the wave generation and propagation in the flume. The final model setup presented in Figure 3.7 was developed during tests, analysing the efficiency of various installations, which reduced the wave generation at the inlet or the wave propagation all the way to the gate structure and the location of the water level measurement. Table 4.15 gives a summary of the tested measures.

During phase 1, only perforated bricks were arranged at the inlet, in order to homogenise the flow. The water surface fluctuations, measured with the laser sensor upstream of the gate, as indicated in Figure 3.7 were of similar magnitude as the fluctuations measured at the gate. The root-mean-square of the water surface fluctuations $h'_{0,\mathrm{rms}}$ had a size of about 2.5 mm during the tests for different pier head lengths l_p (Figure 4.10a).

Subsequently a floating board, spanning the whole flume was fixed in elevation, depending on the water level to suppress water surface fluctuations generated due to the supply

Phase	Added measure	Measurement rate [Hz]
1	two rows of perforated bricks, just downstream of the inlet	50
2	floating board	50
3	floating board	400
4	perforated bricks upstream of the laser sensor	400
5	vertically floating baffle (inlet), riprap	400

TABLE 4.15: Development of measures for wave absorption
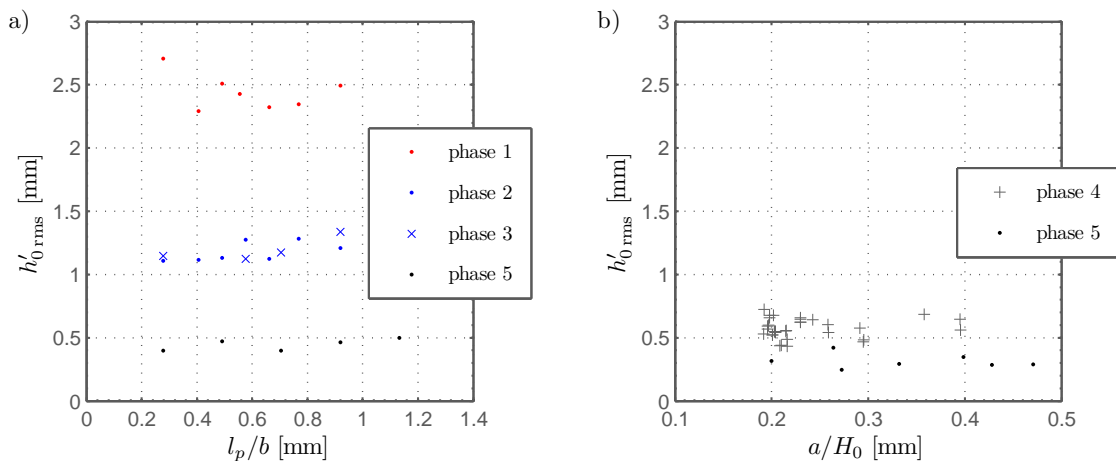
FIGURE 4.10: Effect of measures for wave absorption on the root-mean-square of water surface fluctuations $h'_{0,\mathrm{rms}}$

from the pipe. Different locations in the flume were tested, without finding any distinct differences. Situating it after the inlet seemed to reduce water surface fluctuations due to the turbulent inflow. Long-wave water surface fluctuations could not be damped efficiently. Quantitatively the root-mean-square of the water surface fluctuations $h'_{0,\mathrm{rms}}$ could be reduced by half. Figure 4.10a, phase 2 and 3 gives the measured water surface fluctuations for this setup. The difference of the two phases is the measurement rate, which was 50 and 400 Hz respectively. An influence of the measurement rate is not recognisable. Another row of bricks just upstream of the laser sensor was installed, which reduced $h'_{0,\mathrm{rms}}$ to 0.5 mm. It was tested, if an overflow section would further prohibit water surface fluctuations. As the discharge had to be increased, to keep the same water level the opposite was the case. Subsequently a vertically floating baffle was installed at the inlet. The data of phase 4, is presented in Figure 4.10b, as this test series was performed with varying water level and the measurements presented in Figure 4.10a were measured for varying pier head lengths. A dependency of the magnitude of fluctuations to the water level could not be identified. Installing a riprap to further omit propagation of long-wave water surface fluctuations reduced the fluctuations slightly more. Both, Figure 4.10a&b show data gained from the tests in phase 5. All measurements of the final experimental program were performed with the model setup used during phase 5. An overview of the locations of all installed measures is given in Figure 3.7.

The cause of the spectral peaks of the water surface fluctuations was identified by analysing the wave system in the flumes of the small and large hydraulic model. Lengths of longitudinal and lateral waves were determined depending on the length and width of the flume. Using Equation (3.1) and Equation (3.2) from linear wave theory, circular frequencies and hence periods of water surface fluctuations can be determined, depending on the geometry of the flume. In Equation (3.2) m determines the longitudinal mode of fluctuation and n the lateral one. A combination of both modes results in double series, combining fluctuations determined by longitudinal and lateral boundary conditions. As lower modes are more likely to be excited m and n are varied between 0 and 3. The flow velocity along the flume is neglected as an approximation. The upstream boundary is assumed to be rigid in order to determine the wavelength of longitudinal oscillations. In the small scale model several reservoirs, separated by permeable barriers, are likely to influence the periods of the waves. Therefore the length L in Equation (3.2) was changed according to the distances of the barriers from the gate in order to find significant lengths. The sides of the flume are rigid vertical walls, which determine the wavelengths of any lateral oscillations.

From the time series of water surface elevation, the actual periods of the water surface fluctuations are determined by transformation to the frequency domain. Throughout all experiments similar peaks were identified in the spectra. Hence the envelope functions over each measurement series sufficiently represents the characteristics of water surface fluctuations. Figure 4.11a&b give the spectra derived in the small and large scale model respectively. Substituting the water depth of the different experiments as d in Equation (3.1)
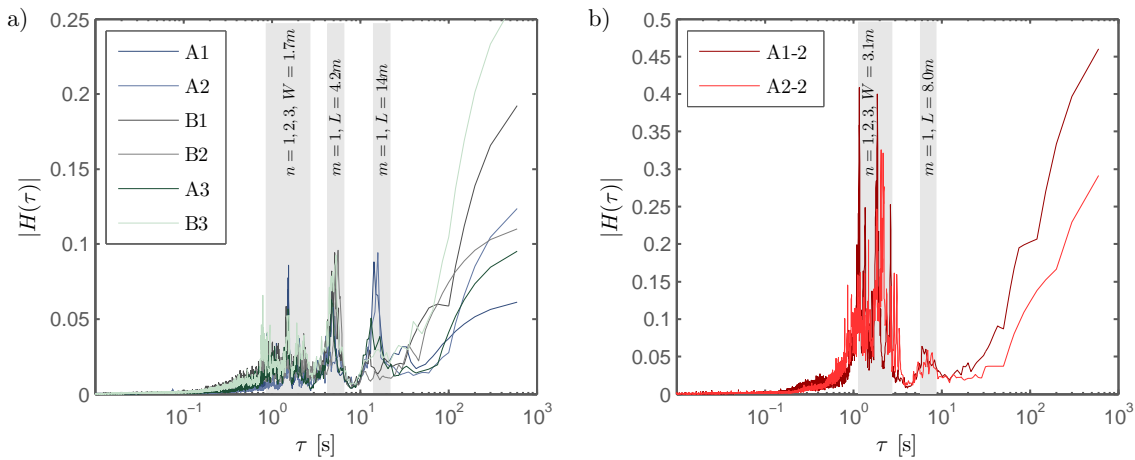
FIGURE 4.11: Spectra of water surface fluctuations

a range for the presumed peaks was determined. The ranges covering the peaks in the experiments are indicated by the grey areas in Figure 4.11. Coincidence of the grey areas and the peaks of the spectra, reveal the cause of the peak.

In the small scale model the waves peaking at short periods were determined to be caused by the wave modes 1 to 3 in lateral direction ($n = 1, 2, 3$). Two further peaks were found to be in the range of the first wave mode in longitudinal direction, whereas the peak with the shorter period was found by using the length of the first reservoir and the waves with long periods fall in the range determined by using the length of the flume. The geometric boundary conditions of the large scale model were simpler. The largest peaks in the spectra

fall in the range of cross-channel waves of mode 1 to 3 and a small peak with larger period is presumed to be the first mode of fluctuations in longitudinal direction. The information about the wave modes (n, m) and length L or width W used to calculate the ranges of periods are summarised in Figure 4.11.

4.1.8   Wave filtering

The influence of the model constraints, such as the slot or the left half pier on the fluctuating part of the data discussed in Section 4.1.5 was taken care of during final data acquisition. The extent of water surface fluctuations has been reduced to a minimum by improving the wave absorption in the flume (see Section 4.1.7). Subsequently the procedure of taking the water surface fluctuations into account is illustrated for one sample record, where all gates were opened to 100 mm, the pier head length l_p was 65 mm, and the discharge was Q is 91.9 l/s. The resulting relative gate opening is $a/H_0 = 0.33$.

In Figure 4.12 the sample records of the pressure measurements are depicted. The figure is split into three graphs, giving the data measured at the lowest (Level 1), the middle (Level 2) and the top row (Level 3) at the gate. The graphs are arranged accordingly. The lateral location of the pressure measurement is indicated by colour. As reference the hydraulic head at each elevation, derived from the measurement of the water level is plotted as well. Different periods of the water surface fluctuations can be realised from the water level measurement and pressure sample records as well. If attention is drawn to the time span of 360 to 420 seconds in Figure 4.12 the mutual progress of the water level and pressure sample records becomes clear. Subsequently the application of spectral subtraction as introduced in Section 3.3.1 is illustrated for this sample record.
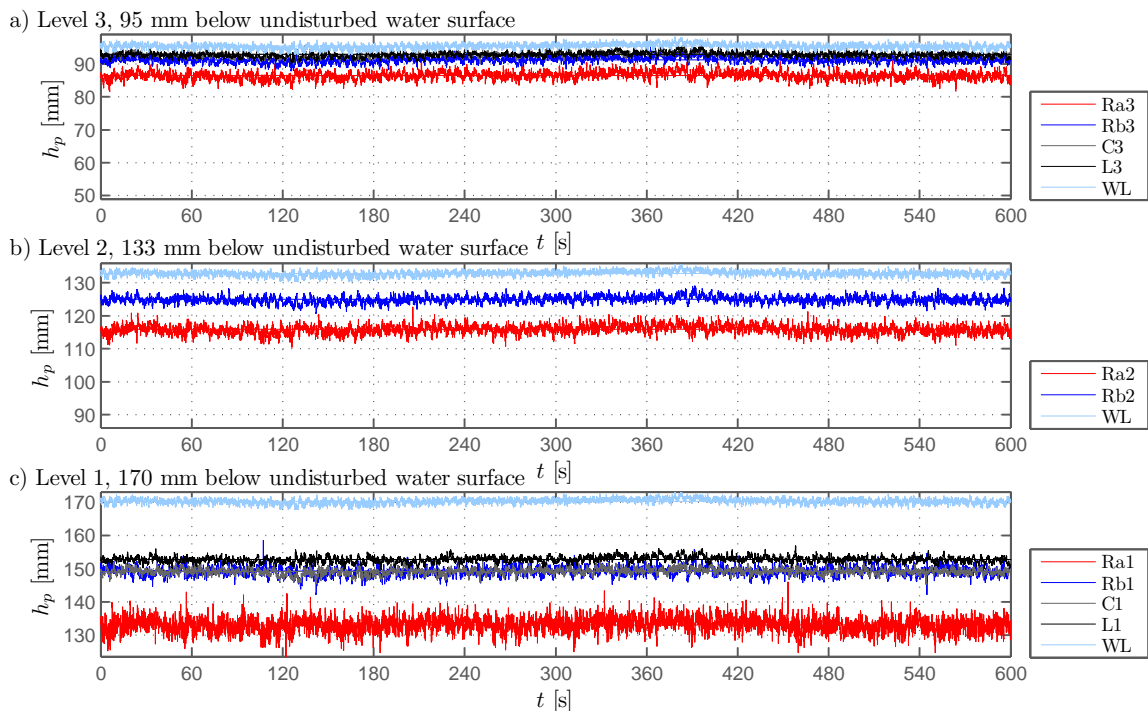
FIGURE 4.12: Unfiltered pressure records and record of water level

As explained in Section 3.3.1, the influence of the water surface fluctuations decays with depth, *i.e.* the influence of the water surface fluctuations on the pressure decreases from the measurement points at Level 3 to Level 1. The rate of decay with depth further depends on the period of the waves. Hence the filter given in Equation (3.7) is evaluated for the three levels of pressure measurements and applied to the spectrum of water surface fluctuations. Thereby the spectrum of the pressure induced by water surface fluctuations is derived. Figure 4.13 gives the spectrum of the measured water surface fluctuations and the spectra after application of the filter. It shows that for the specific boundary conditions of this
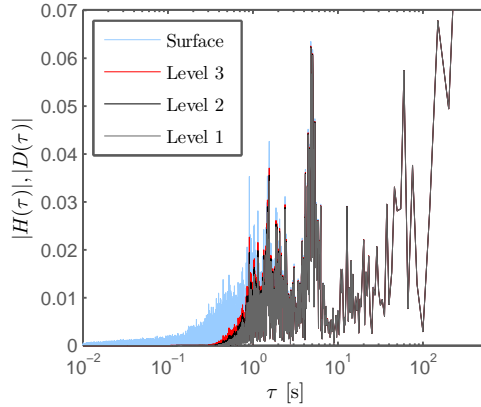
FIGURE 4.13: Spectra of water surface fluctuations and induced pressure (noise estimate)

experiment that waves with periods above 1 second influence the pressure at the three levels of pressure measurement, whereas the pressure fluctuations with shorter periods decay until the depth of the pressure sensors is reached.

Application of spectral subtraction

In Figure 4.14 the spectra of the unfiltered pressure sample records $Y_k = |Y(\tau)|$ are compared to the noise spectra $|D(\tau)|$ represented by the pressure induced due to water surface fluctuations. The peaks of the noise spectrum can also be identified in the spectra of the pressure fluctuations. The coinciding peaks demonstrate the increase of the pressure measurement due to water surface fluctuations. Especially with decreasing pressure fluctuations, as in the top row on the left and at the center of the gate, the coincidence with the spectra of the water surface fluctuations are obvious. The correlation of the unfiltered spectra and the noise spectra is evident, when comparing the first and second spectrum in the top row of Figure 4.14 for location L3 and at C3 respectively.

The results after spectral subtraction according to Equation (3.11) are given in the frequency domain in Figure 4.15. To highlight the effect of spectral subtraction the spectra of the original signal are given in the background in green. The peaks described before are clearly diminished, which again becomes very clear by comparing the spectra of the measurements at locations L3 and C3 in Figure 4.15.

The restored signal in the time domain is derived according to Equation (3.12) and plotted in Figure 4.16. The original water level measurement over time is plotted for direct comparison.
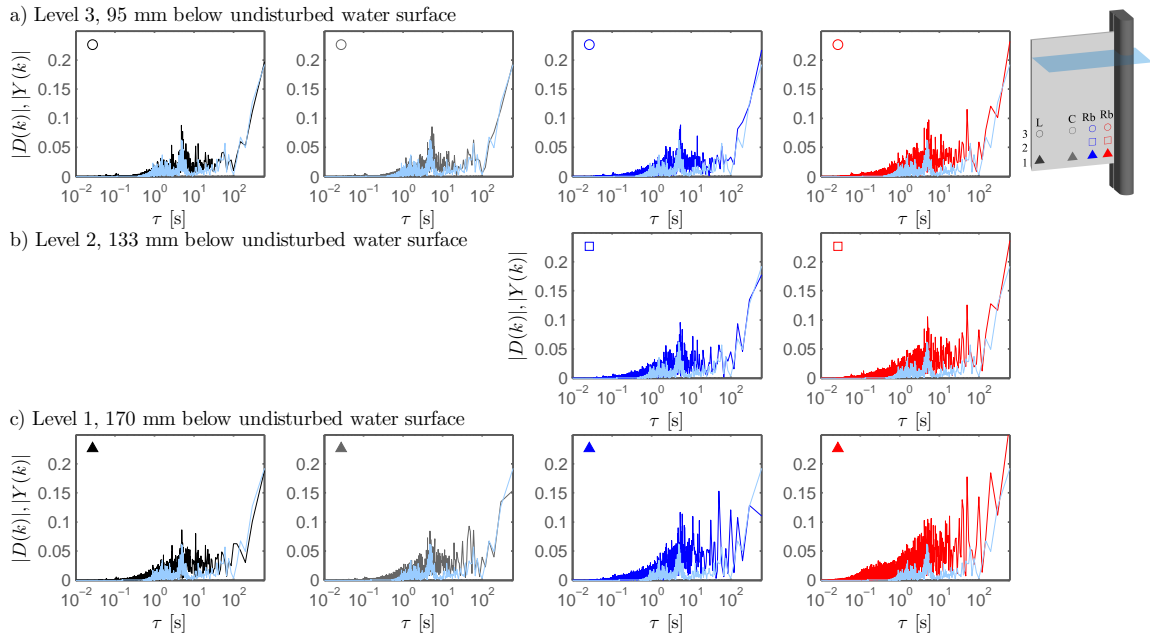
FIGURE 4.14: Amplitude spectra of the pressure records and of noise (light blue)
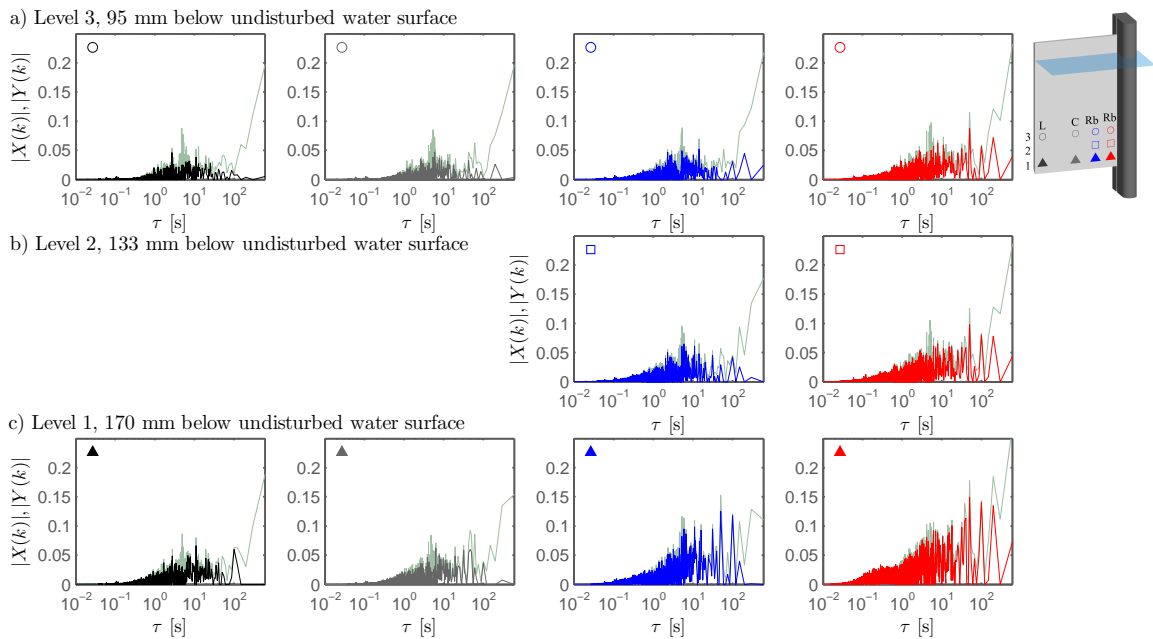
FIGURE 4.15: Amplitude spectra of the pressure records before (light green) and after spectral subtraction

a) Level 3, 95 mm below undisturbed water surface

b) Level 2, 133 mm below undisturbed water surface

c) Level 1, 170 mm below undisturbed water surface
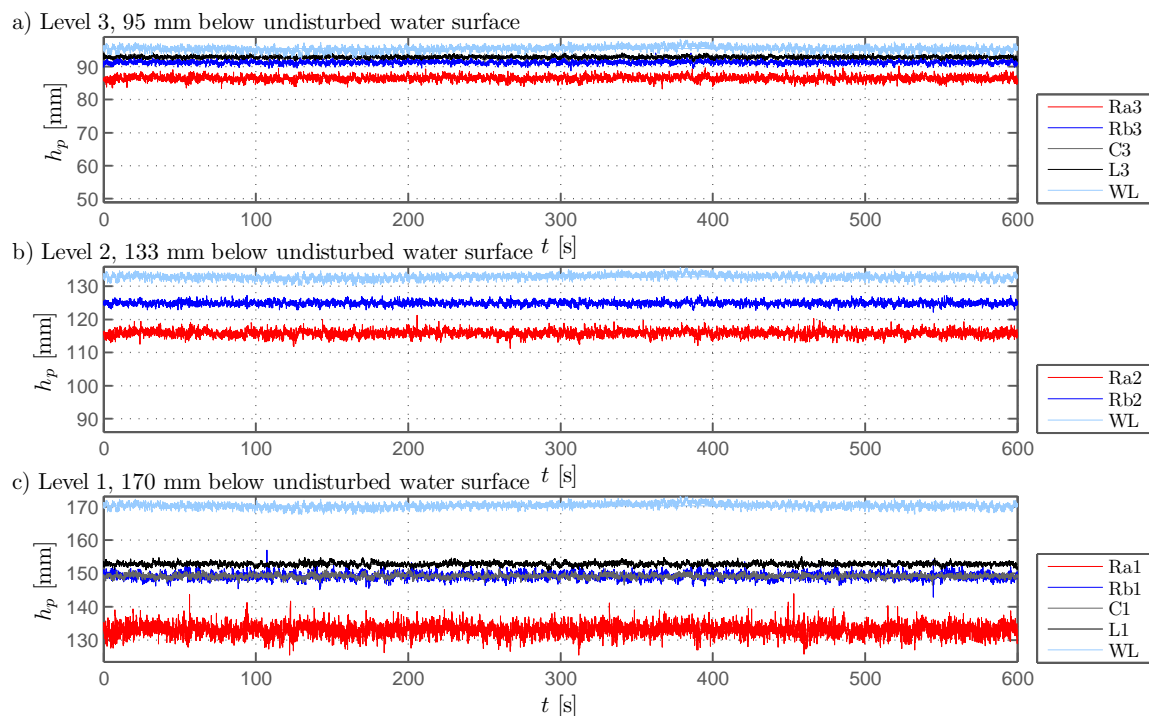
FIGURE 4.16: Pressure signals after spectral subtraction in comparison to water surface fluctuations

As plotted in the same scale as Figure 4.12 it can be recognised that the range of fluctuation of the pressure sample records is decreased by the application of spectral subtraction.

The success of the spectral subtraction is revealed, as the pressure sample records show improved stability of the mean value. This is approved by applying a statistical test for stationarity, as introduced in Section 3.3.1. Accordingly the p-values, giving the probability of obtaining a sample with the calculated number of runs are calculated and summed up in the figures in Appendix A.1. Therein the p-values of time series, with rejected null hypothesis at a level of significance of 5 % are plotted before and after filtering by spectral subtraction. Comparing the number of sample records, with p-values falling below the limit the improvement of stationarity can be rated.

The effect of spectral subtraction could be shown to be an efficient and reasonable approach to standardise the pressure fluctuations of the sample records obtained at different boundary conditions. The analysis shows that independence of the unstable water surface level, as an ambiguous boundary condition, can be achieved by spectral subtraction. As a further indicator the root-mean-square values are investigated next.

Root-mean-square values of filtered signal

The root mean square values of pressure fluctuations were used as indicator for the sufficiency of spectral subtraction. The connection of the unstable water level and pressure oscillation is revealed not only in the time series, as described before, but also by comparing the parameters p'_{rms} and $h'_{0,\mathrm{rms}}$, which are the root-mean-square of pressure fluctuations and

of the water surface fluctuations respectively. The increase of p'_{rms} with the relative gate opening a/H_0 in Figure 4.17 is supposedly related to increasing fluctuations of the water level. Testing the efficiency of spectral subtraction on the overall data analysis the root-mean-square values p'_{rms} were calculated for a data set before and after spectral subtraction and plotted in Figure 4.17. The data set used consists of four experiments with gate openings a from 60 to 120 mm and corresponding discharge Q to hold the water level at about 300 mm. The root-mean-square values of the water level sample record $h'_{0,\mathrm{rms}}$ are given as well. An upward trend of $h'_{0,\mathrm{rms}}$ with increasing relative gate opening a/H_0, caused by increasing required discharge Q is noticeable. This trend is followed by the root-mean-square values p'_{rms} of the pressure record samples, as it is especially clear from the graphs in the top row of Figure 4.17, concerning the measurements at the left side (L) and the center (C) of the gate. The data points at a relative gate opening of $a/H_0 \approx 0.4$ exceed $h'_{0,\mathrm{rms}}$ to a larger
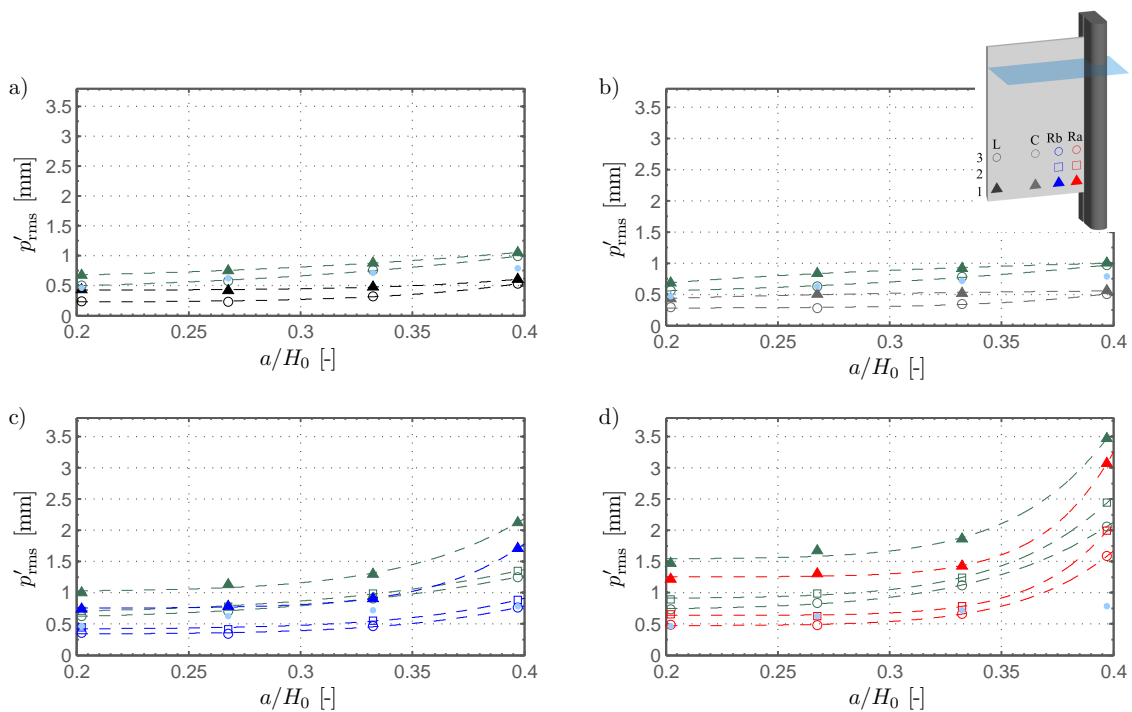
FIGURE 4.17: Comparison of root-mean-square of pressure fluctuations p'_{rms} before (light green colour) and after filtering

extent, *i.e* another source induces pressure fluctuations. This effect is more distinct in the graphs in the bottom row of the figure, giving the results at the right side of the gate, where the vortex forms. The values of p'_{rms} for the data series filtered through spectral subtraction are plotted in the same graphs. Due to the elimination of the effect of the water surface fluctuations through spectral subtraction, the values of p'_{rms} and the inclination of the data set between a/H_0 of ≈ 0.2 and ≈ 0.34 are decreased. As desired, the distinct increase of the pressure fluctuations at low submergence is still revealed by the filtered data.

Spectral subtraction is applied to all obtained time series before the analysis concerning the pressure fluctuations are performed.

4.2   Mean hydrodynamic pressure

The experimental results concerning the mean values were found to be ergodic, *i.e.* the same mean values were obtained repeating a test with the same geometric parameters and discharge. Neither instabilities of the water level nor the model constraints discussed in Section 4.1.5 show an effect on the time averaged mean value of the measured piezometric head $\overline{h}_p$ and hence the mean hydrodynamic pressure $\overline{p}$ and its normalised form, the pressure coefficient C_p.

Applying the method described in Section 3.3.2 leads to data sets defining the fitting parameters k, l and m as introduced in Equation (3.23) as

$$C_p(Z) = k(m - Z)Z^l = \Phi\left(\frac{a}{H_0}, \frac{v_0}{v_a}, \frac{l_p}{b}, Y\right)$$

They are analysed as a function of the dimensionless lateral location at the gate and the respective geometric parameter (a/H_0 or l_p/b) or relative approach flow velocity (v_0/v_a). The pressure distribution is defined on basis of the relative gate opening and effects due to increased pier head length and approach flow velocity are analysed on basis of correction factors. The validity of the parameter model is evaluated by the error of the local pressure coefficient $|\epsilon C_p|$ and the errors of resulting force $|\epsilon F|$ defined in Equation (3.25) and (3.26) respectively.

4.2.1   Pressure distribution

The pressure distribution along a gate is defined on the basis of the fitting parameters k, l and m as a function of the lateral location at the gate Y and the relative gate opening a/H_0. The relative gate opening is a function of the gate opening a and the energy head H_0. The influence of these absolute values on the pressure distribution is analysed. Therefore the function, describing the vertical pressure distribution was fit to the data points obtained in the measurement series A1-2 and A2-2, performed in the larger scale model. Data obtained in the small scale model, *i.e* series A1-1 and A2-1 are aimed to provide conclusions on scale effects. The measurement series are defined in Table 3.2.

Dependency on the gate opening

The sample records obtained from the larger scale model in measurement series A1-2 are used to derive the fitting parameters k, l and m. Therefore the function, describing the vertical pressure distribution was fit to the data points, delineating the pressure coefficients derived from the sample records. The results are depicted in Figure 4.18. The pressure maxima of the curves and their locations agree well with Montes (1997), Kim (2007) and Roth and Hager (1999) and are in the range of $C_p = 0.65$ to 0.88 and $Z = 0.04$ to 0.11.

For determination of the mean pressure distribution at an arbitrary gate contour lines illustrating the dependency of the fitting parameters on the lateral location Y and the
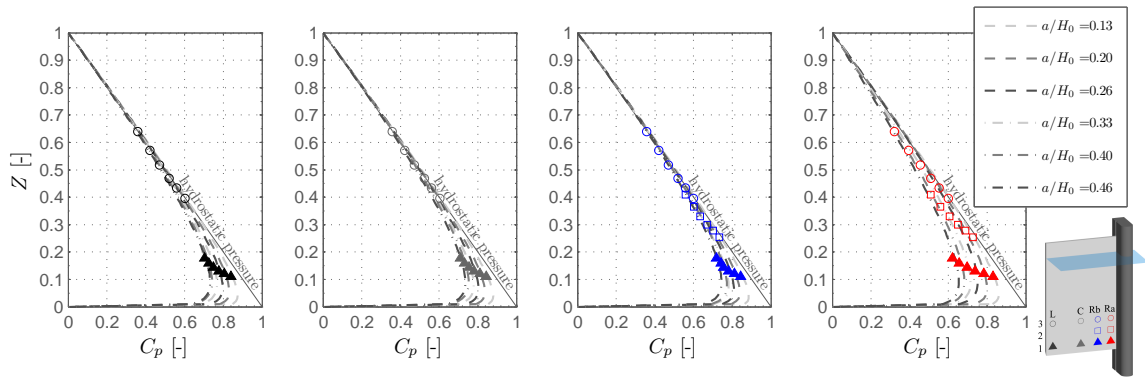
FIGURE 4.18: Discrete data and fitted functions describing the pressure distribution of experiments in series A1-2
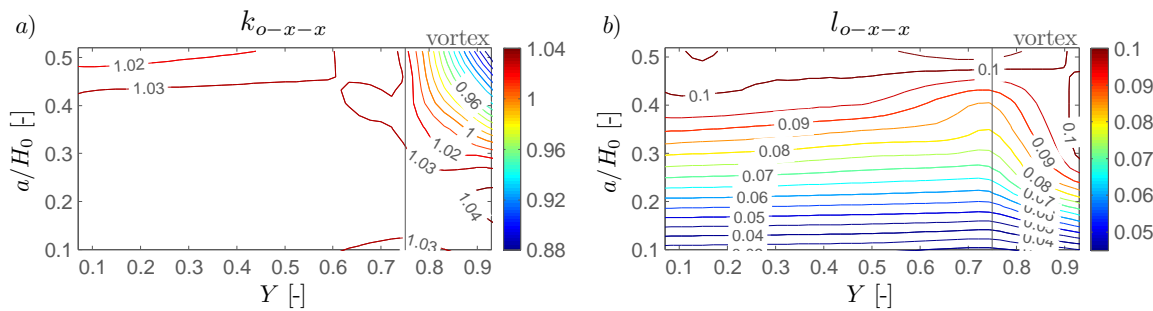
FIGURE 4.19: Fitting parameters k and l $(m = 1)$ derived on the basis of series A1-2

relative gate opening a/H_0 are derived and illustrated in Figure 4.19. Fitting parameter m could be spared, as the fitted functions are not deviating from 0 at $Z = 1$, which can be seen clearly from Figure 4.18, *i.e.* there are no significant energy losses. The developments of parameters k and l in Figure 4.19 imply a decrease of the pressure and an upward shift of the location of the pressure maximum with increasing relative gate opening respectively.

This parameter model derived from the larger scale model is evaluated in two steps. First the validity of the contour lines in Figure 3.15 is investigated by calculating the errors due to interpolation and fitting. Using the fitting parameters according to the data set specified by the contour lines the pressure distributions for the experiments in measurement series A1-2 are redetermined. The errors $|\epsilon C_p|$ defined in Equation (3.25) are determined and illustrated in Figure 4.20a. Thereby the errors of the predicted data points to the pressure coefficients obtained from the measured data are indicated. Further the normalised resultant force is obtained by integrating the pressure distribution along the submerged part of the gate. The errors of the force derived from the function fitted directly and by applying the parameters according to the contour lines are calculated according to Equation (3.25) and given as ϵF in Figure 4.20c. The errors were found to increase up to 0.015 at the right corner of the gate, as the relative gate opening exceeds 0.3. As the errors resulting from interpolation, fitting and smoothing are very small, the methodology for determination of the contour lines could be confirmed.

Subsequently it is tested whether the pressure distribution for the smaller scale model can
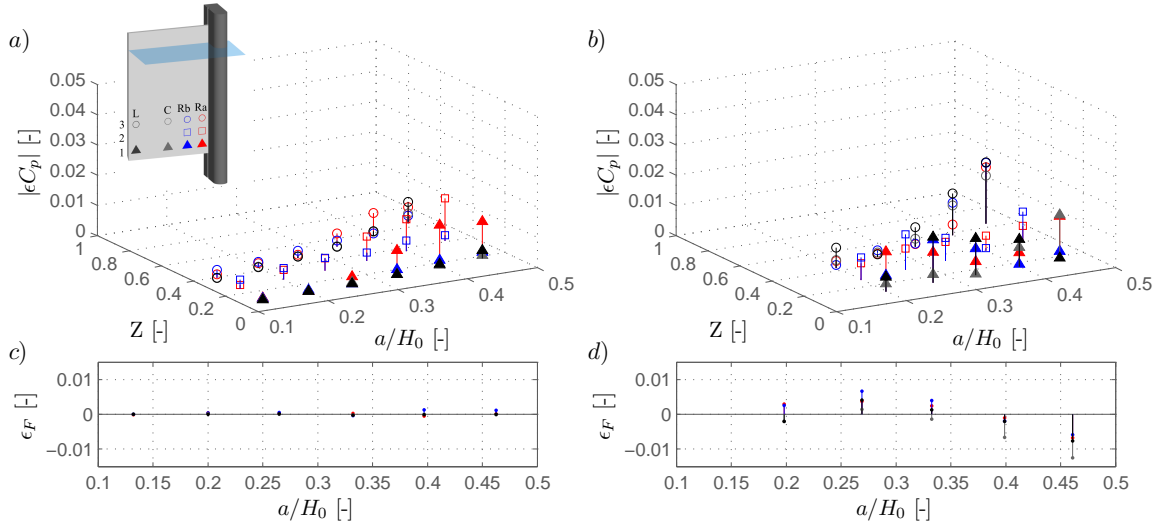
FIGURE 4.20: Evaluation of the parameter model given in Figure 4.19: deviation of pressure coefficient ϵC_p for a) series A1-2, b) series A1-1 and of resultant force ϵF for c) series A1-2, d) series A1-1

be predicted. Hence the pressure distribution is obtained for the experiments in series A1-1, by using the fitting parameters given in Figure 3.15. The errors of the prediction are given as absolute values $|\epsilon C_p|$ in Figure 4.20b. The errors concerning the normalised resultant force ϵF are given in Figure 4.20d. As they are not given as absolute values, the over- or underestimation of the resultant force is indicated. The pressure distributions in the small scale model are above the distributions from the larger model for $a/H0 < 0.35$ and below for $a/H0 > 0.35$. The accordance of the results from the two scale models is demonstrated, as the pressure distribution for the smaller model can be predicted by using the parameters derived from the larger scale model. Increased but still rather small errors occur when the parameter model is applied to the smaller scale model. The results allow to conclude that scale effects are negligible concerning the measurement series with varying gate opening (A1-1 and A1-2).

Dependency on the energy head

The procedure described before was also applied to measurement series A2-2 and A2-1 with variable energy head.

The fitted pressure distributions along the submerged part of the gate are given in Figure 4.21 for the experiments in series A2-2. The pressure distributions for increasing relative gate opening at the right side of the gate end below unity, which was not the case in Figure 4.18. The drawdown of the water level or energy losses due to the vortex can be accounted for the drop. The same effect, was found by Kim (2007) by performing numerical analysis at a cross section of an underflow gate concerning energy losses due to friction and water surface fluctuations as the relative gate opening a/H_0 exceeded 0.4.
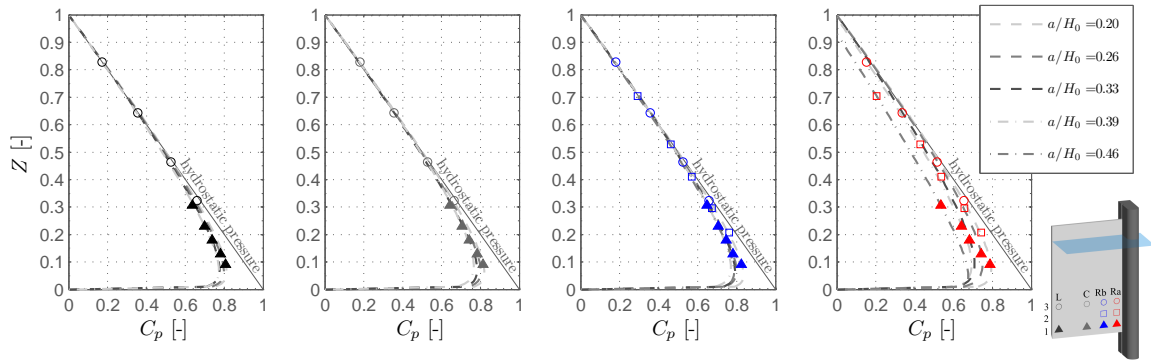
FIGURE 4.21: Discrete data and fitted functions describing the pressure distribution of experiments in series A2-2

The fitting parameters k, l and m are derived by fitting Equation (3.23) to the data points given in Figure 4.21 and illustrated as contour lines in Figure 4.22. Parameter m is required to describe the deviation from unity at the top end of the function.
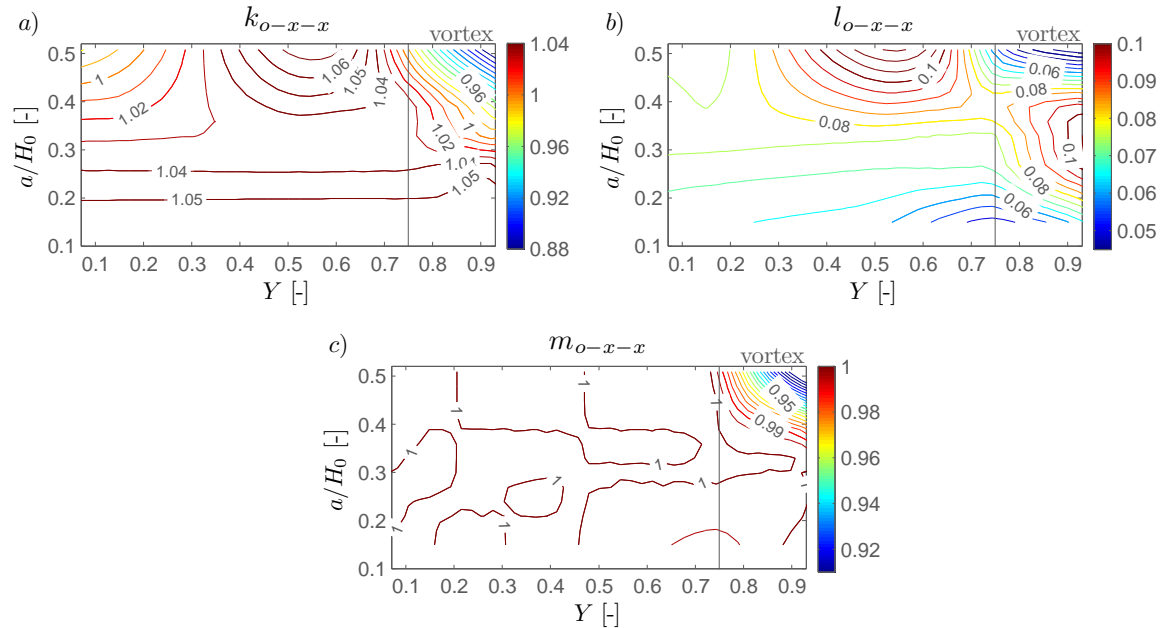
FIGURE 4.22: Fitting parameters k, l and m derived on the basis of series A2-2

Fitting parameter k indicate the decrease of the pressure with increasing a/H_0 in the corners of the gate. The fitting parameter m decreases with increasing value of a/H_0 in the vicinity of the vortex, as a/H_0 falls below 0.4. For smaller values of a/H_0 and therefore decreased vortex intensity m does not deviate from unity, just as m does not deviate at locations without influence of the vortex, further to the left. This effect was observed in both scale models, series A2-1 and A2-2 with variable energy head as the submerged parts of the gate $H_0 - a$ decreases.

Again the validity of the parameter model has been evaluated by determination of the errors of the pressure coefficient derived from measurement data and from the parameter

model, as well as the errors of resultant forces. The errors with respect to the results of the pressure coefficient from the large and the small scale model are given in Figure 4.24a&c respectively. The errors concerning the resultant force in the two scale models are presented in Figure 4.24b&d. The small errors in Figure 4.24a&c support a successful derivation of
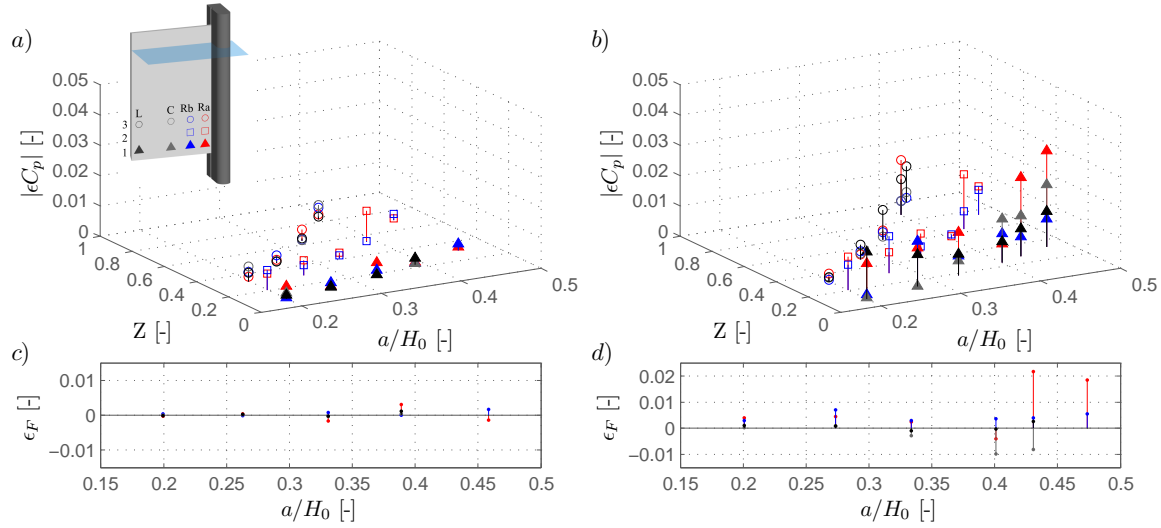
FIGURE 4.23: Evaluation of the parameter model given in Figure 4.22: deviation of pressure coefficient ϵC_p for a) series A2-2, b) series A2-1 and of resultant force ϵF for c) series A2-2, d) series A2-1

the contour lines from the experimental data of series A2-2. Increasing errors were obtained for high values of a/H_0 for the prediction of pressure of the experiments in the small scale model, given in Figure 4.24b&d. The largest errors derived at the right side of the gate suggest that the inaccuracy of the parameter model increases with the influence of the vortex on the pressure. The trend in Figure 4.23d indicates a slight underestimation of the resultant force for relative gate openings below 0.35 and an overestimation with further increasing relative gate opening, which agrees with Figure 4.20d. At the right side of the gate, where the pressure is influenced by the vortex, the force tends to be underestimated by the parameter model, *i.e.* the vortex induced pressure in the large scale model is smaller compared to the small scale model. This phenomenon was not observed for the measurement series with varying gate opening exceeding $a/H_0 = 0.4$ as can be seen in Figure 4.20. Hence it is assumed that influences due to intense vortices or highly intense vortices, causing a drawdown of water level or losses underlie scale effects.

Using the dimensionless geometric parameter a/H_0 the parameter model derived in Figure 4.20 can be used to predict the pressure coefficients for experiments of the series with variable hydraulic head. The errors of the predicted pressure characteristics to the data derived from the measurements are presented in Figure 4.24 as above. Figure 4.24a&c concern the large scale model and Figure 4.24b&d the small scale model. For relative gate openings $a/H_0 < 0.4$ the rather small errors concerning the pressure coefficient at the measurement points and the resultant force imply that the fitting parameters for the pressure distributions derived from measurement series A1-2 can be used to predict the pressure distributions in series A2-2. Increased errors at the right side of the gate, at a relative gate opening exceeding 0.4 in Figure 4.24a&b lead to the conclusion that the losses in the vicinity of the vortex
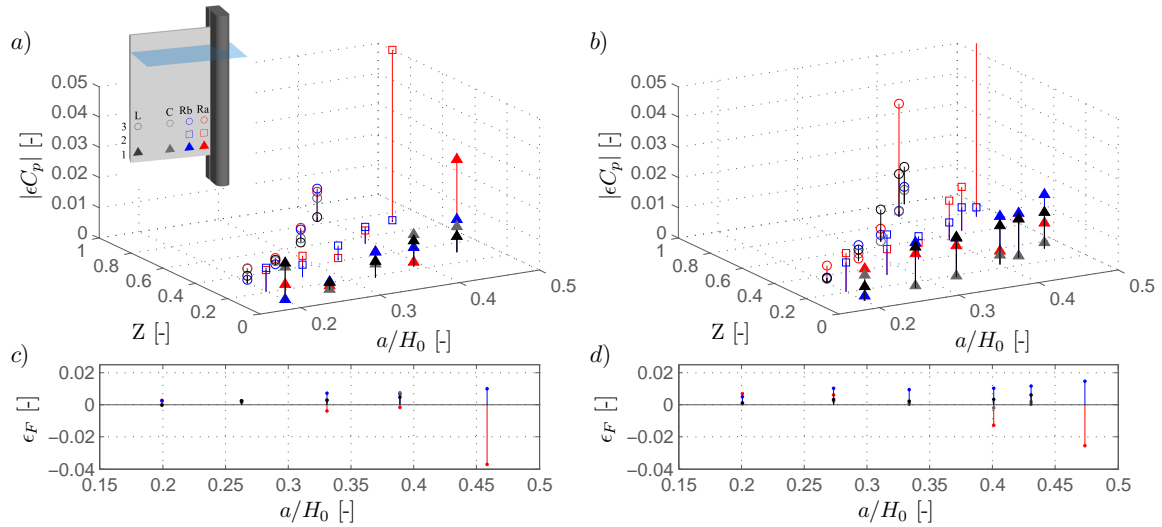
FIGURE 4.24: Evaluation of the parameter model given in Figure 4.19: deviation of pressure coefficient ϵC_p for a) series A2-2, b) series A2-1 and of resultant force ϵF for c) series A2-2, d) series A2-1

are not dependent of the relative gate opening solely. For the small scale model increasing errors were derived for $a/H_0 \leq 0.4$ as well, as indicated by Figure 4.24b&d. Higher errors were found concerning the prediction of pressure characteristics of the smaller scale model.

4.2.2 Correction factors

In order to account for the remaining parameters in the functional relationship in Equation (3.24), correction factors are derived concerning the approach flow v_0/v_a based on measurement series B1 and B2 and concerning the pier head length l_p/b based on measurement series A3 and B3. The definition of the series can be found in Table 3.2. The correction factors can be applied in combination with the basic pressure distribution depending on a/H_0, as derived above.

Increased approach flow (gate operation)

In this investigation the approach flow velocity v_0 has been increased by operating three gates of the weir structure in the hydraulic model instead of only one. Pressure distributions defined by Equation (3.23) were fitted to the data points obtained within the experiments of measurement series B1. The relative gate openings were the same as in Section 4.2.1, but the relative approach flow velocity (v_0/v_a) was increased. The parameters derived indicated an alteration of the mean pressure distribution at a gate due to the increased approach flow velocity. In order to investigate the trend and quantity of the alteration, the contour lines derived for increased relative approach flow velocity were expressed in relation to the contour lines in Figure 4.19 derived for lower relative approach flow velocity. Factors describing the relation of the fitting parameters of high to low approach flow velocities denoted as k_{o-o-o}/k_{o-x-x}, l_{o-o-o}/l_{o-x-x} and m_{o-o-o}/m_{o-x-x} are the results. The derived factors

are depicted as contour lines in Figure 4.25 as a function of the non-dimensionless parameters used before (Y and a/H_0). Minor deviations from unity in Figure 4.25a&c suggest
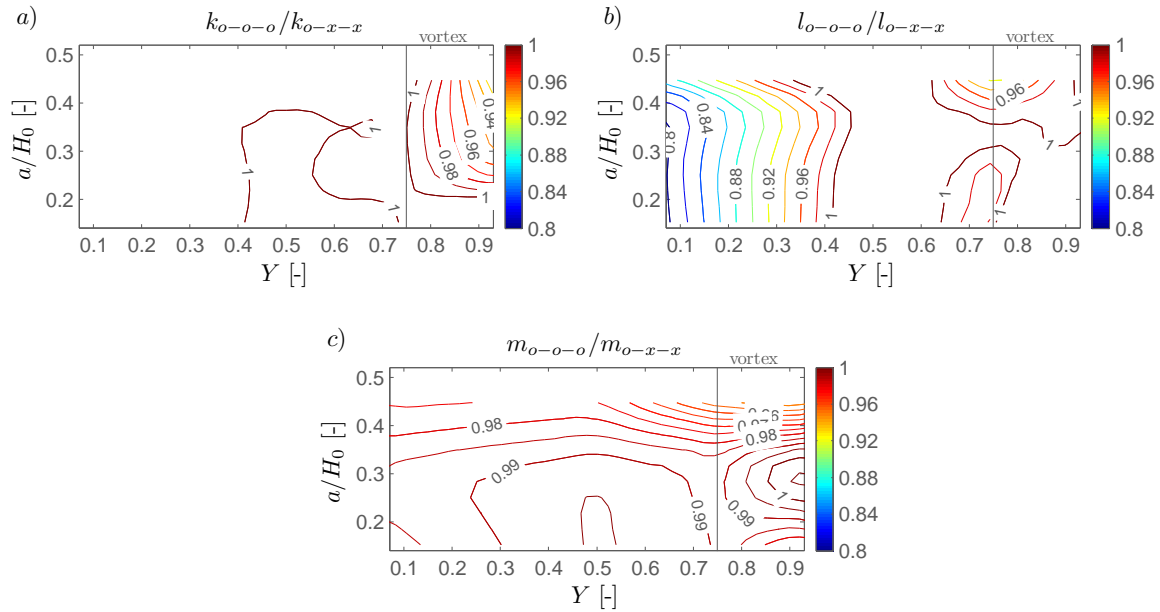
FIGURE 4.25: Correction factors for fitting parameters k, l and m for increased v_0/v_a

similarities to the fitting parameters illustrated in Figure 4.19. The fitting parameter l is decreased at the left side of the gate. But as it solely determines the location of the pressure maxima, the deviation might be neglected. If the fitting model given in Figure 4.19 is applied to measurement series B1, with increased approach flow velocity, a general overestimation of the resultant force, with the largest errors in the vicinity of the vortex was found. Fitting parameter k, which stretches the function in horizontal direction is subsequently used to overcome the systematic error of the fitting model for low approach flow velocity. Therefore fitting parameters l and m have been used as given in Figure 4.19 and k has been adapted in order to receive the best fit of the vertical pressure distribution to the measurement data. The correction factors obtained are given in Figure 4.26. As l and m were held
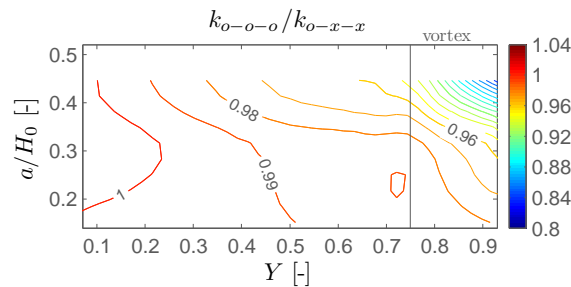
FIGURE 4.26: Correction factor for increased v_0/v_a, to be combined with Figure 4.19

constant, the only correction factor deviating from unity is k_{o-o-o}/k_{o-x-x}. The decrease of k with increasing relative distance from left pier Y indicates a pressure drop compared to the pressure at a gate with lower relative approach flow velocity v_0/v_a. At a relative

distance from left pier between 0 and ∼0.6 the correction factor k declines gently and drops steep at $Y > 0.7$. The fitting parameter k is reduced for up to 6 % in the vicinity of the vortex as indicated by a correction factor of 0.94 at high values of a/H_0. The increased relative approach flow velocity v_0/v_a increases the velocity head and intensifies the vortex formation upstream of the sluice gate.

The parameter model has been evaluated by calculating $|\epsilon C_p|$ and ϵF concerning measurement series B1 and B2 as given in Figure 4.27. As the fitting parameter k was adjusted
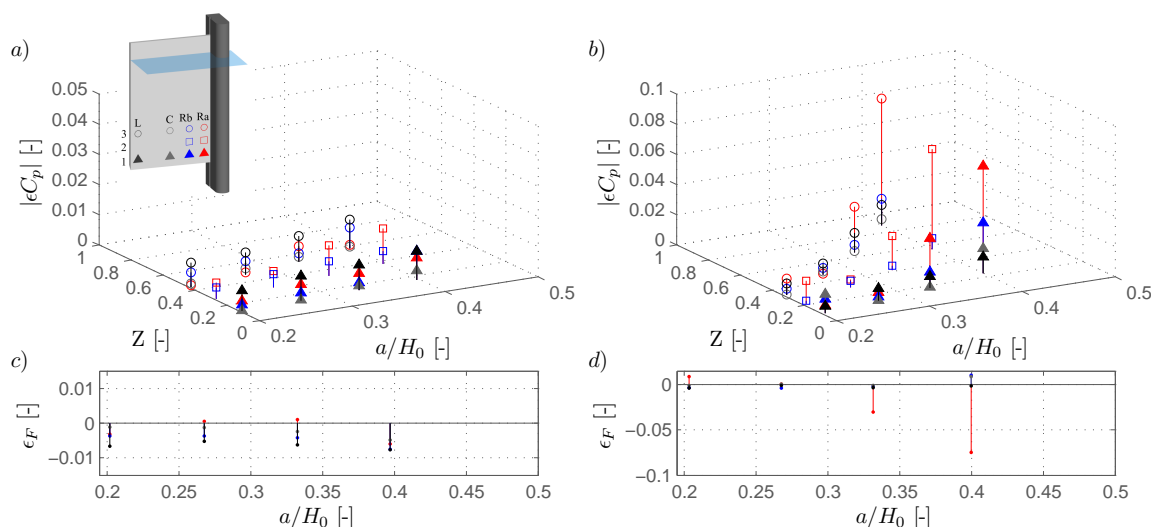
FIGURE 4.27: Evaluation of the parameter model given in Figure 4.26: deviation of pressure coefficient ϵC_p for a) series B1, b) series B2 and of resultant force ϵF for c) series B1, d) series B2

according to measurement series B1 with variable gate opening the calculated errors concerning the single data points and the normalised resultant force, given in Figure 4.27a&c respectively, are low. When applied to the measurement series with varying hydraulic head (B2) the errors increase drastically with increasing relative gate opening, so that the scale of the z-axis had to be increased to 0.1. These largest errors are calculated for the pressure distribution next to the right pier in the vicinity of the vortex, where the losses are supposedly enhanced due to the vortex formation. With the adaptation of k according to Figure 4.26 based on the parameter model for low approach flow velocities the parameter set derived in Figure 4.25 becomes superfluous.

Relative pier head length

Evaluating the pressure distributions derived from measurement series A3 and B3 with variable pier head length and constant relative gate opening of $a/H_0 \sim 0.27$, it was found that the mean pressure varied only slightly. Fitting parameters l and m were used for variable relative gate opening, as provided in Figure 4.19 and 4.26 for discharge under one and three gates respectively. The stretching parameter k was optimised to fit the pressure distribution, caused by the different pier head lengths. In case of discharge under one gate, the fitting parameter k varied in the range of 1.02 and 1.04 and in case of discharge under three gates in the range of 1.01 to 1.04, which indicates the insignificant deviation of the

mean pressure due to changing pier head length at $a/H_0 \sim 0.27$. The relations of the fitting parameter derived for variable pier head length $k(l_p)$ to k for constant pier head length at $a/H_0 \sim 0.27$ according to Figure 4.19 or Figure 4.26 has been calculated. Thereby obtained correction factors for discharge under one gate and under three gates are given in Figure 4.28a&b respectively. As only the stretching parameter k has been adjusted in order
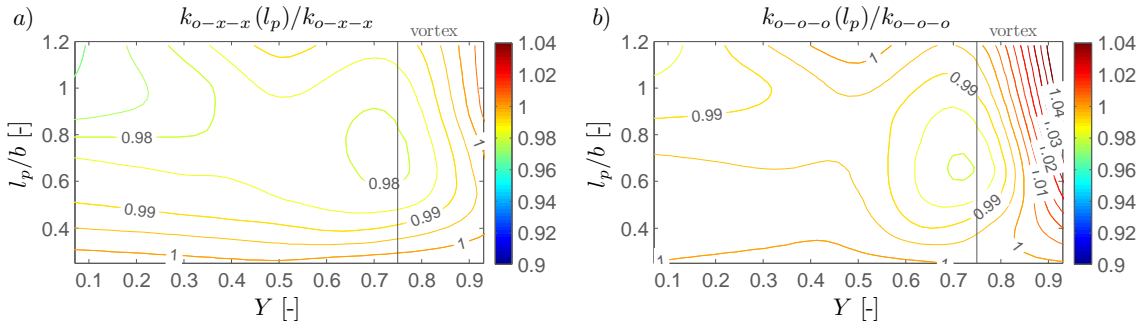
FIGURE 4.28: Correction factor for increasing l_p/b, to be combined with Figure 4.19

to fit the pressure distributions the correction factors for l and m equal unity. The pattern of the correction factor for k is similar for both cases of gate operation. Hence the trend is independent of the gate operation.

The errors using the fitting parameters l and m according to Figure 4.19 and 4.26 and adapted parameter k from Figure 4.28 are given in Figure 4.29. The errors are low which
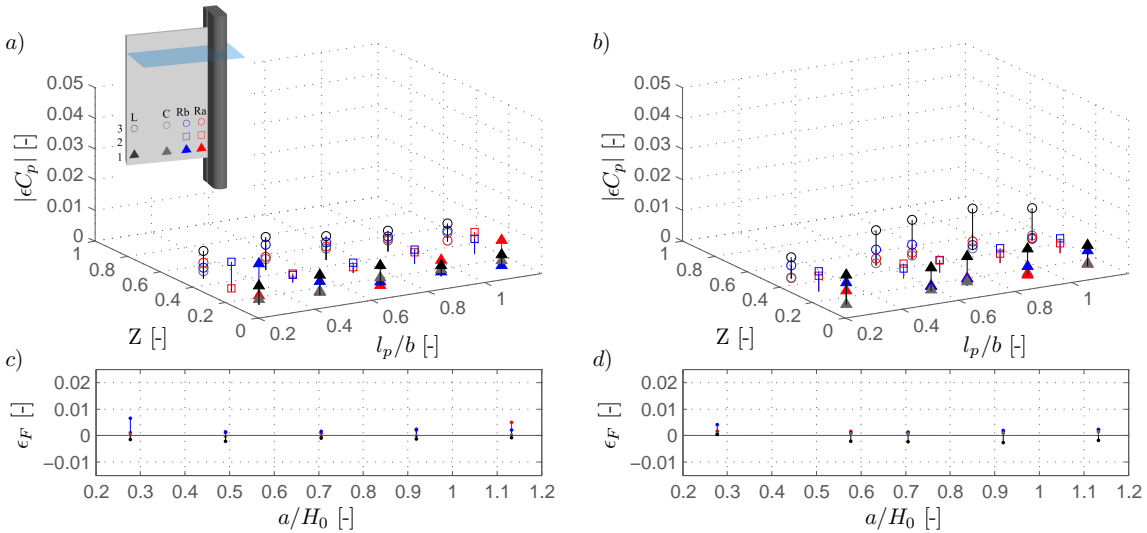
FIGURE 4.29: Evaluation of the parameter model given in Figure 4.28: deviation of pressure coefficient ϵC_p for a) series A3, b) series B3 and of resultant force ϵF for c) series A3, d) series B3

supports that the pressure distribution depending on the pier head length can be modelled sufficiently by adapting fitting parameter k solely. Increasing errors at the left side of the gate in measurement series B3 show a slight deficiency to model the increasing tendency of vortex formation at the left side. A top view of the vortices forming depending variable pier head lengths is given in Figure 4.30 and 4.31 for the experiments in series A3 and B3 respectively.
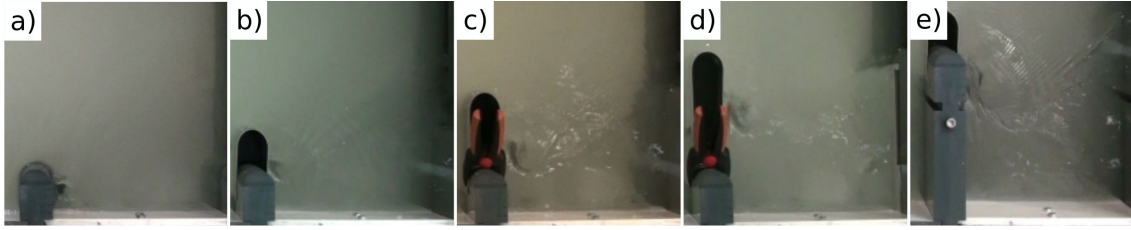
FIGURE 4.30: Vortex appearance at the first gate during test series A3; location of vortices at: a) l_p/b =0.28, b) 0.49, c) 0.71, d) 0.92 and e) 1.13

FIGURE 4.31: Vortex appearance at the third gate during test series B3; location of vortices at: a) l_p/b =0.28, b) 0.58 , c) 0.71, d) 0.92 and e) 1.13

Figure 4.30 shows the vortices forming upstream of the first gate due to discharge under the same gate, whereas Figure 4.31 shows vortices upstream of the third gate, while all gates are opened to the same extent. The vortex appearance is very similar in both picture sequences. It is noticeable that the intensity of the vortex increases and the center of the vortex on the surface is shifted away from the gate with increasing pier head length. Therefore the increased vortex intensity is not measurable to its full extent at the gate face. The longer the piers get the lower is the effect of the asymmetric approach flow. Due to long pier heads the flow gets homogenised and the flow conditions get similar to the conditions upstream of a gate spanning the whole channel width. As a consequence the probability of vortices forming at the left side of the gate increases. Beginning with Figure 4.30d and 4.31d the formation of vortices forming at the left side of the gate is probable.

4.3   Characteristics of pressure fluctuations

Concerning the pressure fluctuations the aspects as introduced in Section 2.3 are investigated, *i.e.* the maximum amplitude of fluctuations is analysed by means of measured maxima as well as probability of occurrence, the characteristics of spatial distribution are investigated by means of the correlation and finally amplitude spectra are derived to include the dynamic aspect of the pressure fluctuations. An example for the application of the results of this section is given in Appendix C.

4.3.1   Pressure maxima

Normalised maximum amplitudes of the pressure fluctuations C_{p+} and C_{p-} have been determined from the filtered record samples. They are plotted as a function of the relative gate

opening or the relative pier head length depending on the respective measurement series, as given in Table 3.2.

Figure 4.32 and 4.33 illustrate the obtained normalised pressure amplitudes at the bottom row of the measurement grid, where the largest fluctuations were identified. Figure 4.32a&b
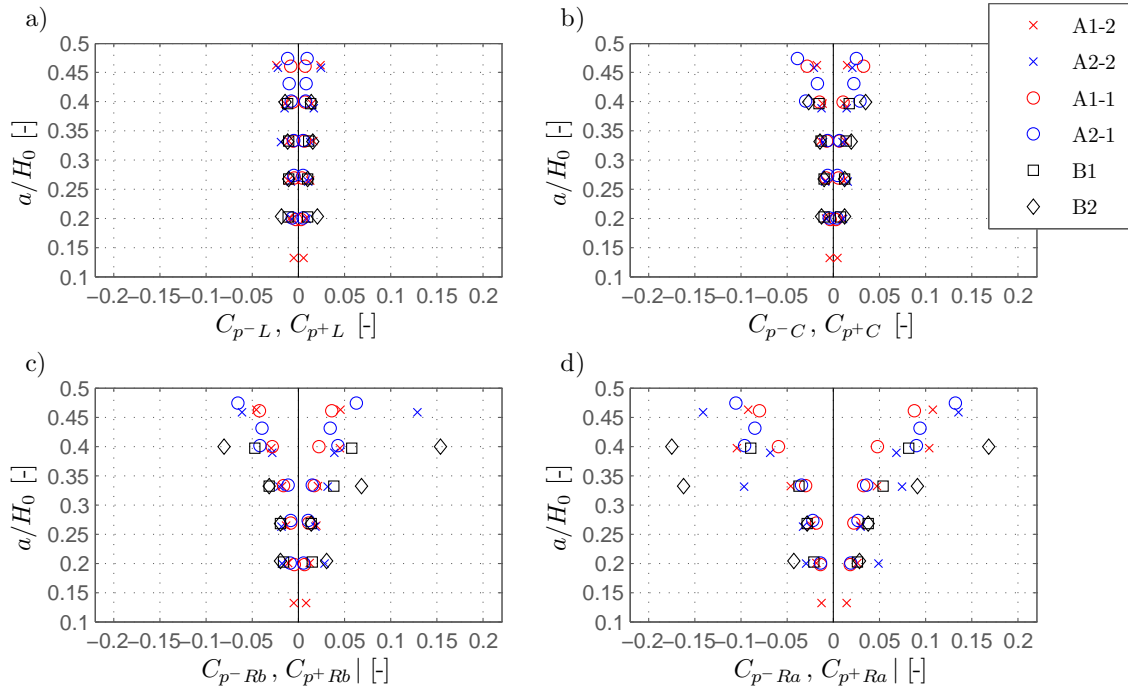
FIGURE 4.32: Pressure maxima depending on a/H_0 at the bottom measurement row

indicate the low fluctuating component of the pressure at the left side of the gate and its center, *i.e.* without a vortex forming upstream of the gate face, the normalised amplitudes C_{p+} and C_{p-} were below 0.04. A slight increase with increasing relative gate opening can be identified. The pressure amplitudes at the right side of the gate, which are affected by the vortex are given in Figure 4.32c&d. They are up to four times as high and reach 15 % or 20 % of the velocity head at the gate lip $(H_0 - a)$ depending on the gate operation. The dependency on the relative gate opening is clear from both Figure 4.32c&d, indication the increasing fluctuations with increasing relative gate opening. Slightly higher fluctuations were identified for measurement series A2-2 and A2-1, where the energy head was varied in order to change a/H_0. Maxima were determined from experiments of series A2-2 in the large scale model concerning flow under one gate (o-x-x). They are exceeded by the fluctuation maxima in measurement series B2, where the approach flow velocity was increased due to flow under three gates (o-o-o). In the second row the range of the amplitudes is between -0.15 and 0.1 and further reduced in the top row to -0.07 and 0.05. The pressure maxima measured at the second and top measurement row are given in Appendix A.2.

Figure 4.33 indicates the effect of the pier head length on the maximum pressure amplitudes at the lowest measurement row. The relative gate opening a/H_0 was 0.26 for the investigations concerning the pier head length in series A3 and B3. With these boundary conditions the pressure fluctuations at the left side of the gate are increasing with the pier head length (Figure 4.33a). The maximum fluctuations at the right side were reached at relative pier
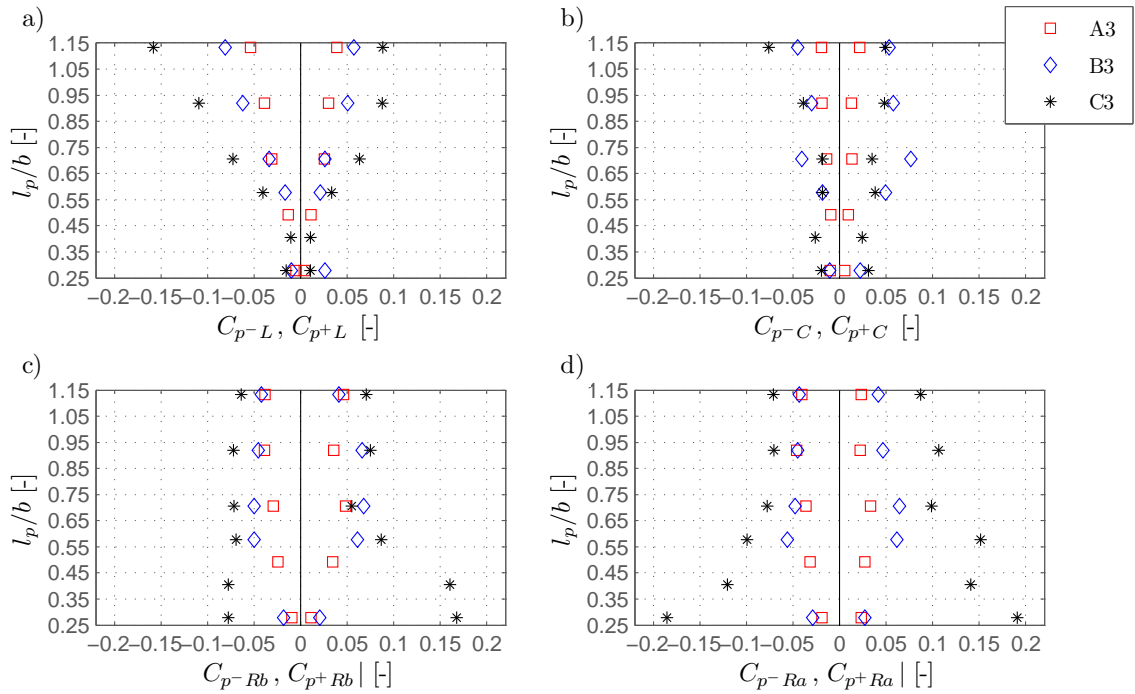
FIGURE 4.33: Pressure maxima depending on l_p/b at the bottom measurement row

head lengths l_p/b between 0.55 and 0.75 (Figure 4.33c d). Due to the low relative gate opening of 0.26, the pressure fluctuations were generally low. With increasing distance to the gate lip the amplitudes were on the range of ±0.5, as illustrated in Appendix A.2. Only the negative fluctuations at the left side were larger. Further the influence of the pier head lengths was tested at $a/H_0 = 0.4$ in measurement series C3. At the left side of the gate the pressure fluctuations are increasing to a larger extent with l_p/b due to the increased relative gate opening(Figure 4.33a). Pressure fluctuations at the right side of the gate decrease with increasing relative pier head length, and thereby approach the values obtained from series A3 and B3 with $a/H_0 = 0.26$ (Figure 4.33d). The opposing trend at the left and right side indicates the different location of a longitudinal vortex just upstream of the gate, which forms at the right side due to short pier head lengths and at the left as the pier head length increases.

4.3.2   Stochastic description of pressure maxima

The maximum pressure amplitude is an important characteristic of the hydrodynamic impact. In stochastic design concepts extreme values are characterised by a specific probability of occurrence, which can be calculated from their distribution. Theoretical probability density distributions are fitted. As introduced in Section 3.3.3 normal and t location-scale distribution are considered. Amplitudes with a specific probability of occurrence can be obtained from the theoretical distribution and the data as well. Their difference characterises the errors due to the fit. Quantifying the errors for the normal distribution at the one hand and the t location-scale distribution at the other hand their goodness of fit can be compared.

As an example the largest errors of the experiments of measurement series A1-2 and A2-2 are given in Figure 4.34a&b for normal and t location-scale distribution respectively. Amplitudes
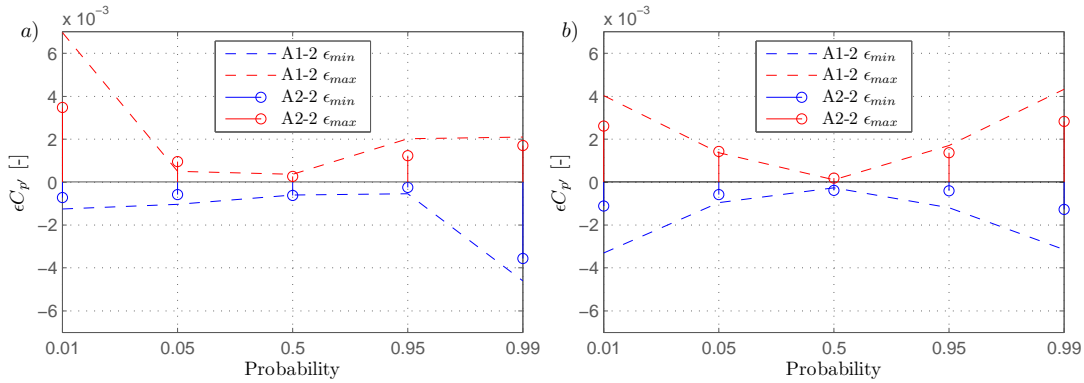
FIGURE 4.34: Maximum errors of fitted probability density distributions: a) normal distribution, b) t location-scale distribution

with exceedance probability of 0.01, 0.05, 0.5, 0.95 and 0.99 are considered therein. The depicted maxima were determined for rather high values of a/H_0, at the right side of the gate, where vortices form. For both probability density distributions it is visualised clearly that the errors increase as the distance to the median at 0.5 increases in either direction, *i.e.* the accuracy decreases at the tails of the distribution. The boundaries illustrated in Figure 4.34 can be interpreted as the accuracy of the probability distribution fitted to measurement series A1-2 and A2-2. The maximum positive and negative errors $\epsilon C_{p'}$ express that the amplitudes are either under- or overestimated by application of the theoretical probability density distribution. The errors due to the normal distribution have a trend to underestimate the amplitudes which is indicated by large positive errors at small probabilities (0.01) and large negative errors at high probabilities (0.99) as recognisable in Figure 4.34a. The origin of these errors is illustrated in Figure 3.16c. Comparably the positive and negative errors due to the t location-scale distribution are almost the same, indicating that over- and underestimation can reach the same extent, if using this distribution.

The maximum amplitude of the pressure fluctuations was described by the quantiles with probability of 0.01 and 0.99, derived from the fitted probability density distribution. Their deviation from the absolute extreme values of the data indicates the accuracy of this assumption. Both, normal and t location-scale distribution were evaluated this way. Differences were insignificantly small, hence the results are depicted for normal distribution solely. They are given in Figure 4.35a&b as $\epsilon C_{p',0.01}$ and $\epsilon C_{p',0.99}$, concerning the errors at the lower and upper tail of the distribution. As the prediction of the extreme values could not be improved by using t location-scale distribution, the assumption of normal distribution was found to be sufficient. Assuming a normal distribution has the advantage that the distribution of data is fully characterised by the mean value and standard deviation.

4.3.3 Amplification factors

Envelope functions of the shape given by Equation (3.29) were fitted to the pressure maxima, described as extreme values as in Section 4.3.1 or by quantiles as introduced in Section 4.3.2.
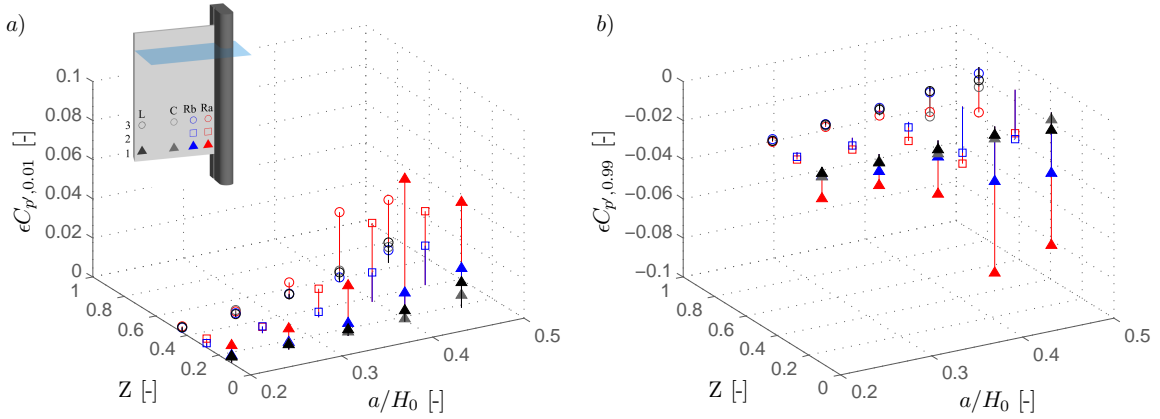
FIGURE 4.35: Deviation of extreme value derived from probability density distribution ($C_{p',0.01}$, $C_{p',0.99}$) to the measured maxima: a) overestimation of minima, b) underestimation of maxima

Subsequently amplification factors κ can be derived relating the minimum and maximum to the mean pressure distribution. Based on κ, the intensity of pressure fluctuations can be analysed in dependency of the relative lateral location at the gate Y, the relative gate opening a/H_0 and relative pier head length l_p/b. The values of κ are calculated separately for the minimum and maximum according to the rearranged form of Equation (3.29) and are averaged subsequently, in order to give contour lines representing both, positive and negative maxima. In order to determine the sufficiency of quantiles of a fitted distribution for characterisation of the amplitudes of pressure fluctuations, their deviation to the maximum pressure amplitude is calculated.

Relative gate opening

The amplification factors in Figure 4.36 are obtained from the pressure maxima of the filtered time series. Contour lines are fitted for flow under one gate (o-x-x) and three gates (o-o-o) and given in Figure 4.36a&b respectively. Increasing pressure amplitudes are
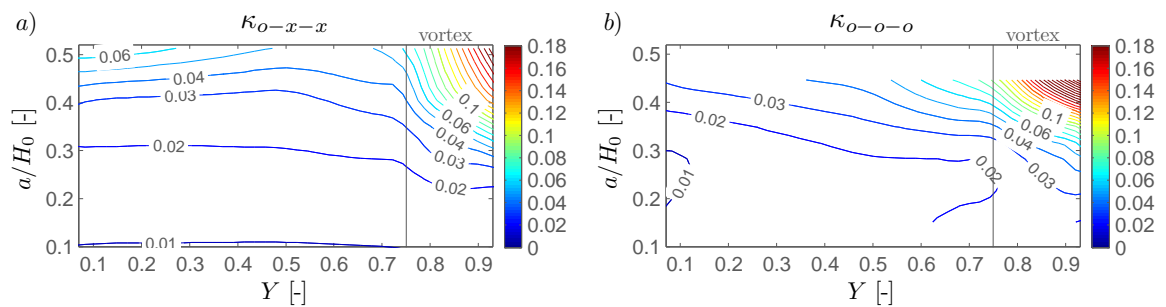
FIGURE 4.36: Amplification factor κ for prediction of maximum pressure amplitudes C_{p+} and C_{p-} depending on a/H_0

characterised by increasing values of κ. An increasing intensity of fluctuations can be related to increasing relative gate openings and to the location of vortex formation. The trend of

κ in Figure 4.36a&b agrees well. For flow under three gates, slightly higher values of κ are obtained at high relative gate openings.

For comparison, envelope functions are derived on the basis of the amplitudes with occurrence probability 0.01 and 0.99 according to the fitted normal distributions. The amplification factors κ obtained are plotted in Figure 4.37a for flow under the left gate (o-x-x) and in Figure 4.37b for increased approach velocity due to flow under three gates (o-o-o). The
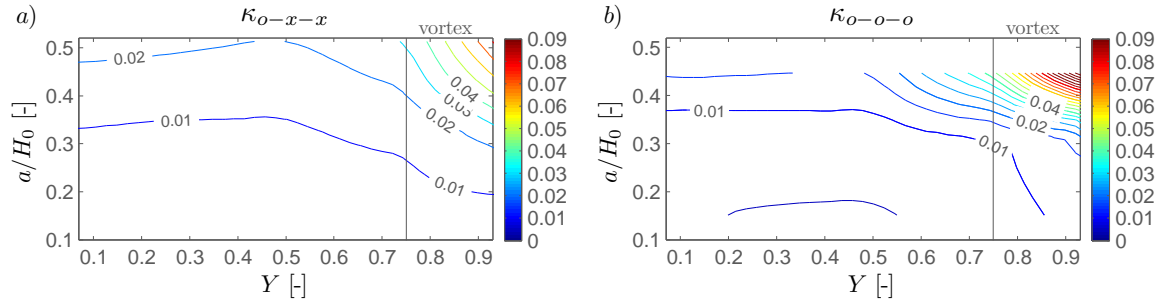
FIGURE 4.37: Amplification factor κ for prediction of $C_{p',0.01}$ and $C_{p',0.99}$ depending on a/H_0

dependency on the lateral gate location Y, the relative gate opening a/H_0 and increased relative approach flow v_a/v_0 and the influence of the vortex are recognisable, just as in Figure 4.36, but the values of κ are considerably smaller. The error for predicting amplitudes by quantiles is obtained by calculating the difference in the measured amplitudes. The results are given in Appendix A.3. Figure A.17 and A.18 give the error concerning the pressure coefficient as well as the error of the resultant force for the measurement series A1-2 and A1-1 in the larger and smaller scale model respectively. For both cases the errors have the same trend and are below $a/H_0 = 0.4$ are in the same range. The deficiency of the normal distribution in modelling the extrema of the data distribution increases with increasing relative gate opening a/H_0, which is indicated by increasing errors. The errors of resultant forces indicate that the negative amplitudes are more likely to be overestimated and the positive amplitudes are more likely to be underestimated, if the amplitudes are redetermined by applying κ values from Figure 4.37. The maximum error is 0.09 concerning the pressure at specific measurement points and -0.04 concerning the resulting force. The errors for the positive amplitudes are slightly below the ones of the negative amplitudes.

Predicting the amplitudes for increased approach flow velocity by using κ from Figure 4.37b deviations with comparable trend and size were derived, as depicted in Figure A.19.

Further it is supposed that the pressure amplitudes for experiments performed in the same range of relative gate opening a/H_0 with variable hydraulic head can be predicted by application of amplification factors given in Figure 4.37. The errors of the measured extreme amplitudes in measurement series A2-2 to the predictions are given in Figure A.20. They show the same trend as for the measurement series with variable gate opening as discussed above. Increased deviations of the pressure coefficient of 0.15 were identified at relative gate openings greater than 0.4 at the right corner of the gate, influenced by the vortex, leading to an overestimation of the minimum resultant force of about 0.065.

The pressure amplitudes predicted from the amplification factors derived from the larger scale model for the smaller scale model resulted in smaller errors. They are given in Figure A.21. From Figure 4.32 it can be concluded that the slightly lower amplitudes in the small scale model are the reason for the smaller errors.

Largest deviations were derived by applying the amplification factor κ given in Figure 4.37b for flow under three gates. Predicting extreme amplitudes for measurement series B2 with variable hydraulic head on the basis of B1 the errors given in Figure A.22 were calculated. They are increasing up to 0.2 at large relative gate openings. The difference of the pressure extrema leads to high errors, up to 15 % for prediction of the resultant force.

Relative pier head length

The influence of the pier head length l_p/b on the pressure fluctuations in measurement series A3 and B3 is expressed by the amplification factors given in Figure 4.38. Figure 4.38a&b show the results for flow under one gate (o-x-x) and three gates (o-o-o) respectively. At
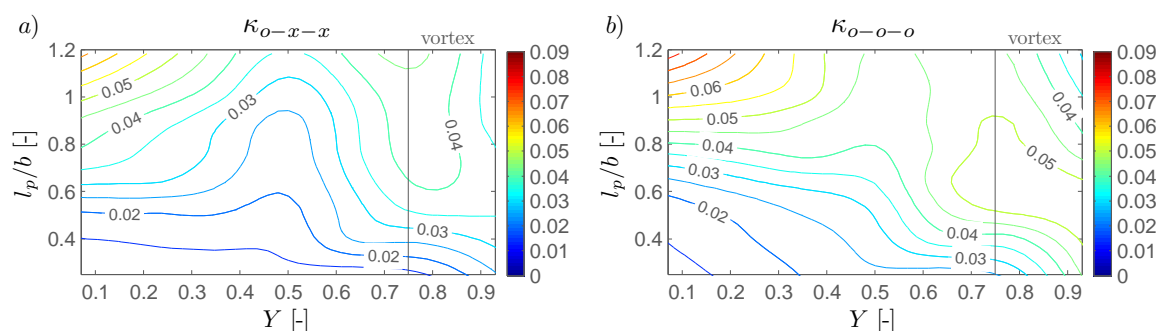
FIGURE 4.38: Amplification factor κ for prediction of maximum pressure amplitudes C_{p+} and C_{p-} depending on l_p/b

the right side of the gate a maximum of κ can be identified, at relative pier head lengths of about $l_p/b = 0.55$ and 0.75. Comparing this result with Figures 4.30 and 4.31, showing the vortices upstream of the gate depending on the pier head length, the enhancement of the vortex with increasing pier head length can be recognised. Further, the increasing pier head length shifts the vortex center upstream and thereby increases the distance to the gate, whereby the impact of the fluctuating pressure is reduced. Another maximum was found at the left side as the relative pier head length exceeds about $l_p/b = 0.8$. With increasing length the piers form a channel, increasing the volume prone to vortices and straightening the asymmetric flow in the vicinity of the gate. The likelihood of vortex formation at both sides of the gate increase. Increased approach flow velocity leads in enhanced fluctuations, as indicated by increased values of κ in Figure 4.38b.

Amplification factors κ were derived on the basis of amplitudes with a probability of 0.01 and 0.99 as well. Figure 4.39a&b give the obtained values for κ depending on the relative pier head length l_p/b for discharge under one gate and three gates respectively. Once again the trend of the pressure fluctuations can be characterised by the quantiles of pressure fluctuations, whereas the amplification factor is underestimated remarkably.
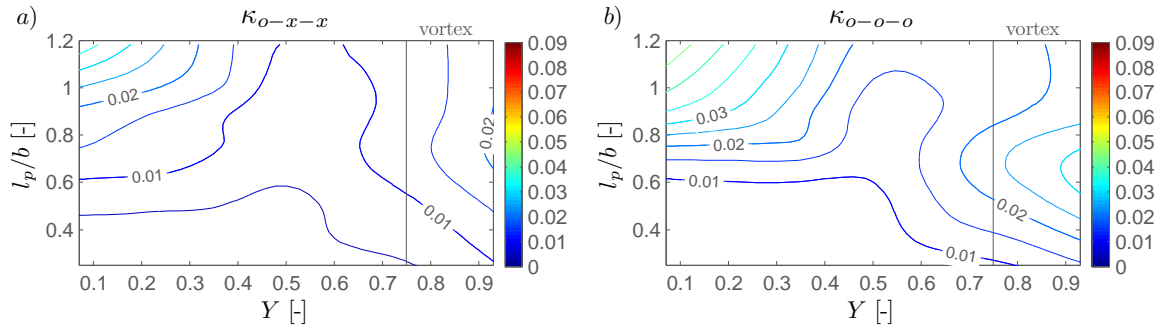
FIGURE 4.39: Amplification factor κ for prediction of $C_{p',0.01}$ and $C_{p',0.99}$ depending on l_p/b

The errors in the actual measured maxima are generally not outstanding as compared to the results discussed in the previous section. They are below 0.1 concerning the pressure and maximum errors of the resultant forces are in the range of 0.01 and 0.025 in Figure A.23 and A.24. The slight overestimation of the positive amplitudes in the vicinity of the vortex was not obtained before. It occurs with increasing pier head length as shown in Figure A.23d and A.24d.

Discussion

Using quantiles of the pressure fluctuations derived from a fitted probability density distribution increases the tendency to underestimate the pressure amplitudes due to vortex formation. The errors result from the lack of the ability to model the tails of the data distribution, as well as the obvious fact that the absolute extreme values are higher. The divergence could be covered by a factor of safety, which can be estimated according to the derived errors, documented in Appendix A.3. Using the absolute measured pressure extrema to derive averaged amplification factors generally leads in smaller errors, as depicted in Appendix A.2 Figure A.13 to A.22. Largest errors were obtained for low submergence of the gate.

Applying the amplification factors in Figure 4.36 and Figure 4.38 combined with the fitting parameters of the mean pressure distribution in Figure 4.19 and 4.26, 4.28 the envelope functions of the pressure extrema can be estimated, depending on the relative gate opening, whereas the effect of increased pier head length and approach flow can be considered.

4.3.4 Spatial correlation

The correlation of the pressure fluctuations is used to analyse their interrelation on the upstream face of the sluice gate. Therefore the correlation coefficient R_p as defined in Equation (2.27) is calculated for the sample records in the lowest row for each simultaneously recorded time series. The correlation coefficients of the sample records are presented in Appendix A.4. The sub-figures denoted with a-d give the correlation coefficient for location Ra1, Rb1, C1 and L1 to all other locations respectively. To give an overview of the results the

data is summarised in Table 4.16. The location (loc.) of the measurement point analysed and the direction or specific measurement point (shift) are given, which are correlated. Further the extent of correlation and the influence of the investigated parameters is described.

Loc.	Shift	Correlation	Influence
Ra1	ΔZ	Max. $R_p \sim 0.5 - 0.7$.	Decreasing with increasing ΔZ, increased for o-o-o: up to 0.9.
	ΔY	Generally low, with $R_p < 0.3$.	Max. for o-o-o: $R_p \sim 0.5$, increasing with increasing l_p/b.
	to row Rb	Generally low.	Correlation increases with l_p/b: up to $R_p \sim 0.4$ (o-x-x) and 0.8 (o-o-o).
	to Rb1	Low negative R_p.	Most distinct for o-o-o, decreasing neg. corr. (approaching 0) with increasing a/H_0 and positive for increased l_p/b: $R_p \sim 0.8$ for o-o-o.
	to top row	Low, highest at Ra3.	For Rb, C, L decreasing with increasing a/H_0.
Rb	ΔZ	Max. $R_p \sim 0.6 - 0.8$.	Decreasing with increasing ΔZ, increased for o-o-o (up to 0.9).
	ΔY	To the left: $R_p \sim 0.5 - 0.6$, negative to the right (Ra).	For o-o-o negative corr. to Ra decreases (approaches 0) with a/H_0, and exceeds 0 with increased l_p/b.
	to row Ra	See Ra1 to Rb (above).	
	to top row	Generally similarly low, except to Ra3 which is lower (ev. negative).	
C, L	ΔZ	Generally high $R_p \sim 0.6 - 0.8$.	
	to top row	Generally high $R_p \sim 0.5 - 0.7$.	R_p for loc. at top row shifted for ΔY slightly lower, R_p dropping with increasing l_p/b; constantly below 0.3 for o-o-o.

TABLE 4.16: Evaluation of derived spatial correlation coefficients R_p

The main correlation was determined for vertically aligned measurement locations. The correlation over ΔZ was found to be rather stable independent of the lateral location Y, $\Delta a/H_0$ or $\Delta l_p/b$. The correlation of the two rows at the right side of the gate, *i.e.* row Ra and Rb, depends on the geometric parameters, just as the appearance of the vortex. For increased relative approach flow velocity, increasing relative pier head lengths l_p/b cause enhancement of the correlation between Ra and Rb up to $R_p = 0.8$, even though increased relative approach flow velocity was found to decrease the correlation coefficients in general. As the correlation coefficient was not found to be consistently high over the gate leaf, a fluid-structure interaction in the hydraulic model can be precluded. Hence the measured pressure

fluctuations were induced by the fluid dynamics solely. High values of the correlation coefficient indicate fluid moving coherently. Thereby the area at the gate face influenced by the same impact characteristics can be identified. The increasing correlation of measurement row Ra and Rb with increasing pier head length indicates an increased area prone to the vortex.

4.3.5   Amplitude spectrum

The amplitude spectra reveal the main periods contributing to the amplitudes of the pressure fluctuations. The normalised amplitudes $C_{p'}(t)$ with a specific normalised periodicity of $\tau_n = 1/f_n$ are determined and given in Appendix A.5 for all experiments of the experimental program in Table 3.2. On the basis of all record samples, envelope functions were derived. Thereby the peaks of each measurement series are summarised. The envelope functions at each location of measurement are presented in Figure 4.40. Rather flat spectra were derived
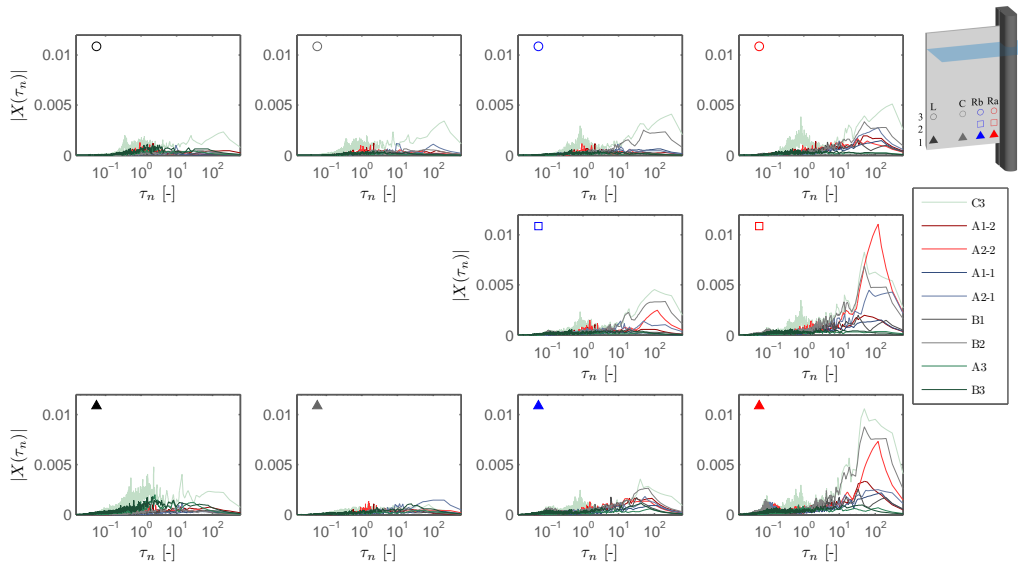
FIGURE 4.40: Envelope functions of amplitude spectra

for the left side as well as at the center of the gate. Spectra at row Ra and Rb peak in the range of $\tau_n = 20 - 170$. Secondary maxima were found in the range of $\tau_n = 0.08 - 0.8$.

Experiments performed at a relative gate opening below 0.4 showed an increasing trend with with increasing normalised period τ_n at row Ra, as well as at measurement point Rb1, in the bottom row (Figure A.34 or A.35). The increased amplitudes at rather long periods characterise the intermittency of the vortex structure upstream of the gate leaf.

Relative gate openings above 0.4 were found to be related to the secondary maxima, which are enhanced by increased approach flow velocity by flow under three gates (Figure A.36). The range of the maxima was rather independent on the relative gate opening a/H_0 (Figure A.38), but was influenced by a change of the pier head lengths. With increasing relative pier head length the range of periods of the secondary maximum tends to be increased, which is very well recognisable from the spectra of series C3 Figure A.42, performed at

$a/H_0 = 0.4$. Relatively long pier head lengths cause an increase of the amplitude components at the left side of the gate (Figure A.40 and A.41), which were found to be in the range of $\tau_n = 0.5 - 3$.

Depending on the spatial correlation of the time series analysed in the foregoing Section 4.3.4 and the appearance of the amplitude spectra characteristic spectra for the different regions at the gate can be defined. A rather constant spectrum describing the impact on the gate leaf at the vortex free zones and a spectrum characterised by increasing amplitudes with increasing period at the area of the vortex, whereas impacts with short periods have to be expected at relative gate openings $a/H_0 \geq 0.4$.

4.4　Discussion

Results from the large and the small scale model were comparable, which supports the sufficiency of the hydraulic model to analyse the pressure conditions or discharge characteristics. Diverging results have been obtained from measurement series with variable gate opening and variable hydraulic head, even though the dimensionless parameter a/H_0 commonly used to describe the boundary conditions of flow under gates and vortex formation is the same. The differences were obtained for relative gate openings above a range of 0.4.

For comparison of the influence of the Reynolds numbers, as derived by dimensional analysis in Section 2.5 are given in Figure 4.41 for the experiments with variable relative gate opening a/H_0, as defined in Table 3.2. The Reynolds numbers were found to be between 1×10^5
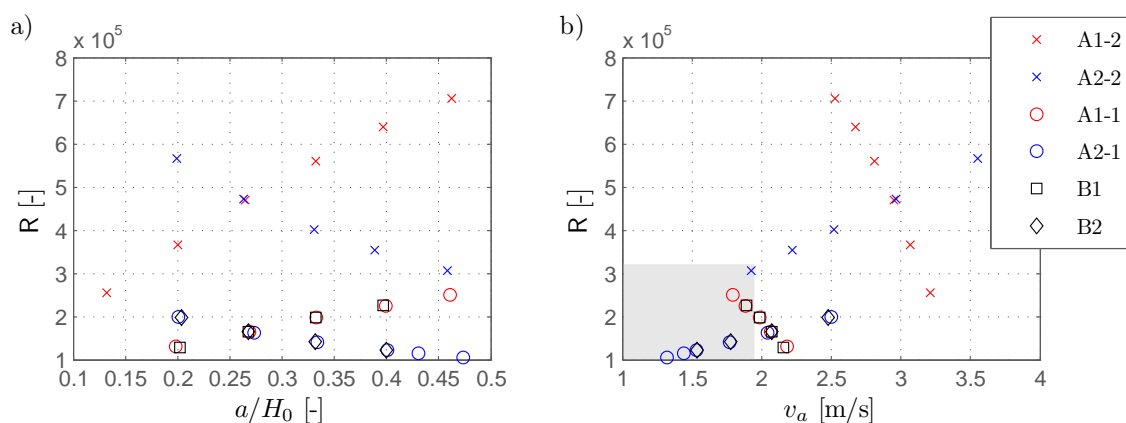
FIGURE 4.41: Reynolds numbers R in the model tests: a) dependency on the relative gate opening a/H_0, b) dependency on the velocity at the gate lip v_a

and 3×10^5 in the small scale model and between 2.5×10^5 and 7×10^5 in the large scale model. Even though the Reynolds numbers were constantly lower in the small scale model the results are consistent. From Figure 4.41a it becomes obvious that the Reynolds number is not explicitly dependent on the relative gate opening. Quite contrary it shows opposite trends whether the gate opening a or the energy head H_0 causes the change of the relative gate opening. These two parameters also affect the discharge, but in different senses. Generally the lowest Reynolds numbers were obtained for experiments with small

gate openings a or with low energy head H_0, independent of the relative gate opening. According to Equation (2.49) the Reynolds number is a function of the gate opening a and the velocity at the gate lip v_a, used as basic variables in the dimensional analysis. The dependency on the gate opening is not significant, considering that it was held constant for measurement series A2-2, A2-1 and B2 and that a/H_0 is directly proportional to a in measurement series A1-2, A1-1 and B1 and hence the trend agrees with Figure 4.41a. Therefore the dependency of the Reynolds number on v_a is investigated and depicted in Figure 4.41b. The grey area in Figure 4.41 marks the range where deviations of the pressure pressure characteristics were detected in the previous sections. They were found concerning the application of the parameter model derived in Section 4.2 and concerning the pressure amplitudes discussed in Section 4.3.

The absolute values of the deviation of the mean pressure ϵF as derived in Section 4.2 are plotted depending on the Reynolds number R. Figure 4.42 shows the deviations at the four cross sections at the gate, denoted as L, C, Rb and Ra in agreement with the previous chapters. The grey area marks the range with errors exceeding 0.01. According to
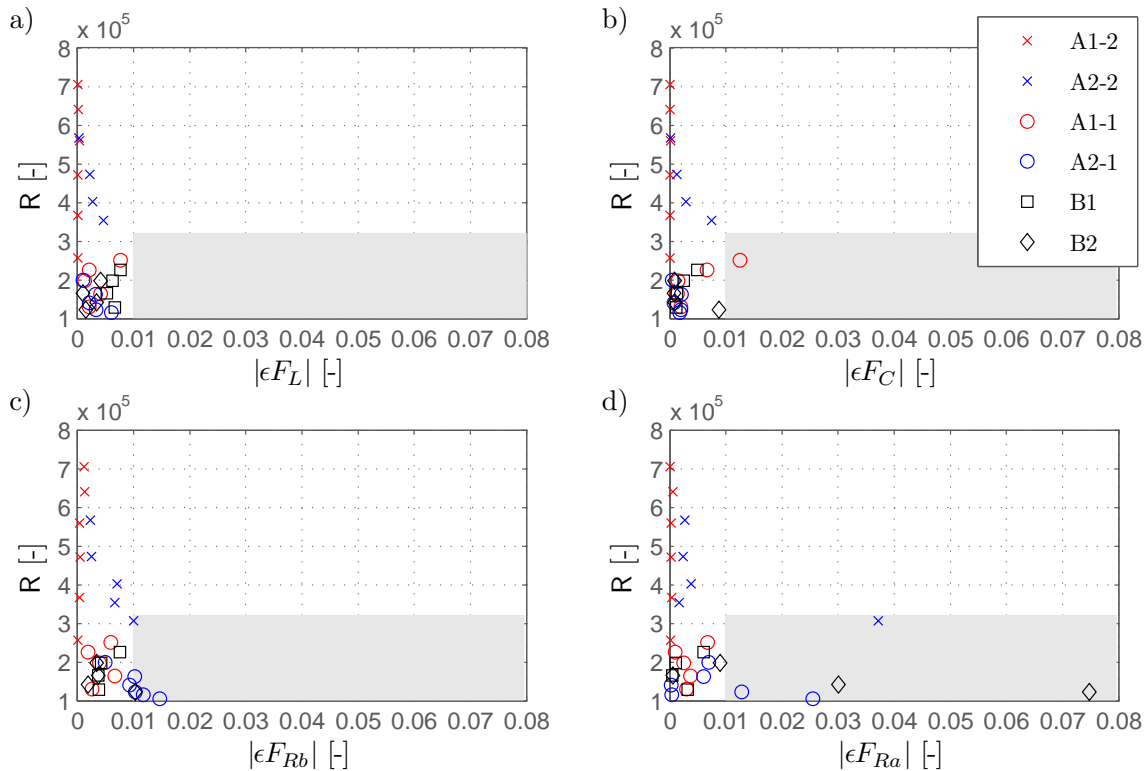
FIGURE 4.42: Accuracy for predicting the force on the upstream face of a sluice gate as a function of Reynolds number R

Figure 4.42a all derived errors are below 0.1 at the left side of the gate . In Figure 4.42b one point lies within the grey area, which is a data point of the experiment with the highest Reynolds number in series A1-1. Taking the velocity at the gate lip v_a into account as in Figure 4.41b, it is revealed that the submerged part of the gate is lower, as compared to the other experiments in the same series. Figure 4.42c reveals three experiments out of series A2-1 with slightly increased errors of the predicted force. The largest errors are found at the very right side of the gate. Figure 4.41d reveals errors above 0.1 for some experiments

of the small model with Reynolds numbers at the lower end of the range, but also for one experiment out of the larger scale model with low energy head, causing low velocity at the gate lip v_a. The grey areas in Figure 4.42 contain the same data points as the grey areas in Figure 4.41, where the parameter model loses accuracy. These data points were all obtained at a small submerged part of the gate $H_0 - a$, which is directly related to v_a as indicated in Figure 3.13. Figure 4.41b shows that the range can be related to low submergence combined with low Reynolds numbers.

An error analysis was performed on the pressure fluctuations as well. Thereby the amplitudes of pressure fluctuations were predicted for the measurement series A2-2 and B2 on the basis of the amplification factors given in Figure 4.36. The error plots obtained are given in Appendix A.2 in Figure A.13 to A.16. Compared to the errors caused by using quantiles for the prediction the errors are generally reduced, which is concluded from comparison with Figure A.17 to A.22. But in both approaches it is clear that the pressure amplitudes at low submergence of the gate can not be predicted to their full extent. It is suggested using the amplification factors as derived from the measured extreme values, combined with a safety factor for low submergence, to account for the pressure drop. The normalised force derived by integration of the hydrostatic pressure equals 0.5. The largest errors concerning the pressure drop are 0.04 and increase to 0.11 for increased approach flow velocity, which can be found in Figure A.14 and Figure A.16 respectively. Hence a dynamic force accounting for the effect would have to be increased between 8 % and 22 % of the hydrostatic force depending on the approach flow conditions. Concerning the extrema of pressure fluctuations a safety factor of $0.14 \times (H_0 - a)$ and $0.2 \times (H_0 - a)$ depending on the approach flow conditions should be sufficient, as concluded from the maximum errors in Figure A.13 to A.16.

Vortex appearance

The weakest and strongest vortices appearing in each experiment of the large scale model are illustrated, showing dependence on the relative gate opening a/H_0. Thereby the range of the vortex intensity, which changed over the time is characterised. In Figure 4.43 the vortices of measurement series A1-2 with variable gate opening are depicted. The top row of Figure 4.43 illustrates the weakest vortices in the range of a surface dimple to pulling in air bubbles referred to as VT2 and VT5 respectively. according to to the vortex classification after (Hecker, 1987) given in Figure 2.8. The bottom row shows the highest observed vortex intensities ranging from VT5 to VT6, whereas VT6 is characterised by a full air core.

For comparison the vortices appearing in series A2-2 are given at the same relative gate openings, between $a/H_0 = 0.2$ and 0.46 in Figure 4.44. The range of the smallest vortex intensity reaches up to VT6, with a full air core, depicted in Figure 4.44e. Comparatively VT5 was observed in Figure 4.43e even though the same relative gate opening was maintained. Concerning the strongest intensities full air cores, *i.e.* VT6 started to form at smaller relative gate openings of $a/H_0 = 0.33$, whereas this intensity was found at $a/H_0 = 0.4$ in measurement series A1-2.

Figure 4.43 represents the vortices of the measurement series, which was used to derive the parameter model in Section 4.2. On this basis the pressure distribution for the measurement
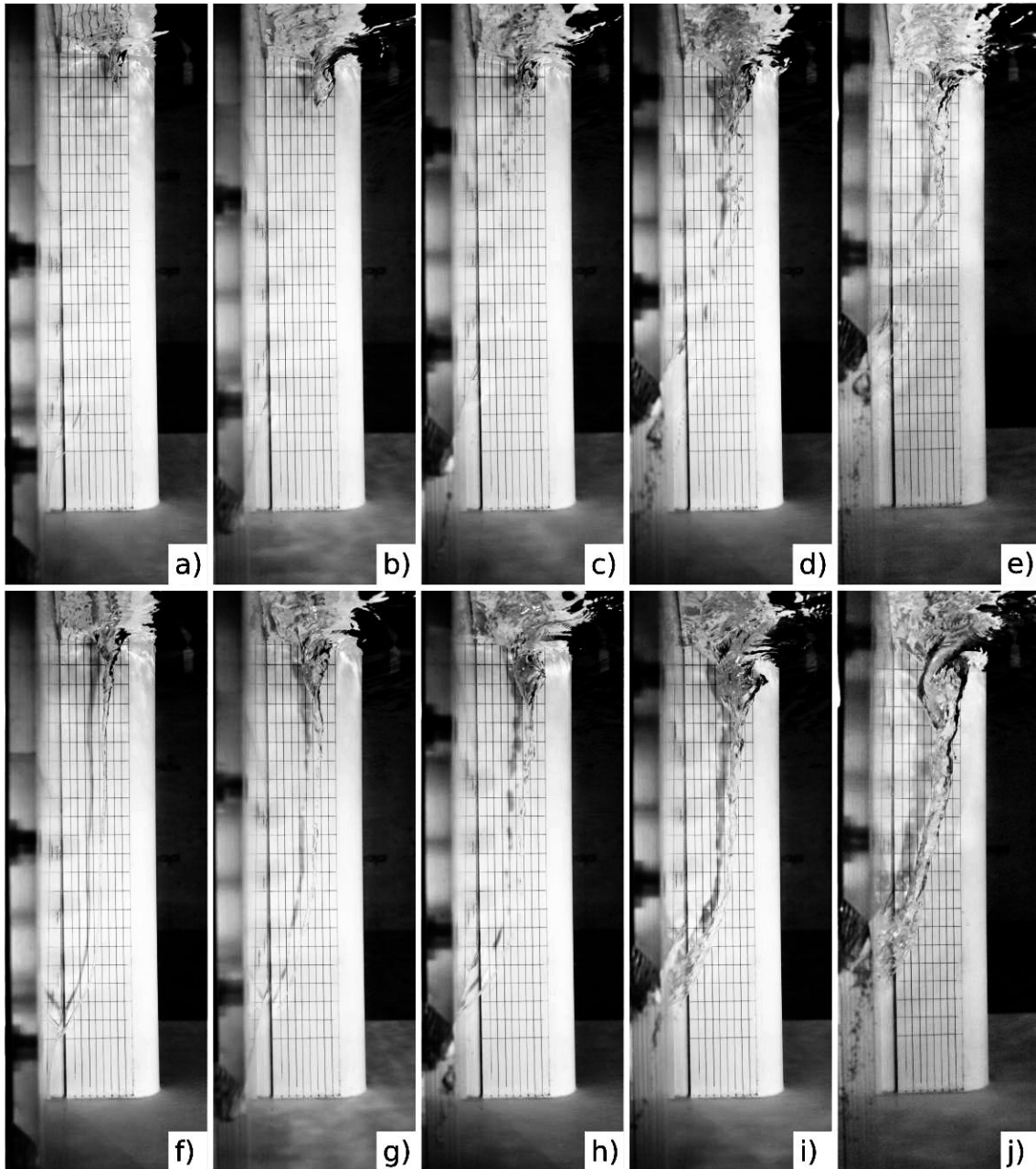
FIGURE 4.43: Vortex appearance at the first gate during test series A1-2: weakest vortices at a) a/H_0 =0.2, b) 0.27, c) 0.33, d) 0.4 and e) 0.46 and strongest vortices at f) a/H_0 =0.2, g) 0.27, h) 0.33, i) 0.4 and j) 0.46
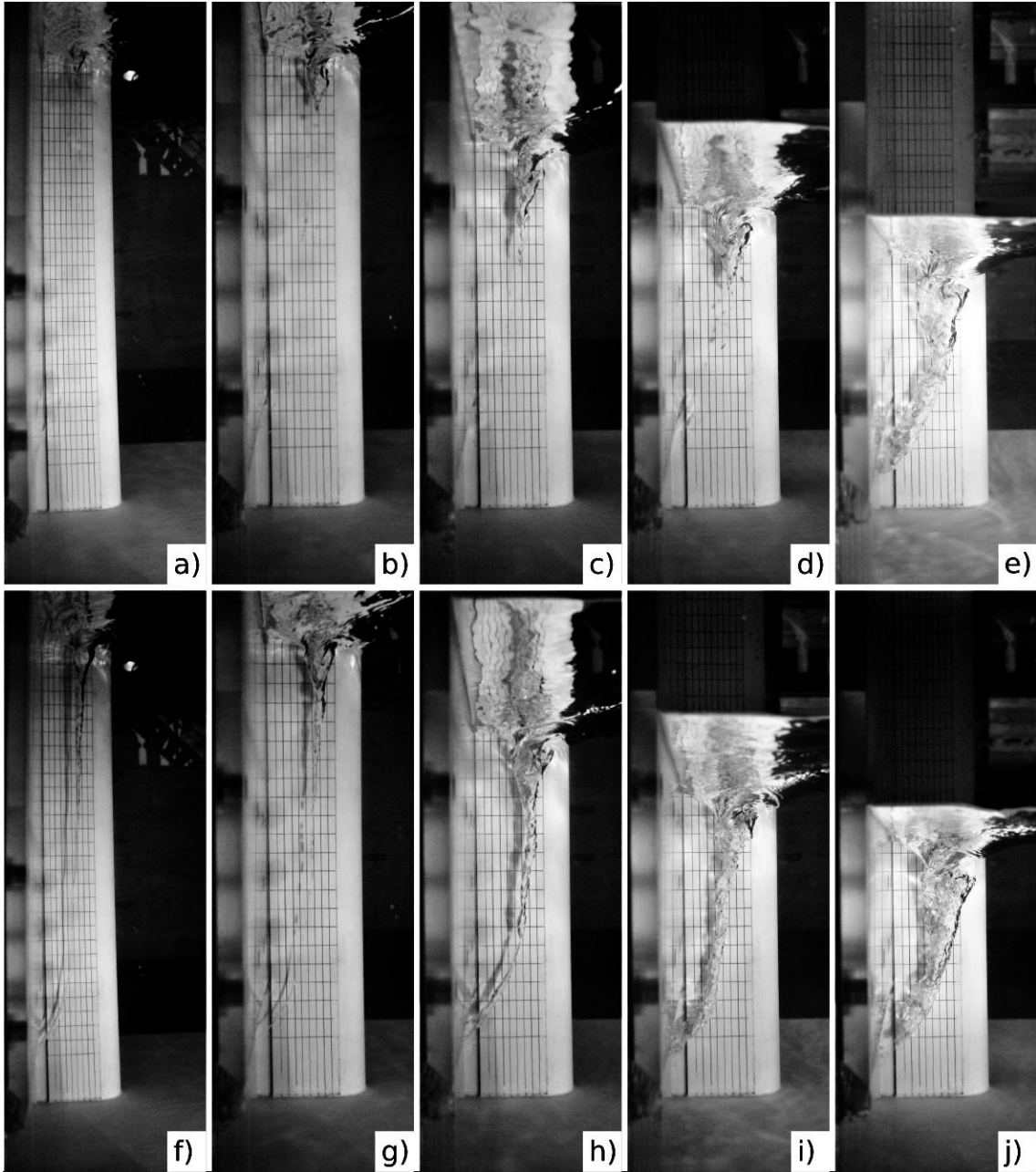
FIGURE 4.44: Vortex appearance at the first gate during test series A2-2: weakest vortices at a) a/H_0 =0.2, b) 0.27, c) 0.33, d) 0.4 and e) 0.46 and strongest vortices at f) a/H_0 =0.2, g) 0.27, h) 0.33, i) 0.4 and j) 0.46

series in the latter figure was predicted. Accurate results were obtained, except for the experiment with a relative gate opening of $a/H_0 = 0.46$, at the cross section closest to the vortex. The comparison of the vortex with the smallest intensity (Figure 4.43e) indicates an increased vortex strength compared to the experiment depicted in Figure 4.44e. The width of the vortex core in Figure 4.44j seems to be increased compared to Figure 4.43j. In Figure 4.44e and j the part of the gate dipping into the water is smaller, causing the enhanced vortex formation. This parameter is not represented by the relative gate opening a/H_0.

The vortex appearance in the smaller scale model could only be observed from the water surface. Particularly the disturbance of the water surface due to highly intense vortices make the comparison difficult. The trend of increasing vortex strength with increasing relative gate opening is recognisable in the illustrations in the Appendix Figure B.1 and B.2.

In comparison to the unstable vortices forming in the pre-tests (Chapter 3) the vortex generation was observed and documented (Section 3.2.2) to be rather stationary in the systematic investigations performed in the flume. Especially vortices of high intensity and therefore high impact on the gate pressure and fluctuations were persistent. With decreasing vortex intensity its stability, but also the influence on the pressure characteristics decreased, such that the visual analysis of the time series did not show distinct non-stationary development for most sample records.

Summary

Considering the relations defined in Figure 3.13, v_a represents the height of the submerged part of the gate $H_0 - a$. Hence according to Figure 4.41 the divergence of results is connected to low submergence of the gate. Enhanced vortex structure forming due to low values of $H_0 - a$ or v_a was identified. A drawdown of the water level due to the large extent of the vortex core was observed in the model tests, which can be realised from the pressure distribution at the gate leaf in the vicinity of the vortex at $a/H_0 = 0.46$ in Figure 4.21.

The vortex formation was found to influence the slope of the function relating the discharge coefficient and the relative gate opening. Hence an effect of the vortex intensity on losses can be assumed. A significant difference of the discharge coefficients derived from measurement series A1-2 and A2-2 at high relative gate openings was not identified, see Figure 4.7. Hence an increased loss due to enhanced vortex formation caused by low submergence is rather small, as limited to the location prone to the vortex.

From Figure 4.41 it could be supposed that small Reynolds numbers in combination with low submergence have an effect on local losses, induced by vortex formation. Due to high submergence of the gate, the vortex intensity is restricted and losses are limited. Hence the limit Reynolds number as for example used in Roth and Hager (1999) for flow under a gate with small vortices due to symmetric approach flow can be assumed to apply in the asymmetric case as well. Increasing the gate opening increases the relative gate opening, the vortex intensity and losses, but also the Reynolds number. Therefore the model test can still be considered to be free of scale effects. Contrarily the Reynolds number as defined in

Equation (2.49) decreases as the relative gate opening is increased by decreasing the energy head, as it is the case for measurement series A2-2, A2-1 and B2. The losses still increase with the vortex intensity and hence with increasing relative gate opening.

It is concluded that the scaling of the pressure distribution, as influenced by vortex formation using the relative gate opening a/H_0 as a dimensionless parameter is limited. Decreasing mean pressure and increasing pressure fluctuations have to be expected as the submergence of the gate drops below a limit value. In both model scales a limit value of about $H_0 - a = 0.2\,m$ as redetermined from v_a in Figure 4.41 would apply.

Chapter 5

Conclusions

The fundamentals of this thesis, concerning the hydraulics of underflow gates, vortex formation, hydrodynamic forces and flow induced vibrations were investigated on the basis of an intensive literature research. Further the fundamentals of physical modelling of hydraulic problems were introduced. For the investigation of the problem concerning the pressure characteristics at the upstream face of the sluice gate and the vortex formation due to asymmetric approach flow two hydraulic models of a weir structure with sluice gates were set up, where various flow conditions could have been considered. In order to achieve reliable results several measurement techniques were tested. Useful approaches for the identification of the origin of pressure fluctuations at the gate were found. By application of dimensional analysis a generalised description of the boundary conditions and pressure characteristics was established, which allows conclusions for prototypes on the basis of the model tests. The qualitative relation of the intensity and location of the vortex to the pressure conditions at the gate as well as to the discharge coefficient could be identified. Finally an example for application of the results is presented in Appendix C.

5.1   Model technique

The most reliable results concerning the pressure measurements were obtained by using piezoresistive pressure sensors with flush-mounted membrane. A small diameter was found to be advantageous. Effects of measurement rate, time and frequency were limited as well as effects due to the model setup. The influence of water surface fluctuations was reduced in the hydraulic model and finally eliminated by subtracting the spectral contributions of surface waves. Repeating two measurement series in a larger scale model, similar results as in the small scale model were obtained and hence scale effects could be precluded. Using the relative gate opening to define the boundary conditions for gate underflow was found to be troublesome in connection with the vortex, if the submerged part of the gate was low. The visual analysis of the vortex intensities support a difference in the flow process due to a small submerged part of the gate, which enhances the vortex formation. Discharge coefficients have been calculated and given depending on dimensionless parameters, where

the influence of the vortex formation causes differences from data in the literature, obtained in cross sectional models.

5.2   Pressure characteristics

Normalised charts concerning the pressure conditions which can be applied to the conditions of prototypes are provided. Thereby the mean pressure and amplitudes of the resultant force and the pressure distribution can be evaluated and disadvantageous flow conditions can be omitted or reduced. Based on the geometry of the gate the vortex formation and main frequencies contributing to the pressure fluctuations can be determined.

The most unbalanced pressure distribution as well as highest pressure fluctuations due to vortex formation was found if only a small part of the gate was submerged. Obviously the resultant force is rather small in this case but added stiffness and damping is reduced as compared to large submergence of the gate. The dynamic condition for low submergence can be estimated by a factor of safety, representing the pressure drop in the vicinity of the vortex and increased fluctuations.

5.3   Vortex formation upstream of a sluice gate

Concerning the vortex formation upstream of sluice gates the following effects were observed:

- Local flow eccentricity, *i.e.* of gate openings, has a stronger influence on the vortex formation than asymmetric location of the whole weir structure.
- The pressure drops at the area prone to the vortex.
- Enhanced vortex intensities enhance turbulent pressure fluctuations.
- The size of the vortex upstream of the gate determines the affected area and therefore the resultant asymmetry of the load distribution as well as resultant dynamic force due to fluctuations.
- Roughness or obstacles in the vicinity of the gate, such as gate slots, contribute to energy dissipation and thereby reduce pressure fluctuations.
- Limit Weber numbers concerning scale effects for free vortices were not relevant for the vortices induced due to the free shear layer separating from the pier.
- Limit Reynolds numbers for scale effects were dependent on the vortex intensity.
- The scaling problem connected to the vortex intensity was related to a combination of small Reynolds numbers and small submergence of the gate.

5.4   Further studies

Concerning the findings within this study several tasks were found to be worth analysing in order to find further insight:

- Methodical tests concerning the evaluation of spectral subtraction as a wave filter in order to evaluate the approach for other applications and optimise the required measurements.

- Scale family tests concerning the vortex formation if a small part of the gate is submerged.

- Extended measurement time could contribute to the insight of the dynamics of vortex breakdown.

- Evaluation of losses due to vortex formation by systematic model tests comparing the discharge coefficients at straight and asymmetric flow conditions.

- Investigation of the effect of gate inclination or radial gates on vortex formation.

- Evaluation of stress induced by asymmetric loading and dynamic impact based on structural models to determine the response.

- Investigation of possible fluid structure interaction.

- Numerical modelling of the problem, where the results from the physical model tests can serve for evaluation.

Bibliography

Anami, K., Ishii, N. (2003): Model tests for non-eccentric dynamic instability closely related to folsom dam tainter-gate failure, *Proceedings - ASME Pressure Vessles and Piping Conference, Cleveland Ohio.*

Anwar, H.O. (1964): Discharge coefficient for control gates, *Water Power*, 17(4):152–159.

Anwar, H.O. (1965): Flow in a free vortex, *Water power.*

Anwar, H.O., Weller, J.A., Amphlett, M.B. (1978): Similarity of free-vortex at horizontal intake, *Journal of Hydraulic Research*, 16(2):95–105.

Batchelor, G.K. (1967): *An introduction to fluid dynamics*, Cambridge University Press.

Belaud, G., Cassan, L., Baume, J.P. (2009): Calculation of contraction coefficient under sluice gates and application to discharge measurement, *ASCE Journal of Hydraulic Engineering*, 135:1086–1091.

Belaud, G., Litrico, X. (2008): Closed-form solution of the potential flow in a contracted flume, *Journal of Fluid Mechanics*, 599:299–307.

Bendat, J.S., Piersol, A.G. (2010): *Random Data - Analysis and Measurement Procedures*, John Wiley & Sons, Inc., fourth edition.

Billeter, P., Staubli, T. (2000): Flow-induced multiple-mode vibrations of gates with submerged discharge, *Journal of Fluids and Structures*, 14:323–338.

Bollrich, G. (1996): *Technische Hydromechanik Band 1 - Grundlagen*, Verlag für Bauwesen Gmbh, Berlin, fourth edition.

Cassan, L., Belaud, G. (2012): Experimental ans numerical investigation of flow under sluice gates, *Journal*, 138.

Chang, E., Prosser, M.J. (1987): *Swirling flow problems at intakes - IAHR Hydraulic Structures Design Manual 8*, chapter Basic results of theoretical and experimental work, pages 13–38, A.A. Balkema, Rotterdam.

Clough, R.W., Penzien, J. (1993): *Dynamics of structures, Second edition*, McGraw-Hill Inernational Editions.

Cooley, J.W., Tukey, J.W. (1965): An algorithm for machine calculation of complex Fourier series, *Mathematics of Computation*, 19(90):297–301.

Dagget, L.L., Keulegan, G.H. (1974): Similitude in free-surface vortex formations, *ASCE Journal of the Hydraulics Division*, 100(11):1565–1581.

Dean, R.G., Dalrymple, R.A. (1991): *Water wave mechanics for eengineer and scientists*, World Scientific Publishing Co. Pte. Ltd.

Defina, A., Susin, F.M. (2003): Hysteretic behavior of the flow under a vertical sluice gate, *Physics of Fluids*, 15(9):2541–2548.

Deutsches Institut für Normung (2012): *Stahlwasserbauten - Teil 1: Berechnungsgrundlagen*, Deutsches Institut für Normung.

Emmerling, R. (1973): Die momentane Struktur des Wanddruckes einer turbulenten Grenzschichtströmung, *Mitteilungen Max-Planck-Institut für Strömungsforschung. Göttingen, Germany*, 56.

Erdbrink, C.D. (2012): *Physical model tests on vertical flow-induced vibrations of an underflow gate*, Deltares.

Erdbrink, C.D., Krzhizhanovskaya, V.V., Sloot, P.M. (2014a): Free-surface flow simulations for ddischarge-based operation of hydraulic structure gates, *Journal of Hydroinformatics*.

Erdbrink, C.D., Krzhizhanovskaya, V.V., Sloot, P.M. (2014b): Reducing cross-flow vibrations of underflow gates: Experiments and numerical studies, *Journal of Fluids and Structures*, 50:25–48.

Fenton, J.D. (2015): *Coastal and Ocean Engineering, Lecture notes*, Vienna University of Technology, URL `http://johndfenton.com/Lectures/Coastal-and-Ocean-Engineering/Coastal-and-Ocean.pdf`.

Finnie, J.I., Jeppson, R.W. (1991): Solving turbulent flows using finite elements, *ASCE Journal of Hydraulic Engineering*, 117(11):1513–1530.

Guo, J. (2002): Simple and explicit solution of wave dispersion equation, *Coastal Engineering*, 45:71–74.

Habibzadeh, A., Vatankhah, A.R., Rajaratnam, N. (2011): Role of energy loss on discharge characteristics of sluice gates, *ASCE Journal of Hydraulic Engineering*, 137(9):1079–1084.

Haller, G. (2005): An objective definition of a vortex, *Journal of Fluid Mechanics*.

Hardwick, J.D. (1974): Flow induced vibration of vertical-lift gate, *Journal of the Hydraulics devision*, 100(5):631–644.

Hecker, G.E. (1987): *Swirling flow problems at intakes - IAHR Hydraulic Structures Design Manual 8*, chapter Fundamentals of vortex intake flow, pages 13–38, A.A. Balkema, Rotterdam.

Husain, D. (1999): Dynamic study of simultaneous underflow-overflow past low head sluice gates, *Journal of King Abdulaziz University*, 11(1):51–67.

Ishii, N., Anami, K., Knisely, C.W. (2017): *Dynamic stability of hydraulic gates and engineering for flood prevention*, IGI Global.

Ishii, N., Knisley, C.W. (1990): Shear layer behaviour under a streamwise vibrating gate and its significance to vibration, *JSME International Journal.*

Jain, A.K., Raju, K.G.R., J.Garde, R. (1978): Vortex formation at vertical pipe intakes, *ASCE Journal of the Hydraulics Division*, 104(10):1429–1445.

Jongeling, T.H. (1988): Flow induced self-excited in-flow vibrations of gate plates, *Journal of Fluid and Structures*, 2:541–566.

Kampel, I. (2014): Durch Wirbelbildung beeinflusste, hydrodynamische Belastung auf Freispiegelverschlüsse, *Mitteilungen des Leichtweiß-Instituts für Wasserbau*, 161.

Kampel, I., Prenner, R., Krouzecky, N. (2017): Pressure fluctuations on underflow gates of weirs due to upstream vortex generation, *Materials Today: Proceedings*, 4(5).

Keir, G., Unny, T.E., M.Hill, H. (1969): Pressure fluctuations on a submerged sluice gate, *ASCE Journal of the Hydraulics Division*, 95(HY6).

Keller AG (accessed: 06.09.2015a): Product Shot Series 35 X, URL `http://www.keller-druck.com/picts/hires/25_35.jpg`.

Keller AG (accessed: 06.09.2015b): Product Shot Series 46 X, URL `http://www.keller-druck.com/picts/hires/46x.jpg`.

Khader, M.H., Elango, K. (1974): Turbulent pressure field beneath a hydraulic jump, *IAHR Journal of Hydraulic Research*, 12(4).

Kim, D.G. (2007): Numerical analysis of free flow past a sluice gate, *KSCE Journal of Civil Engineering*, 11(2):127–132.

Knapp, F.H. (1960): *Ausfluss, Überfall und Durchfluss im Wasserbau - Eine angewandte Hydraulik auf physikalischer Grundlage*, Verlag G. Braun, Karlsruhe.

Knauss, J. (1987): *Swirling flow problems at intakes - IAHR Hydraulic Structures Design Manual 1*, chapter Introduction, pages 1–13, A.A. Balkema, Rotterdam.

Kolkmann, P.A. (1976): *Flow-induced gate vibrations - Prevention of self-excitation, computation of a dynamic gate behaviour and the use of models*, Ph.D. thesis, Delft University of Technology.

Kolkmann, P.A. (1984): *Developments in hydraulic engineering*, chapter "Gate vibrations", pages 55–112, Elsevier, London and New York.

Kolkmann, P.A. (1994): *Discharge Characteristics - IAHR Hydraulic Structures Design Manual 8*, chapter Discharge relationships and component losses for hydraulic structures, pages 55–151, CRC Press.

Köpf, A. (2017): Einfluss von Wirbelbildung auf die Abflusskapazität unterströmter Schütze, Projektarbeit (Interdisziplinären Seminararbeit), Institut für Wasserbau und Ingenieurhydrologie, TU Wien.

Kostecky, S.W. (2011): Numerical analysis of hydrodynamic forces due to flow instability at lift gate, *Archives of Civil and Mechanical Engineering*, 11(4):943–961.

Lesleighter, E.J. (1971): Pressure fluctuations in large energy dissipation structures, in *Fourth Australian Conference on Hydraulics and Fluid Mechanics*.

Levi, E. (1972): Experiments on unstable vortices, *Journal of the engineering mechanics division*, EM 3:539–559.

Lewin, J. (2001): *Hydraulic Gate and Valves in Free Surface Flow and Submerged Outlets*, MPG Books, Bodmin, Cornwall, Great Britain, second edition.

Lugt, H.J. (1983): *Vortex Flow in Nature and Technology*, John Wiley & Sons, Inc.

Miller, D. (editor) (1994): *Discharge Characteristics - IAHR Hydraulic Structures Design Manual 8*, CRC Press.

Möller, G., Dettert, M., Boes, R. (2012): Air entrainment due to vortices - state-of-the-art, *Proc. 2nd IAHR Europe Congress 2012*.

Montes, J.S. (1997): Imeasurement flow and real fluid effects under planar sluice gates, *ASCE Journal of Hydraulic Engineering*, 123:219–232.

Montes, J.S. (1999): Closure to 'Irrotational flow and real fluid effects under planar sluice gates' by J.S. Montes, *ASCE Journal of Hydraulic Engineering*, 125(2):208–213.

Nago, H. (1978): Influence of gate-shapes on discharge ccoefficient of underflow gates, *Transactions of the Japanese Society of Civil Engineers*, 10:116–119.

Nago, H. (1984): Scale effects in free efflux from an underflow gate, in H. Kobus (editor), *Symposium on scale effects in modelling hydraulic structures*, Institut für Wasserbau, Universität Stuttgart, Germany.

Narayanan, R., Reynolds, A.J. (1972): Reattaching flow downstream of leaf gate, *ASCE Journal of Hydraulics Division*, 98(5).

Naudascher, E. (1962): Vibration of gates during over and underflow, *Transactions of the American Society of CIvil Engineering*, 127.

Naudascher, E. (1984): Scale effects in gate model tests, in H. Kobus (editor), *Symposium on scale effects in modelling hydraulic structures*, Institut für Wasserbau, Universität Stuttgart, Germany.

Naudascher, E. (1987): Flow-induced streamwise vibrations of structures, *Journal of Fluids and Structures*, 1:265–298.

Naudascher, E. (1991): *Hydrodynamic Forces - IAHR Hydraulic Structures Design Manual 3*, A.A. Balkema, Rotterdam.

Naudascher, E., Rockwell, D. (1994): *Flow-induced Vibrations - IAHR Hydraulic Structures Design Manual 7*, A.A. Balkema, Rotterdam.

Noutsopoulos, G.K., Fanariotis, S. (1978): Discussion to 'Free flow immeduately below sluice gates' by N. Rajaratnam, *ASCE Journal of the Hydraulics Division*, 104(3).

Rajaratnam, N. (1977): Free flow immediately below sluice gates, *ASCE Journal of the Hydraulics Division*, 103(4):345–351.

Rajaratnam, N., Humphries, J. (1982): Free flow upstream of vertical sluice gates, *Journal of Hydraulic Research*, 20(5):427–437.

Rajaratnam, N., Subramanya, K. (1967): Flow equation for the sluice gate, *Journal of Irrigation and Drainage Engineering*, 93(3):167–186.

Ranga Raju, K.G., Garde, R.J. (1987): *Swirling flow problems at Intakes - IAHR Hydraulic Structures Design Manual 8*, chapter Modelling of vortices and swirling flows, pages 77–90, A.A. Balkema, Rotterdam.

Rogala, R., Winter, J. (1985): Hydrodynamic Pressure Acting Upon Hinged-Arc Gate, *ASCE Journal of Hydraulic Engineering*, 11:584–599.

Roth, A., Hager, W.H. (1999): Underflow of Standard Sluice Gate, *Experiments in Fluids*, 27:339–350, URL `http://link.springer.com/article/10.1007%2Fs003480050358`.

Shuy, E.B., Chua, H.C. (1999): Fluid dynamic feed-back in shear layer oscillation below a submerged sluice gate, *Journal of Hydraulic Research*, 37(1):107–120.

Smith, C.D. (1977): Discussion to 'Free flow immeduately below sluice gates' by N. Rajaratnam, *ASCE Journal of the Hydraulics Division*, 103(11).

Speerli, J., Hager, W.H. (1999): Discussion to 'Irrotational flow and real fluid effects under planar sluice gates' by J.S. Montes, *ASCE Journal of Hydraulic Engineering*, 125(2):208–213.

Suzuki, Y., Sakurai, A., N.Nakumoto (1973): A design of a chute spillway jointly serving as the roof slab of a hydropower station, *Proceedings - 11th International Congress on Large Dams, Madrid*.

Thang, N.D. (1990): Gate vibrations due to unstable flow separation, *Journal of Hydraulic Engineering*, 116(3):342–361.

Thang, N.D., Naudascher, E. (1983): Approach-flow effects on downpull of gates, *Journal of Haydraulic Engineering*, 109(11):1521–1539.

Thang, N.D., Naudascher, E. (1986a): Self-excited vibration of vertical-lift gates, *Journal of Hydraulic research*, 24(5):391–404.

Thang, N.D., Naudascher, E. (1986b): Vortex excited vibrations of underflow gates, *Journal of Hydraulic Research*, 24(2):133–404.

Todd, R.V. (1999): Spillway tainter gate failure at Folsom Dam, California, *Waterpower Conference*.

Toso, J.W., Bowers, C.E. (1988): Extreme pressures in hydraulic-jump stilling basins, *ASCE Journal of Hydraulic Engineering*, 114(8):829.

U.S. Army Corps of Engineers (1977): *Hydraulic Design Criteria - Volume 2*, Waterways Experiment Station, Vicksburg, MS.

U.S. Army Corps of Engineers (1997): *Engineer Manual 110-2-2701 - Vertical Lift Gates*, U.S. Army Corps of Engineers, Washington DC.

U.S. Army Corps of Engineers (2000): *Engineer Manual 1110-2-2702 - Design of Spillway Tainter Gates*, U.S. Army Corps of Engineers, Washington DC.

USBR (1987): *Design of Small Dams - A Water Resources Technical Publication*, United States Department of the Interior - Bureau of Reclamation.

Vanden-Broeck, J. (1997): Numerical calculationgate the free-surface flow under a sluice gate, *Journal of Fluid Mechanics*, 330:339–347.

Vaseghi, S.V. (2008): *Advanced Digital Signal Processing and Noise Reduction*, John Wiley & Sons, Ltd., fourth edition.

Webby, M.G. (1999): Discussion to 'Irrotational flow and real fluid effects under planar sluice gates' by J.S. Montes, *ASCE Journal of Hydraulic Engineering*, 125(2):208–213.

Westergaard, H.M. (1933): Water pressure on dams during earthquakes, *Transactions of the American Society of Civil Engineers*, pages 418–472.

List of Figures

List of Tables

Acknowledgements

I hereby highly appreciate the support and patience of all people committed to my work.

For the scientific exchange, sharing their expertise and their time spent on discussion and comments:

<div align="center">

Ao.Univ.Prof. Dipl.-Ing. Dr.techn. Reinhard Prenner
Prof. Sigurdur M. Gardarsson Ph.D.
Prof. Dr.Eng. Dimitar Kisliakov
Prof. John D. Fenton Ph.D.
Dipl.-Ing. Dr.techn. Freddy Flórez

</div>

For the support during my time at TU Vienna and for being the heart of the Institute of Hydraulic Engineering and Water Resources Management:

<div align="center">

Ao.Univ.Prof. Dipl.-Ing. Dr.techn. Norbert Krouzecky
Kornelia Selig

</div>

For their professional work and great help at the hydraulic lab:

<div align="center">

Dipl.-Ing. Dr.techn. Boris Huber
Andreas Leopoldseder
Andreas Kothmayer
Harald Kornherr

</div>

Thanks to all my dear friends and family for their indispensable encouragement.

Appendix A

Statistical data

A.1   Stationarity of time series

Herein the results of the run tests performed to evaluate the stationarity of the time series before and after filtering using spectral subtraction as derived in Section 3.3.1 and discussed in Section 4.1.8. The data p-values of the time series, falling below the level of significance of 5 % are plotted for the original data in comparison to the p-values resulting from the run tests performed on the filtered time series. The reduced number of time series with p-values below 0.05 are an indicator for the success of the filtering.
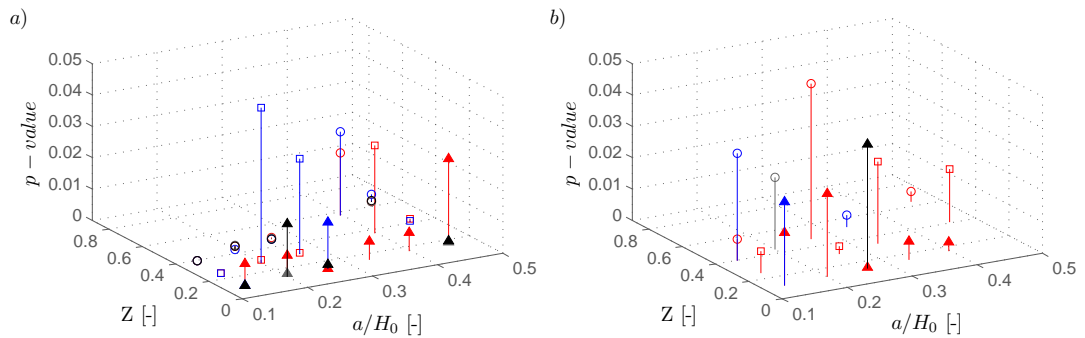
FIGURE A.1: Experiments in series A1-2 with p-values below 5 % level of significance: a) before filtering, b) after filtering
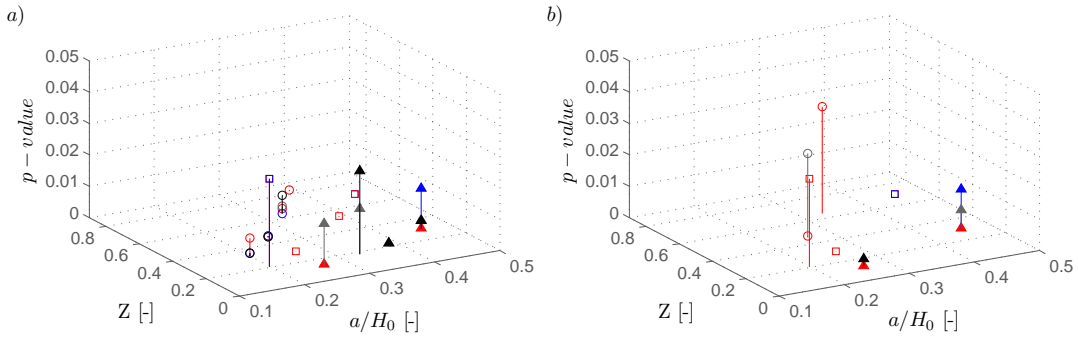
FIGURE A.2: Experiments in series A2-2 with p-values below 5 % level of significance: a) before filtering, b) after filtering
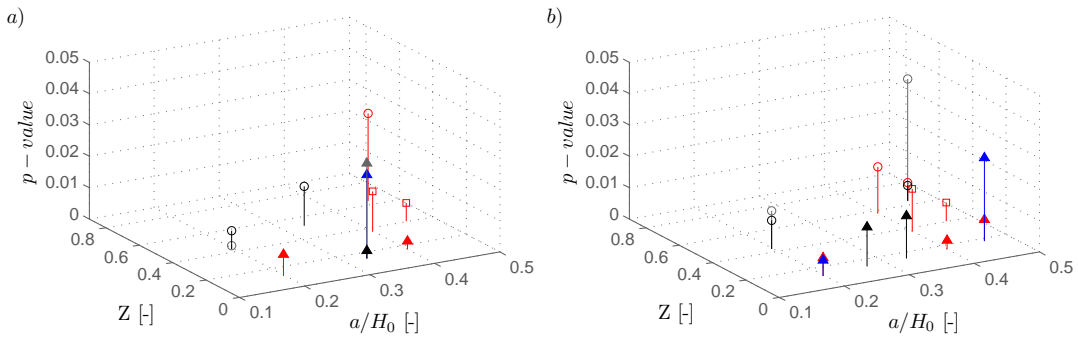
FIGURE A.3: Experiments in series A1-1 with p-values below 5 % level of significance: a) before filtering, b) after filtering
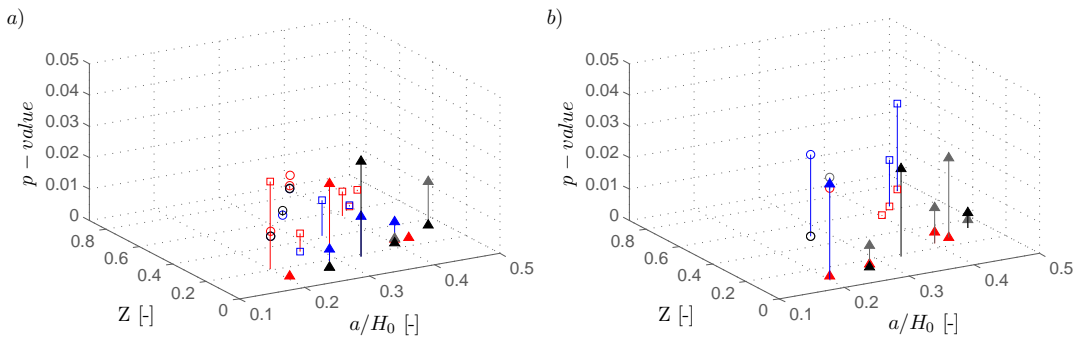
FIGURE A.4: Experiments in series A2-1 with p-values below 5 % level of significance: a) before filtering, b) after filtering
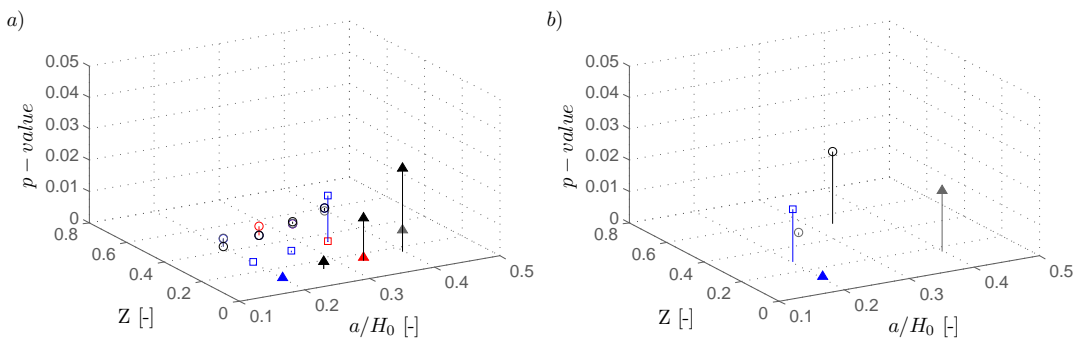
FIGURE A.5: Experiments in series B1 with p-values below 5 % level of significance: a) before filtering, b) after filtering
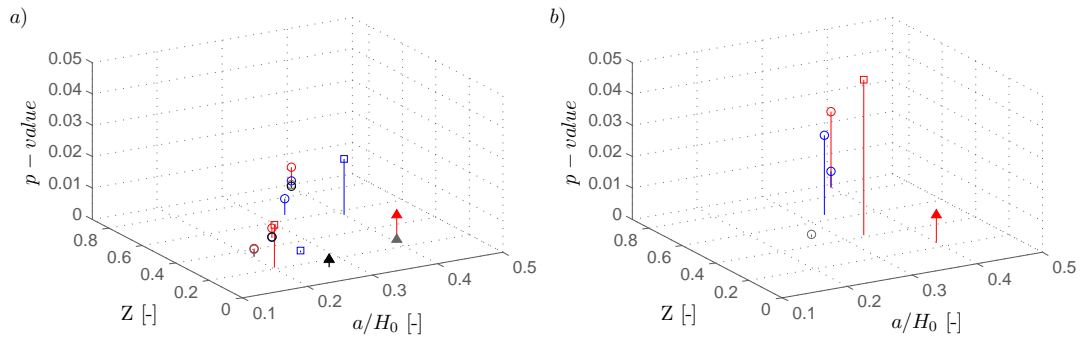
FIGURE A.6: Experiments in series B2 with p-values below 5 % level of significance: a) before filtering, b) after filtering
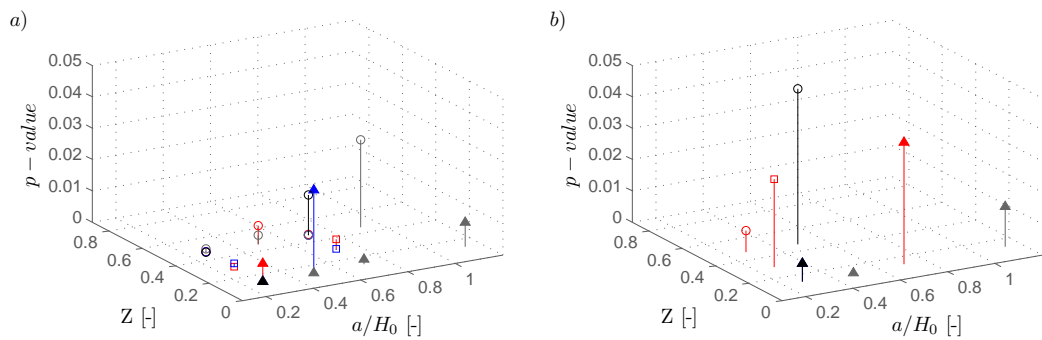
FIGURE A.7: Experiments in series A3 with p-values below 5 % level of significance: a) before filtering, b) after filtering
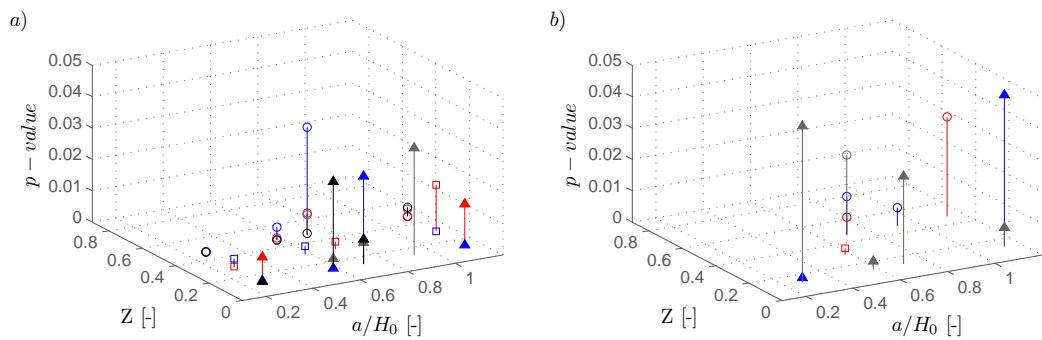
FIGURE A.8: Experiments in series B3 with p-values below 5 % level of significance: a) before filtering, b) after filtering

A.2   Pressure maxima

The measured pressure maxima in the second and top row of the gate are illustrated, which are discussed in Section 4.3.1. Further the error plot evaluating the validity of the amplification factors as introduced in Section 4.3.3 derived on the basis of the pressure maxima in measurement series A1-2 and B1 are illustrated.
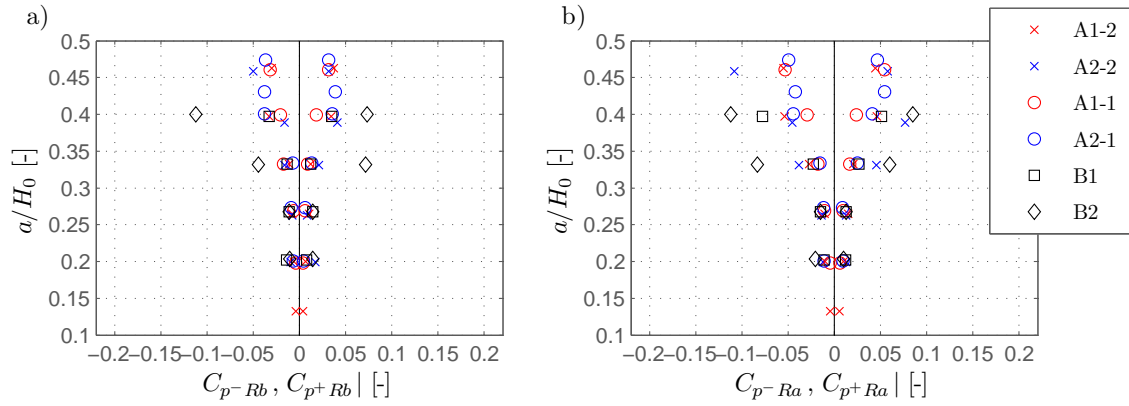
FIGURE A.9: Pressure maxima depending on a/H_0 at the second measurement row
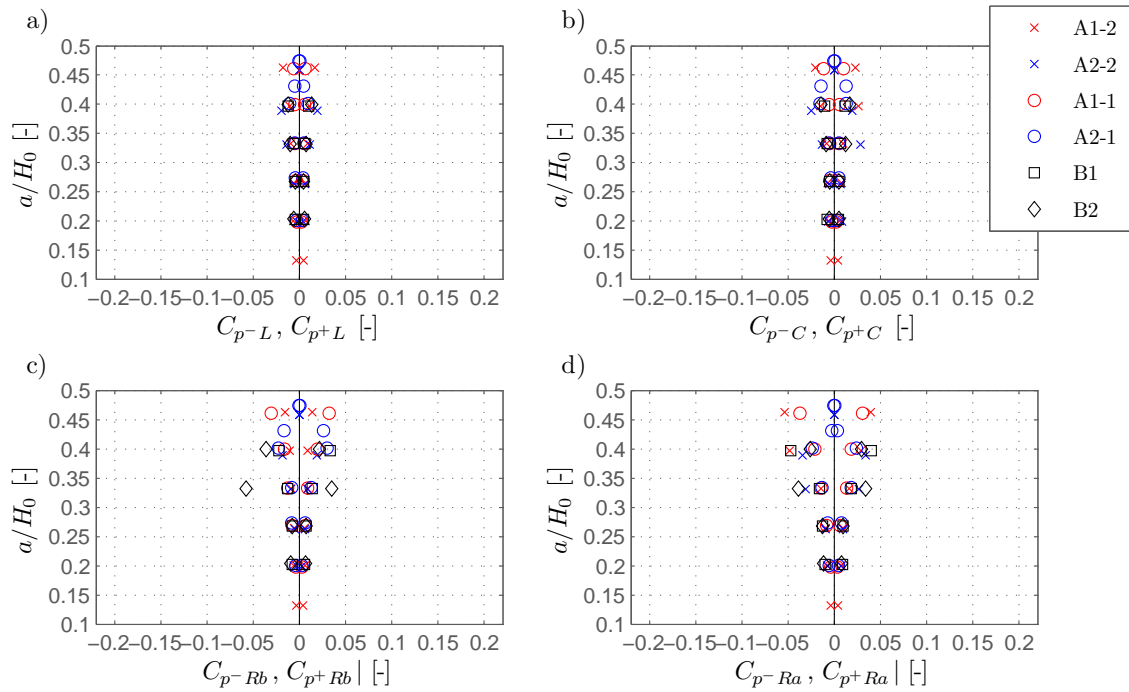
FIGURE A.10: Pressure maxima depending on a/H_0 at the top measurement row
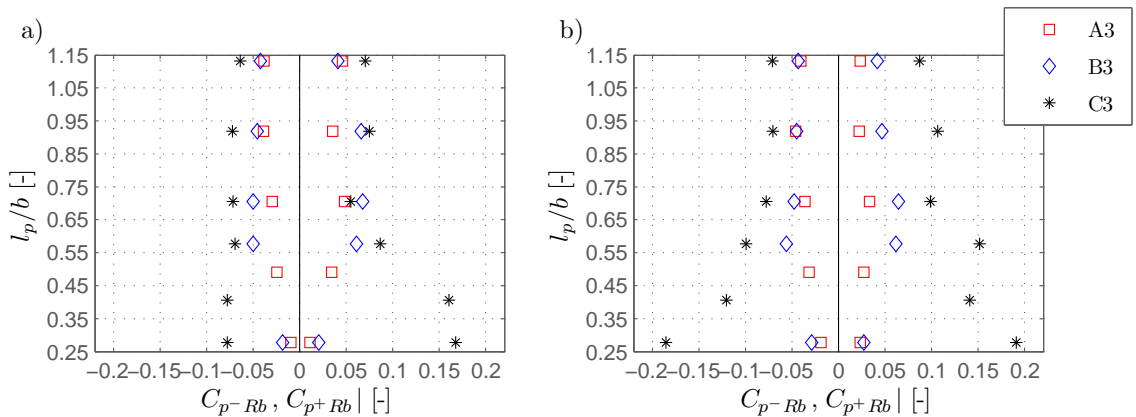
FIGURE A.11: Pressure maxima depending on l_p/b at the second measurement row
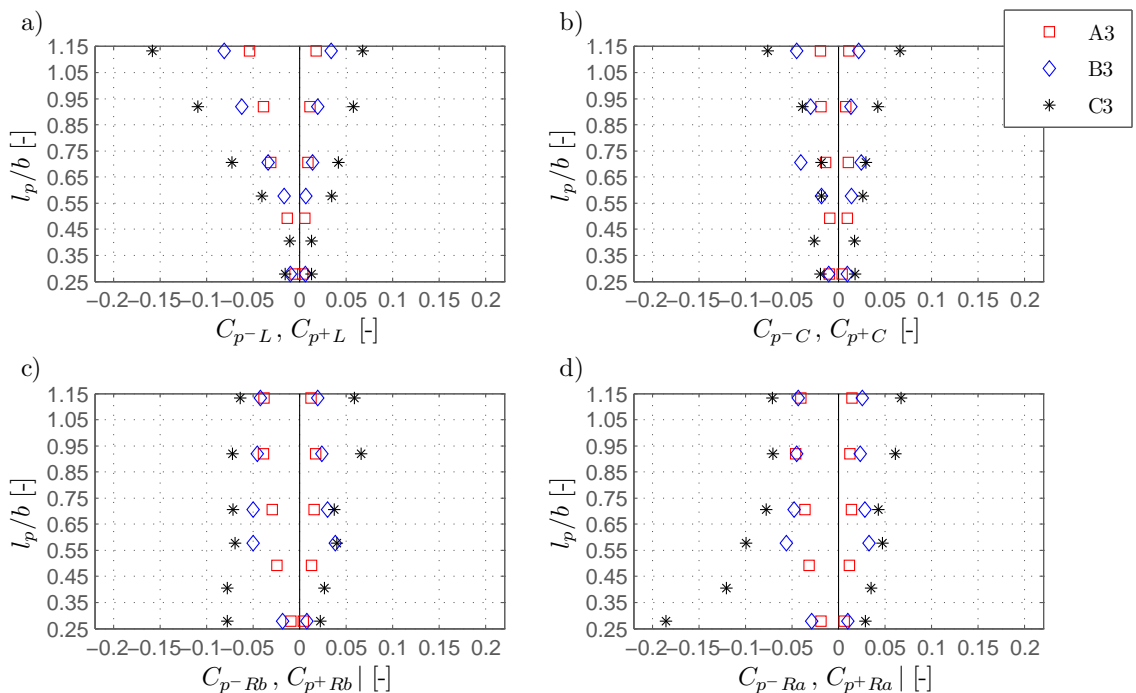
FIGURE A.12: Pressure maxima depending on l_p/b at the top measurement row
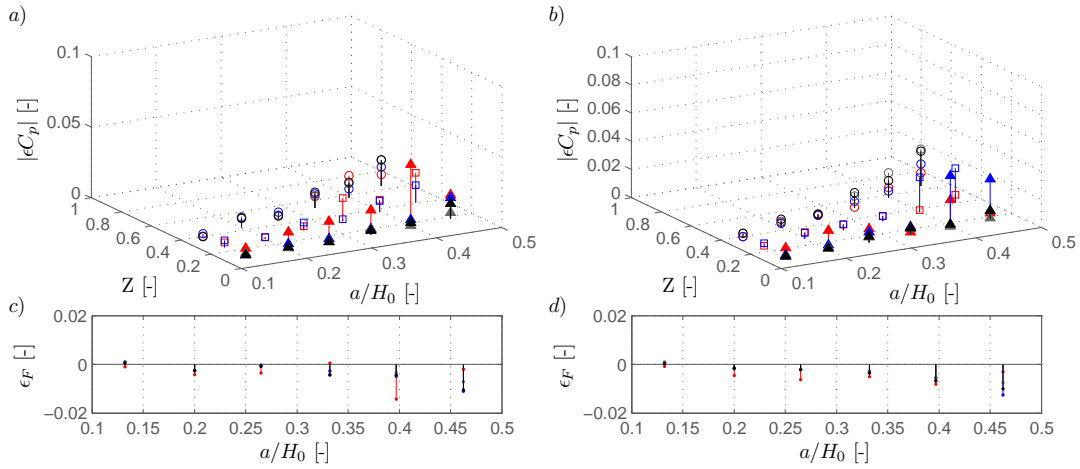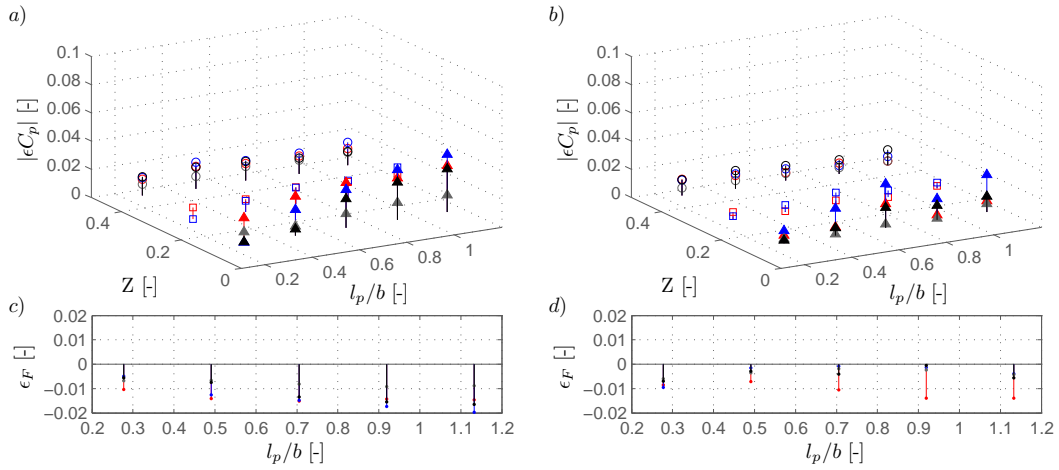
FIGURE A.13: Deviation of prediction from A1-2 to measured extrema in series A1-2: a) pressure minima, b) pressure maxima, c) min. force d) max. force
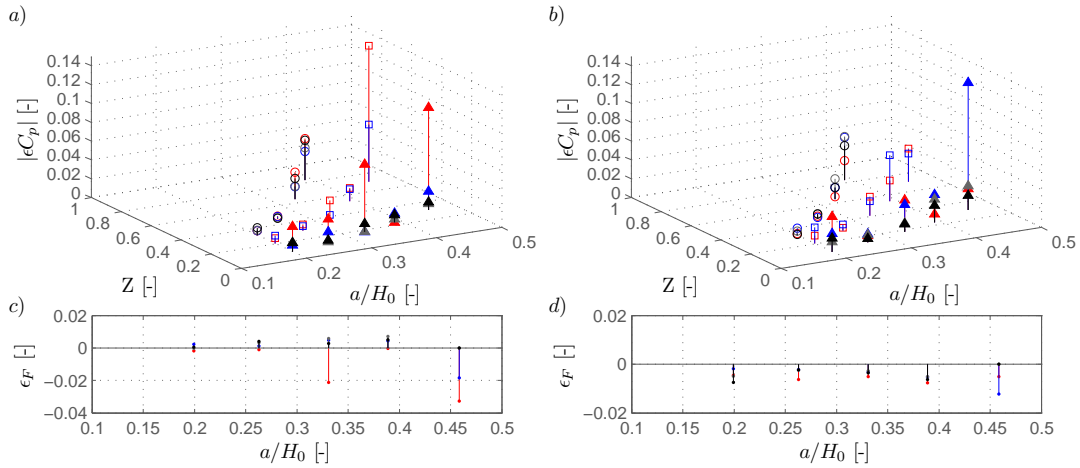

FIGURE A.14: Deviation of prediction from A1-2 to measured extrema in series A2-2: a) pressure minima, b) pressure maxima, c) min. force d) max. force
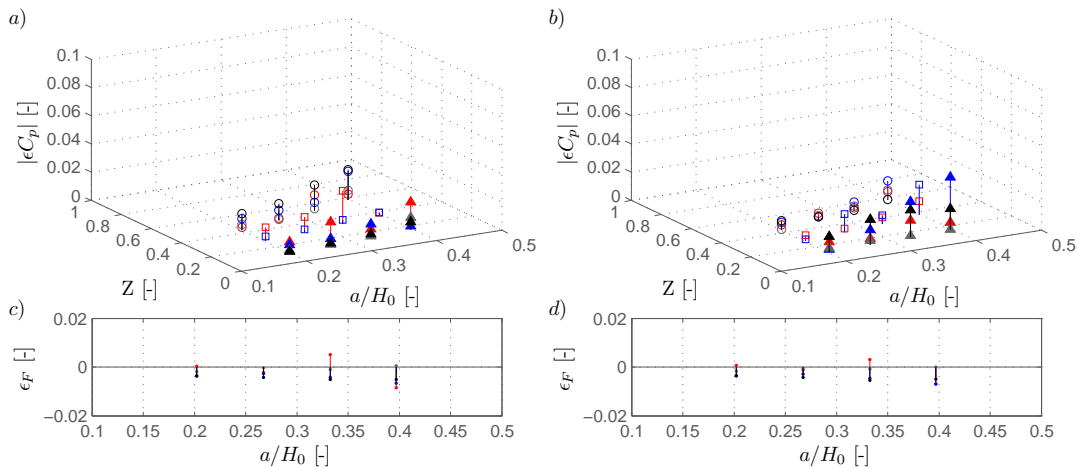
FIGURE A.15: Deviation of prediction from B1 to measured extrema in series B1: a) pressure minima, b) pressure maxima, c) min. force d) max. force
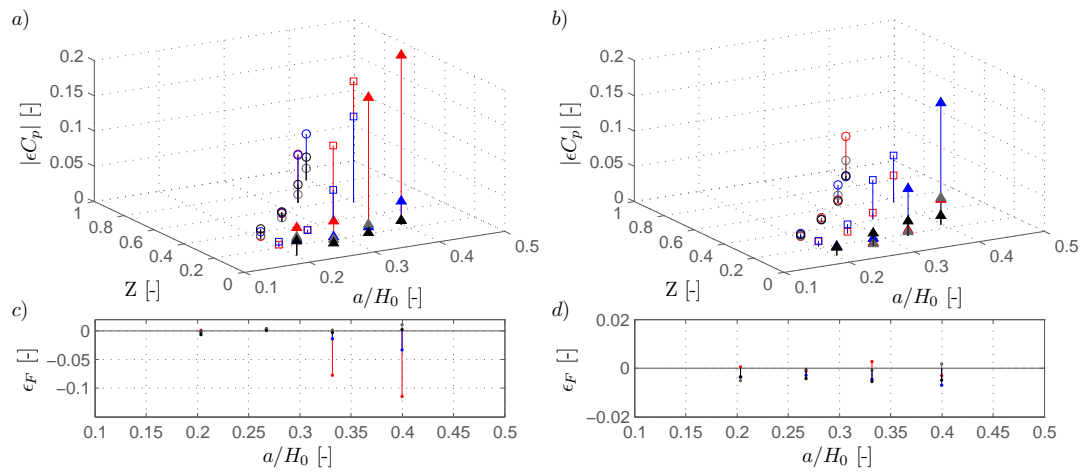
FIGURE A.16: Deviation of prediction from B1 to measured extrema in series B2: a) pressure minima, b) pressure maxima, c) min. force d) max. force

A.3 Errors of pressure maxima based on quantiles

The subsequent error plot illustrate the deviations of the pressure maxima predicted from 0.01 and 0.99 quantiles, as derived in Section 4.3.3 of measurement series A1-2, B1, A3 and B3 to the measured maxima.
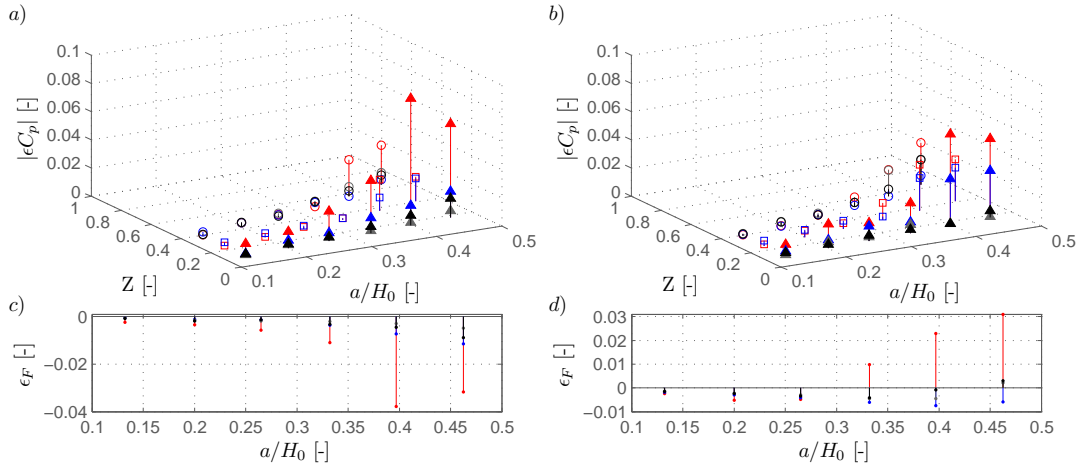
FIGURE A.17: Deviation predicted 0.01 and 0.99 quantile to measured extrema in series A1-2: a) pressure minima, b) pressure maxima, c) min. force d) max. force
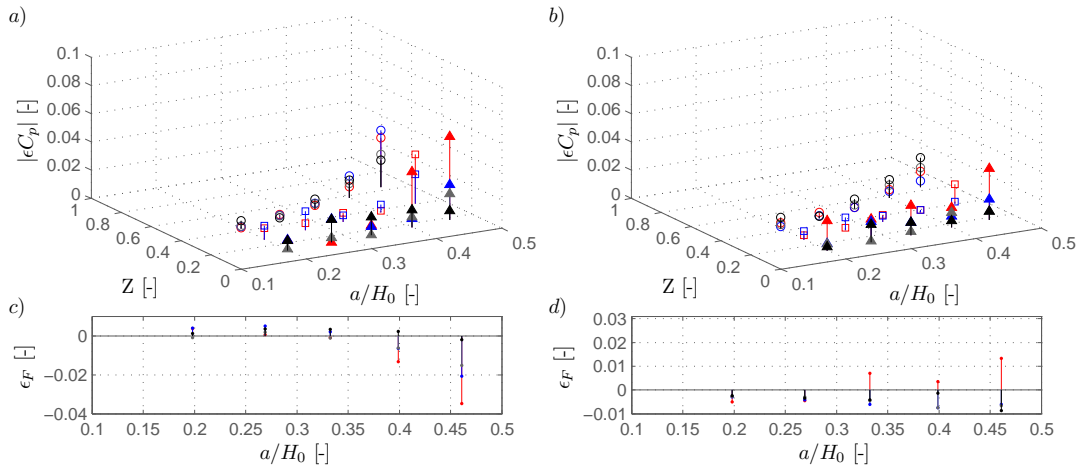
FIGURE A.18: Deviation predicted 0.01 and 0.99 quantile to measured extrema in series A1-1: a) pressure minima, b) pressure maxima, c) min. force d) max. force
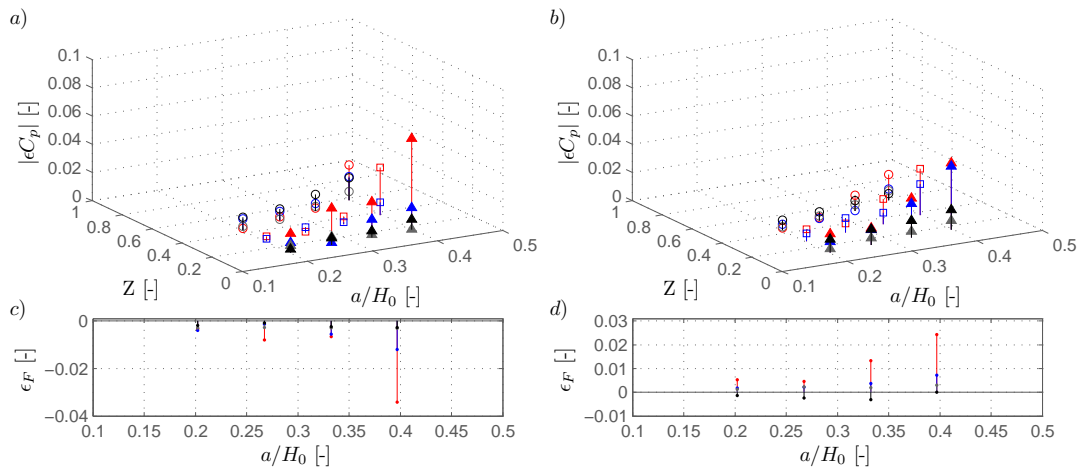
FIGURE A.19: Deviation predicted 0.01 and 0.99 quantile to measured extrema in series B1: a) pressure minima, b) pressure maxima, c) min. force d) max. force
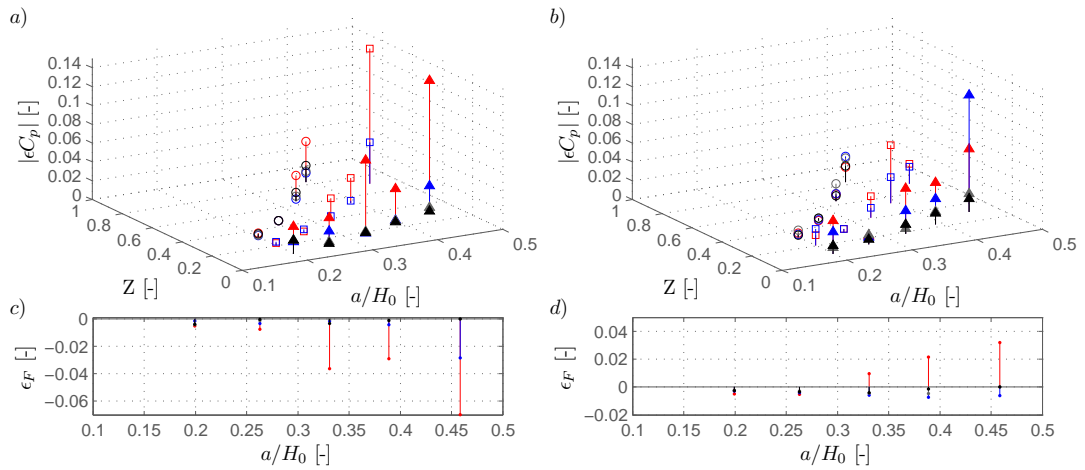
FIGURE A.20: Deviation predicted 0.01 and 0.99 quantile to measured extrema in series A2-2: a) pressure minima, b) pressure maxima, c) min. force d) max. force
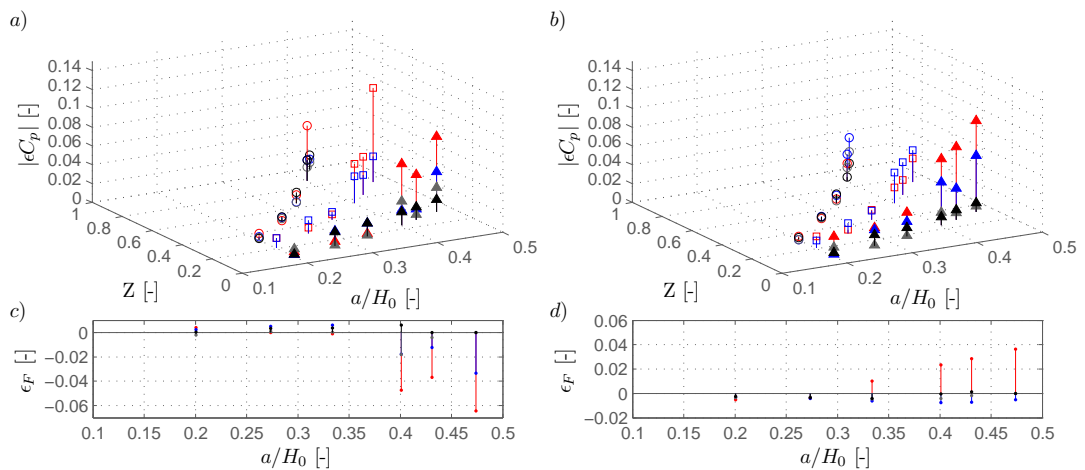
FIGURE A.21: Deviation predicted 0.01 and 0.99 quantile to measured extrema in series A2-1: a) pressure minima, b) pressure maxima, c) min. force d) max. force
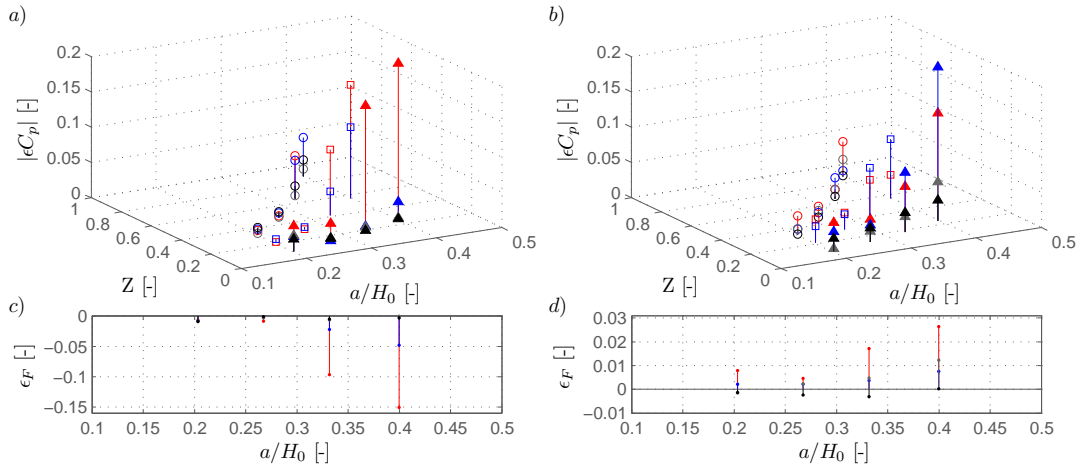
FIGURE A.22: Deviation predicted 0.01 and 0.99 quantile to measured extrema in series B2: a) pressure minima, b) pressure maxima, c) min. force d) max. force

FIGURE A.23: Deviation predicted 0.01 and 0.99 quantile to measured extrema in series A3: a) pressure minima, b) pressure maxima, c) min. force d) max. force
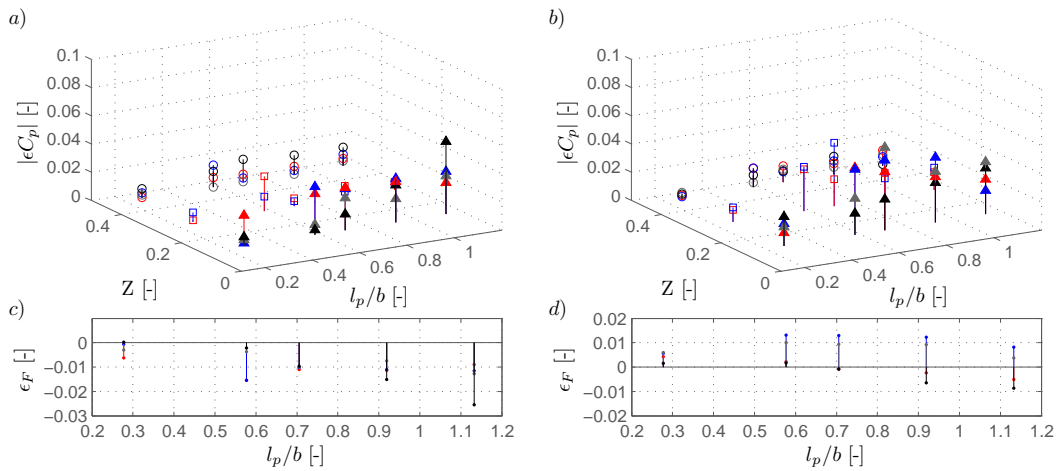
FIGURE A.24: Deviation predicted 0.01 and 0.99 quantile to measured extrema in series B3: a) pressure minima, b) pressure maxima, c) min. force d) max. force

A.4   Spatial correlation

The subsequent figures illustrate the correlation of the data point at the lowest measurement row to each other measurement point at the gate for all measurement series, as discussed in Section 4.3.4. A correlation of one implies the maximum correlation, as achieved if the auto correlation without time shift is calculated. Decreasing coefficients show the decreasing mutuality.
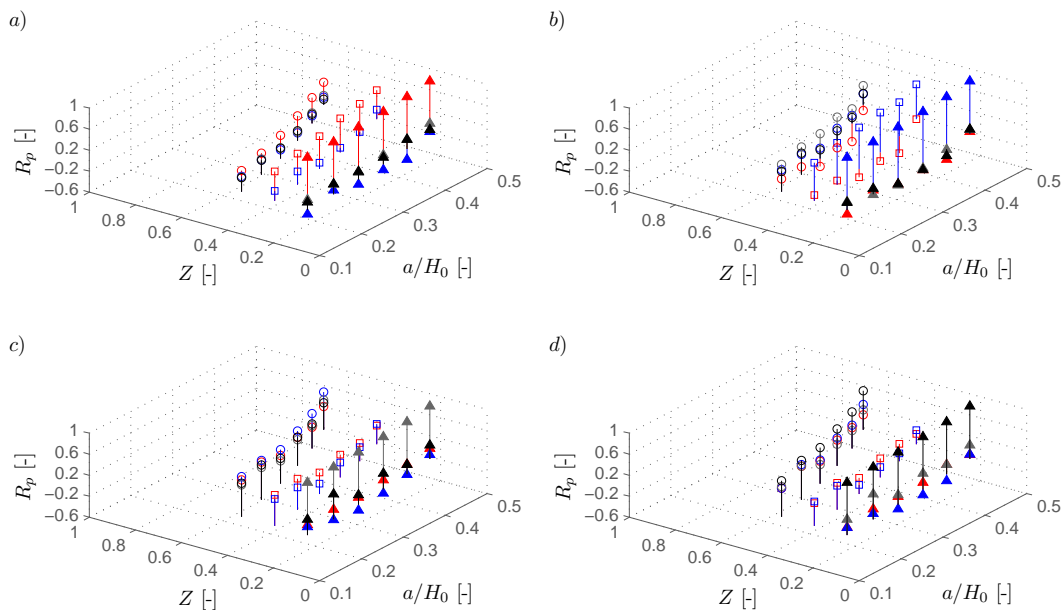
FIGURE A.25: Correlation coefficients for measurement series A1-2: Correlation of locations a) Ra1, b) Rb1, c) C1 and d) L1 to sample records at all available locations
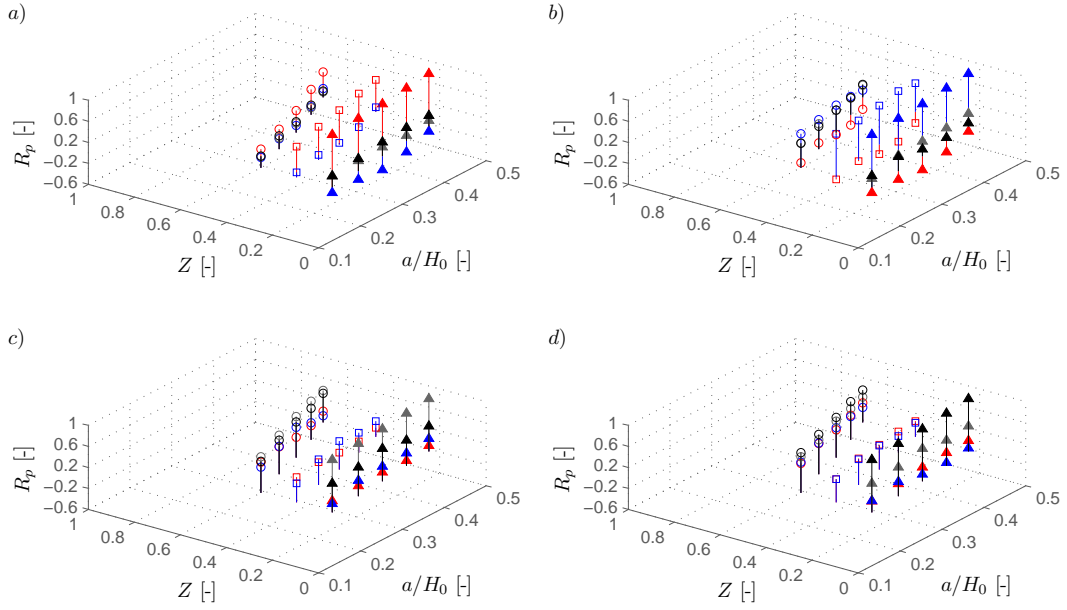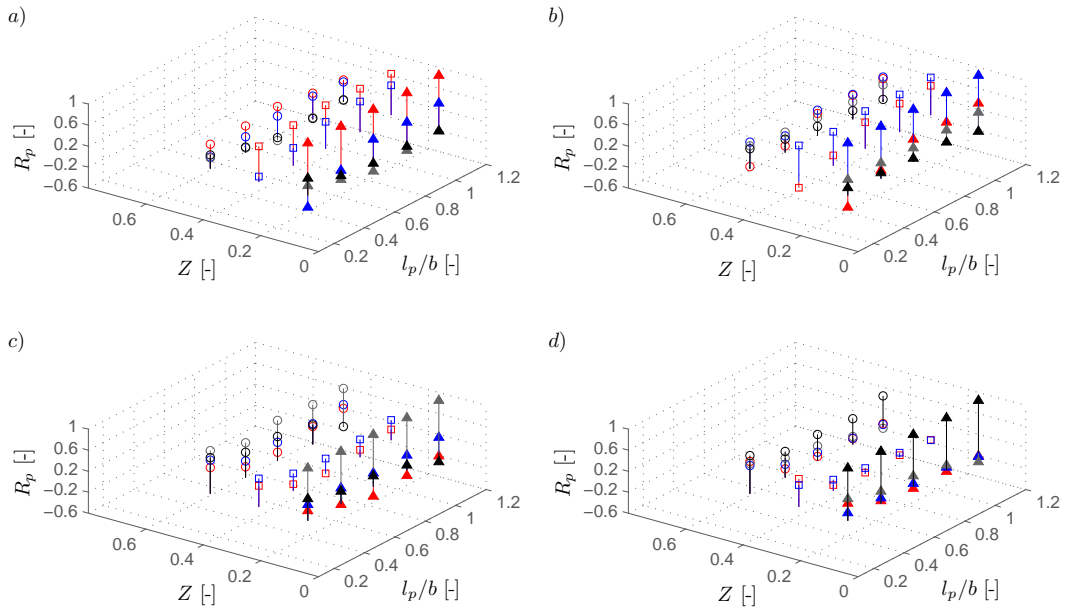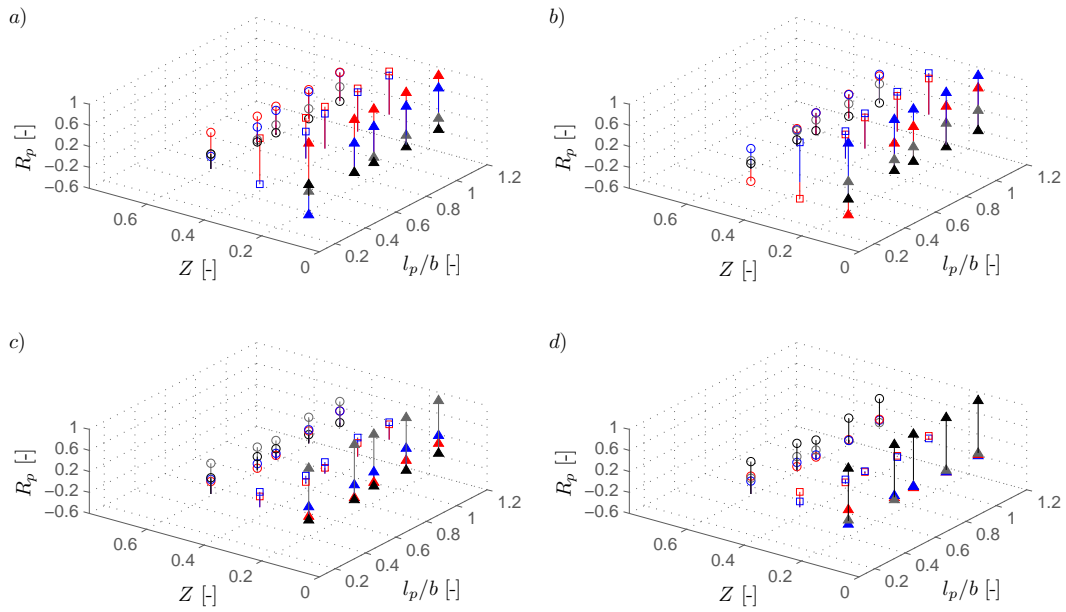
FIGURE A.26: Correlation coefficients for measurement series A1-1: Correlation of locations a) Ra1, b) Rb1, c) C1 and d) L1 to sample records at all available locations
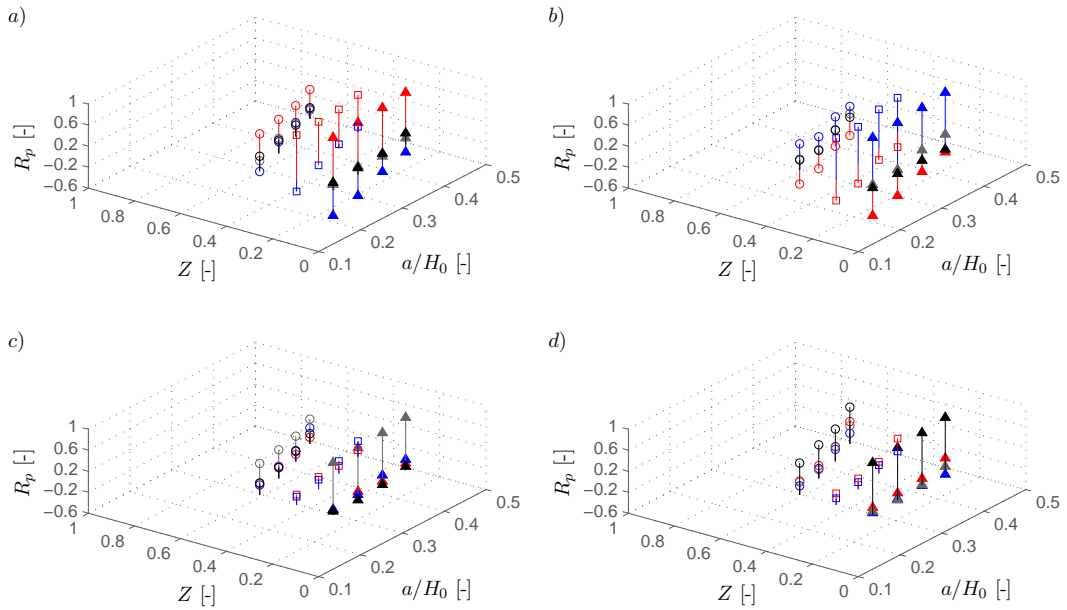
FIGURE A.27: Correlation coefficients for measurement series B1: Correlation of locations a) Ra1, b) Rb1, c) C1 and d) L1 to sample records at all available locations
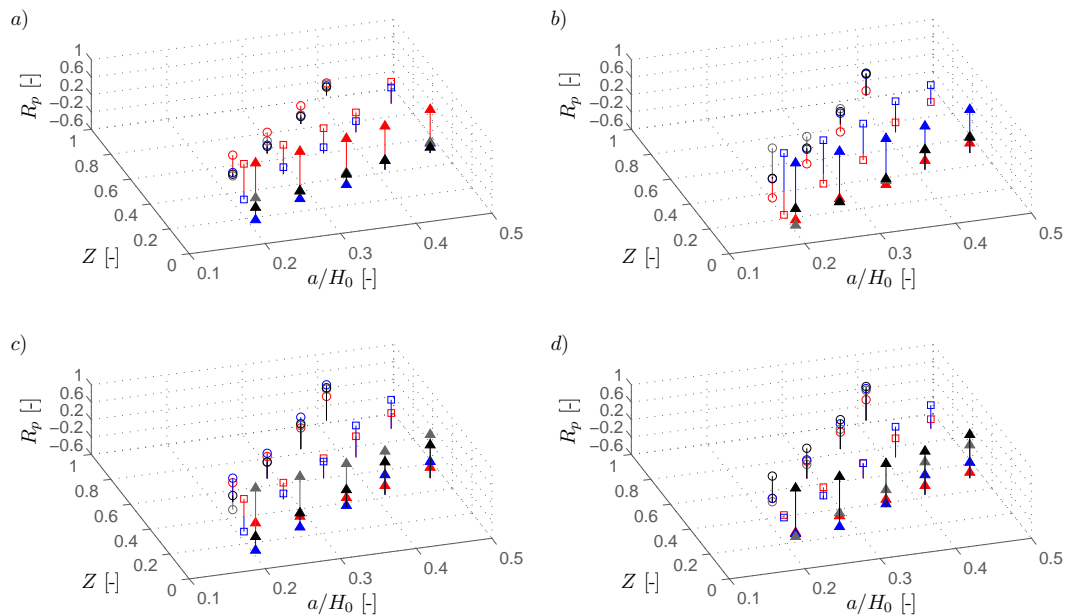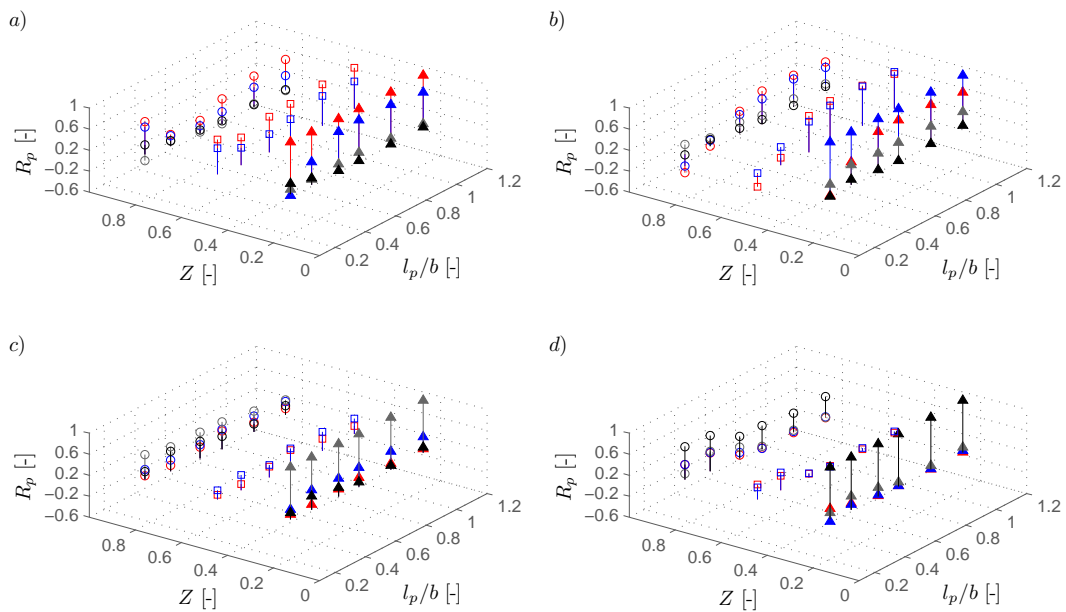
FIGURE A.28: Correlation coefficients for measurement series A2-2: Correlation of locations a) Ra1, b) Rb1, c) C1 and d) L1 to sample records at all available locations
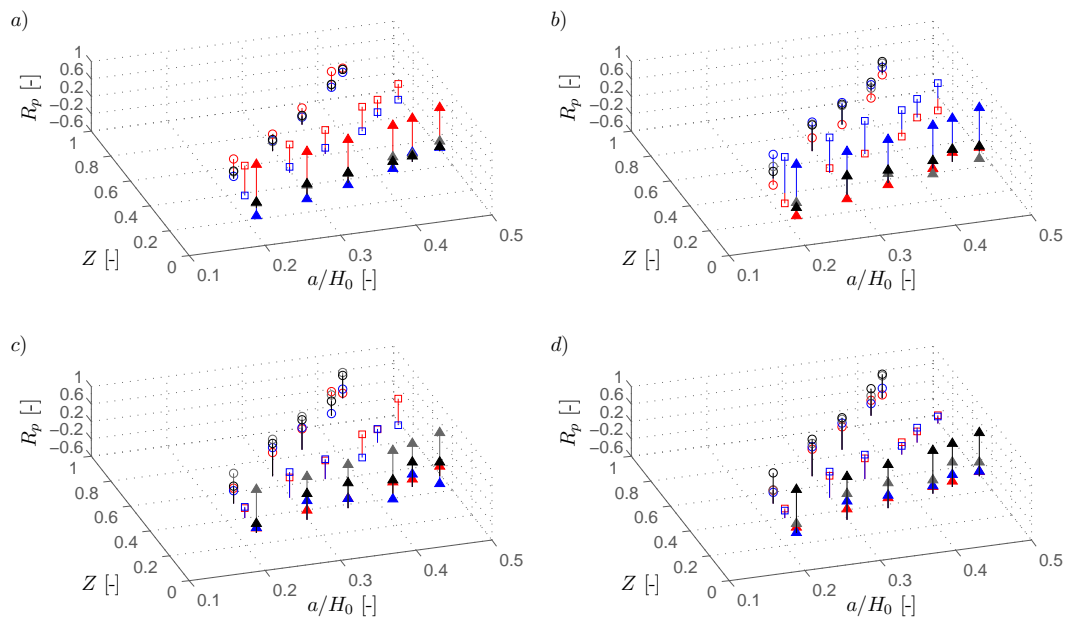
FIGURE A.29: Correlation coefficients for measurement series A2-1: Correlation of locations a) Ra1, b) Rb1, c) C1 and d) L1 to sample records at all available locations
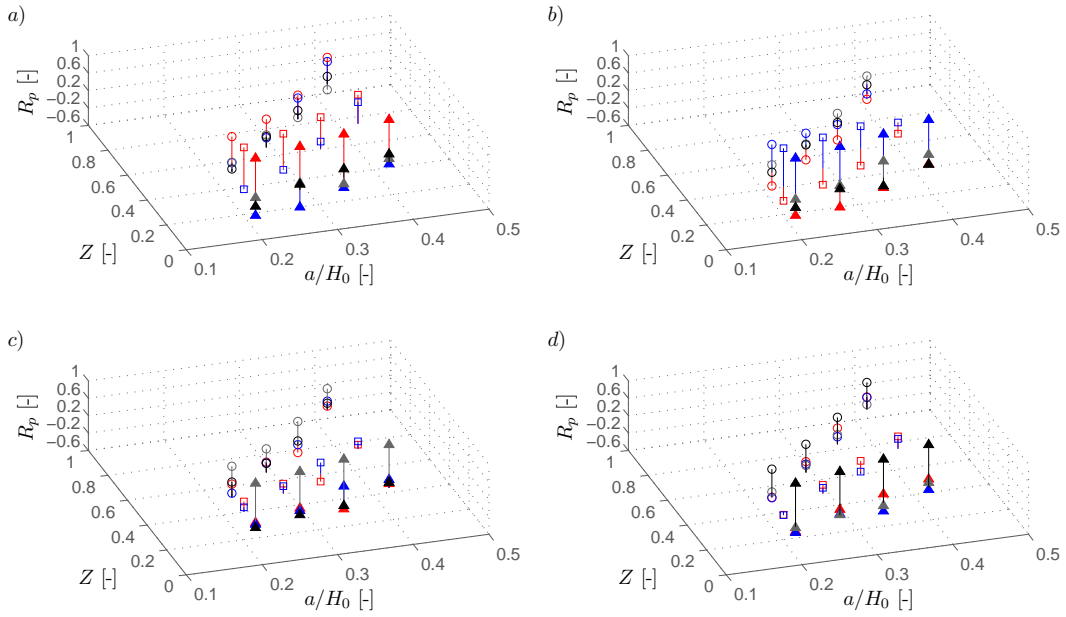
FIGURE A.30: Correlation coefficients for measurement series B2: Correlation of locations
a) Ra1, b) Rb1, c) C1 and d) L1 to sample records at all available locations

FIGURE A.31: Correlation coefficients for measurement series A3: Correlation of locations
a) Ra1, b) Rb1, c) C1 and d) L1 to sample records at all available locations

FIGURE A.32: Correlation coefficients for measurement series B3: Correlation of locations a) Ra1, b) Rb1, c) C1 and d) L1 to sample records at all available locations

FIGURE A.33: Correlation coefficients for measurement series C3: Correlation of locations a) Ra1, b) Rb1, c) C1 and d) L1 to sample records at all available locations

A.5 Amplitude spectra
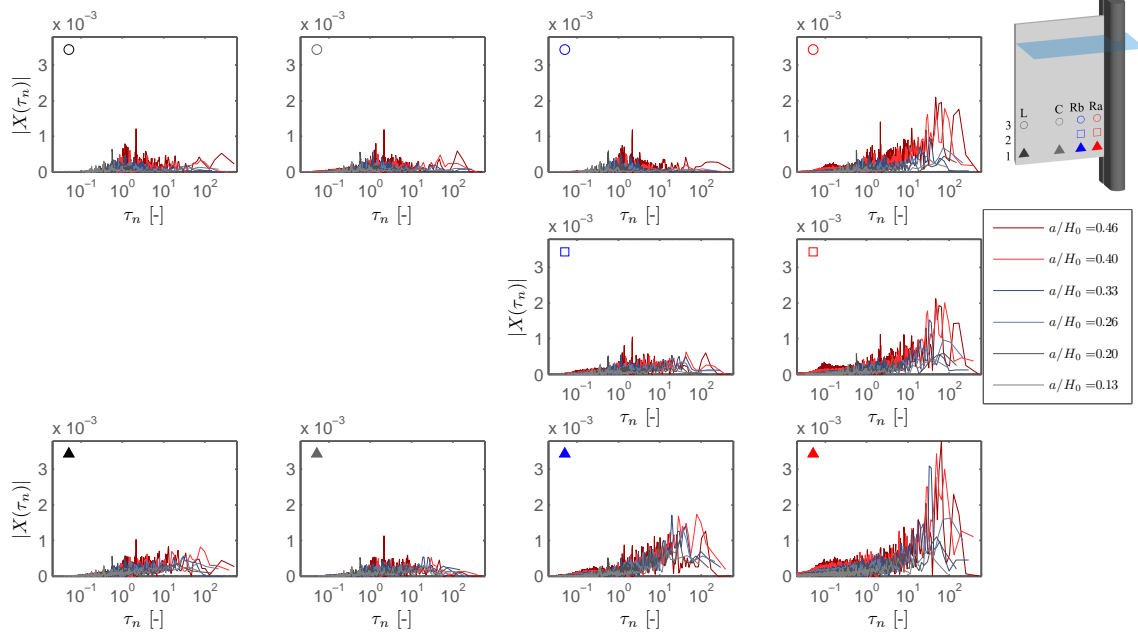
FIGURE A.34: Amplitude spectra derived from measurement series A1-2
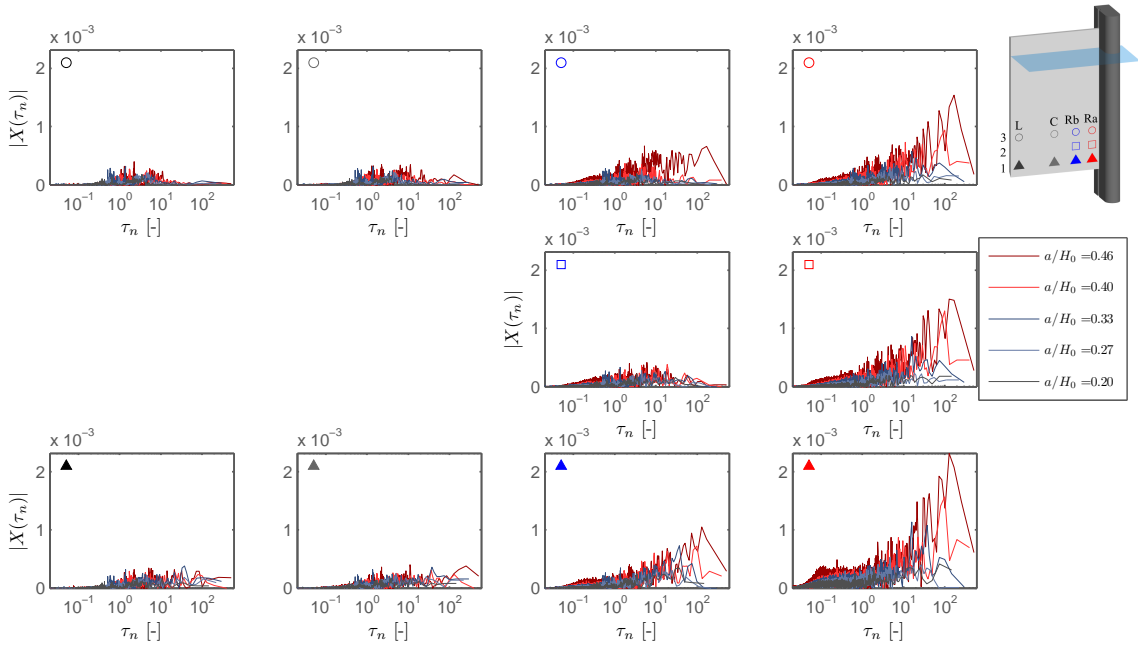
FIGURE A.35: Amplitude spectra derived from measurement series A1-1
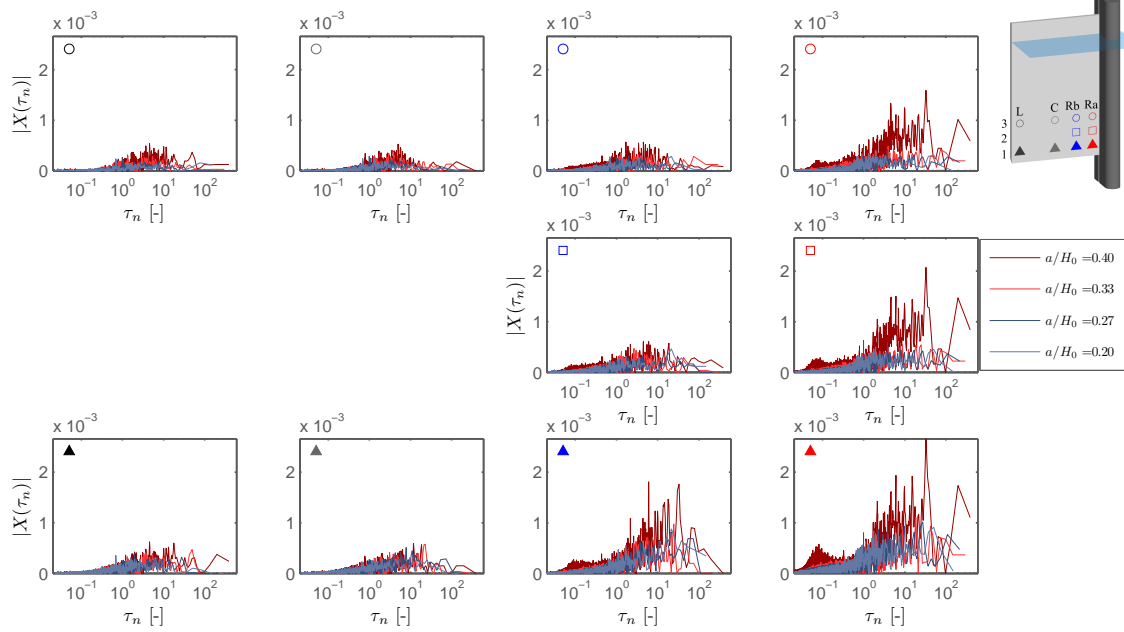
FIGURE A.36: Amplitude spectra derived from measurement series B1
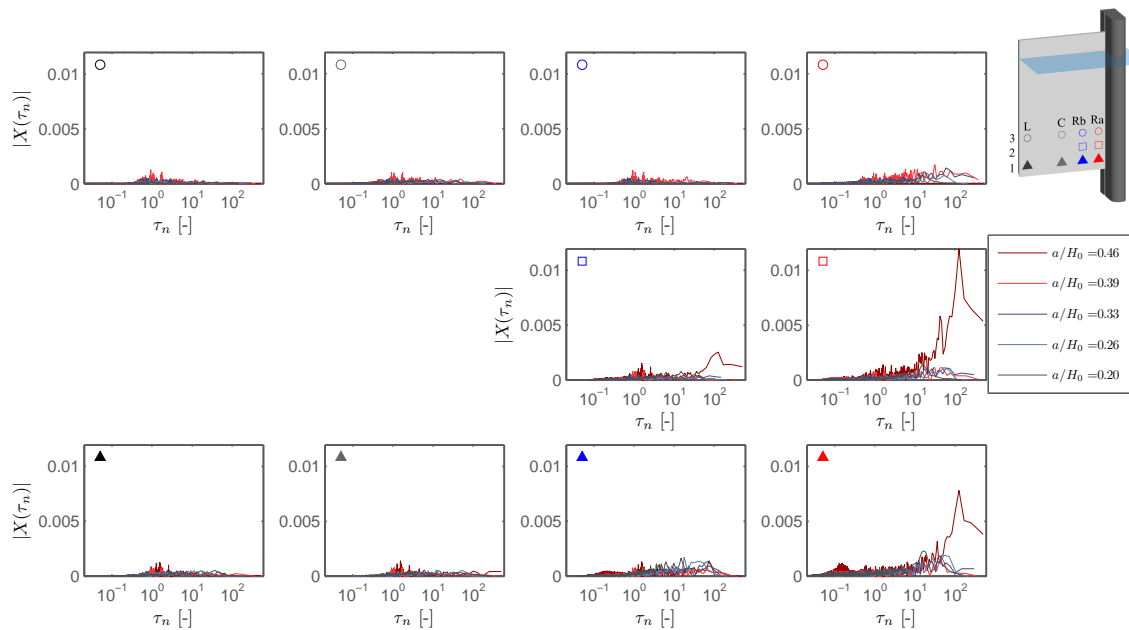
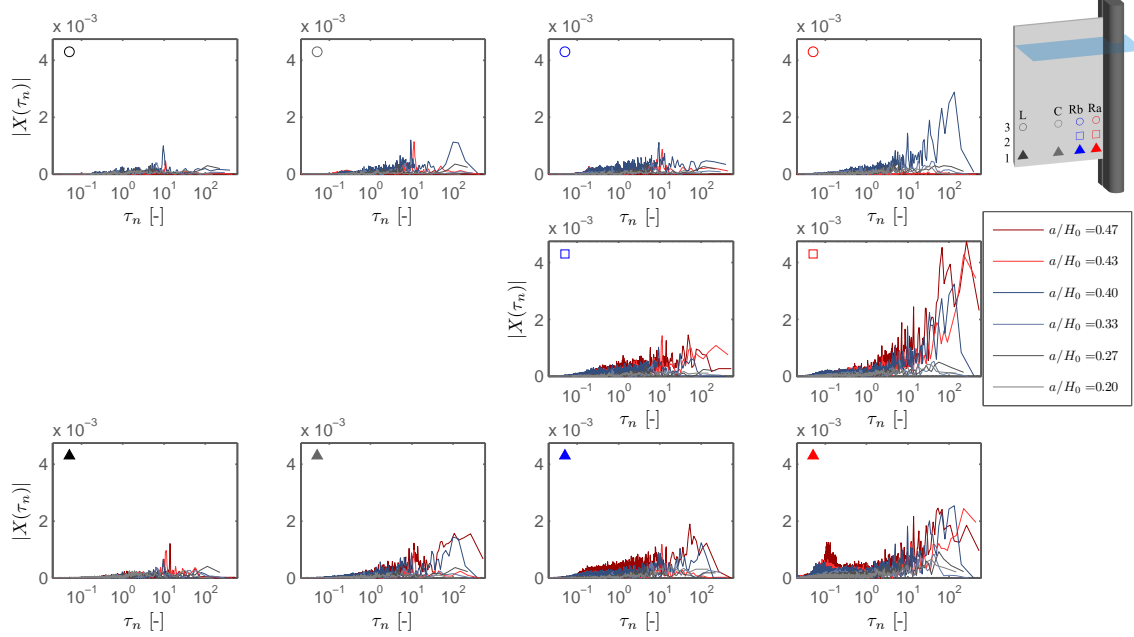FIGURE A.37: Amplitude spectra derived from measurement series A2-2

FIGURE A.38: Amplitude spectra derived from measurement series A2-1
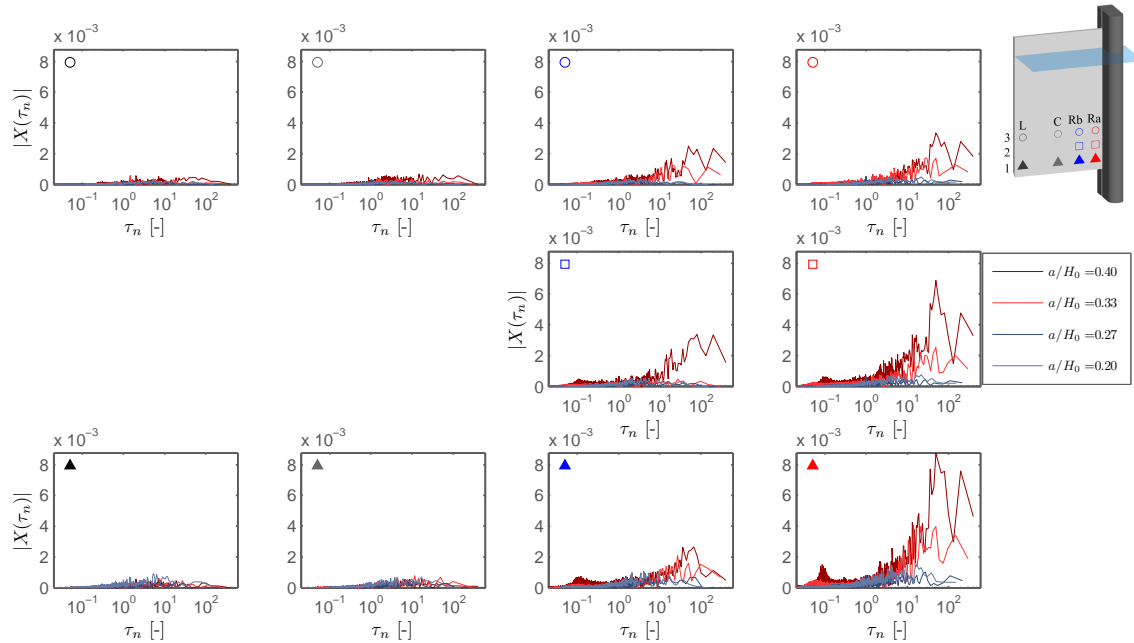

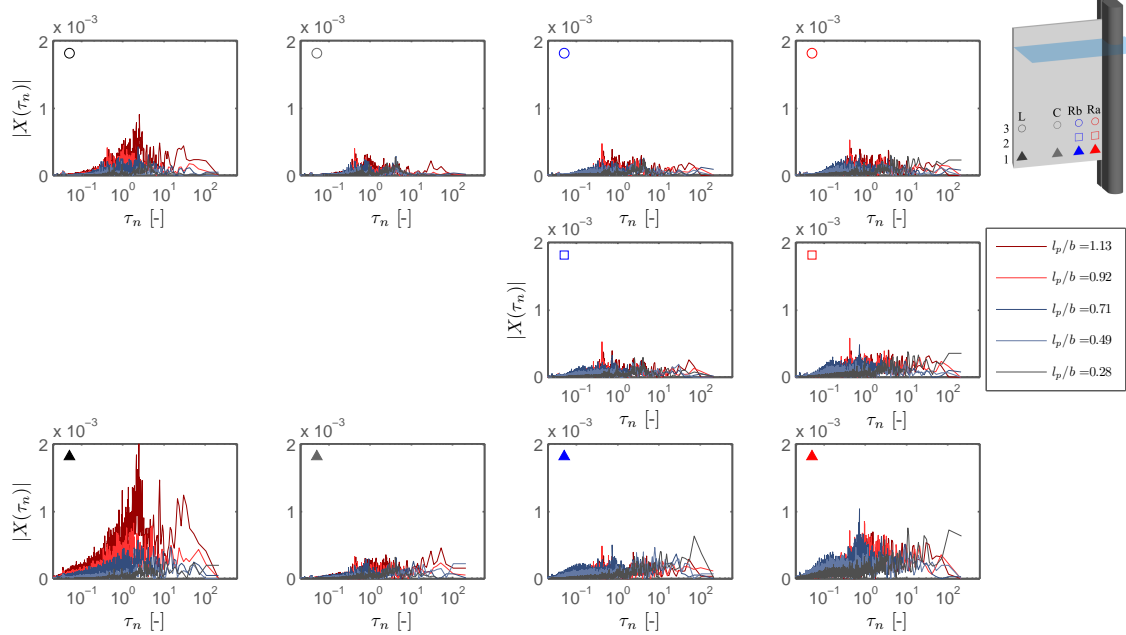FIGURE A.39: Amplitude spectra derived from measurement series B2

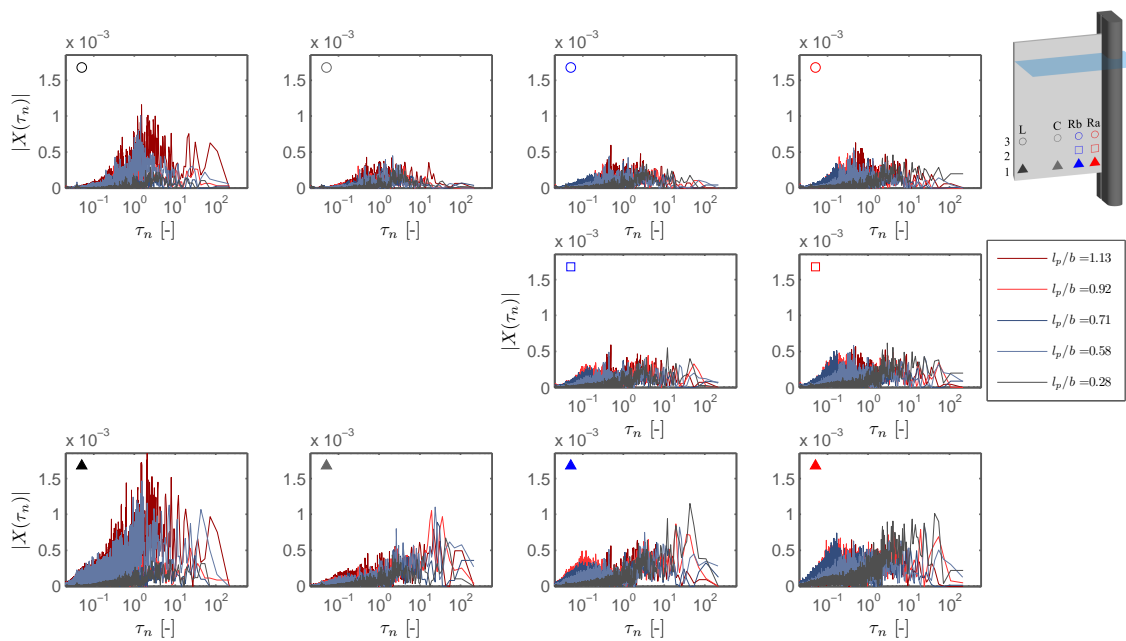FIGURE A.40: Amplitude spectra derived from measurement series A3

FIGURE A.41: Amplitude spectra derived from measurement series B3
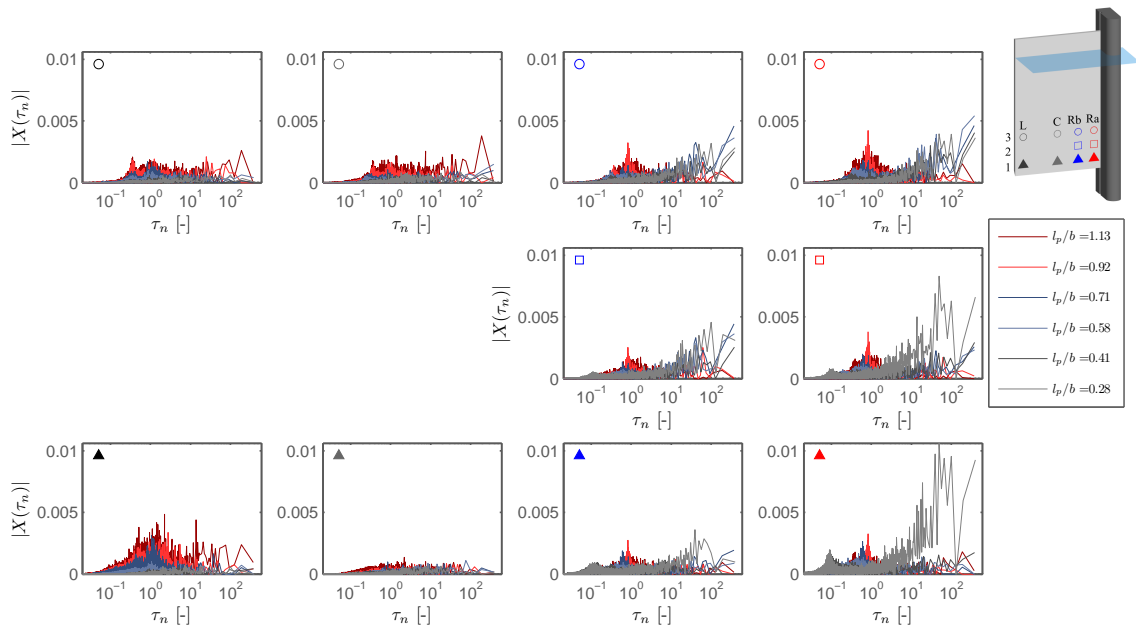
FIGURE A.42: Amplitude spectra derived from measurement series C3
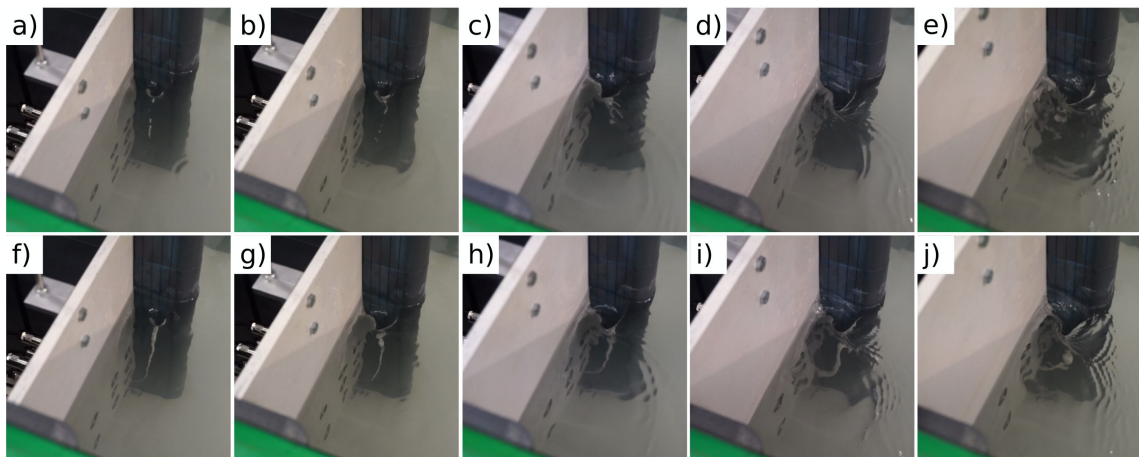
Appendix B

Vortex appearance

FIGURE B.1: Vortex appearance at the first gate during test series A1-1: weakest vortices at a) a/H_0 =0.2, b) 0.27, c) 0.33, d) 0.4 and e) 0.46 and strongest vortices at f) a/H_0 =0.2, g) 0.27, h) 0.33, i) 0.4 and j) 0.46
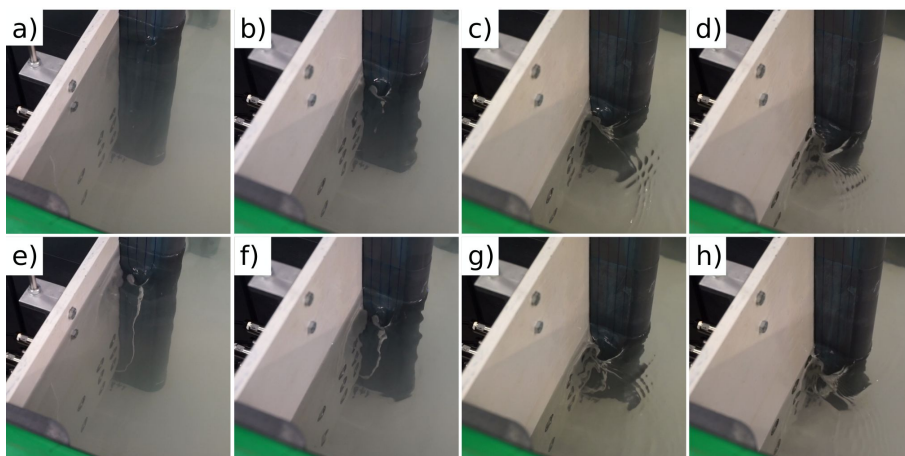

FIGURE B.2: Vortex appearance at the first gate during test series A2-1: weakest vortices at a) a/H_0 =0.2, b) 0.27, c) 0.33 and d) 0.4 and strongest vortices at e) a/H_0 =0.2, f) 0.27, g) 0.33 and h) 0.4

FIGURE B.3: Vortex appearance at the third gate during test series B1: weakest vortices at a) a/H_0 =0.2 and b) 0.27, strongest vortices at c) a/H_0 =0.2 and d) 0.27 and constant vortex strength at e) 0.33 and f) 0.4
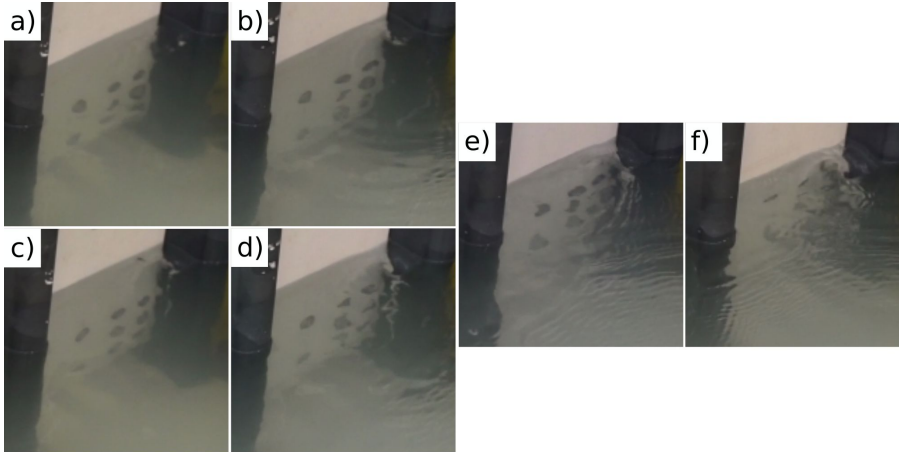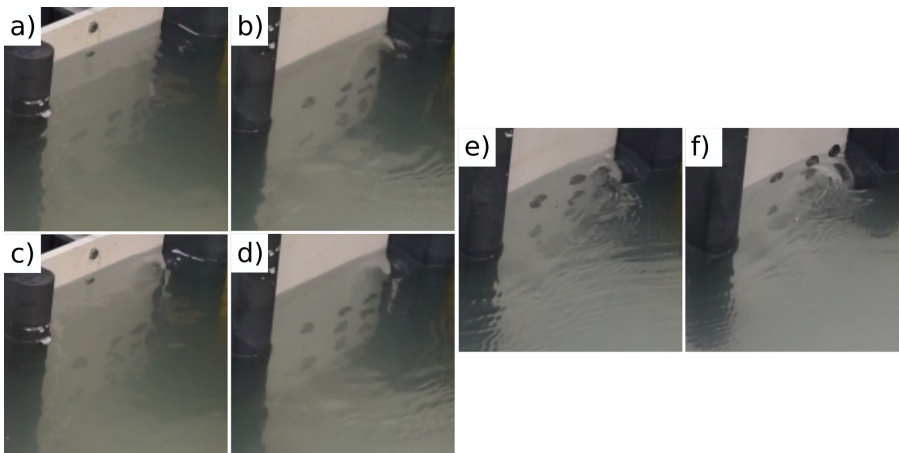

FIGURE B.4: Vortex appearance at the third gate during test series B2: weakest vortices at a) a/H_0 =0.2 and b) 0.27, strongest vortices at c) a/H_0 =0.2 and d) 0.27 and constant vortex strength at e) 0.33 and f) 0.4

Appendix C

Example of application

The application of the research results presented in this thesis is the prediction of pressure conditions at real gate structures. Subsequently the prototype of the model used for the pre-tests (see Section 3.1) is used to demonstrate the practical application in the following way:

- First the required input parameters are summarised in model scale and prototype scale.
- Second the flow conditions and hence the area at the gate prone to the vortex is discussed.
- Finally the charts provided for determination of the mean pressure and the pressure amplitudes are applied in accordance with the dimensionless parameters of the gate and the dynamic characteristics are investigated.

C.1   Input parameters

The parameters defining the problem are given in model scale (1:35) and prototype scale, indicated by the subscripts m and p respectively:

- Gate opening: $a_m = 200\,\text{mm}$, $a_p = 7.0\,\text{m}$
- Total head: $H_{0,m} = 529\,\text{mm}$, $H_{0,p} = 18.5\,\text{m}$
- Gate width: $b_m = 257\,\text{mm}$, $b_p = 9.0\,\text{m}$
- Pier head length: $l_{p,m} = 208\,\text{mm}$, $l_{p,p} = 7.3\,\text{m}$
- 4 gates: x-x-o-o

The deduced dimensionless parameters are:

- Relative gate opening: $a/H_0 = 0.39$
- Relative pier head length: $l_p/b = 0.42$

C.2   Flow conditions

The weir structure was located at the left side of the reservoir. Out of four gates, the two gates at the right side were opened (x-x-o-o). The goal is to predict the pressure condition at the third gate, at cross sections where data was obtained in the pre-test. Closing the two gates at the left caused an asymmetric approach flow from the left and a vortex forming at the left side upstream of the gate leaf.

It can be assumed that the vortex influences at least ~25 % of the gate width, which might be increased and shifted depending on the pier head length. The opening of the fourth gate increases the approach flow velocity and thereby enhances the asymmetry of the mean pressure and the pressure fluctuations. Hence the influence of both, the relative pier head length and relative approach flow velocity, is considered in the following application.

Two characteristic lateral locations are defined in order to represent the pressure conditions due to the vortex and at vortex free zones respectively. One cross section is defined at the left side of the gate and the second at the center of the gate, according to the location of the pressure taps in the pre-test, *i.e.*

- $y_1 = 0.101 \times b$ ($y_m = 26\,\text{mm}$, $y_p = 0.91\,\text{m}$ from left pier)
- $y_2 = 0.5 \times b$ (center line of the gate)

The vortex forms at the left side in the application problem, but is represented on the right side in the charts. Hence the input for the charts are the mirrored dimensionless lateral locations defined by $Y = 1 - y/b$. The dimensionless locations defining the input are

- $Y_1 = 0.9$ at the vortex zone and
- $Y_2 = 0.5$ at the center of the gate.

Finally all dimensionless geometric input parameters required are obtained and the increased relative approach flow will be considered qualitatively.

C.3   Mean pressure distribution

With the dimensionless parameters the pressure coefficient at an arbitrary point of the gate can be obtained by using the data represented in the charts given in Section 4.2. Thereby the fitting parameters k, l and m are determined in order to calculate the pressure distribution at the required cross sections at the gate according to

$$C_p(Z) = k(m - Z)Z^l$$

For the basic case the fitting parameters k and l are determined from Figure 4.19 and m is equal to unity. Subsequently correction factors for increased approach flow and pier head length can be obtained from Figure 4.26 and Figure 4.28. The correction factors concern the fitting parameter k, whereas l and m are not changed. The fitting parameters and

correction factors required to derive the mean pressure distribution at the above defined cross sections are summarised in Table C.1. The correction factor for increased approach

Y	$k = k_{o-x-x}$	l	m	$\frac{k_{o-x-x}}{k_{o-o-o}}$	k_{o-o-o}	$\frac{k_{o-o-o}(l_p)}{k_{o-o-o}}$	$k_{o-o-o}(l_p)$
0.9	0.975	0.099	1	0.923	0.900	1.007	0.906
0.5	1.034	0.091	1	0.975	1.009	0.997	1.006

TABLE C.1: Basic fitting parameters

flow velocity decreases k at both cross sections, *i.e.* the pressure is reduced. Due to the slightly longer relative pier head length compared to the basic case, the respective correction factor increases k slightly.

C.4 Extreme pressure

The pressure extrema can be characterised by obtaining the amplification factors given in Section 4.3.3. Hence envelope functions depending on the amplitudes of fluctuations are obtained by stretching the mean pressure distribution obtained above. Therefore amplification factors κ are obtained from Figure 4.37a&b for the basic case and increased approach flow velocity respectively. The parameters k_{min} and k_{max} for calculation of the envelope functions are obtained according to

$$k_{min} = k(1 - \kappa) \quad \text{and} \quad k_{max} = k(1 + \kappa)$$

The stretching factors κ obtained for low and increased approach flow are given in Table C.2, along with the adapted fitting parameters k_{min} and k_{max}.

Y	κ_{o-x-x}	$k_{min_{o-x-x}}$	$k_{max_{o-x-x}}$	κ_{o-o-o}	$k_{min_{o-o-o}}$	$k_{max_{o-o-o}}$
0.9	0.095	0.883	1.067	0.122	1.009	0.790
0.5	0.025	1.009	1.060	0.033	0.975	1.042

TABLE C.2: Amplification factor and fitting parameter k for different approach flow conditions

The amplification factors depending on the pier head length are given in Figure 4.38 at a relative gate opening of $a/H_0 = 0.27$. Assuming the same rate of change of amplification for other relative gate openings, the influence of the pier head length can be estimated. Therefore $\Delta\kappa$ has been determined by subtracting the amplification factor at $a/H_0 = 0.27$ given in Figure 4.36 from the amplification factors in Figure 4.38 according to

$$\Delta\kappa = \kappa(l_p) - \kappa(a/H_0)$$

The calculated values are represented by the contour lines in Figure C.1. With the data in Table C.2 and $\Delta\kappa$ the fitting parameters k_{min} and k_{max} for determination of the envelope
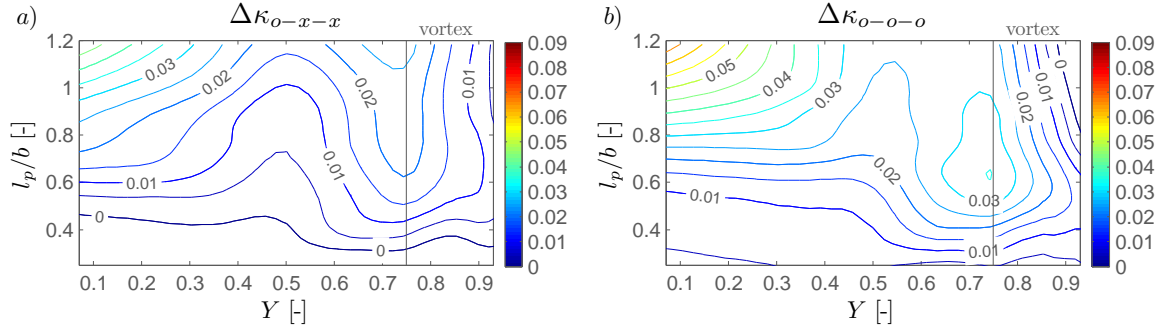
FIGURE C.1: Difference of the amplification factor due to the pier head length

functions can be determined according to

$$k_{min} = k(1 - (\kappa(a/H_0) + \Delta\kappa)) \quad \text{and} \quad k_{max} = k(1 + \kappa(a/H_0) + \Delta\kappa)$$

The values of $\Delta\kappa$ and calculated k_{min} and k_{max} are given in Table C.3. Finally the envelope

Y	$\Delta\kappa$	$k_{min_{o-o-o}}$	$k_{max_{o-o-o}}$
0.9	0.012	0.7853	1.027
0.5	0.010	0.962	1.049

TABLE C.3: Difference of amplification factor and fitting parameter k for increased pier head length

functions representing the pressure fluctuations about the mean pressure are defined for the basic case, increased approach flow and increased pier head length.

C.5 Results - mean and extreme pressure

The mean pressure distribution and envelope functions of fluctuations are plotted for three cases, *i.e.* the basic case, increased approach flow ($\uparrow v_0$) and considering the pier head length ($\uparrow l_p$). Figure C.2a characterises the pressure conditions due to the upstream forming vortex andFigure C.2b shows the conditions at vortex free zones. The primary and secondary x- and y-axis give the dimensionless pressure conditions (C_p, Z) as well as in prototype scale ($\overline{h}_p$, z_p). In Figure C.2a the mean pressure is smaller and the amplitudes of pressure fluctuations larger compared to Figure C.2b. A pressure drop due to increased approach flow velocity is recognisable at both cross sections, but is larger at the cross section with the upstream forming vortex (Figure C.2a). The influence of the pier head length is rather negligible. The pressure fluctuations are predicted to be considerably larger in the vortex region, reaching about ±8 % of the velocity head at the gate lip, fluctuating about the mean dynamic pressure. The mean pressure coefficients obtained at a discrete number of points in the pre-tests given in Figure 3.3 are plotted for comparison. They fit the results of the prediction considering increased approach flow.
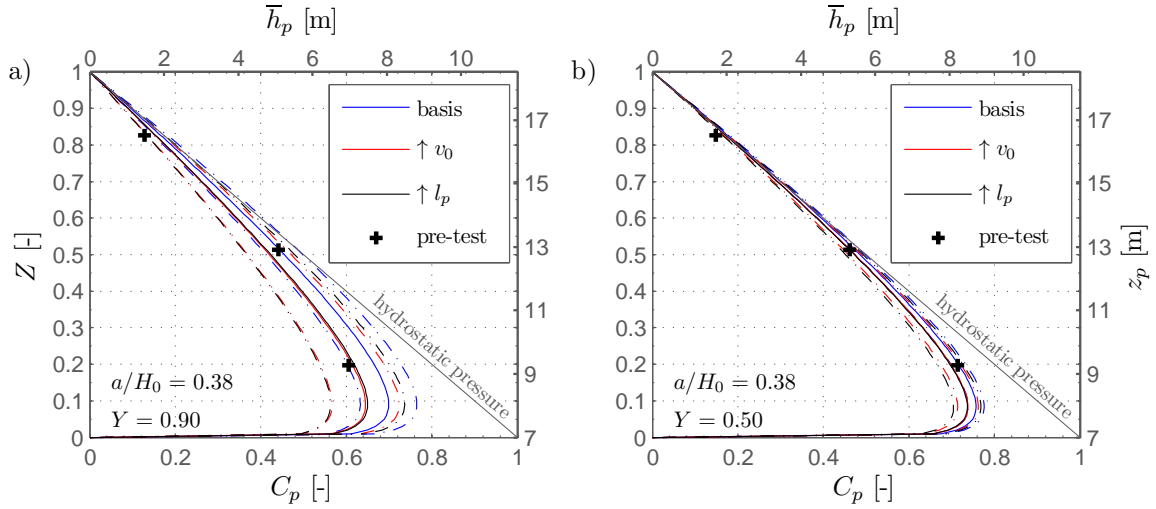
FIGURE C.2: Pressure characteristics at a vortex influenced region in comparison to the center of the gate

The submergence of the model gate is calculated as $v_{a,m}{}^2/2g = H_{0,m} - a_m = 0.33$ m, resulting in $v_{a,m} = 2.5$ m/s. According to Figure 4.41b it can be expected to predict the losses due to the vortex with low errors, and changing the fitting parameter m or considering a safety factor is not required. For further explanations see Section 4.4.

C.6 Dynamics of the impact

Dimensionless periods, characterising the components contributing to the pressure fluctuations are defined by the amplitude spectra in Figure 4.40. Relevant dimensionless periods were found to be $\tau_n \approx 0.08 - 0.8$ and $\tau_n \approx 20 - 170$, with amplitudes of $\sim 0.5\,\%$ and $\sim 1\,\%$ of the velocity head at the gate lip.

Equation (2.46) defines the dimensionless periods. In rearranged form the periods for the specific example can be calculated according to

$$\tau = \frac{a}{v_a}\tau_n$$

Substituting the dimensions in model scale ($a_m = 0.2$ m and $v_{a,m} = 2.5$ m/s) the specific periods in the hydraulic model (τ_m) are determined. Using the geometric parameters of the prototype ($a_p = 7$ m and $H_{0p} = 18.3$ m) the periods which should be tested for resonance in the prototype (τ_p) are determined. Considering the model scale of 1:35, and the scale factor for time, as given in Table 2.4, τ_p can also be calculated by $\tau_m \times \sqrt{35}$. The specific periods and frequencies ($f = 1/\tau$) calculated for the hydraulic model and the prototype are given in Table C.4.

In Lewin (2001) natural frequencies of gated structures at $5\,\%$ damping are cited to be between 3 and 12 Hz. The secondary maximum in the amplitude spectra at $\tau_n \approx 0.08 - 0.8$ scales to excitation frequencies of $\sim 3 - 30\,Hz$. Hence the natural frequency and the excitation frequency are possible to coincide. Frequency ratios below unity, $\omega/\omega_n \approx 0.25 - 10$ and

τ_n	τ_m [s]	τ_p [s]	f_m [Hz]	f_p [Hz]
~0.08-0.8	0.006-0.06	0.04-0.4	15.9-158.8	2.7-26.8
~20-170	1.6-13.4	9.3-79.2	0.07-0.6	0.01-0.1

TABLE C.4: Dynamic characteristic of the impact (period- and frequency range)

therefore transmissibility ratios above 1 are possible as indicated by Figure 2.13. Resonance in the range of the highest peak of the spectra is unlikely, due to the low frequencies of $f_p \approx 0.01 - 0.1$.